EUROPEAN ORGANIZATION FOR NUCLEAR RESEARCH

CERN-SPSC-2019–022
SPSC-P-360
October 13, 2019

Proposal for Measurements at the M2 beam line of the CERN SPS

– Phase-1 –

COMPASS++*/AMBER†

B. Adams[14,13], C.A. Aidala[1], G.D. Alexeev[15], M.G. Alexeev[42,43], A. Amoroso[42,43], V. Andrieux[45,20], N.V. Anfimov[15], V. Anosov[15], A. Antoshkin[15], K. Augsten[15,32], W. Augustyniak[47], C.D.R. Azevedo[4], B. Badełek[48], F. Balestra[42,43], M. Ball[8], D. Banerjee[45,20], J. Barth[8], R. Beck[8], J. Berenguer Antequera[42,43], J.C. Bernauer[35,46], J. Bernhard[20,o], M. Bodlak[31], F. Bradamante[40], A. Bressan[39,40], M. Büchele[17], V.E. Burtsev[41], C. Butler[3], C. Chatterjee[39,40], M. Chiosso[42,43], A.G. Chumakov[41], S.-U. Chung[18,b], A. Cicuttin[40,c], M. Connors[3], A. Contin[6], P. Correia[4], M.L. Crespo[40,c], S. Dalla Torre[40], S.S. Dasgupta[11], S. Dasgupta[40,11], N. Dashyan[51], I. Denisenko[15], O.Yu. Denisov[43], L. Dhara[11], F. Donato[44], S.V. Donskov[33], N. Doshita[50], Ch. Dreisbach[18], W. Dünnweber[d], R.R. Dusaev[41], A. Dzyuba[19], A. Efremov[15], P. Egelhof[16], F. Ehrler[21], A. Elagin[14], P.D. Eversheim[8], P. Faccioli[23], M. Faessler[d], J. Fedotova[26], M. Finger[31], M. Finger jr.[31], H. Fischer[17], C. Franco[23], J.M. Friedrich[18], V. Frolov[15], A. Futch[45], F. Gautheron[45], O.P. Gavrichtchouk[15], S. Gerassimov[28,18], S. Gevorkyan[15], Y. Ghandilyan[51], J. Giarra[25], I. Gnesi[42,43], M. Gorzellik[17], A. Grasso[42,43], A. Gridin[15], M. Grosse Perdekamp[45], B. Grube[18], R.I. Gushterski[15,k], A. Guskov[15], G. Hamar[40], D. von Harrach[25], X. He[3], R. Heitz[45], F. Herrmann[17], M. Hoffmann[8], N. Horikawa[30,e], S. Huber[18], A. Inglessi[19], A. Ilyichev[26], S. Ishimoto[50,g], A. Ivanov[15], N. Ivanov[51], T. Iwata[50], M. Jandek[31], V. Jary[32], C.-M. Jen[24], R. Joosten[8], P. Jörg[17], K. Juraskova[32], E. Kabuß[25], A. Karpishkov[34], F. Kaspar[18], D. Keller[12], A. Kerbizi[39,40], B. Ketzer[8], G.V. Khaustov[33], Yu.A. Khokhlov[33,h], M. Kim[1], O. Kiselev[16], Yu. Kisselev[15], F. Klein[9], J.H. Koivuniemi[45], V.N. Kolosov[33], K. Kondo[50], I. Konorov[28,18], V.F. Konstantinov[33], A.M. Kotzinian[43,j], O.M. Kouznetsov[15], A. Koval[47], Z. Kral[31], F. Krinner[18], Y. Kulinich[45], K. Kurek[47], R.P. Kurjata[49], A. Kveton[31], S. Levorato[40], J. Lichtenstadt[36], K. Liu[24], M.X. Liu[24], R. Longo[45], W. Lorenzon[1], M.J. Losekamm[18], V.E. Lyubovitskij[41,m], E. Maev[19], A. Maggiora[43], V. Makarenko[26], N. Makins[45], N. Makke[40], G.K. Mallot[20], A. Maltsev[15], S.A. Mamon[41], B. Marianski[47], A. Martin[39,40], H. Marukyan[51], J. Marzec[49], N. Masi[7], J. Matoušek[39,40], T. Matsuda[27], G. Mattson[45], G.V. Meshcheryakov[15], W. Meyer[5], M. Meyer[45], Yu.V. Mikhailov[33], M. Mikhasenko[20], M. Minot[13],

*COmmon Muon Proton Apparatus for Structure and Spectroscopy

†Apparatus for Meson and Baryon Experimental Research

E. Mitrofanov[15], Y. Miyachi[50], E. Montbarbon[20,o], A. Moretti[39,40], A. Nagaytsev[15], G. Nigmatkulov[29], A. Mkrtchyan[51], H. Mkrtchyan[51], M. Nefedov[34], J. Nový[32], W.-D. Nowak[25], F. Nozzoli[38], G. Nukazuka[50], A.G. Olshevsky[15], M. Ostrick[25], D. Panzieri[43,n], B. Parsamyan[42,43], S. Paul[18], H. Pekeler[8], J.-C. Peng[45], I. Peric[21,p], D.V. Peshekhonov[15], M. Pešek[31], M. Pešková[31], G. Petrov[19], N. Pierre[25], C. Menezes Pires[23], J. Pochodzalla[25], V.A. Polyakov[33], T. Pöschl[18], J. Pretz[9,i], L. Quadrani[6], M. Quaresma[23], C. Quintans[23], R. Raymond[1], G. Reicherz[5], P.E. Reimer[2], C. Riedl[45], D.I. Ryabchikov[33,18], A. Rybnikov[15], A. Rychter[49], A. Rymbekova[15], R. Salac[32], V. Saleev[34], V.D. Samoylenko[33], A. Sandacz[47], S. Sarkar[11], M. Sarsour[3], I.A. Savin[15], G. Sbrizzai[40], S. Scherrers[17], R. Schimassek[21], H. Schmieden[9], A. Selyunin[15], T. Shin[2], A. Shipilova[34], H. Simon[16], L. Sinha[11], M. Slunecka[31], J. Smolik[15], A. Srnka[10], D. Steffen[18], M. Stolarski[23], O. Subrt[32], M. Sulc[22], X. Sun[3], H. Suzuki[50,e], A. Szabelski[39,40], P. Sznajder[47], V. Tchekhovski[26], S. Tessaro[40], F. Tessarotto[40], A. Thiel[8], J. Tomsa[31], F. Tosello[43], V. Tskhay[28], S. Uhl[18], B.I. Vasilishin[41], A. Vassiliev[19], A. Vauth[9], B.M. Veit[20,25], J. Veloso[4], M. Virius[32], A. Vorobyev[19], M. Wagner[8], S. Wallner[18], A. Weber[21,q], K. Zaremba[49], P. Zavada[15], M. Zavertyaev[28], E. Zemlyanichkina[15], Y. Zhao[40], N. Zhuravlev[15], M. Ziembicki[49], P. Zuccon[37]

[1] Randall Laboratory of Physics, University of Michigan, Ann Arbor, MI 48109-1040, USA
[2] Physics division, Bldg 203, Argonne National Laboratory, 9700 S. Cass Ave., Lemont, IL 60439, USA
[3] Georgia State University, Atlanta, GA 30302, USA
[4] University of Aveiro, i3N, Dept. of Physics, 3810-193 Aveiro, Portugal
[5] Universität Bochum, Institut für Experimentalphysik, 44780 Bochum, Germany
[6] Unicersità di Bologna and INFN Sezione di Bologna, Bologna, Italy
[7] INFN Sezione di Bologna, Bologna, Italy
[8] Universität Bonn, Helmholtz-Institut für Strahlen- und Kernphysik, 53115 Bonn, Germany
[9] Universität Bonn, Physikalisches Institut, 53115 Bonn, Germany
[10] Institute of Scientific Instruments, AS CR, 61264 Brno, Czech Republic
[11] Matrivani Institute of Experimental Research & Education, Calcutta-700 030, India
[12] Department of Physics, University of Virginia, 382 McComick Rd., PO Box 400714, Charlottesville, VA 22904-4714
[13] Incom Inc., Charlton, MA 01507, USA
[14] Enrico Fermi Institute, University of Chicago, Chicago, IL 60637, USA
[15] Joint Institute for Nuclear Research, 141980 Dubna, Moscow region, Russia
[16] GSI Helmholtzzentrum für Schwerionenforschung, 64291 Darmstadt, Germany
[17] Universität Freiburg, Physikalisches Institut, 79104 Freiburg, Germany
[18] Technical University of Munich, Department of Physics, 85748 Garching, Germany
[19] Petersburg Nuclear Physics Institute, 188300 Gatchina, Russia
[20] CERN, 1211 Geneva 23, Switzerland
[21] Karlsruhe Institute of Technology, P.O. Box 6980, 76049 Karlsruhe, Germany
[22] Technical University in Liberec, 46117 Liberec, Czech Republic
[23] LIP, 1649-003 Lisbon, Portugal
[24] Physics Division, Los Alamos National Laboratory, Los Alamos, NM 87545, USA
[25] Universität Mainz, Institut für Kernphysik, 55099 Mainz, Germany
[26] Institute for Nuclear Problems of Belarusian State University, Minsk, Belarus
[27] University of Miyazaki, Miyazaki 889-2192, Japan
[28] Lebedev Physical Institute, 119991 Moscow, Russia
[29] National Research Nuclear University MEPhI, Moscow, Russia
[30] Nagoya University, 464 Nagoya, Japan
[31] Charles University in Prague, Faculty of Mathematics and Physics, 18000 Prague, Czech Republic
[32] Czech Technical University in Prague, 16636 Prague, Czech Republic

[33] State Scientific Center Institute for High Energy Physics of National Research Center 'Kurchatov Institute', 142281 Protvino, Russia
[34] Department of Physics, Samara National Research University,443086 Samara, Russia
[35] Stony Brook University, SUNY, Stony Brook, NY 11794-3800, USA
[36] Tel Aviv University, School of Physics and Astronomy, 69978 Tel Aviv, Israel
[37] Università degli Studi di Trento and INFN-TIFPA, Trento, Italy
[38] INFN-TIFPA, Trento, Italy
[39] University of Trieste, Dept. of Physics, 34127 Trieste, Italy
[40] Trieste Section of INFN, 34127 Trieste, Italy
[41] Tomsk Polytechnic University,634050 Tomsk, Russia
[42] University of Turin, Dept. of Physics, 10125 Turin, Italy
[43] Torino Section of INFN, 10125 Turin, Italy
[44] Università di Torino and INFN-Torino, Turin, Italy
[45] University of Illinois at Urbana-Champaign, Dept. of Physics, Urbana, IL 61801-3080, USA
[46] RIKEN BNL Research Center, Brookhaven National Laboratory, Upton, NY 11973-5000, USA
[47] National Centre for Nuclear Research, 02-093 Warsaw, Poland
[48] University of Warsaw, Faculty of Physics, 02-093 Warsaw, Poland
[49] Warsaw University of Technology, Institute of Radioelectronics and Multimedia Technology, 00-665 Warsaw, Poland
[50] Yamagata University, Yamagata 992-8510, Japan
[51] A.Alikhanyan National Science Laboratory, Yerevan Physics Institute Foundation, Alikhanian Br. Street, 0036, Yerevan, Armenia

[a] The groups Institute of Physics, Academia Sinica from Taipei (Taiwan), Institute of Modern Physics, Chinese Academy of Science from Lanzhou (China), and Tsinghua University from Beijing (China) have confirmed their interest in the physics case as described in this proposal document. They have signed the LoI and are intending to join the collaboration once manpower issues will have been clarified
[b] Also at Physics Dept., Brookhaven National Laboratory, Upton, NY 11973, USA
[c] Also at Abdus Salam ICTP, 34151 Trieste, Italy
[d] Supported by the DFG cluster of excellence 'Origin and Structure of the Universe' (www.universe-cluster.de) (Germany)
[e] Also at Chubu University, Kasugai, Aichi 487-8501, Japan
[f] Also at Dept. of Physics, National Central University, 300 Jhongda Road, Jhongli 32001, Taiwan
[g] Also at KEK, 1-1 Oho, Tsukuba, Ibaraki 305-0801, Japan
[h] Also at Moscow Institute of Physics and Technology, Moscow Region, 141700, Russia
[i] Present address: RWTH Aachen University, III. Physikalisches Institut, 52056 Aachen, Germany
[j] Also at Yerevan Physics Institute, Alikhanian Br. Street, Yerevan, Armenia, 0036
[k] Also at Institute for Nuclear Research and Nuclear energy, Bulgarian Academy of Sciences, Bulgaria
[l] Also at Dept. of Physics, National Kaohsiung Normal University, Kaohsiung County 824, Taiwan
[m] Also at Institut für Theoretische Physik, Universität Tübingen, 72076 Tübingen, Germany
[n] Also at University of Eastern Piedmont, 15100 Alessandria, Italy
[o] Having contributed to several studies, the member of CERN personnel does not take position nor responsibility towards the required approval processes as established by the organization.
[p] Also at Institute for Data Processing and Electronics, Karlsruhe Institute of Technology, P.O. Box 6980, 76049 Karlsruhe, Germany
[q] Also at Heidelberg University, Grabengasse 1, 69117 Heidelberg, Germany

Contents

Preamble

In the context of the Physics Beyond Colliders initiative at CERN, the COMPASS++/AMBER proto-collaboration recently submitted a Letter of Intent (LoI) [1] to the SPSC in order to establish a "New QCD facility at the M2 beam line of the CERN SPS". Such an unrivalled installation would make the experimental hall EHN2 the site for a great variety of measurements to address fundamental issues of strong interactions in the medium and long-term future. The proposed measurements cover a wide range in the squared four-momentum transfer Q^2 and hence in the distance scale for probing the hadron. At lowest values of Q^2, or equivalently large distances, we want to determine the proton charge radius through elastic muon-proton scattering, at intermediate Q^2 we want to perform spectroscopy of mesons and baryons by using dedicated meson beams, and at high Q^2, *i.e.* small distances, we plan to study the structure of mesons and baryons via the Drell-Yan process.

In the LoI, submitted in the middle of 2018, we describe physics goals, sensitivity reach and competitiveness for such a future general-purpose fixed-target facility at CERN. In response to the LoI, the SPSC requested a proposal for those measurements that we plan to perform in the years 2022 to 2024. We submitted the original version of the proposal (version v1) to the SPSC in late May 2019 [2]. This document describes phase-1 of our long-term project, *i.e.* our prioritised list of measurements planned to be performed at the M2 beam line using the existing muon beam and conventional hadron beams.

The present document, *i.e.* version v2 of our proposal, was submitted to the SPSC in late September 2019. It was produced to keep pace with the progress in preparing the proposed measurements. The table below shows the actual list of updates contained in the present document, where v2(new), v2(+), v2(++) or v2(+++) is appended to the headline of every (sub)subsection that was newly written or updated in v2 with respect to v1 with minimal, medium, or substantial changes, respectively.

Beyond LS3, we propose an upgrade of the M2 beam line by installing a radio-frequency (RF) separation stage for kaon and antiproton beams of high energy and high intensity. Such beams allow for further unique measurements that cannot be performed elsewhere. The proposed RF upgrade of the M2 beam line is presently under study at CERN EN-EA. The full project described in the LoI is expected to stretch across the next 10 to 15 years. As it continues to attract physicists world-wide, the physics scope of the facility should remain open for future exciting ideas, using (RF-separated) hadron beams or the muon beam. Proposals for further measurements, based upon ideas already discussed in the LoI or possible new ones, will be submitted in due time.

Section name	**Section number v2**	**Section number v1**	**Status v2 w.r.t. v1**
Executive summary			v2(++)
Introduction	1	1	v2(+++)
Proton radius experiment	2.1	2.1	v2(+++)
	2.2	2.1.1	v2(+)
	2.3	—	v2(new)
	2.6	2.2.1	v2(++)
	2.7	2.6.1	v2(++)
	2.8	2.7.1	v2(++)
	2.9	—	v2(new)
Drell-Yan measurements	3.1	3.1	v2(+++)
	3.2	3.2	v2(+)
	3.3	3.3	v2(++)
	3.4.1	3.4.1	v2(+)
	3.5.1	3.5.1	v2(++)
	3.6	3.6	v2(+)
	3.7	3.7	v2(+)
	3.8	3.8	v2(++)
Anti-particle cross sections	4.1	4.1	v2(+)
	4.6	4.6	v2(+)
	4.7	4.7	v2(+++)
Instrumentation	5.3.1	5.3.1	v2(+)
	5.4.1	—	v2(new)
	5.4.2	5.4.1	v2(+)

Executive Summary [v2(++)]

The COMPASS++/AMBER (proto-)collaboration proposes to establish a

"New QCD facility at the M2 beam line of the CERN SPS"

and perform in phase-1 (see Table 1 for the tentative schedule) three experiments that will use either muons or hadrons delivered by the existing M2 beam line:

(1) Proton charge-radius measurement using muon–proton elastic scattering

This experiment aims at a precision determination of the electric mean-square charge radius of the proton. The proposed measurement using elastic muon-proton scattering appears timely, since in spite of many years of intense activity the proton-radius puzzle remains unsolved up to now. Given the presently available experimental techniques, a complete answer to this problem requires four key measurements: elastic lepton scattering to measure the Q^2-dependence of the electric form factor and atomic spectroscopy to study finite-size effects in atomic levels. Both types of experiments can be carried out with electrons or muons. To date, results are available for three types of experiments, but not yet for elastic muon–proton scattering.

Presently, a discrepancy as large as five standard deviations exists between the two most recent precision measurements: $r^{\rm rms}_{\rm CREMA} = 0.841 \pm 0.001$ fm from line-splitting measurements in laser spectroscopy of muonic hydrogen and $r^{\rm rms}_{\rm MAMI} = 0.879 \pm 0.008$ fm from elastic electron-proton scattering.

We propose to perform the muon–proton experiment using high-energy muons of the CERN M2 beam line. Our measurement will provide a new and completely independent result on the proton charge radius with a statistical accuracy of 0.01 fm or better and considerably smaller systematic uncertainty. Using muons instead of electrons is highly advantageous, as several experimental systematic effects and also theoretical corrections are considerably smaller. The measurement will employ a time-projection chamber filled with pure hydrogen up to pressures of 20 bar, which serves at the same time as a target and as detector gas.

The accuracy to be reached by the proposed muon-proton scattering experiment is expected to be comparable to that obtained in electron-proton scattering at MAMI. Comparing the results on the proton charge-radius from these two complementary measurements may allow probing interpretations of the proton-radius mismatch based on lepton-flavour effects.

(2) Drell-Yan and J/ψ production experiments using the conventional M2 hadron beam

The main objective of these measurements is to study the structure of the pion, *i.e.* to determine the poorly known pion valence and sea-quark parton distribution functions (PDFs). Modern theory reveals that the properties of the nearly-massless pion are the cleanest expression of the mechanism that is responsible for (almost) all the visible mass in the Universe [3]; the associated theory simultaneously reconciles the emergence of the proton mass with the masslessness of the pion in the chiral limit [4]. It shows, too, that a determination of the valence-quark PDF of the pion provides the needed sensitivity to the mechanism(s) responsible for the emergence of mass in QCD. The planned measurements will also provide benchmarks for testing recent predictions of non-perturbative QCD calculations performed on the lattice or in the framework of the Dyson-Schwinger equations.

Furthermore, an analysis that simultaneously accounts for the differential cross section and for the degree of polarisation of the charmonia resonances produced is expected to provide stringent experimental constraints on their production mechanisms. J/ψ production provides an alternative access to both quark and gluon distributions in the incoming meson.

In parallel to pion structure measurements, the availability of heavier nuclear targets in the setup will allow the study of cold nuclear effects such as nuclear PDFs and parton energy loss.

(3) Measurement of proton-induced antiproton production cross sections for dark matter searches

The purpose of this experiment is the measurement of the antiproton production cross sections in proton-proton and proton-^{4}He scattering for projectile energies from several tens to a few hundred GeV. In combination with similar measurements by LHCb in the TeV range, our measurements will provide a fundamental data set that is expected to allow for a significantly higher accuracy of the predicted natural flux of antiprotons in galactic cosmic rays. This is of great importance as the indirect detection of dark matter (DM) is based on the search for products of DM annihilation or decay, which are expected to appear as distortions in the spectra of rare cosmic ray components like positrons, antiprotons, or even antideuterons. Our new data set will thus substantially improve the sensitivity of existing (and future) very accurate antiproton flux measurements to DM signals, which is presently limited by the poor knowledge of the antiproton production cross sections.
The existing M2 hadron beam line with its momentum range between 20 and 280 GeV/c is an ideal place to perform this measurement. The antiproton production cross section will be measured double-differentially in momentum and forward angle, using the spectrometer in EHN2 equipped alternatively with liquid-hydrogen and liquid-helium targets, as well as the antiproton-identification capabilities of the RICH detector. The cross section will be measured for several beam momenta in $20x20$ bins of antiproton momentum and pseudorapidity. A 1% statistical uncertainty will be reached for the cross section, with an anticipated point-to-point systematic uncertainty of less than 5%.

Novel **instrumentation** using modern detector architecture will be constructed and installed in the experimental hall EHN2, where the upgraded multi-purpose two-stage magnetic spectrometer will serve as experimental backbone of the new facility. New or upgraded hardware will be designed to serve for as many individual experiments as possible and installed along the lifetime of the facility according to actual needs and availabilities.

The **tentative schedule of the measurements proposed in this document at the M2 beam line** is outlined in Table 1, according to the information given in [5].
The proposed measurements are attributed to beam times in the years 2021-24. The current planning is made assuming that SPS operation after LS2 starts in 2021. Should the start-up of the machine be delayed, our planning can easily be adapted accordingly. Since the physics cases that we discuss are of longer-term character and without time-critical competition, their relevance will be untouched by such a delay. In the present estimate, the total requested time will exceed the available beam time in Run 3, such that the Drell-Yan measurements may have to be continued after LS3.

Table 1: Tentative schedule for the proposed measurements at the M2 beam line for the time period between LS2 and LS3. The numbers of days in parentheses are times for setting up and commissioning. For the proton radius measurement, the proposed running time is based on the conservative estimate discussed in the main text along with Eq. 11.

Year	**Activity**	**Duration**	**Beam**
2021	Proton radius test measurement	20 days	μ
2022	Proton radius measurement	120 (+40) days	μ
	Antiproton production test measurement	10 days	p
2023	Antiproton production measurement	20(+10) days	p
	Proton radius measurement	140 (+10) days	μ
2024 2024+	Drell-Yan: pion PDFs and charmonium production mechanism	$\lesssim$ 2 years	p, K^+, π^+, $\bar{p}$, K^-, π^-

The **Outlook** of the proposal recapitulates the future plans of COMPASS++/AMBER in accordance with what was already sketched in our Letter of Intent [1]. Beyond phase-1, we propose a major upgrade of the M2 beam line by equipping it with radio-frequency (RF) separation to produce kaon and antiproton beams of high energy and high intensity. Such an upgrade is presently under study by CERN EN-EA in the framework of the Physics Beyond Colliders Initiative. Once realised, it would make the CERN SPS M2 beam line unique in the world for many years to come.
As an overview, brief descriptions are provided of all presently available ideas for further experiments to be performed with RF-separated hadrons or muons at the M2 beam line:

Drell-Yan physics and hadron spectroscopy with high-intensity kaon and antiproton beams

- Valence-quark distributions in the kaon
- Separation of valence and sea-quark contributions in the kaon
- J/ψ production mechanism and gluon distribution in the kaon
- Measurement of the electric polarisability of the kaon via the Primakoff reaction
- High-precision strange-meson spectroscopy
- Study of the gluon distribution in the kaon via prompt-photon production
- Studies of the spin structure of the nucleon with antiproton beam and a transversely polarised target
- Heavy-quark meson spectroscopy with low-energy antiprotons
- Direct measurement of the lifetime of the neutral pion
- Vector-meson production off nuclei by pion and kaon beams

Hard exclusive reactions with muon beam and transversely polarised target

- Measurement of the GPD E in Deeply Virtual Compton Scattering
- Measurements of Deeply Virtual Meson Production

1 Introduction [v2(+++)]

Everything we see and use is built from atoms. Their properties are readily understood, using quantum mechanics augmented by quantum electrodynamics (QED) at higher energies. Within every atom, however, lies a compact nucleus, comprised of neutrons and protons; the structure and arrangements of all these (composite) objects is supposed to be described by quantum chromodynamics (QCD). Yet, fifty years after the discovery of quarks [6–8], science is only just beginning to grasp how QCD moulds the most elementary hadrons: pions, neutrons, protons, etc.; and it is far from understanding how QCD produces nuclei. However, enormous progress is nowadays being made by theory. Results obtained using novel QCD lattice algorithms, which are steadily approaching realistic descriptions of hadronic matter based on the physical pion mass, are beginning to agree with those from recent QCD continuum analyses. Predictions are being made that may also allow modern facilities to experimentally address the fundamental and unresolved issue of the emergence of hadronic mass. Here the Higgs mechanism, whilst critical in so many areas of Standard Model physics, only plays a minor role. It is the mass-scale characteristic of hadronic matter which sets the scale for almost all visible mass in the Universe.

The dynamical emergence of the large proton mass-scale $m_p \approx 1\,\mathrm{GeV}/c^2$ is one of the most striking features of the Standard Model. Its value is correlated with the size of the proton and hence with attempts to explain the confinement of gluons and quarks. Today there is a puzzle over that size; namely, elastic electron scattering experiments and laser spectroscopy measurements are in marked disagreement. This discrepancy may point to physics beyond the Standard Model or it could mean that low-Q^2 scattering is more subtle than previously thought. In either case, solving the puzzle is crucial so that a hard mark is set for the value of the proton radius as a rigorous test of quantitative strong interaction theory; new experimental results are therefore of utmost priority.

The role of emergent mass is strikingly expressed in the properties of the Nambu-Goldstone (NG) modes [9, 10] of the Standard Model. Their internal structure is complex; and that structure provides the clearest window onto the emergence of mass. Theory predicts that the gluon content within the pion – the only near-pure NG mode – is far greater than that in any other hadron. This can be observed directly in the valence-quark distribution function of the pion and highlighted in a comparison between the valence-quark distributions in the pion and the much heavier kaon. It appears not too optimistic to expect that developments in theory will lead to more predictions in the near and medium-term future. Hence very soon new-era experiments capable of validating such predictions are expected to be of very high priority. Eventually, an entire chapter of the Standard Model, whose writing began with Yukawa [11] more than eighty years ago, can be completed and closed with elucidation of the structural details of the Standard Model's only NG modes, whose existence and properties are critical to the formation of everything from nucleons, to nuclei, and on to neutron stars. Evidently, no claim to have understood the Standard Model is supportable until an explanation is provided for the emergence and structure of NG modes.

In compelling contrast lies the question of invisible or dark matter (DM). Empirical evidence indicates that DM constitutes the vast majority of all matter in the Universe. It surrounds galaxies and other large structures, forming the major component of the gravitational fabric of the Universe; but its origin and nature are completely unknown. Weakly interacting massive particles (WIMPs), cold thermal relics of the big bang, present the most appealing solution to these puzzles [12]. Their discovery would herald a new age in physics; and any experimental input that can shed light onto this "dark" arena would be highly prized.

As of today, the CERN beam lines bear great potential for future significant improvements in understanding hadron spectroscopy and structure; and going further, by providing experimental data that may explore completely unknown territory. In particular, the SPS M2 beam line can readily be used for three pivotal measurements:

1. Operating with muons, the charge radius of the proton will be determined in a muon-proton elastic scattering experiment. Such a measurement constitutes an invaluable complementary approach in this area of world-wide activity.

2. Operating with pions, the existing M2 beam line will be used to study the Drell-Yan process. In particular, the essentially unknown parton distribution functions of the pion will be determined, which constitutes a significant contribution to studying the question of the emergence of hadronic mass.

3. Operating with protons, the poorly known cross section for antiproton production on hydrogen and ^{4}He targets will be measured. This will provide crucial input to the interpretation of data from cosmic-ray experiments and help substantially in advancing the search for dark matter.

In this document, we propose to establish a "New QCD facility at the M2 beam line of the CERN SPS". Starting in 2022 with phase-1, the measurements sketched above will be realised using muons, pions or protons delivered by the existing M2 beam line. The two-stage forward spectrometer in the experimental hall EHN2, upgraded with modern technology, will serve as experimental backbone of the facility. For every individual experiment, specific equipment will have to be developed and installed, in particular solutions for the target region.

As described in our Letter of Intent [1], and briefly also in the Outlook section of this proposal, this facility can later be turned into a unique installation for many years to come, by upgrading the M2 beam line to provide radio-frequency (RF) separated kaon and antiproton beams of high energy and high intensity.

2 Proton-radius measurement using elastic muon-proton scattering

Two quite different experimental approaches are presently being pursued to measure the electric mean-square charge radius of the proton. In elastic lepton-nucleon scattering, the slope of the electric form factor G_E is measured at small values of the squared four-momentum transfer Q^2. In laser spectroscopy, the Lamb shift is measured in electronic or muonic atoms. The numerous results published over the last decade are still contradicting, thereby constituting the so-called proton radius puzzle.
We propose to measure the proton radius in high-energy low-Q^2 elastic muon-proton scattering at the M2 beam line of the CERN Super Proton Synchrotron (SPS) starting in the year 2022. A high-precision measurement at low Q^2 realised with a high-pressure hydrogen time-projection chamber (TPC) can contribute to a solution of the puzzle, especially in view of the different systematics of this approach compared to electron scattering.
As will be shown below, the accuracy to be reached by the proposed muon-proton scattering experiment is expected to be comparable to that of earlier electron-proton scattering experiments at MAMI. Comparing the results on the proton charge radius from these two complementary measurements may allow probing interpretations of the proton-radius mismatch based on lepton-flavour effects.

2.1 Introduction and physics motivation [v2(+)]

The electromagnetic form factors G_E and G_M encode the response of the proton to external electric and magnetic fields, respectively, and are fundamental quantities describing the inner structure of the proton. As will be detailed below, the squares G_E^2 and G_M^2 can be measured in spin-independent elastic lepton scattering off the proton. These measurements were pioneered in the 1950s by R. Hofstadter [13], and are still actively pursued. The gross feature of the form factors is a dependence on the squared four-momentum transfer Q^2 given by

$$G_E(Q^2) \approx G_M(Q^2)/\mu_p \approx G_D(Q^2) = \frac{1}{\left(1 + Q^2/a^2\right)^2}, \tag{1}$$

which is called dipole approximation. Here, $\mu_p \approx 2.79$ is the total magnetic moment of the proton. The constant a was determined in electron scattering to be about $a^2 \approx 0.71\,\mathrm{GeV}^2/c^2$. The parametrisation in Eq. 1 with $a^2 = 0.71\,\mathrm{GeV}^2/c^2$ is used as the standard reference dipole form factor $G_D(Q^2)$.

A Taylor expansion of the electric form factor yields, for a spherically symmetric charge distribution, the definition of the mean-square charge radius at $Q^2 = 0$:

$$\langle r_E^2 \rangle = -6\hbar^2 \left.\frac{\mathrm{d}G_E(Q^2)}{\mathrm{d}Q^2}\right|_{Q^2=0} \qquad \left[\overset{G_E=G_D}{=} \frac{12\hbar^2}{a^2} \approx (0.81\,\mathrm{fm})^2 \equiv \langle r_D^2 \rangle\right] \tag{2}$$

Since the dipole form is motivated by and fitted rather to the gross features of the form factors at larger Q^2, $\langle r_D^2 \rangle$ can not be taken as a precise estimate for the details of the form factor near Q^2=0. The mean-square magnetic radius is defined in a similar way using G_M. Refined parametrisations of the measured Q^2-dependence are often given as polynomials or other analytic functions of Q^2 multiplying the dipole approximation shown in Eq. 1. The so far most elaborate measurement of the proton form factors by elastic electron scattering was carried out in 2010 at the Mainz University accelerator MAMI [14, 15], and parametrisations of the results at Q^2-values smaller than 0.1 $\mathrm{GeV}^2/\mathrm{c}^2$ are shown in the upper panel of Fig. 1. While G_M shows a more shallow slope at Q^2 values close to zero than G_D, G_E shows a steeper one resulting in $r^{\mathrm{rms}}_{E,\mathrm{MAMI}} = \sqrt{\langle r^2_{E,\mathrm{MAMI}}\rangle} = (0.879 \pm 0.008)\,\mathrm{fm}$. The uncertainty represents statistical and systematic uncertainties added in quadrature, where the systematic one is obtained by summing up its components linearly. This value for the proton radius is at variance with $r^{\mathrm{rms}}_{E,\mu H} = (0.841 \pm 0.001)\,\mathrm{fm}$

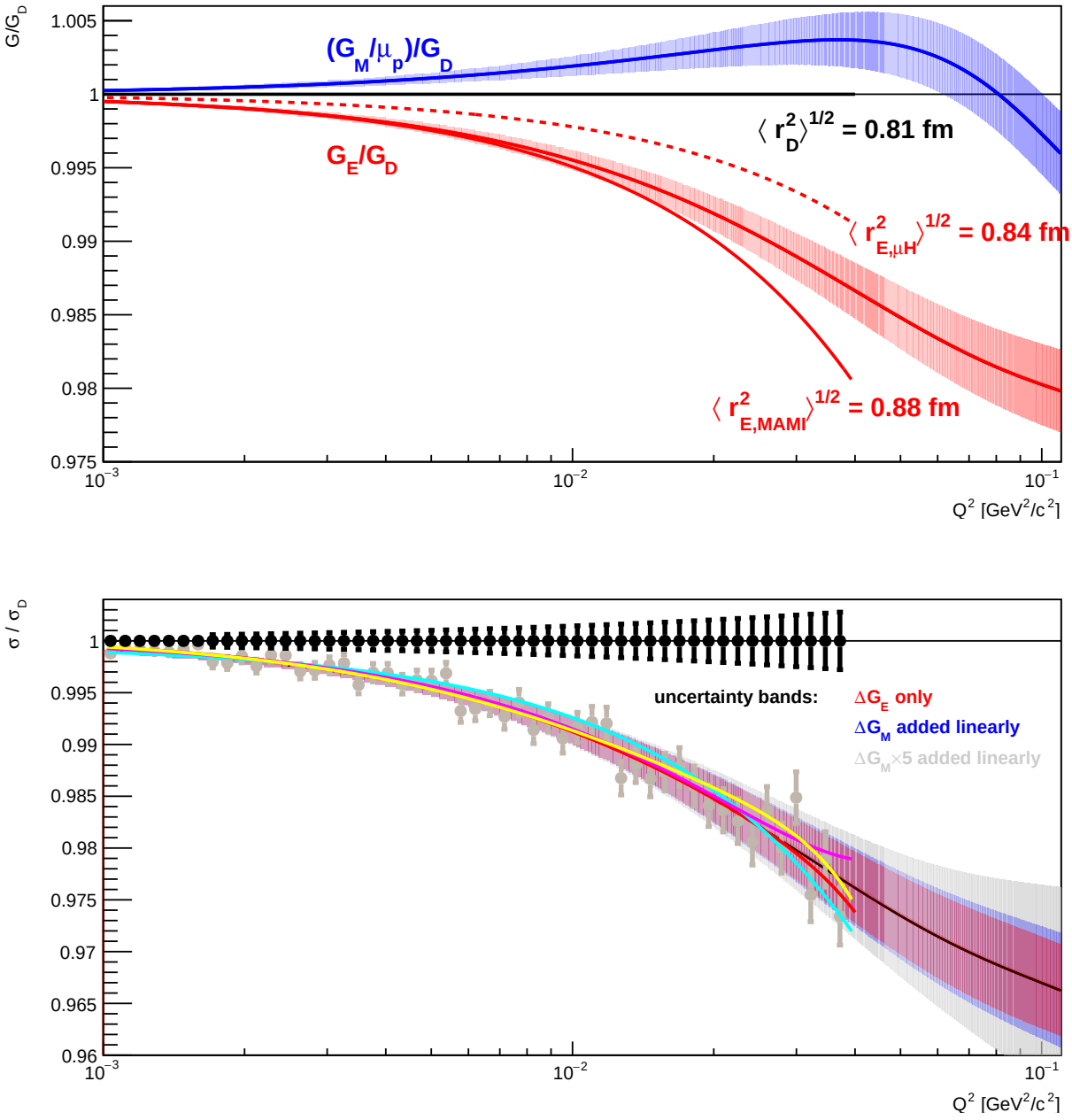

Figure 1: Top panel: proton form factors G_E (red curve) and G_M (blue curve) as determined from measurements at MAMI, shown as ratio to the dipole form factor G_D (black line) as given in the text. For two radii, 0.84 and 0.88 fm, the respective constant-slope polynomials (up to order Q^2) of G_E are shown. Bottom panel: ratio of the cross section measured at MAMI over the prediction for the cross section using the standard dipole form factors. The innermost (red) uncertainty band corresponds to the effect of the uncertainty of G_E only, while for the (blue) middle band the uncertainty from G_M was added linearly, and for the outer (gray) band the contribution from ΔG_M was increased by a factor of five. The dots with error bars, arbitrarily placed at a cross-section ratio of unity, and in grey for one of the replicas used to determine the uncertainties of the fitted parameters, represent the anticipated statistical precision of the proposed measurement, down to $Q^2 = 0.001\,\mathrm{GeV}^2/c^2$. The curves are the fits to the shown replica to order Q^2 (light blue), Q^4 (purple) and Q^6 (yellow). The red curve in the lower panel corresponds to the red curve in the upper panel (*i.e.* extrapolation of the dipole-form deviation only to order Q^2).

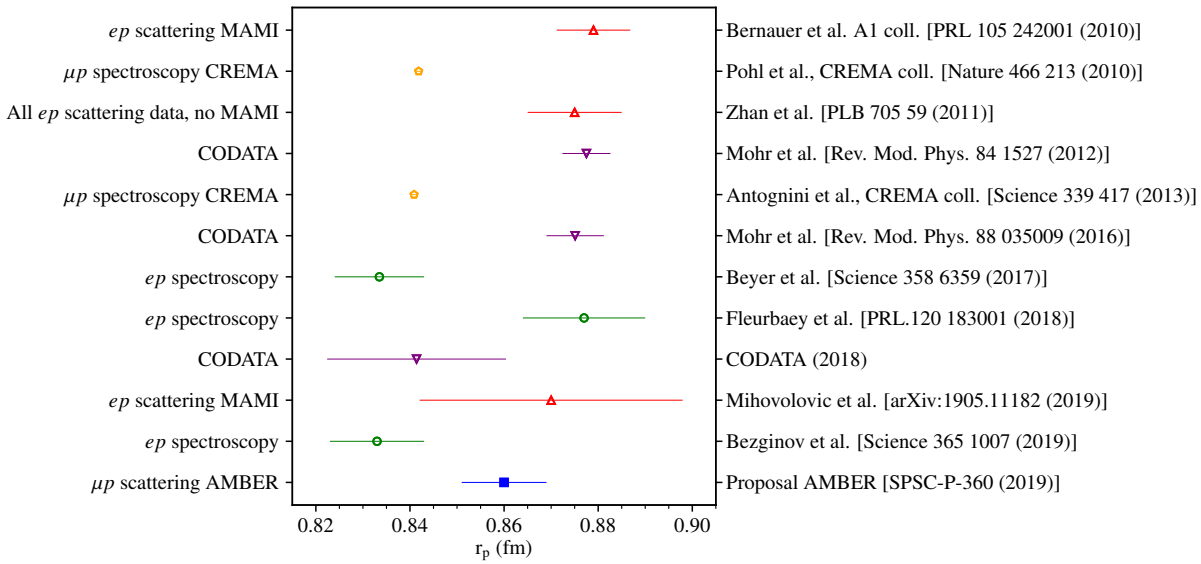

Figure 2: Compilation of data on the proton radius puzzle, sorted by time. Electron-proton scattering and spectroscopy (red/green), muon-proton spectroscopy (orange) and summary data (purple) is shown with the value of this proposed measurement (blue) arbitrarily placed at 0.86 fm, with the projected uncertainties. There are several reanalyses of different subsets of the electron scattering data. We refer to [18] for an overview and to [19] for a critical discussion. Error bars represent statistical and systematic uncertainties added in quadrature.

that was found at the same time in 2010 in laser spectroscopy of muonic hydrogen [16, 17]. This striking discrepancy of about five standard deviations has triggered many efforts to clarify its origin.

2.2 Previous experiments facing the proton radius puzzle [v2(+)]

In order to solve the proton radius puzzle, several new experiments were proposed and are still in preparation or already running. For a recent and complete compilation of the various data and studies, we refer to the discussion in [18]. In Fig. 2 we show, sorted by time, a compilation of published results including those from CODATA meta-analyses, complemented by the projected accuracy of the measurement proposed in this document.

There are, on the one hand, many efforts on acquiring more data on the atomic spectroscopy of both electronic and muonic hydrogen. The highest precision on proton-radius measurements was achieved by the investigation of atomic level splittings in muonic atoms [16, 17, 20, 21], which are very accurately measured by laser spectroscopy. From 2S-2P transitions in muonic hydrogen, the above-mentioned value of 0.841 fm was determined by correcting the measured frequency for all known QED effects and attributing the remaining effect to the finite size of the proton. Additional information in this regard comes from spectroscopy of other transitions and on heavier atoms, allowing also for a reevaluation of the Rydberg constant. While until very recently the results from electron scattering and spectroscopy were in agreement, for some time a systematic difference had been observed between electronic and muonic systems. Newer results obtained in 2017 [22] put this difference into question, while equally recent results [23] tend to confirm it. Recently published results [24] are consistent with the small radius found by muonic spectroscopy. So far, no explanation has been found for the tension between the results in electronic spectroscopy (see open green circles in Fig. 2).

On the other hand, there are efforts ongoing to collect new data on lepton-proton scattering in the relevant kinematic region. In scattering experiments, the proton radius is determined by measuring the Q^2-dependence of the electric form factor over an extended range and then extrapolating the form factor towards $Q^2 = 0$. This approach, besides initially targeting at the proton radius, offers the additional

option to study the Q^2-dependence of the electric form factor, which is a topic of even deeper physics interest. A tension between the theoretical dispersion approach for the proton, involving the more general Q^2-dependence, and the slope of the form factor near zero was already noted earlier (see *e.g.* [25]). This discrepancy became also obvious in 2010 by comparing experimental results, as can be seen in the interpretation of the MAMI A1 data on *e-p* scattering in Fig. 2. If the full constraints from dispersion theory are taken into account, a significantly lower radius is found [25], in line with the muonic spectroscopy value, although this fit gives a significantly larger value of χ^2.

2.3 Competitivity and complementarity of the proposed measurement [v2(new)]

Several experiments are currently ongoing or proposed with the goal to refine the knowledge of the proton charge radius by *lepton-proton* elastic scattering:

The PRad experiment [26] at Jefferson Laboratory has already collected data in 2016 to measure the electric form factor in the range $2 \cdot 10^{-4} < Q^2/(\mathrm{GeV}^2/c^2) < 6 \cdot 10^{-2}$ using beam energies of 1.1 and 2.2 GeV, forward tracker, calorimeter and a windowless hydrogen gas-flow target. The so-far preliminary PRad results [27] indicate a radius smaller than, but compatible with, the small radius from muon spectroscopy. However, the extracted form factors show a significantly smaller drop over PRad's Q^2-range than any earlier cross section data sets (see, e.g., [28, 29]), as well as the original fits of the Mainz data set [30] and [31], fits to the Mainz data with forced small radius [32] and the theoretical calculations of Alarcon et al. [33], calculated using the precise radius from muonic spectroscopy. These data necessitate an independent verification. If verified, and assuming that all earlier data is also not faulty, a possible cause of the puzzle is an insufficient description of radiative effects. This might be due to higher-order radiative corrections not captured correctly in the available generators, or even due to BSM physics. Our proposed experiment, by using a high-energy muon beam, will provide a unique cross check as well as key information on the source of this discrepancy: our approach combines substantially smaller radiative corrections and the ability to cancel two-photon-exchange effects in the data itself, with having forward kinematics similar to PRad. No other planned or running experiment has this unique combination of traits.

At ELPH, an electron-proton scattering experiment with beam energies of 20-60 MeV is being prepared [34], with data taking foreseen as early as 2019. At the Mainz Microtron, several elastic *ep* scattering experiments are running or in preparation. One is based on initial-state radiation kinematics. First results [35], using three beam energies smaller than 500 MeV to reach Q^2-values as low as 10^{-3} GeV^2/c^2, are inconclusive regarding the proton radius. A future second run will make use of a cluster jet target currently in development. The same target will also be used for a 'classical' elastic-scattering experiment planned both at MAMI-A1 and at the future MESA-MAGIX facility, using very low energies down to 25 MeV. The MAGIX-MESA experiment is expected to extract both electric and magnetic charge radii of the proton after the start of MESA that is expected beyond 2022. All these experiments rely on low-energy electron beams and scattered-electron detection at larger angles, implying large radiative corrections. Our approach, in contrast, has the advantage of the above-mentioned small radiative corrections. Our small scattering angles make us insensitive to G_M.

In the approach closest to ours, the 720 MeV MAMI electron beam is used with detection of the recoil proton in an active-target TPC [36], and simultaneous detection of the scattered electron with a dedicated tracker inside the TPC. The goal is to measure the *ep* elastic cross section in the Q^2-range from $0.001\,\mathrm{GeV}^2/c^2$ to $0.04\,\mathrm{GeV}^2/c^2$. The design of this experiment is very similar to that of the present proposal, except that a low-energy electron beam is used. In this regard, we consider it as complementary to our approach.

So far, in scattering experiments the proton radius has only been studied using electron beams. Measurements with muon beams are complementary and will test systematic effects such as those related

to bremsstrahlung emission, which substantially differ due to the larger mass of the muon. Elastic muon-proton scattering at low energies, with the muon still non-relativistic with energies between 115 and 210 MeV, is proposed by the MUSE experiment at PSI [37]. The experiment is optimised to test possible differences between electron-proton and muon-proton scattering in non-forward kinematics. The forward kinematics of our proposal greatly suppresses Coulomb-distortion effects, which at MUSE are of substantial size and have to be dealt with in the analysis.

Altogether, the proposed measurement appears unique and complementary when compared to finished, ongoing and other planned experiments. It offers a favourable combination of systematic effects known to exist in measurements of the proton radius.

2.4 Formalism and measured quantity

The cross section for elastic muon-proton scattering, $\mu p \to \mu' p$, is to first order given by

$$\begin{aligned}\frac{d\sigma}{dQ^2} &= \frac{\pi\alpha^2}{Q^4\, m_p^2\, \vec{p}_\mu^{\,2}} \left[\left(G_E^2 + \tau\, G_M^2\right) \frac{4E_\mu^2 m_p^2 - Q^2(s - m_\mu^2)}{1+\tau} - G_M^2 \frac{2m_\mu^2 Q^2 - Q^4}{2} \right] \\ &= \frac{4\pi\alpha^2}{Q^4}\, R\, \left(\varepsilon\, G_E^2 + \tau\, G_M^2\right), \end{aligned} \tag{3}$$

with the recoil and longitudinal-polarisation variables

$$\begin{aligned} R &= \frac{\vec{p}_\mu^{\,2} - \tau(s - 2m_p^2(1+\tau))}{\vec{p}_\mu^{\,2}(1+\tau)}, \\ \varepsilon &= \frac{E_\mu^2 - \tau(s - m_\mu^2)}{\vec{p}_\mu^{\,2} - \tau(s - 2m_p^2(1+\tau))} \end{aligned} \tag{4}$$

and with $Q^2 = -t = -(p_\mu - p_{\mu'})^2$, $\tau = Q^2/(4m_p^2)$ and $s = (p_\mu + p_p)^2$. Here, E_μ and $\vec{p}_\mu$ denote energy and three-momentum of the incoming muon, respectively. For a collision with a proton at rest, the squared centre-of-momentum energy s is given in the laboratory system by $s = 2E_\mu m_p + m_p^2 + m_\mu^2$.

As G_M^2 enters in two terms, the first being for small Q^2 proportional to E_μ^2 and the second to m_μ^2, measuring at different energies around $E_\mu \approx m_\mu$ would enable us to separate the contributions from G_E^2 and G_M^2 ("Rosenbluth separation"). This is not possible at the high energies proposed here. However, at the small values of Q^2 (*i.e.* small τ) of interest here, the contribution from G_M is small and can be corrected for by assuming some shape for G_M, so that only G_E is left as a free parameter. Even with large variations of G_M, *i.e.* assuming that its deviation from the dipole form is a factor of five larger than the deviation obtained in the MAMI analysis, the uncertainty on G_E and thus on the proton charge radius stays well below 0.1%.

2.5 Goal of the measurement and corresponding requirements

We propose to measure *elastic muon-proton scattering* with a high-energetic muon beam impinging on a hydrogen gas target, over a momentum-transfer range that is particularly sensitive to the proton charge radius. The cross section has hence to be measured, on the one hand, coming as close as possible to $Q^2 = 0$ as required in Eq. 2, and on the other hand covering a sufficiently large range in momentum transfer in order to constrain the Q^2-slope of the cross section near zero with the desired level of precision. As illustrated in Fig. 1, this range is approximately $0.001 < Q^2/(\mathrm{GeV}^2/c^2) < 0.04$. At values of Q^2 smaller than $0.001\ \mathrm{GeV}^2/c^2$, the deviation from a point-like proton is on the level of 10^{-3} and thus smaller than

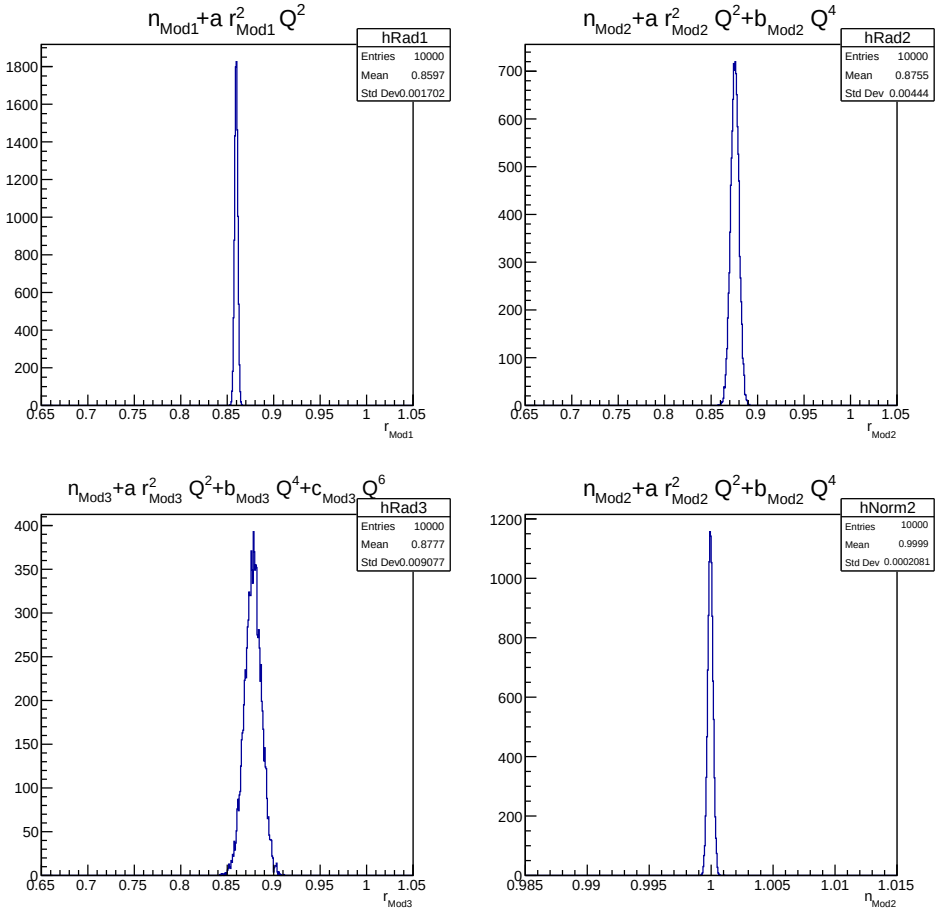

Figure 3: Statistical precision on the radius for different numbers of free parameters in the fit. The subscript Modn is used when fitting with a polynomial up to order Q^{2n}.

unavoidable systematic effects, as the variation of the detector efficiencies with Q^2 cannot be controlled more accurately with the currently available methods. At values of Q^2 larger than $0.04\,\mathrm{GeV}^2/c^2$, the remaining non-linearity of the Q^2 dependence, when simultaneously fitting the term proportional to Q^4, becomes the predominant source of uncertainty, and the data cannot be used to determine the proton charge radius unless more elaborate theory input is used.

Within this range, the dependence of the measured cross section on Q^2 has to be fitted with a polynomial in Q^2 up to some order Q^{2n}. With the overall normalisation as a free parameter, there are n+1 parameters in a fit up to Q^{2n}. The impact of the fit on the the radius determination has been studied; for this proposal with polynomials up to order Q^6, see below, and also up to Q^8 in [38]. For 70 million elastic events in the considered Q^2 range, generated according to the form factors fitted to the Mainz data, the statistical precision in 51 bins is shown in Fig. 1 and the corresponding uncertainties in Fig. 3. The determined radii must be compared to the input value $r_{E,MAMI} = 0.879\,\mathrm{fm}$. From 10 000 replicas of the corresponding event distribution, it follows that the radius can be reproduced from a fit leaving the parameters free up to order Q^6 with an uncertainty of

$$\Delta r_{E,p}(N_{par} = 4) = 0.009\ \mathrm{fm} \tag{5}$$

and a small bias $< 0.002\,\mathrm{fm}$. Here, N_{par} denotes the number of free parameters. When leaving the parameters free only up to order Q^4,

$$\Delta r_{E,p}(N_{par} = 3) = 0.004\ \mathrm{fm} \tag{6}$$

is obtained, with a larger bias of about 0.0035 fm. These biases originate from the fact that the truncation

of the Q^2 series is equivalent to setting all higher-order terms to zero. On the one hand, one may account for the impact of the neglected higher orders by taking the corresponding terms as determined by other experiments, or/and inspired by theory. This makes, however, the interpretation of the actual experiment dependent on the correctness of the input that one aims to test. On the other hand, the values obtained elsewhere can be taken at least as an estimation of their size, and they are reflected here in the given biases. A more detailed description of the fitting procedures for the Q^2 spectrum can be found in Sec. 2.9.3.

The estimated uncertainties given in Eqs. 5 and 6 reflect that the goal to measure the proton radius with a statistical precision of 0.009 fm, thus on the level of 1%, is reached with 70 million events in the Q^2 range from 0.001 to 0.04 GeV^2/c^2.

In order to reach the precision on the determination of Q^2 required at small momentum transfer, it is important to observe the recoil proton. Due to its small energy, this requires an active target, *i.e.* the target being the detector at the same time. This can be realised by a Time Projection Chamber (TPC) operated with pure hydrogen gas. Such a target has been developed by PNPI [39, 40], and it is in the testing phase for a similar experiment using electron scattering at Mainz.

2.6 Setup and running plan [v2(++)]

We propose to measure elastic muon-proton scattering using a 100 GeV muon beam and a pressurised hydrogen gas target. For a precise measurement of the proton radius, the relevant momentum transfer region is $0.001 < Q^2/(\mathrm{GeV}^2/c^2) < 0.04$, which requires to operate the target as a TPC in order to detect the track of the recoil proton.

The integrated cross section according to Eq. 3 over this Q^2 range is

$$\sigma_{\mu p}^{\mathrm{elastic}}(0.001 < Q^2/(\mathrm{GeV}^2/c^2) < 0.04) = 0.255\,\mathrm{mbarn} \tag{7}$$

for a point-like proton. It is diminished by about 2.5% due to the finite size described by the form factors, which are at these low values of Q^2 predominantly governed by the proton radius effect. The total number of elastic scattering events within the cuts is 70 million in order to achieve the precision as presented in Fig. 1.

For a 160 cm long target with a hydrogen pressure of 20 bar, the target thickness is

$$N_p = 2.687 \cdot 10^{19}\mathrm{protons/cm}^3 \cdot 2 \cdot (20\,\mathrm{bar}/1.013\,\mathrm{bar}) \cdot 160\,\mathrm{cm} = 1.70 \cdot 10^{23}\ \mathrm{protons/cm}^2. \tag{8}$$

At a muon beam intensity of $\Phi_\mu = 2 \cdot 10^6/\mathrm{s}$, the event rate in the Q^2 range of interest is thus

$$N_{\mu p}^{\mathrm{elastic}}(0.001 < Q^2/(\mathrm{GeV}^2/c^2) < 0.04) = \sigma_{\mu p}^{\mathrm{elastic}} \cdot N_p \cdot \Phi_\mu = 86.6/\mathrm{s}. \tag{9}$$

Due to the strong increase of the cross section towards smaller values of Q^2, the rate in the adjacent interval,

$$N_{\mu p}^{\mathrm{elastic}}(0.0005 < Q^2/(\mathrm{GeV}^2/c^2) < 0.001) = \sigma_{\mu p}^{\mathrm{elastic}} \cdot N_p \cdot \Phi_\mu = 89.0/\mathrm{s}, \tag{10}$$

is about equally large.

Thus for collecting 70 million events at 20 bar target pressure, $8.14{\cdot}10^5$ seconds with beam on target are needed, and with an average spill-over-cycle ratio of 0.14, an SPS efficiency of 0.81, and taking into account the useful fraction of the target volume of 90%, it takes

$$8.14 \cdot 10^5\ \mathrm{s}/(0.14 \cdot 0.81 \cdot 0.90) = 92\ \mathrm{days\ of\ beam\ time}. \tag{11}$$

Since at 20 bar target pressure, the proton recoil tracks that correspond to the lowest values in $Q^2 \lesssim 0.0025\,\mathrm{GeV}^2/c^2$ are too short to be measured accurately, this part of the Q^2 spectrum must be covered in a separate data set at lower hydrogen pressure of 4 bar. The necessary 10 million events require

$$5.81 \cdot 10^5\ \mathrm{s}/(0.14 \cdot 0.81 \cdot 0.90) = 67\ \mathrm{days\ of\ beam\ time}. \tag{12}$$

The pressure of the gas will be optimised for having, on the one hand, sufficiently low stopping power such that a proton recoil track is detectable, and on the other hand it still stops in the TPC volume. The respective gas system has been developed and is in the test phase at MAMI. The details of the read-out electronics, which are to be adapted to the COMPASS environment, are currently under study. At Q^2 values larger than 0.04 GeV$^2/c^2$, recoil protons can no longer be stopped in the gas volume.

In order to control the most important systematic effects for the measurement, we foresee to take data, keeping the lower pressure setting, also with oppositely charged muons, and with the beam energy lowered to 60 GeV. The two data sets with opposite charge allow us to measure and cancel to first order any two-photon-exchange effects without theory input (for an overview over two-photon exchange, see e.g. [41]). A comprehensive summary of the proposed settings is given in Table 2.

Table 2: The settings proposed for the proton radius measurement in 2022 and 2023. The first two settings are required to achieve the statistical precision as explained in the text, while the further two settings with opposite beam charge and lowered beam energy, respectively, serve to control the systematic uncertainties.

Beam setting	**TPC pressure setting**	**Duration**	**Purpose**
μ^+, 100 GeV	20 bars	92 days	$2.5 < Q^2/(10^{-3}\text{GeV}^2) < 40.0$
μ^+, 100 GeV	4 bars	67 days	$1.0 < Q^2/(10^{-3}\text{GeV}^2) < 8.0$
μ^-, 100 GeV	4 bars	67 days	control of charge dependence
μ^+, 60 GeV	4 bars	34 days	control of energy dependence

The scattered muon will be measured with the COMPASS spectrometer using its standard muon setup with optimisations for the new kinematics. In order to allow for the detection of the elastically scattered muon track, the beam killer components have to be excluded from the trigger. The central parts of the tracking detectors will be activated, and silicon telescopes surrounding the TPC will be used for measuring the muon scattering angle with high accuracy. In addition, the electromagnetic calorimeter detect the (rare) radiative events, by which soft photons with energies up to 2 GeV are emitted. Muon identification is performed using muon filter and hodoscopes.

Since triggering only on the proton recoil would imply Q^2-dependent efficiency variations that could not be controlled using the data themselves, a trigger component from the muon trajectory has to be added. As presently the beam rate is too high to record all events, the beam trigger will have to be extended by a new component that allows to veto muons with a scattering angle below about 5 μrad. This suppresses those muons that have experienced multiple (small-angle) scattering only, which amounts to about 99% of the incoming muons. In contrast, muons are efficiently selected if their scattering angle is larger than 100 μrad, which corresponds to momentum transfers larger than 10^{-4} GeV$^2/c^2$. A possible detector system to realise this trigger would be an upgrade of the silicon telescopes by using new scintillating fibre tracking detectors. However, solutions with thinner detectors, such as silicon pixel detectors with a sufficiently fast read-out, would be desirable for minimising multiple scattering as a source of systematic uncertainty. Proton recoil measurement, muon measurement, and the trigger of this experiment are detailed in Sec. 2.7.

A continuous read-out is planned to solve current issues of rate capability and will allow for implementing the above described event selection in an elegant and efficient manner. Its development is therefore pursued with great effort in the context of this proposal and further discussed in Sec. 5.2.4.

The statistical uncertainties that can be achieved in the proposed experiment are shown in Fig. 1, using a suitable segmentation of the data in Q^2 bins. The data set is sufficient to constrain the proton radius to a precision better than 0.01 fm.

The current layout for the proton radius measurement from 2022 on employs several new detector components that must be tested with the muon beam under different conditions at an early stage, with

intensities in the order of 2 to $10{\cdot}10^6$ muons per second, with beam momenta of 60 and 100 GeV. We therefore propose a dedicated test of the new components (active-target TPC, tracking detectors, DAQ) in a setup located at the CEDAR position for 20 days in the beginning of the 2021 beam time prior to the transverse-deuteron COMPASS run. Furthermore we propose a test setup (*i.e.* move the detector components) downstream of COMPASS about 6 m long, to continue the tests parasitically to the transverse-deuteron COMPASS run in 2021.

2.7 Layout of the setup [v2(++)]

Figure 4 shows a schematic overview of the experimental setup required for the proton-radius measurement (PRM setup). The three detector systems specific to the proposed measurement are shown enlarged in the upper part of the figure: a hydrogen-filled TPC acting as active target for muon-proton scattering; two silicon-pixel-detector telescopes for precise tracking of the (scattered) muons; and a track trigger setup consisting of three scintillating-fiber (SciFi) tracking detectors. In addition to these new systems, several parts of the existing COMPASS setup (see [42]) will be used with minor adaptions: the inner tracking detectors (existing SciFi detectors and GEMs) that will be used together with the bending magnet SM2 for measuring the momentum of a scattered muon; the second muon filter and hodoscopes for separating muons from secondary particles; and the second electromagnetic calorimeter (ECAL2) for detecting photons created in radiative events. In Fig. 5 (left) the track position along the spectrometer is shown in both lateral projections, *i.e.* x and y. The trajectory of beam particles scattered at the target position with only a small momentum transfer is bent by spectrometer magnet SM2 for momentum measurement. The inertial gradient of the beam and the scattering extends the track position up to $\sigma_{x,y} = 8$ cm. Only small-angle tracking detectors like SciFi and GEM detectors will contribute to the measurement of the muon momentum.

The central part of the experiment is the hydrogen-filled TPC, operated at pressures of up to 20 bar (see Sec. 5.3.1 for a detailed description of the TPC design). It acts as active target and measures angle and energy of recoil protons. Two silicon telescopes are located immediately upstream and downstream of the TPC to measure the deflection of muons scattered in the hydrogen gas. Each consists of four MuPix8 silicon-pixel detectors arranged in two pairs that are separated by as large a distance as possible (see below). Upstream of the TPC, a SciFi tracker is placed in front of each pair of silicon trackers; downstream, only one SciFi tracker is located behind the last pair of silicon detectors.

In order to accommodate the PRM setup in the COMPASS target area, *i.e.* between the end of the M2 beam line and the SM1 magnet, the PRM setup must not be longer than about 9 m, *c.f.* Fig. 4. Apart from the (old) SciFi tracker that is installed just after the M2 beam line exit window, all other presently installed detectors in the target area will be removed to make room for the new detectors described above and detailed in Sec. 5.3.

The upstream part of the setup will be close to the SM1 magnet. To ensure, that the magnetic field does not influence the tracking at this position, it will not be used. Instead, the existing COMPASS tracking detectors, *i.e.* SciFis, GEMs, and Pixel-GEMs, will be used in conjunction with the SM2 magnet to measure the momentum of muons scattered in the hydrogen gas of the TPC.

The TPC length of 2.2 m leaves about 3.0 m space for the two silicon-tracker telescopes on each side of the TPC. Figure 5 (right) shows the resulting upper limit on the z-vertex resolution of about $\sigma_z = 8$ cm for the smallest scattering angles, *i.e.* the lowest values of Q^2 to be measured.

Since the measurement of low Q^2-values requires a precise measurement of the scattering angle of the deflected muon, multiple scattering effects are crucial. A conservative estimate of the material budget of the proposed setup is listed in Table 3 with the distribution along the target area depicted in Fig. 6.

Figure 6 shows the conservative distribution of the material radiation lengths in the target area together with the total radiation length. Material between the most upstream and most downstream tracking

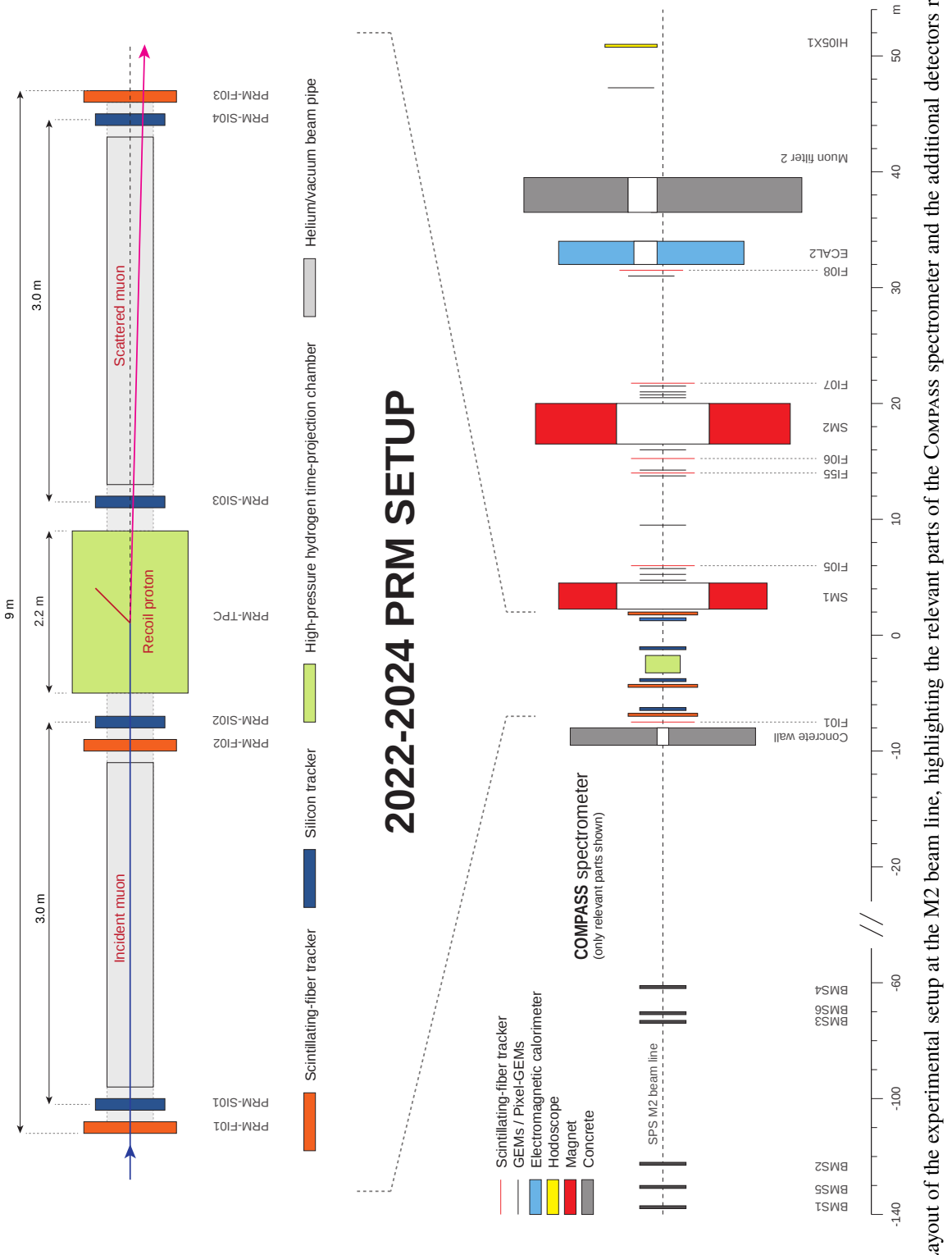

Figure 4: Layout of the experimental setup at the M2 beam line, highlighting the relevant parts of the COMPASS spectrometer and the additional detectors required for the proton radius measurement.

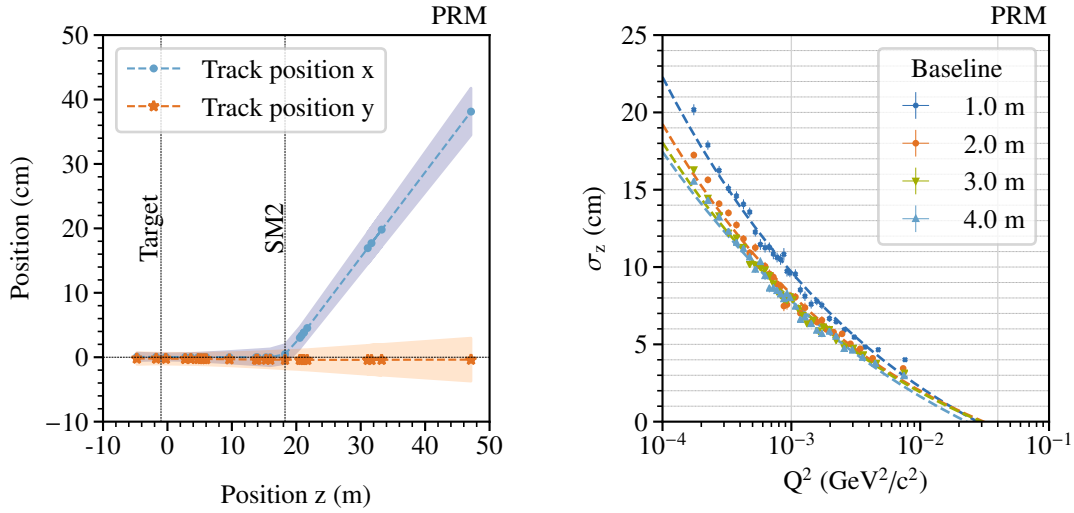

Figure 5: *Left*: Simulated track positions of scattered muons, shown along the COMPASS spectrometer. Using only SM2 as bending magnet for the momentum measurement results in a clear deflection in the (horizontal) bending plane. Scattered beam particles are bent by at most ±4 cm. *Right*: Simulated z-vertex resolution vs. Q^2, shown for four different lever-arm lengths of the two silicon-tracker telescopes.

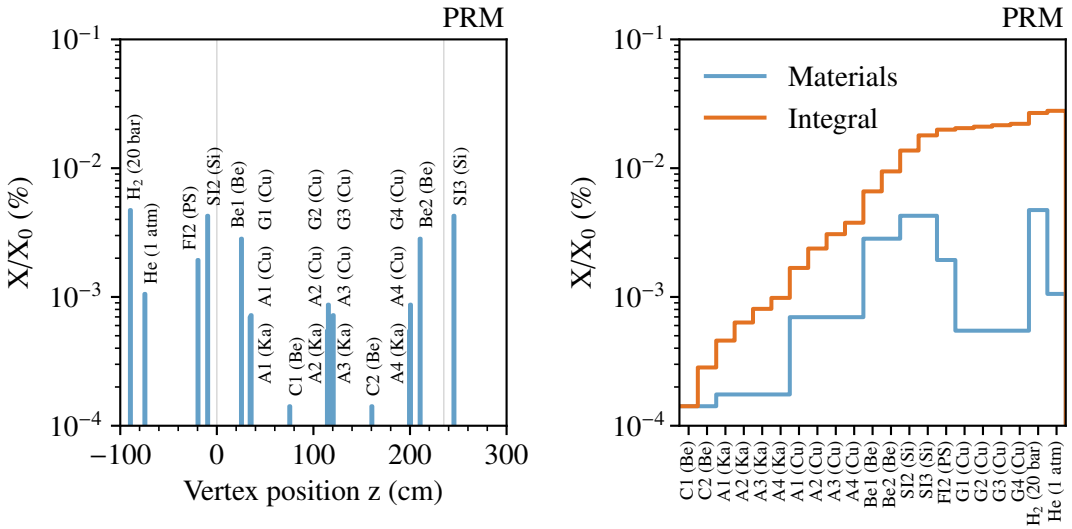

Figure 6: Reduced radiation lengths for material contributing to multiple scattering in the target area. *Left*: shown per item in dependence on the z-position (arbitrary), except for the arbitrarily placed contribution of hydrogen and helium. *Right*: material budget shown for each single component and integrated.

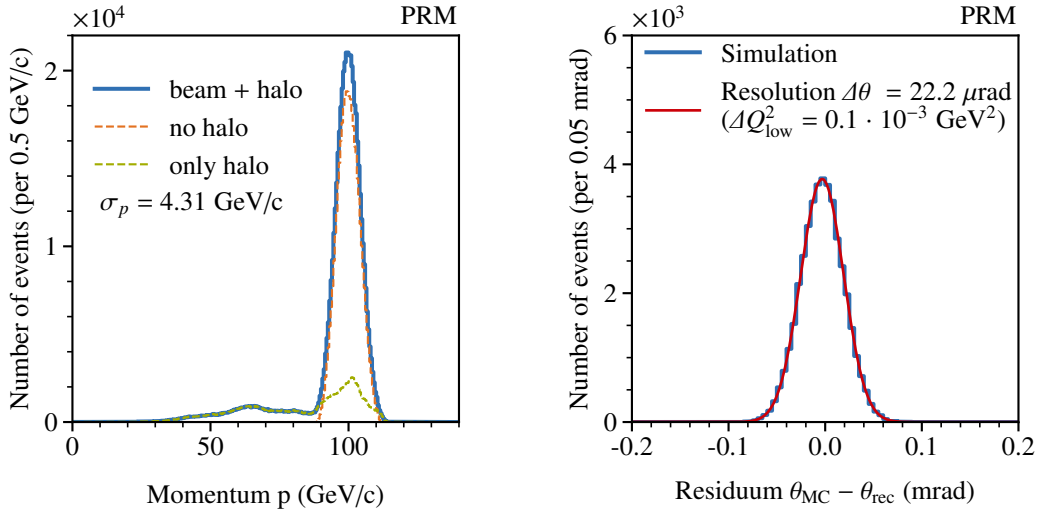

Figure 7: *Left*: Simulated beam momentum with halo component for the M2 beam line with a momentum of 100 GeV/c based on a beam file [43]. Whereas the halo component contributes especially in the lower momentum region of the beam particles, the main component has a spread of 4.31 GeV/c. *Right*: Resolution of the scattering angle extracted from the simulation. It is in agreement with the theoretical value. The resolution is dominated by effects of multiple scattering. With a resolution of $\Delta\theta = 22.2$ μrad a relative resolution in Q^2 at its lowest value of $\Delta Q^2_{\text{low}} = 0.1 \cdot 10^{-3}$ GeV^2 can be achieved.

detector in the target area contributes to multiple scattering that deteriorates the scattered muon tracking. The main contributions are due to the TPC beryllium windows and the silicon tracker detector material. About 71.1% of the events located in the target area will originate from non-target material. Optimisations of the material budget along the muon track are ongoing to further reduce the material budget and to minimise the effect of multiple scattering, in order to improve the reconstruction accuracy.

Based on the total radiation length $(X/X_0) = 27.44$ ‰ of the setup, the resulting influence due to multiple scattering on the scattering angle can be calculated to $\Delta\theta = 19.45$ μrad for a beam energy of 100 GeV. The relative uncertainty at the lowest proposed $Q^2 = 10^{-3}\text{GeV}/c^2$ is about $(\Delta Q^2/Q^2) = 12.30$ %. The theoretical value is in agreement with the value extracted from the simulation shown in Fig. 7 (right). Since the major contribution is due to the material of the TPC windows and silicon detectors, studies are ongoing to further reduce the material budget (see Sec. 5.3.3).

2.8 Beam requirements [v2(++)]

The intensity of the required muon beam is limited by the maximum rate that is allowed by the noise level and the correct matching of the TPC signals with the muon scattering information, and currently assumed to be

$$\Phi_\mu = 2 \cdot 10^6/s. \tag{13}$$

The main data taking is planned with

$$E_\mu = 100\,\text{GeV}, \tag{14}$$

however also data taking with 60 GeV is foreseen. This allows for systematic studies of effects of multiple scattering and of the angular resolution of the muon detection, since the cross section (Eq. 3) practically does not depend on E_μ, but only on Q^2. Figure 7 (left) shows the simulated beam momentum for the M2 beam line with a momentum of 100 GeV/c. The spread of the beam is 4.31 GeV/c. Halo components accompanying the beam particles are included. Studies are ongoing on the influence on the detector and trigger systems. All beam related subjects are pursued in close collaboration with CERN's Beam Working Group, with further information in [43].

Table 3: Conservative list of the material budget of different materials used in the setup. Based on the used thickness d and the density ρ of the material, the respective ratio of $x = d \cdot \rho$ and X_0 is calculated together with its contribution to the setup. Values marked with a * are used for the final setup with their respective contribution to the total radiation length. Material properties are taken from [44].

material	planes	d/plane [cm]	density ρ [g/cm^3]	X_0 [g/cm^2]	x/X_0 [‰]	contribution [%]
Environment and tracking:						
Dry Air	2	300.00	0.00120	36.62	22.94	
Helium*	2	300.00	0.00016	94.32	1.06	3.85
Fibre (polystyrene)*	4	0.02	1.04	43.79	1.94	7.06
Silicon*	8	0.02	2.33	21.82	8.54	31.15
TPC components:						
Hydrogen (4 bar)	4	40.00	0.00033	63.05	0.85	
Hydrogen (20 bar)*	4	40.00	0.00166	63.05	4.26	15.53
TPC-Anode (Kapton)*	4	0.050	1.42	40.58	0.70	2.55
TPC-Anode Grid (Cu)*	4	0.0008	8.96	12.86	2.19	7.98
TPC-Anode (Cu)*	4	0.001	8.96	12.86	2.79	10.17
TPC-Cathode (Be)*	2	0.005	1.85	65.19	0.29	1.03
TPC-Window (Be)*	2	0.100	1.85	65.19	5.67	20.68
Total:					27.44	100.00

The exact sharing of the beam time in terms of such systematic studies can only be fixed along with the decision on the optimum target geometry and the corresponding relevance of these systematic studies. At the same time, the beam is required to be narrow in the target region

$$\sigma_{x,y} \lesssim 0.5\,\text{cm} \tag{15}$$

and have a dispersion

$$\sigma_{dx/dz,dy/dz} \lesssim 1.0\,\text{mrad}, \tag{16}$$

as shown in Fig. 8. It is currently investigated, which the best beam optics will be, especially the influence of the halo component and whether the lower beam intensity allows for a more narrow beam as compared to the full-intensity beam, e.g. by the use of the scrapers. Changing the beam polarity between μ^+ and μ^- for systematic studies will only have minor influence on its properties.

2.9 Systematic uncertainties [v2(new)]

A full understanding of the systematic uncertainties can only be obtained with the Monte Carlo simulations of the setup, which are currently still ongoing. Here, we collect the systematics effects that we expect to dominate in this experiment together with some preliminary results.

2.9.1 Event selection [v2(new)]

In order to extract the Q^2 spectrum for the determination of the proton charge radius, selection criteria need to be imposed on the recorded events. Figure 9 shows the list of currently used constraints and the

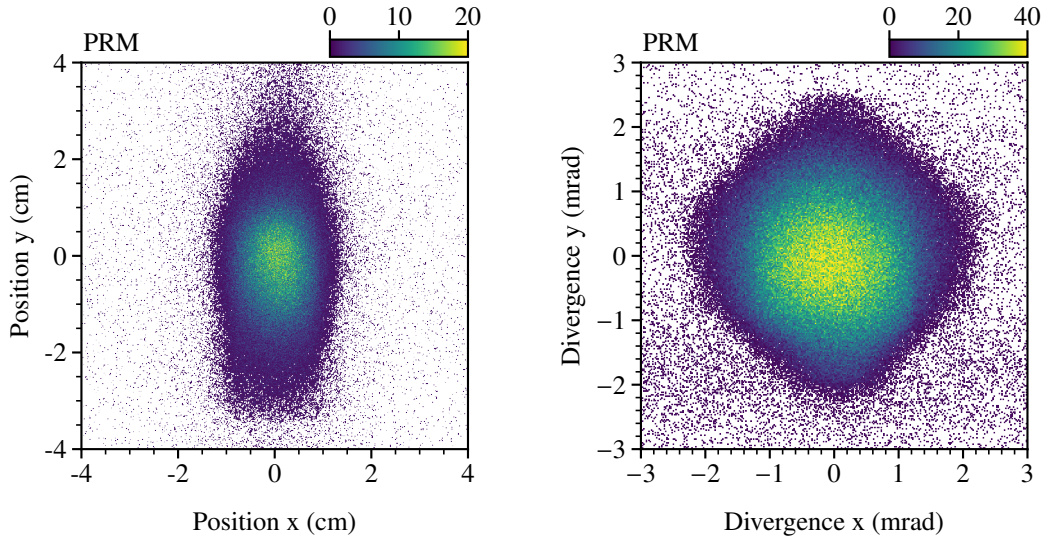

Figure 8: Simulated beam profile at target location and divergence of beam particle trajectories for the M2 beam line with a momentum of 100 GeV/c. Beam properties based on [43].

percentage of remaining events after a constraint was applied. A more detailed description is given in Table 4. After all constraints were applied, about 0.7% of the recorded data remain for further analysis.

The selection requires an event to have one vertex and the scattered muon track. A trigger selection on the scattered muon by the fibre trigger array gives a trigger decision on a deflected muon, and together with the exclusivity criteria an elastic scattering event is selected. In order to prevent tracks from traversing unwanted material, the trajectories of the incoming and outgoing particles are required to traverse the TPC beryllium windows. Measuring the scattered muon by the spectrometer and using its kinematics and position in the xy-plane allows to match those events with the ones recorded by the TPC. The vertex z resolution of the TPC (σ_z = 0.4 mm), as determined by the resolution of the drift time, allows one to select that the scattering occurred only in the hydrogen gas.

Figure 11 shows the effects of the selection criteria on the reconstructed Q^2-spectrum shown in Fig. 10 for the TPC. Without any selection applied, the reconstructed Q^2-spectrum using the muon only introduces artefacts that are resolved by using the kinematic matching. Other criteria do not affect the shape of the measured spectrum in this case. The extracted Q^2-spectrum using the recoil-proton data only tends to be quite clean without any constraints applied and does not change with those selection criteria applied.

2.9.2 Calibration of the recoil-proton energy scale using muon-electron scattering [v2(new)]

In order to calibrate the energy scale, *i.e.* the Q^2 values determined from TPC recoil-proton measurements, the value determined from muon scattering has to be used. Since measuring muon energy and scattering angle for larger event samples is on average better than 10^{-3}, the TPC calibration can be determined on the same level by correlating muon and recoil-proton information. Later on, the information gained in the experiment with a similar TPC in Mainz can be used to refine this procedure.

Figure 12 shows the absolute beam energy resolution using the reconstructed muon track. Based on the standard Compass muon setup a precision of about 0.49% is achieved. Further optimisations of the detector positions are ongoing and together with the measurement of the momentum by the Compass Beam Momentum Stations (BMS), the required improvement down to 0.2% can be achieved.

At this level, the knowledge of the involved magnetic field strengths must be controlled, best in an independent way. We foresee to use the elastic muon-electron scattering events that occur along with

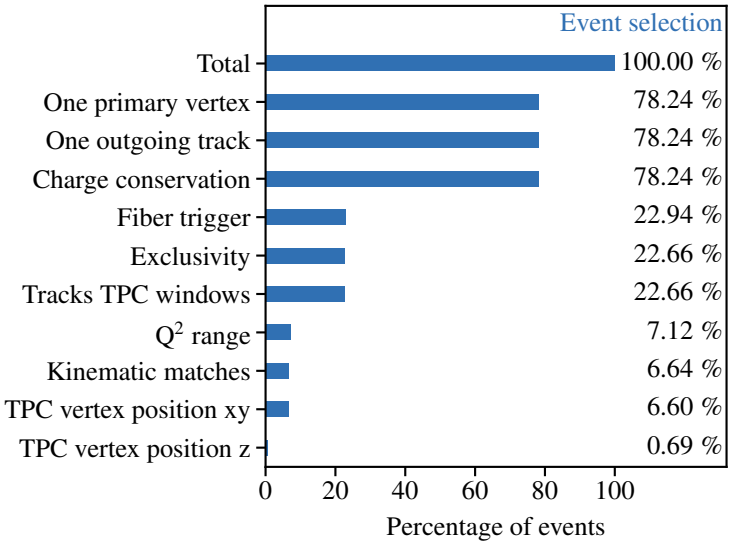

Figure 9: Event selection criteria and resulting percentage of events. A detailed description of the criteria is listed in Table 4.

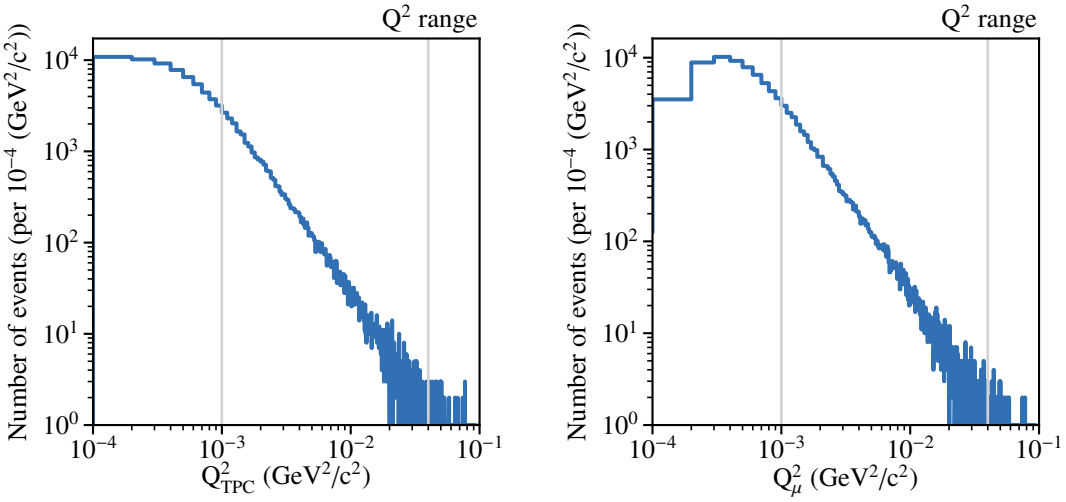

Figure 10: Reconstructed Q^2-spectrum using the recoil-proton data of the TPC (left) and using the muon scattering (right) with all selection criteria applied except the one on the Q^2-range, which is indicated by the gray lines.

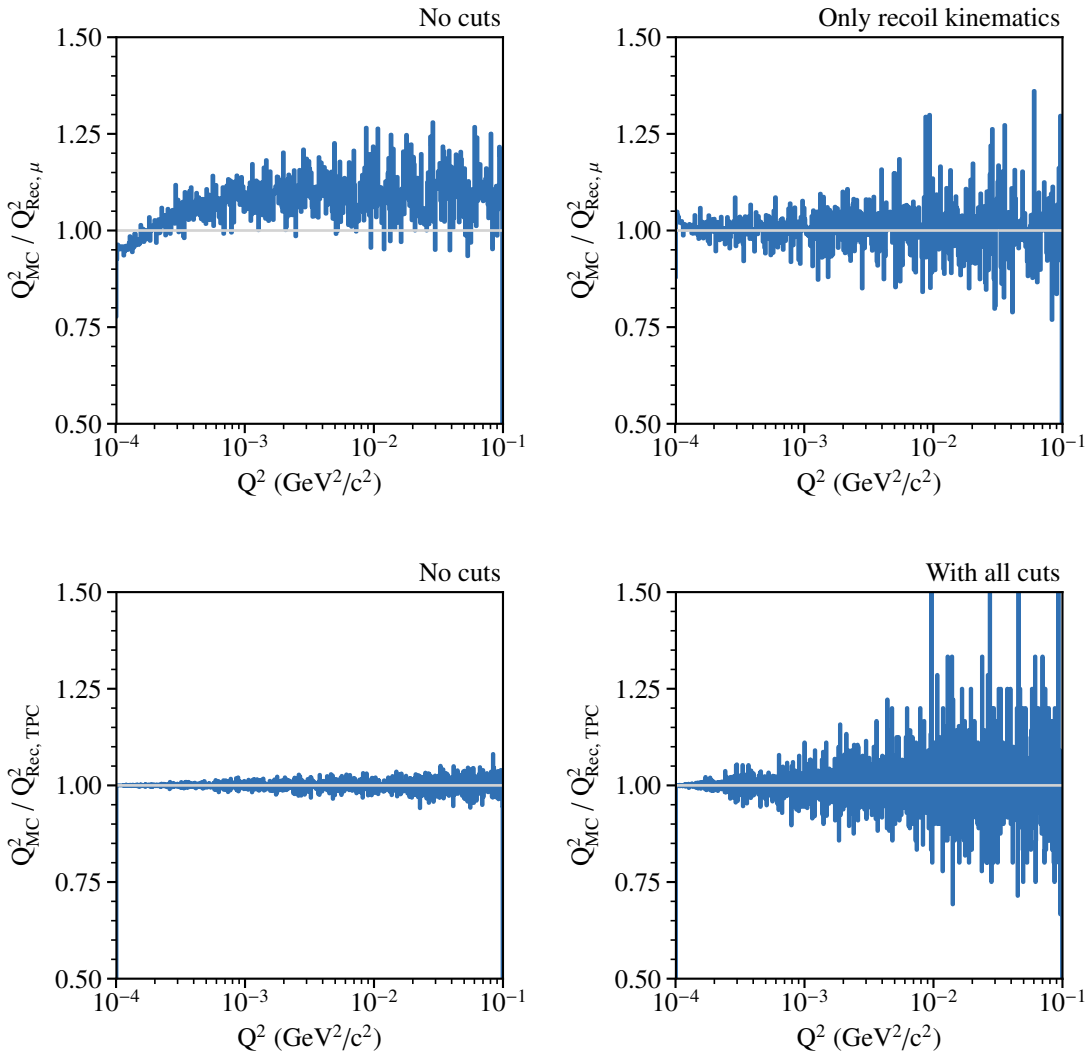

Figure 11: Influence on the reconstructed Q^2-spectrum due to selection criteria. The upper row shows the reconstructed Q^2-spectrum using only the muon scattering. The lower row shows the reconstructed Q^2-spectrum using only the TPC recoil proton. Whereas the main influence on the shape in the muon spectrum originates from the kinematic matching with the recoil proton, the measured TPC spectrum is expected to be clean before and after selection cuts.

Table 4: Overview of the criteria for the event selection with a brief description. Those criteria ensure a clean data sample for the extraction of the Q^2 spectrum.

name	description
Total	Total number of recorded events
One primary vertex	Only one interaction between the beam particle and the target material
One outgoing track	Only one outgoing track
Charge conservation	Charge conserved between incoming and outgoing track
Fibre trigger	Selected by fibre trigger
Exclusivity	Energy conservation
Track TPC window	Particle tracks pass TPC windows
Q^2 range	Restrict to Q^2 range
Kinematic matches	Matching between muon and proton kinematic
TPC vertex position xy	Vertex position xy in TPC
TPC vertex position z	Vertex position z in gas volume of TPC

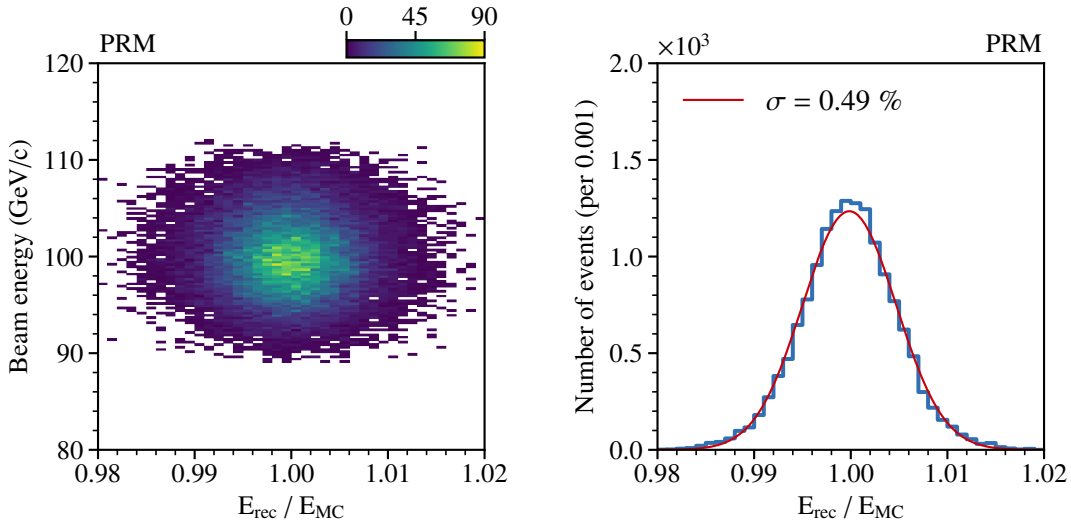

Figure 12: Absolute beam energy resolution using the reconstructed muon track. Based on the standard COMPASS muon setup and assuming no systematic effect from the field calibrations, a precision of about 0.49% is achieved.

muon-proton scattering in terms of Q^2, with approximately the same intensity. It is sufficient to measure only the angles of the outgoing muon and electron (with respect to the incoming beam muon direction), in order to calculate the beam energy, as shown in Fig. 13. This provides an independent method to control the beam energy calibration along the data taking. Since the scattering off electrons in the narrow structures as the readout planes and the TPC windows can be used, the high event-rate will provide sufficiently large statistics to control the calibration at the aimed permille level on a daily base.

2.9.3 Fitting procedure [v2(new)]

The extraction of the proton radius from the measured Q^2 spectrum is planned to be done in a fully Bayesian manner. All acceptance corrections and nuisance parameters that could affect the proton-radius

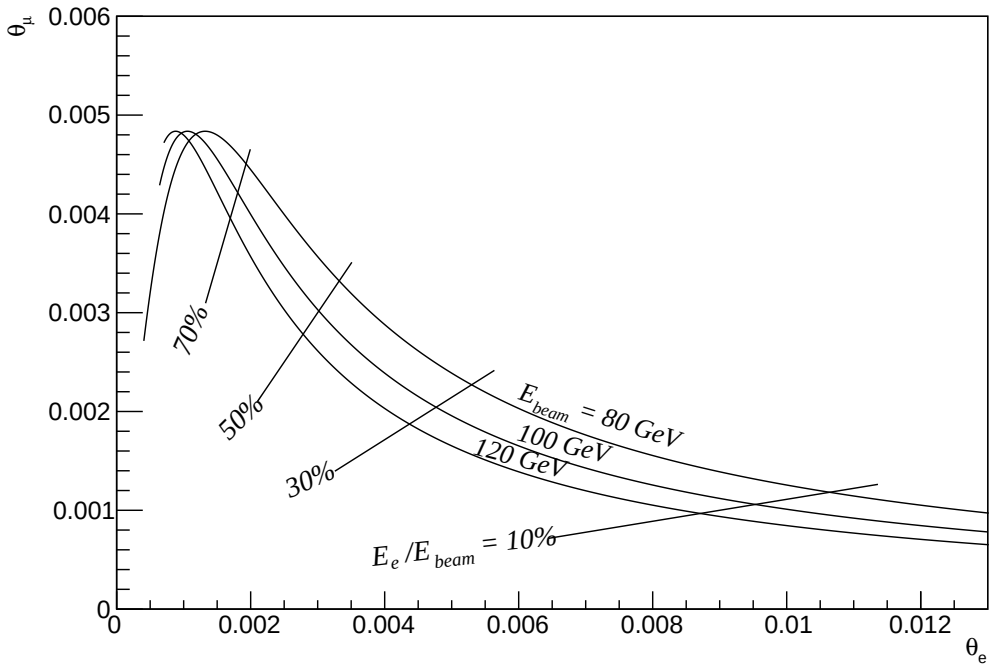

Figure 13: Kinematics of elastic muon scattering off the atomic shell electrons, in large-momentum approximation of the electrons (thus neglecting their initial binding, *i.e.* "delta electrons". The measurement of the outgoing muon and electron angles uniquely defines the beam energy.

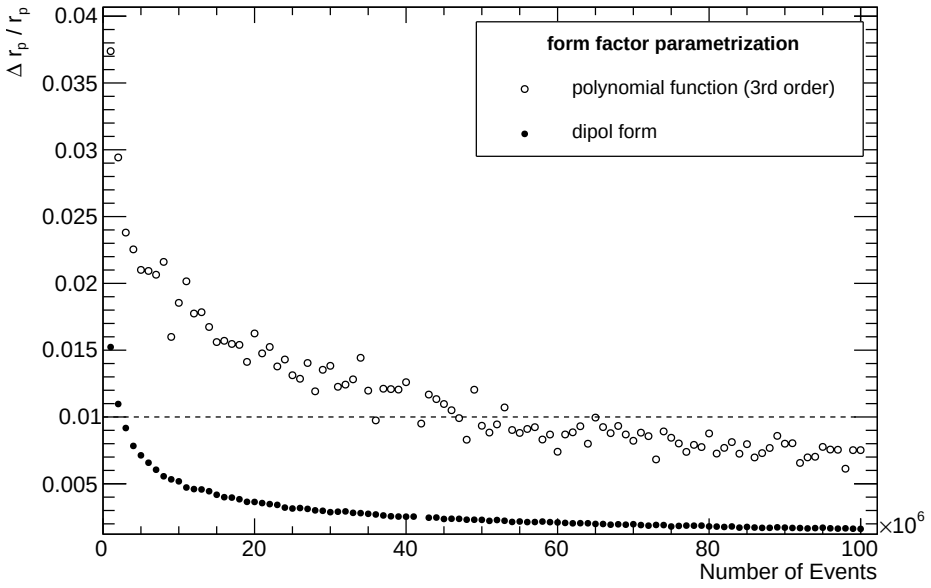

Figure 14: Dependence of the statistical uncertainty of the measured proton radius on the recorded number of events, given for two different parametrisations of the electric form factor. In order to achieve a relative statistical precision of below 1% for most of the form-factor models, at least 50 million events have to be recorded in the foreseen Q^2 range.

parameter are included in the fit. This encompasses the use of free fit parameters from the form-factor models like the higher-order terms in the polynomial representation, as well as the normalisation parameter(s) of the absolute cross-section measurement. Parametrised or binned acceptance corrections, as for example from the trigger efficiency or other event-selection constraints, are included in the fit as parameters with prior information. Using importance-sampling algorithms such as Markov-Chain Monte Carlo methods [45], the correlation of these acceptance-correction parameters with the proton-radius parameter can be quantified and potential biases of the result can be studied and mitigated.

For the extraction of the proton radius a functional form of the electric form factor has to be assumed. In order to verify the robustness of the extracted proton radius from different form-factor parametrisations and to estimate the systematic uncertainty of the underlying form-factor model, systematic studies of the fit procedure with different models have to be performed, as they are exemplarily suggested in [46].

For the assessment of the statistical uncertainty on the extracted proton radius from the measured Q^2 spectrum for different amount of events, we perform fits on Monte-Carlo generated pseudo data in the expected Q^2 measurement range of our experiment. The fits are performed using the standard dipole form of the electric form factor as a standard-reference model, and a polynomial form up to the Q^6 term, which has been found to fit existing data much more robust and with less bias. However, the variance of this model is quite large as it has in total 4 free parameters that are strongly correlated in the applied measurement range. Thus we use this model as some kind of upper limit on the statistical uncertainty. Figure 14 shows the expected statistical uncertainty on the proton radius as a function of the number of recorded events in the measurement range $0.001 < Q^2/(\mathrm{GeV}^2/c^2) < 0.04$. In order to achieve a statistical uncertainty of the measurement below 1%, independent of the applied form-factor model, at least 50 million events in the relevant Q^2 range have to be collected.

2.9.4 Inefficiencies in the proton-recoil and scattered-muon measurement [v2(new)]

In order to obtain the high level of control on the relevant acceptance and efficiency corrections that are needed in order to determine a cross section shape with 10^{-3} precision, the redundancy between the muon and proton detection of the elastic scattering process is of key importance. This requires to obtain the highest possible precision on the scattering kinematics from both the recoiling proton and the scattered muon. While for the final result the Q^2 information from the proton recoils are the most precise and thus most relevant ingredient, it is important that the definition of a clean muon-proton elastic scattering event sample can be determined from the muon kinematics alone. Only this way, the performance of the TPC can be cross-checked independently.

2.9.5 Emission of real bremsstrahlung photons in elastic lepton-proton scattering [v2(new)]

Elastic lepton-proton scattering is always accompanied by the emission of real bremsstrahlung photons. While the effect is small for muons, it is still of interest to check this next-to-leading order process experimentally. For photons above 500 MeV the emission probability, relative to the non-radiative elastic scattering process at the same muon scattering angle, is about $3 \cdot 10^{-4}$, and together with the 70 million non-radiative (rather: low-radiative) events about 20 000 radiative events are expected. Since the photons are emitted predominantly under forward angles, as shown exemplarily for a larger-angle scattering kinematics in Fig. 15, it is sufficient to operate the central region of the forward electromagnetic calorimeter.

2.9.6 Synopsis of systematic uncertainties on the cross-section measurement

We collect the discussed uncertainties on the the cross-section measurement, excluding the overall normalisation uncertainty of about 1%, in Table 5. We conclude at this stage, that the precision of the cross-section slope determination will involve a systematic uncertainty of less than 0.6%.

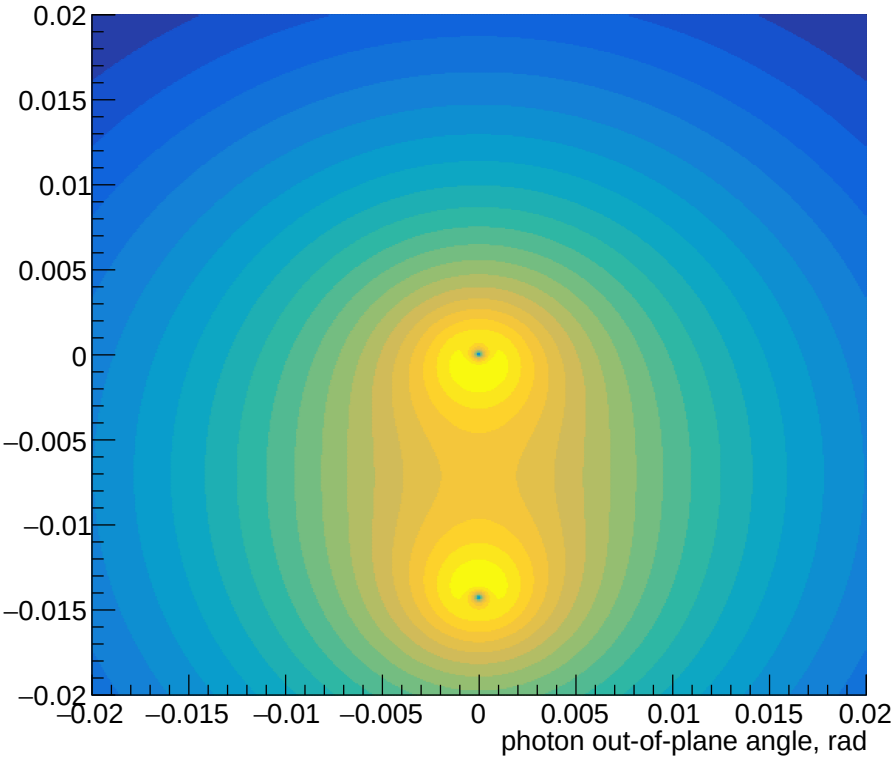

Figure 15: Angular spectrum of bremsstrahlung photons in forward direction, for muon beam energy 100 GeV, muon scattering angle 14 mrad and photon energy 1 GeV. The photon emission angle in the muon scattering plane (vertical axis) is shown versus the photon out-of-plane angle, both in rad. The colour scale shows the intensity on a logarithmic scale, indicating the strong forward peaking of bremsstrahlung along the particle directions.

Table 5: Systematic uncertainties in Percent for the bin-to-bin measurement of the cross-section shape of muon-proton scattering in the Q^2 range 0.001 to 0.04 GeV$^2/c^2$. For a conservative upper limit, the uncertainties are added linearly. The uncertainties are meant as introducing a relative shift of cross section for the outermost Q^2 bins, and thus the same relative effect on the determination of the cross-section slope.

uncertainty source	**estimate in ‰**
Monte-Carlo acceptance correction	0.2
Q^2 resp. beam energy calibration	0.2
radiative corrections	0.1
fitting procedure	0.1
(linear) sum	<0.6

2.10 Results of the test in 2018 [v2(+)]

In parallel to the COMPASS run in 2018, we performed an about 2-months feasibility test using the basic detector setup for the proposed measurement of the proton charge radius. At the downstream end of the experimental hall EHN2, *i.e.* downstream of the COMPASS spectrometer, a TPC was installed together with four silicon trackers, similar to the proposed setup in Fig. 4, although at smaller scale. For the COMPASS Drell-Yan measurement π and μ beams with an energy of 190 GeV were used, and an absorber was located directly behind the COMPASS target. Thus rather broad muon beams had to be used, with different intensities and geometrical properties, to study in particular the behaviour of the TPC acting as active target.

The silicon trackers, comprising four detector layers each in different projections, were used previously in the COMPASS beam telescope. Their size of 7 cm × 5 cm roughly matches the size of the entrance windows of the TPC. Two scintillating counters (one segmented, one monolithic) provided a beam trigger for the read-out of the silicon detectors if both incoming and outgoing muon were detected.

The TPC, filled with hydrogen gas at a pressure of 8 bar, served as active target. The anode of the TPC was segmented in a radial pad structure, similar to the proposed TPC, allowing for a measurement of direction and energy of recoil protons. The TPC triggered itself, the read-out of the connected ADCs being independent of the silicon DAQ. Both DAQs could be synchronised via recorded time stamps.

After the reconstruction of incoming and outgoing muon tracks from the data of the silicon trackers, events with scattering angles $\theta \geq 0.2$ mrad were selected. In addition, a radial cut on the entrance windows of the TPC was applied. Figure 16 shows the difference in the time stamps of the silicon and the TPC data. Further constraints on the vertex coordinate along the beam line and the condition that one of the two central anode pads of the TPC was hit, improve the signal-to-noise ratio significantly. A detailed description of the analysis can be found in [47].

Figure 17 shows the difference of the reconstructed azimuthal angle φ of the silicon detector and the TPC data. The width corresponds reasonable well to the angular segmentation of the TPC anode, and demonstrates the high purity of the correlated event sample.

Figure 18 shows the recoil proton energies determined by both detector systems. The resolution obtained through the TPC signals is much better than the one by the muon scattering kinematics, which encourages the usage of a TPC for recoil-proton detection in a high-precision Q^2-measurement. Also, the clear correlation between both signals indicates that this principle of ensuring elastic muon-proton scattering works with the available detectors. With enlarging the base lines of the silicon telescopes, and measuring at lower beam energy, we expect for the main experiment a reduction of the uncertainty by at least a factor two, which may allow a lower constraint on energy (in fact scattering angle) in order to fully cover the range down to 0.5 MeV.

In Fig. 19, the drift time in the TPC, which is a precise tool to determine the interaction point in beam

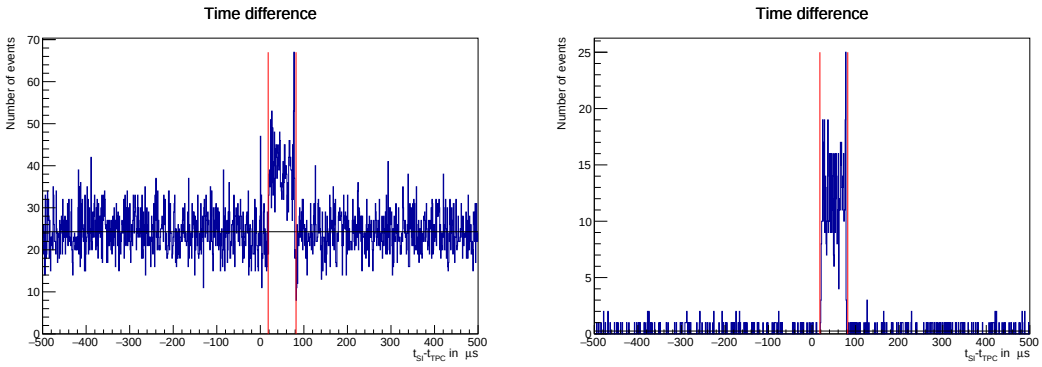

Figure 16: Difference between the time stamps of the silicon detectors and the TPC. *Left*: only with θ and radial constraints. *Right*: with additional constraints that the z coordinate (along the beam) of the vertex lies within the active area of the TPC and the condition that central TPC anode pads were hit. There is a correlation in time between 18 and 82 μs, which corresponds well to the expected maximum drift time in the TPC of around 60 μs.

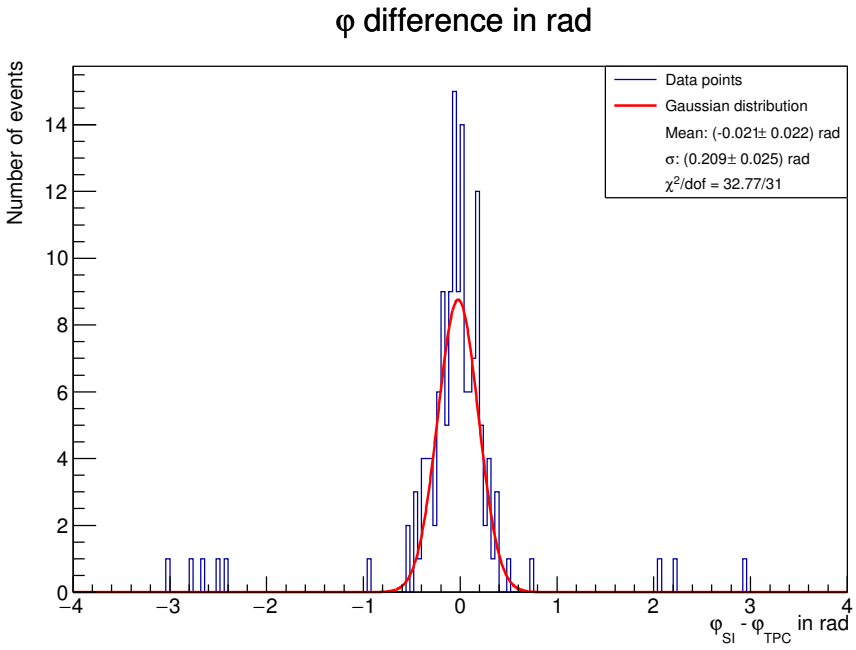

Figure 17: The difference in the azimuthal angle φ between the tracks measured with the silicon detectors and the ones reconstructed with the TPC. The width of the peak originates mainly from the $\pi/8$ segmentation in single pads of the TPC anode.

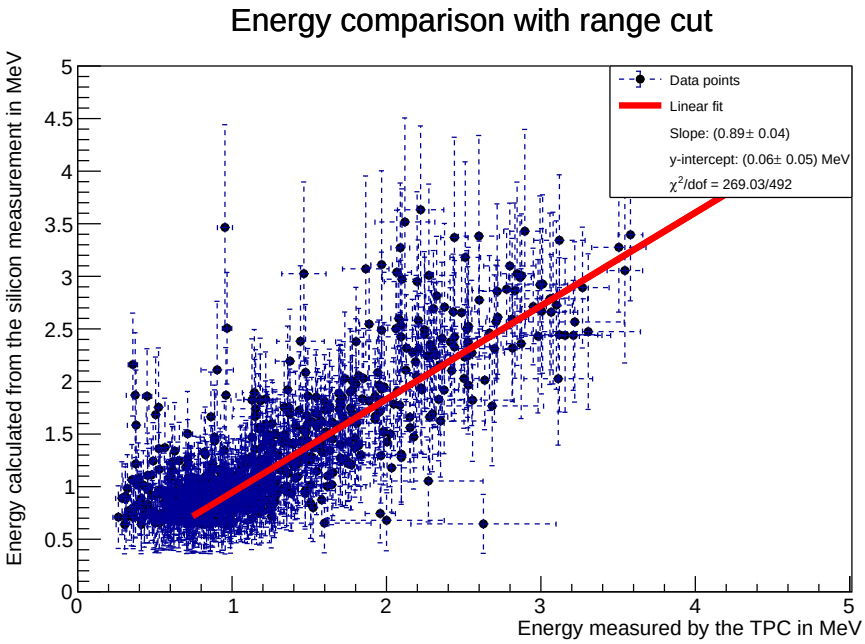

Figure 18: The energy of the recoil proton calculated from the scattering angle θ measured by the silicon trackers versus the energy deposit measured in the TPC.

direction, is compared to the information from the silicon detectors. From the trajectories of incoming and scattered muon, the interaction point can be determined as well, however with inferior resolution. The large uncertainties in the determination of the vertex position from the silicon detectors display most clearly, in which regard the main measurement has to be enhanced as compared to the test setup, namely to provide the best possible resolution in the vertex finding, which is crucial in order to select the correlated event sample down to smallest scattering angles.

Altogether, in the test during the 2018 COMPASS beam time we acquired important experience regarding the detector properties, and how the data analysis of the proposed experiment will be performed by relating the muon-scattering and proton-recoil kinematics for high-energy elastic scattering at low momentum transfers. The broad-beam conditions during the test were not optimised for the readout geometry of the TPC. Still, the obtained results give confidence in the idea of using a TPC for recoil-proton detection in order to achieve the required high resolution in Q^2 for a successful measurement of the proton charge radius in high-energy elastic muon-proton scattering.

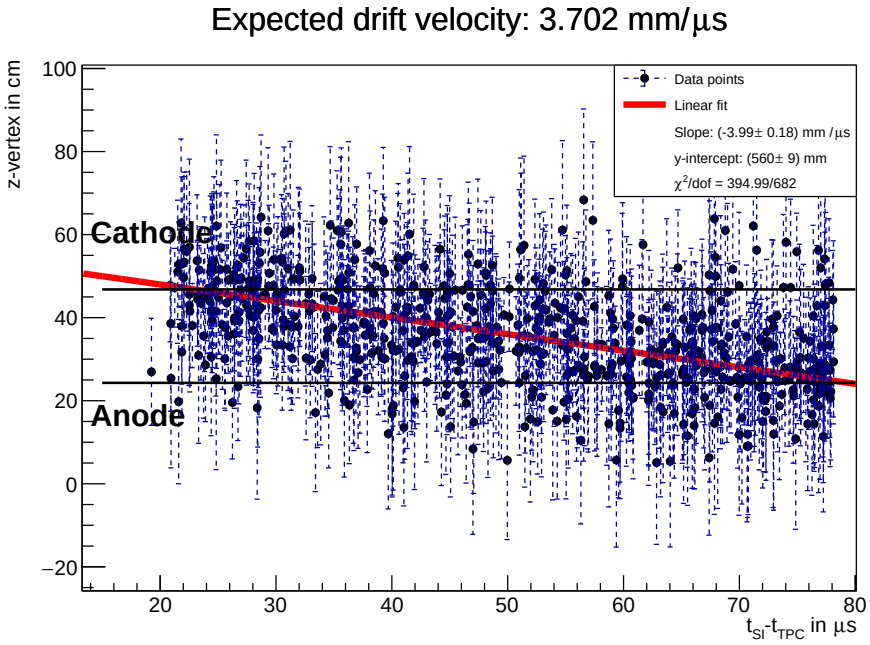

Figure 19: z coordinate of the vertex versus time difference of the TPC and silicon data. The linear fit determines the drift velocity, which is slightly larger than the one expected from simulations (taking into account mainly properties of the hydrogen gas).

3 Drell-Yan and charmonium production using conventional hadron beams

3.1 Physics motivation [v2(+++)]

In phase-1 of the COMPASS ++/AMBER project, it is planned to use the existing CERN M2 hadron beam. Three major physics goals are envisaged:

(1) The structure of the pion: determination of the pion valence and sea-quark distributions;

(2) Investigation of flavour-dependent effects in nuclear targets;

(3) Study of the charmonium production mechanism.

ad 1) The structure of the pion: determination of the pion valence and sea-quark distributions
The natural energy scale for strong interactions is the proton mass: $m_p \approx 1\,\text{GeV} \approx 2000\,m_e$, where m_e is the electron mass. In the Standard Model, m_e is rightly attributed to the Higgs boson; but what is the source of the enormous enhancement to produce m_p? This is the crux: the source of the vast majority of visible mass in the Universe is unknown; a realisation which leads one to appreciate that the existence of our Universe depends critically on, *inter alia*, the following empirical facts, that must be somehow explained by QCD: (*i*) the proton is massive, *i.e.* the mass scale for strong interactions is vastly different to that of electromagnetism; (*ii*) the proton is absolutely stable, despite being a composite object constituted from three valence quarks; and (*iii*) the pion is unnaturally light, possessing a lepton-like mass despite being a strongly interacting composite object built from a valence quark and valence antiquark.

The QCD Lagrangian, $\mathcal{L}_{\rm QCD}$, is simple: comparing with QED, the *solitary* difference is the gluon self-interaction term. Nonetheless, $\mathcal{L}_{\rm QCD}$ is responsible for the origin, mass, and size of almost all visible matter in the Universe. The only apparent energy scales in $\mathcal{L}_{\rm QCD}$ are the current quark masses, generated by the Higgs boson; but focusing on the quarks that define nucleons, *i.e.* up and down, this scale is more than 100 times smaller than m_p. No amount of "staring" at $\mathcal{L}_{\rm QCD}$ can reveal the source of that enormous amount of "missing mass"; yet, it must be there. This contrasts starkly with QED, wherein the scale of phenomena is set by m_e, a prominent feature of $\mathcal{L}_{\rm QED}$ that is generated by the Higgs boson.

This *emergence* of mass is a signature feature of strong dynamics in four-dimensional asymptotically-free quantum field theories; and understanding the phenomenon is a prerequisite to an explanation of how the Universe came into being. Basic to this is the QCD scale anomaly; namely, even in the absence of a Higgs mechanism, the scale invariance in QCD is broken by strong dynamics so that the trace of the QCD energy-momentum tensor does not vanish, $T_{\mu\mu} \neq 0$. However, knowing a trace anomaly exists only indicates that there is a mass scale. The crucial issue is whether one can compute and/or understand the magnitude of that scale. One can certainly measure the size of the scale anomaly because, evaluated in the proton state: $\langle p|T_{\mu\mu}|p\rangle = m_p^2$. Evidently, the scale anomaly is measurably large; and given the operator expression for $T_{\mu\mu}$, that property must owe to gluon self-interactions. However, there is a related issue, *i.e.* $\langle \pi|T_{\mu\mu}|\pi\rangle = m_\pi^2$; hence, $\langle \pi|T_{\mu\mu}|\pi\rangle = 0$ in the chiral limit because the pion is a massless Nambu-Goldstone (NG) mode [9, 10]. Consequently, the source of the proton mass cannot be completely understood unless the simultaneous absence of a pion mass is also explained. Any solution of QCD is impossible before this conundrum is resolved [4].

Modern theory reveals that dynamical chiral symmetry breaking (DCSB) within the Standard Model explains the character and qualities of NG bosons. In fact, the properties of the nearly-massless pion are the cleanest expression of the mechanism that is responsible for (almost) all the visible mass in the Universe [3]; and the associated theory simultaneously reconciles the emergence of m_p with the masslessness of the pion in the chiral limit [4]. It shows, too, that a determination of the valence-quark PDF of the pion provides the needed sensitivity to the mechanism(s) responsible for the emergence of mass in QCD.

One of the earliest QCD predictions for the pion valence PDF is [48–50]: $u^\pi(x;\zeta=\zeta_H) \sim (1-x)^2$, where ζ_H is an energy scale characteristic of nonperturbative dynamics. Pion-induced Drell-Yan measurements are ideally suited to extracting $u^\pi(x;\zeta)$. However, the most recent measurements[1] are thirty years old [51–56]; and conclusions drawn from those experiments have proved controversial [57]. For example, using a leading-order (LO) pQCD analysis, Ref. [56] (the E615 experiment) reported (at the scale given by the average dimuon mass accessed, $\zeta_5 = 5.2\,\text{GeV}$): $u^\pi_{\text{E615}}(x;\zeta_5) \sim (1-x)^1$, in striking contradiction with the QCD prediction. Subsequent calculations [58] confirmed the original theory prediction and eventually prompted reconsideration of the E615 analysis, with the result that, at next-to-leading order (NLO) and including soft-gluon resummation [59, 60], the E615 data can be viewed as consistent with QCD. Notwithstanding these advances, uncertainty over $u^\pi(x)$ remains because more recent analyses of the E615 data have failed to incorporate threshold resummation effects [61] and, crucially, more precise data are lacking. Pressure is also being applied by modern advances in theory. Novel lattice-QCD algorithms [62–66] are beginning to yield results for the pointwise behaviour of $u^\pi(x)$ [67–70]; and recent continuum analyses are also yielding new insights: the first parameter-free predictions of the valence, glue and sea distributions within the pion [71] reveal that the pion valence PDF is hardened as a direct consequence of emergent mass. Very significantly, the new continuum prediction for $u^\pi(x;\zeta_5)$ matches that obtained using lattice-QCD [70]. A remarkable, modern confluence has thus been reached, demonstrating that real strides are being made toward understanding pion structure. The Standard Model prediction: $u^\pi(x;\zeta=\zeta_H) \sim (1-x)^2$, is stronger than ever before; and an era is dawning in which the ultimate experimental checks can be made.

Presently, a new generation of experiments appears at the horizon. In the realm of DIS experiments, it was recently proposed to study the pion structure through final-state tagged DIS at JLab [72], while for preparing the long-range future the feasibility of pion and kaon-structure measurements at a future Electron-Ion Collider has been evaluated [73]. In the realm of Drell-Yan experiments, the existing high-intensity, pion-rich hadron beam delivered by the CERN M2 beam line provides already today a world-unique opportunity to study the structure of pions and nucleons through pion-induced dimuon production on unpolarised nuclear targets. High-statistics experiments using both pion beam charges would provide the long-awaited new Drell-Yan data to be confronted with the recent theoretical calculations discussed above. By their improved sensitivity to valence and sea contributions a clear separation would become possible between valence and sea in the pion.

The potential of such measurements to expose emergent mass is greatly enhanced if one includes similar kaon measurements. The combined power of continuum and lattice-QCD analyses has revealed that strange-quark physics lies at the boundary between dominance of strong (emergent) mass generation and weak (Higgs-connected) mass. Hence, comparisons between distributions of truly light quarks and those describing strange quarks are ideally suited to exposing measurable signals of emergent mass in counterpoint to Higgs-driven effects; and a most striking example can be found in the contrast between the valence-quark PDFs of the pion and kaon. A significant disparity between these distributions would point to a marked difference between the fractions of pion and kaon momentum carried by the other bound-state participants, particularly gluons.

A prediction for the ratio $u^K(x)/u^\pi(x)$ is available [74]: agreement with data [51] indicates that the gluon content of the kaon at the hadronic scale ζ_H is just $5 \pm 5\%$, whereas that for the pion is more than 30% at this scale. Hence, there are striking differences between the gluon content of the pion and kaon; and they persist to large resolving scales, *e.g.* at $\zeta = 2\,\text{GeV}$ the gluon momentum fraction in the pion is still 50% greater than that in the kaon. This difference in gluon content is clearly expressed in the large-x behaviour of the π and K valence-quark PDFs. It is a striking empirical signal of the almost pure NG-boson character of the pion in contrast to the explicitly broken symmetry of the s-quark-containing

[1] A more recent measurement of the pion-induced Drell-Yan production was done by Compass in 2015 and 2018. The cross-section results are not yet available.

kaon. The issue again, however, is that there is only one forty-year-old measurement of $u^K(x)/u^\pi(x)$ [51]. It is hence of utmost interest to upgrade the existing CERN M2 beam line by an RF-separation stage in a later phase of the COMPASS ++/AMBER project. Such a unique high-energy high-purity kaon beam would for the first time allow a detailed measurement of the kaon's parton structure, which would pave the way to address the fundamental physics questions sketched above (see also Sec. 6.2).

ad 2) Investigation of flavour-dependent effects in nuclear targets
The new insight into the pion structure, as addressed above, will allow revisiting the convolution of PDFs present in the Drell-Yan cross section and the modifications of nucleon PDFs induced by the nuclear medium. Experimental evidence came first from the CERN EMC experiment [75] and their observation of the so-called EMC effect that was explored in-depth over the last 30 years. However, a complete understanding of the mechanisms governing these PDF modifications has not been reached yet. Their possible flavour dependence is one of the open questions that will be addressed in the proposed new experiment.

The Drell-Yan cross section measured from interactions occurring in a light isoscalar target serves as reference for the cold nuclear matter effects, which are encoded in the Drell-Yan cross section as measured using a heavy target. Unrivalled sensitivity to these effects can be reached by building up a novel observable out of 4 cross sections, see sect. 3.3, making use of the two pion beam charges in combination with the light and heavy targets. For this goal to be reached, excellent control over systematic uncertainties affecting the absolute cross sections is mandatory. An experimental assessment of the systematics can be provided by measuring (in parallel) the charmonium production cross section, see below. For an isocalar target, the J/ψ production cross section must be the same for either pion beam polarity, as it was experimentally verified by NA3 (see [76]), providing a useful experimental check of the absolute cross section normalisations.

ad 3) Study of the charmonium production mechanism
The interest to study charmonium production goes far beyond the above mentioned measurement. Understanding the formation mechanisms of charmonium bound states is of central importance in QCD. The observable mesons can evolve from a variety of $c\bar{c}$ pre-resonant states having different quantum properties, each one characterised by different short-distance production cross sections, *i.e.*, by different observable transverse-momentum and Feynman-x distributions and different polarisations. Measuring with high statistical precision the Feynman-x dependence of the cross section and the decay-angular distribution can hence establish the relative importance of such pre-resonant contributions, thereby providing a direct probe of the long-distance bound-state formation processes. In the kinematic regime of the proposed experiment, charmonium is produced with relatively low transverse momentum and $2 \rightarrow 1$ processes are dominant as compared to $2 \rightarrow 2$ ones. This is fundamentally different from the kinematic regime accessible at LHC, so that a complementary picture of the charmonium production mechanisms will be obtained. Furthermore, the opportunity of a simultaneous measurement of pion and proton-induced J/psi cross sections (both particles are contained in the positive hadron beam) should provide an additional way of disentangling hadron-structure and production-mechanism effects.

A comparison of predictions from different models of quarkonium formation to the measured momentum distribution and polarisation of the J/ψ will represent a thorough test of the theory in the low-transverse-momentum domain. Moreover, the proposed measurement can be used as a new constraint on the relative contributions of the quark-antiquark annihilation and gluon-gluon fusion processes and, when the polarisation information is added, even on their kinematic shapes. This means that eventually charmonium production data could be used as a probe of the gluon distribution in the pion.

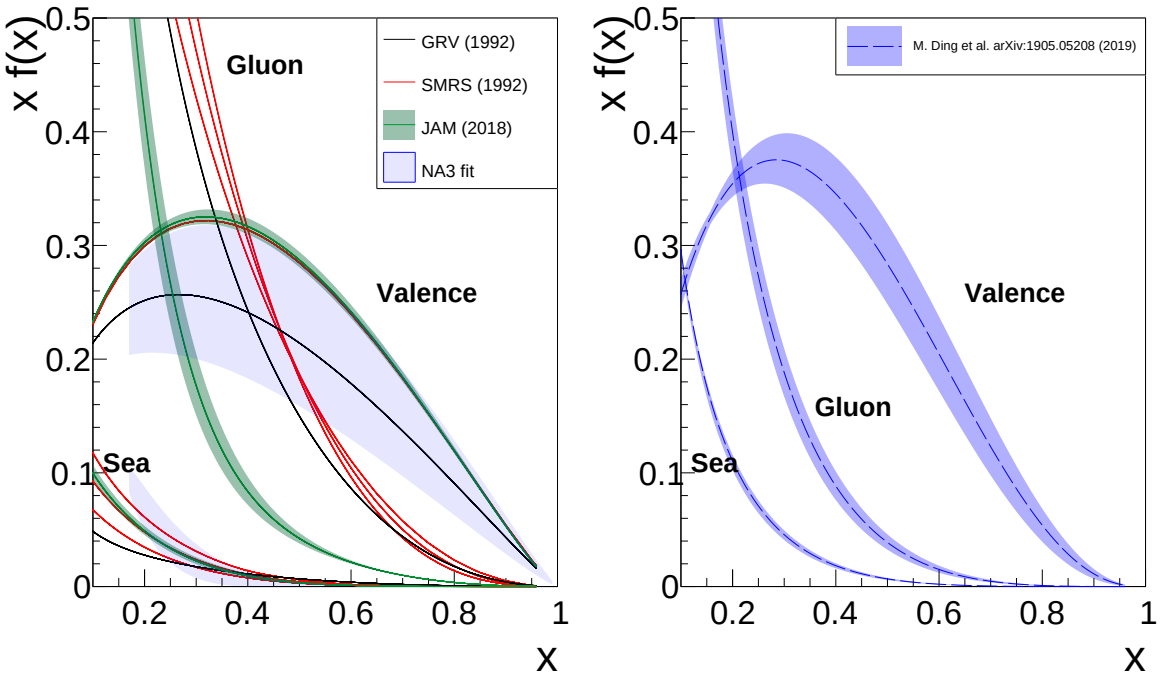

Figure 20: Left: valence, sea and gluon distributions for the pion from global fits of GRV/S [81, 82], SMRS [80], and JAM [85], shown together with the NA3 extraction [52]. The three sea curves labelled SMRS correspond to three different hypotheses for the sea quark content. As a result, there are also three curves for the gluon contribution. The shaded area accounts for the experimental uncertainty, evaluated using the published NA3 data. Right: Same as left for the most recent calculation based on continuum analyses [71].

3.2 Drell-Yan pair production measurements as a tool for sea-valence separation in the pion [v2(+)]

The pion-induced Drell-Yan process is the most direct way to access information on the pion valence structure, in particular at a large fraction of quark momentum with respect to the parent pion, denoted by x_π. Constraints on the gluon component in the pion are imposed by other reactions, like direct-photon production in hadron-hadron collisions. Pion-induced Drell-Yan data were collected by the NA3 [52], NA10 [53], and WA39 [77] collaborations at CERN and by the E615 [56] collaboration at Fermilab, more than 30 years ago. Some of these experiments used both π^+ and π^- beams (NA3 and WA39) in order to access also the sea distributions in the pion. The available data from direct-photon production were also obtained at that time, by the WA70 [78] and the NA24 [79] experiments at CERN.

The above data sets were used in the first global analyses focused on the pion structure; the most cited ones being SMRS [80] and GRV, GRS [81, 82]. More recently, the leading-neutron DIS-production data from the ZEUS [83] and H1 [84] experiments at HERA became available, giving valuable input to constrain the pion structure at values of x_π as low as 0.001, since pion exchange is believed to be the dominating mechanism here. The Jefferson Lab JAM collaboration indeed observed a strong impact of these low-x_π data in their newest global fits [85]. Figure 20 summarizes the present knowledge on the pion PDFs. The left-hand side panel shows the pion distribution from the three global analyses, done by the GRV/S, SMRS and JAM groups. The first two extractions rely on the π^- Drell-Yan data from E615 and NA10, as well as the direct-photon measurements of WA70 and NA24. Although they are more than 20 years old, they are still commonly in use. Due to the limited data sets, part of the contributions, in particular the sea quark distribution, is derived from momentum-sum-rule conservation. No uncertainty estimates are available; instead SMRS provides three scenarios of sharing the pion momentum fraction between the gluon and the sea quark distributions. These three scenarios describe equally well the data and correspond to 10%, 15%, and 20% of the pion momentum fraction carried by the sea. The JAM extraction, using

pion-induced Drell-Yan and leading-neutron data, is closest to the SMRS result with maximum sea quark and minimum gluon contributions. In the same figure, the valence and sea quark distributions from NA3 are also shown, together with their respective error bands. The NA3 result was derived from the published fit coefficients and correlation matrix, using the NA3 data sets alone.The right-hand side of Fig. 20 shows the newest theory predictions, a continuum analysis (based on DSE formalism) from [71]. Other recent predictions, like those from the light-front wave function approach [86], [87] or from lattice QCD calculations [88], although not shown, seem to agree reasonably well with this latter.

3.2.1 Formalism

In the pion-induced Drell-Yan process with an incoming charged pions ($\pi^{\pm}$) scattering off a nucleon (N) from a nuclear (A) target, a pair of opposite-charge leptons is produced:

$$\pi^{\pm}(P_\pi) + N(P_N) \rightarrow \gamma^*(q) \rightarrow l^+l^- + X. \tag{17}$$

Here, P_π (P_N) is the four-momentum of the beam (target) hadron, and q is the four-momentum of the virtual photon or equivalently the sum of the four-momenta of the two leptons. In the proposed measurement, pairs of opposite-sign muons (the so-called dimuons) are detected in the final state. The relevant kinematic variables describing the process are:

$s = (P_\pi + P_N)^2$	the total centre-of-mass energy squared,
$x_{\pi(N)} = q^2/(2P_{\pi(N)} \cdot q)$	the momentum fraction carried by a parton from $\pi^{\pm}(N)$,
$x_F = x_\pi - x_N$	the Feynman variable,
$y = \ln \frac{x_\pi}{x_N}/2$	the dilepton rapidity,
$M_{ll}^2 = Q^2 = q^2 = s x_\pi x_N$	the invariant mass squared of the dilepton.

The Drell-Yan cross section at lowest order can be written as [85]

$$\frac{d^2\sigma}{dM_{ll}^2 dy} = \frac{4\pi\alpha_{em}^2}{9M_{ll}^2 s} \sum_{ij} \int_{x_\pi}^1 \frac{dx_\pi}{x_\pi} \int_{x_N}^1 \frac{dx_N}{x_N} C_{ij}(x_\pi, x_N, M_{ll}/\mu)\, f_i^\pi(x_\pi, \mu)\, f_j^N(x_N, \mu), \tag{18}$$

with f_i^π being the pion PDF for parton flavour i and f_j^N the nucleon PDF for parton flavour j. In this expression, μ is the renormalization scale, and C_{ij} the hard-scattering kernel.

In order to determine the shape of the sea-quark distribution in the pion and better constrain the region of phase space corresponding to $x_\pi > 0.1$, data will be collected with pion beams of positive and negative charge impinging on a light isoscalar target.

The valence quarks in the pion are defined as $u_{val}^{\pi^+} = u^{\pi^+} - \bar{u}^{\pi^+}$ and $d_{val}^{\pi^-} = d^{\pi^-} - \bar{d}^{\pi^-}$, charge and SU(2)-flavour symmetry being assumed:

$$u_{val}^{\pi^+} = \bar{d}_{val}^{\pi^+} = \bar{u}_{val}^{\pi^-} = d_{val}^{\pi^-} \tag{19}$$

Additionally, SU(3) flavour-symmetry is assumed for the sea quarks in the pion:

$$\bar{u}_{sea}^{\pi} = u_{sea}^{\pi} = \bar{d}_{sea}^{\pi} = d_{sea}^{\pi} = \bar{s}_{sea}^{\pi} = s_{sea}^{\pi} \tag{20}$$

Having an isoscalar target (D), it is possible to build the two linear combinations of pion-induced Drell-Yan cross sections:

$$\Sigma_{val}^{\pi D} = -\sigma^{\pi^+ D} + \sigma^{\pi^- D} \tag{21}$$

$$\Sigma_{sea}^{\pi D} = 4\sigma^{\pi^+ D} - \sigma^{\pi^- D} \tag{22}$$

The first combination contains only valence-valence terms, while the second one comprises only sea-valence and valence-sea terms [89].

3.2.2 Proposed Drell-Yan measurement

In order to accomplish with our measurement the sea-valence separation in the pion, a carbon target is proposed. As a light isoscalar material, carbon is clearly advantageous as compared to the heavy and non-isoscalar platinum and tungsten targets used by the NA3, NA10 and E615 experiments.

As can be seen in Fig. 20, the relative contribution from the sea quarks increases as x_π decreases. Therefore, the sea-valence separation becomes better at lower x_π values, which in turn are easier to reach for larger incident beam momenta. Another aspect to consider is the decrease in pion-beam purity as the momentum increases (see Fig. 21), which directly translates into a decrease of pion beam intensity, because the total beam intensity is limited by radio-protection considerations. The proposed beam momentum of 190 GeV/c provides a reasonable experimental acceptance for values as low as $x_\pi = 0.10$, without compromising on the achievable statistics.

Projections for the achievable Drell-Yan statistics are done assuming 213 days of data taking, *i.e.* in two years, using a π^+ beam with momentum of 190 GeV/c and three consecutive carbon targets of 25 cm length each. A full Monte-Carlo simulation is performed, based on the PYTHIA generator for the Drell-Yan process at leading order, and a GEANT4 description of the experimental apparatus. In Table 6, the LO PYTHIA cross sections are given for the two pion beam charges and separately for proton and neutron targets. In these simulations GRV/S was used for the pion PDFs and GRV98 LO [90] for the proton ones.

Table 6: PYTHIA Drell-Yan cross sections in LO, for the dimuon mass range $4.3 < M_{\mu\mu}/(\mathrm{GeV}/c^2) < 8.5$.

beam and target	$\sigma_{\mathrm{LO}}^{\mathrm{DY}\to\mu\mu}$ (nb)
$\pi^+ p$	0.026
$\pi^+ n$	0.039
$\pi^- p$	0.106
$\pi^- n$	0.051

A correct estimate of the experimentally measurable Drell-Yan cross section requires a correction factor $K_{\mathrm{DY}} = 2$ to be applied to the PYTHIA LO calculation, in accordance with experimental measurements. This K-factor accounts for all higher-order contributions to the Drell-Yan process.

In order to perform the sea–valence separation, the π^+ data should be complemented with 67 days of data taking with a π^- beam. The difference in data-collection time between the two beam charges is explained by the Drell-Yan cross-section difference itself (as seen in Table 6) and by the different hadron composition of positive and negative beams, see Fig. 21. Altogether, the two effects lead to a ratio of 3:1 between the π^+ and π^- running times.

Beam intensities of 7×10^7 particles per second, delivered in pulses of 4.8 seconds and an average of 3800 pulses per day are assumed. The identification of the incoming beam particle will be ensured with an efficiency of 90% by two CEDAR detectors, described in Sec. 5.2.3. The achievable Drell-Yan statistics is calculated according to the expression

$$N \;=\; \mathcal{L}\left(Z\,\sigma_{\pi p}^{\mathrm{DY(LO)}\to\mu\mu} \;+\; (A-Z)\,\sigma_{\pi n}^{\mathrm{DY(LO)}\to\mu\mu}\right) K_{\mathrm{DY}}\,\epsilon, \tag{23}$$

where $\mathcal{L}$ is the integrated luminosity, Z and A the atomic and mass numbers of the considered nuclear

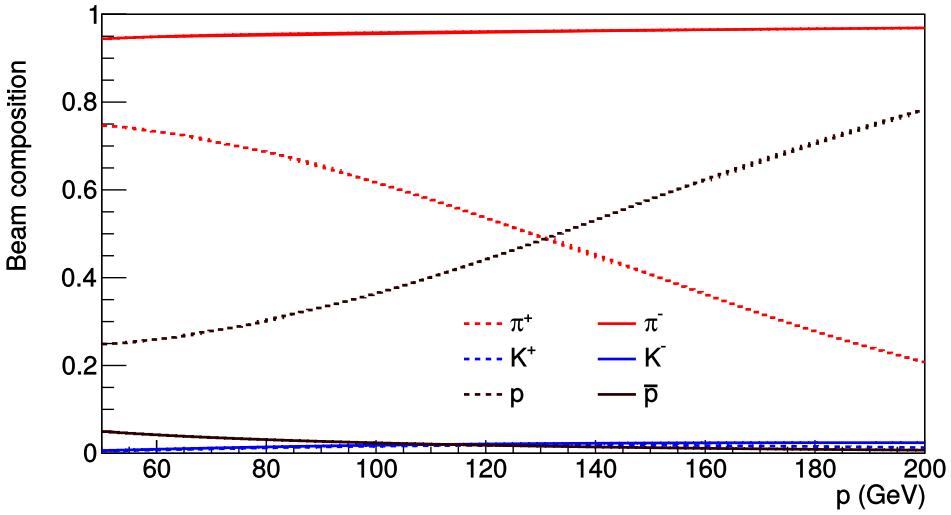

Figure 21: Dependence of the hadron-beam composition on the momentum at the EHN2 location of the M2 beam line.

target, and ϵ is the product of all relevant efficiencies and the geometrical acceptance. The integrated luminosity is given by

$$\mathcal{L} = \frac{I\, L_{eff}\, \rho\, \mathrm{N}_A}{M}\, d_{spill}\, N_{spills}\, N_{days}. \tag{24}$$

Here, I is the beam intensity per second for a given hadron species and L_{eff} the effective length of the target, taking into account the pion interaction length in that target material, ρ the density of the target material, N_A the Avogadro number, $d_{spill} = 4.8$ s the duration of each beam pulse, $N_{spills} = 3800$ the number of spills per day, and N_{days} the number of days of the measurement. The product of all efficiencies and acceptance is

$$\epsilon = \mathrm{Acc}\, \epsilon_{\mathrm{SPS}}\, \epsilon_{\mathrm{spectro}}\, \epsilon_{\mathrm{trig}}\, \epsilon_{\mathrm{CEDAR}}\, \epsilon_{\mathrm{rec}} \tag{25}$$

In this expression, Acc (0.4) is the geometrical acceptance of the spectrometer for the considered dimuon-mass range, and ϵ_X contains the estimated efficiencies of beam extraction (0.85), experiment data-taking availability (0.8), trigger (0.8), CEDARs (0.9) and dimuon offline reconstruction (0.8). The considered values take into account the experience gathered during earlier measurements in fixed-target mode at the SPS M2 beam line. The global efficiency is estimated to be $\epsilon = 0.16$.

In order to minimize the systematic uncertainties when evaluating Eqs. 21 and 22, precise cross-section determinations are required. We aim at absolute cross-section measurements at the level of a 3% systematic uncertainty. A cross check of the relative normalisation can be performed by comparing the J/ψ cross sections for π^- and π^+, as for isoscalar targets the J/ψ cross section does not depend on the charge of the incident meson. The cross-section ratio for π^- and π^+-induced J/ψ production on a platinum target was measured to be (1.016 ± 0.006) by NA3 [76].

Figure 22 shows accuracy estimates for the ratio $\Sigma_{sea}/\Sigma_{val}$ as a function of x_π, in the dimuon mass range $4.3 < M_{\mu\mu}/(\mathrm{GeV}/c^2) < 8.5$, which is a background-free Drell-Yan mass range. The dimuon mass range $4.0 < M_{\mu\mu}/(\mathrm{GeV}/c^2) < 8.5$, accessible with an improved mass resolution thanks to new vertex detectors, is also represented. The curves labelled SMRS represent the predictions [80] for three possible contributions of the sea quarks to the pion momentum, ranging from 10% to 20%. The three different assumptions for the pion sea yield increasingly different predictions for x_π values below 0.5. The shaded

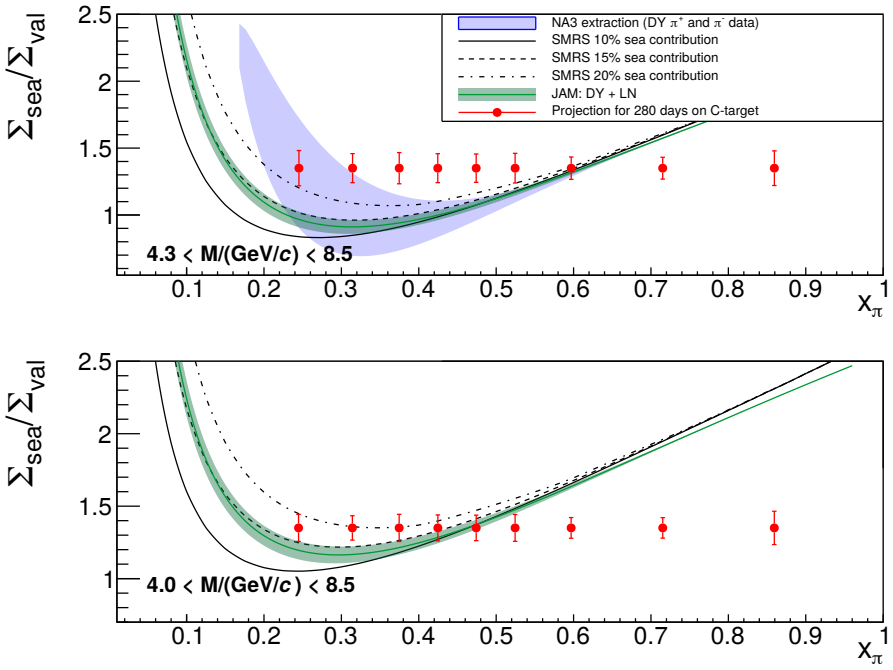

Figure 22: The ratio $\Sigma_{sea}/\Sigma_{val}$ as a function of x_π, using three different sea-quark distributions from [80] for two mass ranges. The ratio is also calculated with the sea-quark distribution from [85], which includes leading-neutron DIS data from ZEUS [83] and H1 [84]. The shown statistical accuracy is expected when using the data-taking conditions presented in the text. The blue shaded area is the uncertainty derived from the statistics quoted in the NA3 paper [52].

area represents the uncertainty band on the sea distribution as estimated from the sea-valence separation of NA3 that is based solely on their own data.

In Table 7, the achievable statistics for a running period of two years, *i.e.* 2×140 days is compared to the Drell-Yan statistics of earlier experiments. In the experimental conditions assumed above, the sea contribution to the pion momentum could be evaluated with an accuracy better than 5%.

The Drell-Yan mass range considered in Table 7 is adequate for a mass resolution of the order of 200 MeV/c^2. For events originating from the carbon target, the background contamination to the Drell-Yan signal is estimated to be below 5%. As will be explained in Sec. 5.4, the inclusion of a target telescope in the setup, with fast and highly granular (possibly pixelized) detectors in between the target cells, improves significantly the muon tracking upstream of the hadron absorber, and it positively impacts the vertexing precision and consequently the dimuon mass resolution. The simulations presently available using such an improved setup indicate that a resolution of the order of 100 MeV/c^2 can be expected, in which case the mass interval for a pure Drell-Yan sample can be safely enlarged to $4.0 < M_{\mu\mu}(/(GeV/c^2)) < 8.5$, which would lead to an increase in statistics by 35%.

Recently developed techniques of data analysis, as *e.g.* machine-learning, are planned to be employed in order to disentangle the different physics contributions to the dimuon mass spectrum. Machine-learning algorithms allow for the multidimensional clusterisation of data, by simultaneously parametrising over a chosen set of physics variables. Such new methods are presently being developed and tested with the Compass Drell-Yan data. Monte-Carlo data is used to train deep neural networks that classify each event according to its probability to originate from a particular physics process. Two types of approaches can be followed, either by selecting the probability value, above which events can be safely considered as signal, or by using all events weighted by their probabilities to be signal or background. With such techniques,

Table 7: Statistics collected by earlier experiments (top rows), compared with the achievable statistics of the proposed experiment (bottom rows), in 213 days (π^+ beam) + 67 days (π^- beam).

Experiment	Target type	Beam energy (GeV)	Beam type	Beam intensity (part/sec)	DY mass (GeV/c^2)	DY events
E615	20 cm W	252	π^+ π^-	17.6×10^7 18.6×10^7	4.05 – 8.55	5000 30000
NA3	30 cm H_2	200	π^+ π^-	2.0×10^7 3.0×10^7	4.1 – 8.5	40 121
	6 cm Pt	200	π^+ π^-	2.0×10^7 3.0×10^7	4.2 – 8.5	1767 4961
NA10	120 cm D_2	286 140	π^-	65×10^7	4.2 – 8.5 4.35 – 8.5	7800 3200
	12 cm W	286 194 140	π^-	65×10^7	4.2 – 8.5 4.07 – 8.5 4.35 – 8.5	49600 155000 29300
COMPASS 2015 COMPASS 2018	110 cm NH_3	190	π^-	7.0×10^7	4.3 – 8.5	35000 52000
This exp	75 cm C	190	π^+	1.7×10^7	4.3 – 8.5 4.0 – 8.5	21700 31000
		190	π^-	6.8×10^7	4.3 – 8.5 4.0 – 8.5	67000 91100
	12 cm W	190	π^+	0.4×10^7	4.3 – 8.5 4.0 – 8.5	8300 11700
		190	π^-	1.6×10^7	4.3 – 8.5 4.0 – 8.5	24100 32100

the analysis can be extended beyond the traditionally considered “Drell-Yan safe mass range", to an enlarged region where the Drell-Yan process is still dominant. Research in the field of machine-learning techniques applied to particle physics has seen enormous and very fast progress in recent years, making it realistic to consider their use in our proposed measurement.

3.3 Drell-Yan nuclear-dependence studies [v2(++)]

The parton distributions in a bound nucleon differ from those in a free nucleon. Experimental evidence of this fact was first observed by the European Muon Collaboration (EMC) in 1983 [75]. Deep inelastic scattering of a lepton off a heavy nuclear target, when compared to using a deuterium target, revealed a drop in the cross-section ratio as the momentum fraction of the struck parton increases above 0.2 . Such behaviour is contradicting the (naively) expected rise due to Fermi motion in the nucleon. This so-called EMC effect was later confirmed by an impressive amount of DIS measurements carried out in several laboratories around the world [91, 92], revealing a plethora of phenomena: (1) a “shadowing" region ($x \lesssim 0.06$), (2) an “antishadowing" region ($0.06 \lesssim x \lesssim 0.3$), (3) the “EMC-effect region" ($0.3 \lesssim x \lesssim 0.8$), and (4) the region where the Fermi motion behaviour dominates ($x \gtrsim 0.8$) [92]. On the theoretical side, many models have been proposed to explain the physics behind each of these regimes, in particular for the “EMC effect region", for which a satisfactory explanation is still missing [93]. The situation has recently become more perplexing, after a JLab experiment on light nuclei [94] provided evidence that the nuclear dependence is not only a function of the atomic number or the mean nuclear density.

A possible flavour dependence of the differences between nucleon and nuclei PDFs is one of the presently open questions. Inclusive DIS experiments are in this respect not helpful, since they are only sensitive to the charge-weighted sum of the quark and antiquark distributions. On the contrary, if nuclear effects are different for up and down quarks, the Drell-Yan process might be an ideal tool to figure this out as with opposite pion beam charges one or the other valence quark distribution is preferentially probed. This fact

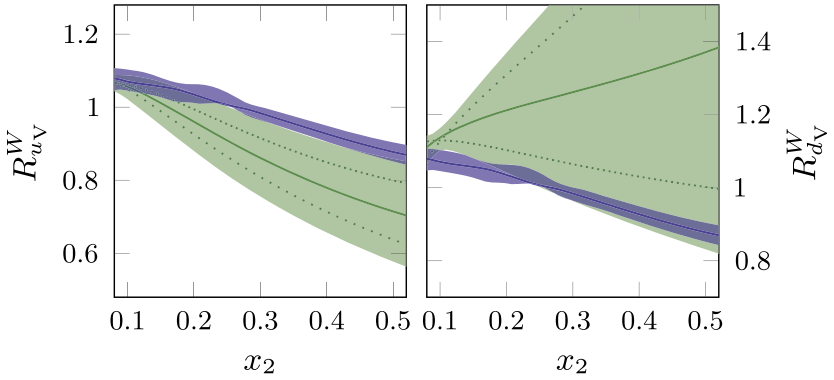

Figure 23: The modification of u_v (left) and d_v (right) distributions in tungsten, as obtained by the nCTEQ15 global fit in green, and by the EPS09 global fit in blue. Figure from Paakkinen et al. [95]. While nCTEQ15 allows for different up and down-quark modifications in tungsten without data to constrain the flavour-dependence hypothesis, EPS09 constrains these modifications to be flavour independent.

was raised by several authors, most recently by [95]. The inclusion of pion-induced Drell-Yan data may have strong impact on global fits of nuclear PDFs. This is illustrated in Fig. 23 where the assumption of a flavour independence of these differences in the valence distribution in tungsten has been released by the nCTEQ15 group [96]. The resulting over-estimated green error bands are a consequence of this under-constrained analysis due to the absence of data effectively constraining the flavour dependence. On the contrary, the EPS09 [97] extraction shown by the blue band in the figure, which imposes the same nuclear modifications for up and down quarks, severely underestimates the uncertainties.

In 2016, global fits aiming at the extraction of more precise nuclear PDFs were published by the EPPS2016 group [98], which included for the first time the low energy pion-induced Drell-Yan data (from NA3, NA10 and E615 experiments), as well as very recent W and Z-production data in proton-lead collisions from CMS and ATLAS, and neutrino DIS data from the CHORUS experiment. However, the impact of the currently available pion-induced data was not found significant, mainly due to their large statistical uncertainties and the limited data sets. A new measurement with high statistics and low systematics, as the one proposed here, could significantly change this scenario.

In order to allow for nuclear-dependence studies, two tungsten cell targets of 6 cm length each are proposed to be placed downstream of the carbon target discussed above. According to EPPS2016, while for carbon the modifications to the valence quark PDFs are of the order of 5% or lower, tungsten is exhibiting much stronger effects. These two target materials provide hence a good lever arm in the atomic number for nuclear studies. The achievable statistics in a two-year measurement is presented in Table 7 for a carbon target of 1.4 pion-interaction length, followed by a one pion-interaction-length tungsten target, and with the experimental conditions described in Sec.3.2.

The projected statistical uncertainties on the Drell-Yan cross-section ratio of positive-over-negative pion beam polarity on tungsten are shown in the top panel of Fig. 24. The results are compared to the previous measurement performed by E615 [99] and to a leading-order calculation using two recent nuclear PDFs. The bottom panel of this figure shows another observable introduced by [100], $\frac{\sigma^{\pi^- W} - \sigma^{\pi^+ W}}{\sigma^{\pi^- C} - \sigma^{\pi^+ C}}$, where the sensitivity to the nuclear valence asymmetry is enhanced as it can be inferred from the larger error bands. This new observable makes the best usage of the statistics to be collected by the proposed experiment.

Among the theory attempts to explain the mechanism leading to flavour-dependent nuclear PDFs, the Cloet-Bentz-Thomas (CBT) model [101, 102] is successful in so far as it is able to account [102] for a large fraction of the so-called NuTeV anomaly of the weak mixing angle. An important feature of this model, which is based on the Nambu-Jona-Lasinio (NJL) approach, is that for nuclei with N>Z,

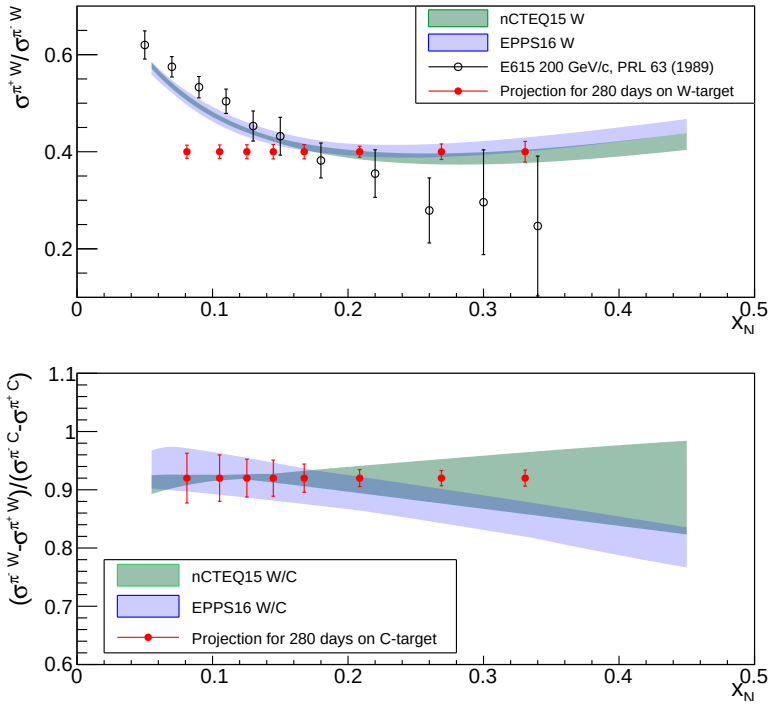

Figure 24: Top panel: Drell-Yan cross-section ratio for positive-over-negative pion beam polarity, shown *vs.* x_N. The expected statistical uncertainties from the proposed experiment (shown as full red dots) are compared to E615 results and two sets of nuclear PDFs. Bottom panel: Drell-Yan ratio of the cross-section beam-charge differences for tungsten over carbon, shown *vs.* x_N. The expected accuracy of the proposed experiment is shown together with two sets of nuclear PDFs.

the isovector mean field affects the lighter quarks differently as compared to the heavier ones, leading to the prediction of different nuclear modifications for up and down quarks. The very good accuracy of the proposed measurement on the cross-section ratio $\sigma^{\pi^+ W}/\sigma^{\pi^- W}$ (see Fig. 24) will have an important discriminating power for such CBT-types of analyses.

The observation of jet quenching phenomenon in heavy ions collisions at LHC and RHIC highlighted the role of radiation energy loss effects of quarks and gluons propagating in a QCD medium, see Refs. [103–105]. Studying hard processes in hadron-nucleus collisions provides another way of understanding the mechanism of nuclear suppression. The nuclear medium in this case, *i.e.* cold nuclear matter, is simpler as its density and size are known. A recent analysis [106] of the available fixed-target Drell-Yan data in proton-nucleus and pion-nucleus collisions demonstrated that the energy loss plays a key role in the interpretation of the measured heavy-over-light-target cross-section ratios. Except at very large x_F, the suppression observed by the E866 experiment [107] at 800 GeV/c originates mostly from nuclear PDFs. In contrast, for lower incident momenta the energy-loss effect becomes dominant over the effects of nuclear PDFs. This conclusion is based upon data from NA10 [108] for a 140 GeV/c pion beam and E906 [109] for a 120 GeV/c proton beam.

The large statistics dimuon data discussed in this proposal can be used for studying the interaction between the initial beam parton and the nuclear medium. The authors of Ref. [106] provide predictions for the x_F-dependent Drell-Yan ratio of tungsten to carbon for a 190 GeV/c momentum pion beam, as illustrated in Fig. 25. The predicted ratio shows that for large values of x_F AMBER data become sensitive to the energy loss, whereas the effect of the nuclear PDFs remains nearly constant.

The energy-loss effect can be further quantified by comparing Drell-Yan and J/ψ production data. In the Drell-Yan case only the initial parton undergoes gluon emission in the nuclear medium, whereas for

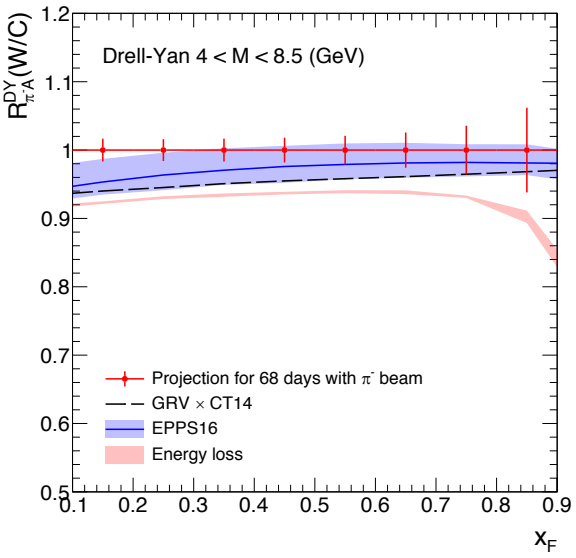

Figure 25: Projected uncertainties on the pion-induced DY cross-section ratio of ^{184}W to ^{12}C as a function of x_F. The dashed line accounts for the different number of neutrons and protons in ^{184}W. The blue and red bands represent the effect of the nuclear PDFs [95] and energy loss effects, respectively, together with the uncertainties on their determination. The energy-loss uncertainty comes from the uncertainty on the pion PDFs. Figure provided by the authors of Ref. [106].

J/ψ production both initial and final partons contribute. Due to the different colour factors, a strong J/ψ suppression is observed at both fixed-target and collider energies [110]. For the two processes the energy loss is described by one single parameter, *i.e.* the transport coefficient. Since the transport coefficient is inferred from the data, the accuracy on its value is related to the uncertainty of the measurement. The large statistics expected by AMBER ($\sim$ 1.8 M events on ^{12}C and $\sim 7 \times 10^5$ events on ^{184}W) will therefore provide cross-section ratios with high accuracy, allowing for a strong experimental constraint on the transport coefficient.

The same conclusions should be reached by analysing the transverse momentum distributions in both Drell-Yan and J/ψ processes. In a way similar to the x_F distributions, the p_T distributions of these processes are modified due to the transverse kick resulting from the soft gluon emission in the nuclear medium (Cronin effect). Since the magnitude and the broadening of the Cronin effect are also connected to the transport coefficient and depend on the colour charge, a comparison between the ^{12}C and ^{184}W targets should serve as a cross check of the value of the transport coefficient determined as explained above.

3.4 Charmonium studies

3.4.1 J/ψ production as a probe of hadron formation mechanisms [v2(+)]

Quarkonium production is a classical case study for the understanding of QCD bound-state formation. Non-relativistic QCD (NRQCD) addresses its description assuming the factorization of short- and long-distance effects in the limit of small relative velocity (v) of the heavy quark and antiquark ($Q\overline{Q}$) forming the bound state [111]. Perturbative calculations fix the kinematics-dependent short-distance production cross sections of $Q\overline{Q}$ production for the relevant spin, angular-momentum (S, L, $J = 0, 1, 2, \ldots$) and colour ($c = 1, 8$) configurations $Q\overline{Q}(^{2S+1}L_J^{[c]})$. The nonperturbative evolution of such pre-resonance states to the observed meson is described, for each quarkonium state, by a set of constant and "universal" long-distance matrix elements (LDMEs). According to an expansion in powers of v, only a few leading $Q\overline{Q}(^{2S+1}L_J^{[c]})$ terms are considered. Their LDMEs are not calculated directly, but determined by comparison with

experimental results at collider energies. The analysis of fixed-target experiments [112] indicates that the resulting color-octet LDMEs must be reduced by an order of magnitude in order to explain the J/ψ and $\psi(2S)$-production cross-section data, an observation that challenges [113] the NRQCD factorisation at the lowest values of p_T.

An alternative framework is the colour-evaporation model (CEM) [114, 115], starting from the same "factorization" hypothesis but making no distinction between $Q\overline{Q}$ colour and angular momentum configurations: one universal hadronization factor per quarkonium state, equal for all underlying sub-processes, multiplies the short- distance $Q\overline{Q}$ production cross section. The two theoretical approaches represent different answers to the fundamental question: how are the observable kinematic properties of the produced quarkonium related to the quantum state of the unobservable $Q\overline{Q}$ pre-resonance? Their predictions are, in principle, different, because the several contributing short-distance processes are weighted differently. The two approaches are not necessarily mutually exclusive [116]. It is an open question, which of the two describes the data better. On the one hand, NRQCD is a rigorous effective theory designed starting from the QCD Lagrangian. After decades-long inconsistencies [117] with Tevatron and, recently, LHC data, concerning in particular the polarisation [118], it was shown that NLO calculations can accommodate the observed lack of polarisation [119] and describe well the surprising state-independence of the $p_{\rm T}/M$ distributions of mid-rapidity LHC data [120], where M is the quarkonium mass. The seemingly higher level of complexity of the theory description with respect to the simplicity of the data patterns raises, however, questions about the naturalness of the assumed $Q\overline{Q}(^{2S+1}L_J^{[c]})$ expansion [121]. On the other hand, the CEM with its empirical formulation where all states have by construction the same kinematic distributions and the spin states of the $Q\overline{Q}$ pre-resonances are averaged out without assuming any hierarchy, seems, a priori, to naturally fit the simplicity of the universal/unpolarised scenario of the LHC measurements. The traditional CEM was recently enhanced [122] to include intermediate heavy quark-antiquark pairs with invariant masses larger than the mass of the quarkonium state. The Improved CEM (ICEM) provides results in good agreement with the data, in particular for the J/ψ and $\psi(2S)$ p_T-spectra. Employing the k_T-factorization approach, the ICEM was also used to calculate [123] the p_T-dependence of prompt J/ψ polarisation at both collider and fixed-target energies.

The proposed experiment focuses on the $p_{\rm T} < M({\rm J}/\psi)$ domain, complementary to that explored by LHC data. This kinematic region is dominated by the $2 \to 1$ partonic processes $q\bar{q} \to {\rm J}/\psi$ and $gg \to {\rm J}/\psi$, where the quarkonium is produced without recoil object. In this limit, the mass and measured laboratory momentum of the observed meson fully constrain the momenta of the colliding partons through the relations $x_1 - x_2 = x_{\rm F}$ and $x_1 x_2 = M({\rm J}/\psi)^2/s$, modified with $M^2 \to M_T^2 = M^2 + p_{\rm T}^2$ when the intrinsic parton transverse momenta are taken into account, with $|\vec{k}_{\rm T1} + \vec{k}_{\rm T2}| = p_{\rm T}$. In fact, the short-distance partonic cross sections of $q\bar{q}, gg \to Q\overline{Q}$ are constant and the observed kinematic dependencies directly reflect the shapes of the parton distribution functions. Moreover, the intrinsic polarisation of the colliding partons are transferred directly to the produced J/ψ, determining a preferred angular momentum projection $J_z = \pm 1$ for $q\bar{q}$ and $J_z = 0$ for gg along the relative direction of the colliding partons, corresponding to values $\lambda = +1$ and -1 of the polar- anisotropy parameter, respectively, for the dilepton decay distribution of the directly produced J/ψ.

Because of the parton $k_{\rm T}$, slightly smeared λ values are expected in the Collins-Soper frame. While the feed-down from ψ(2S) does not change the picture, the one from χ_c states reduces further the magnitudes of λ values expected in the $q\bar{q}$ and gg cases, because the relation between J_z state and λ is very different for the J/ψ coming from χ_c decays: for example, a χ_{c1} having $J_z = \pm 1$ ($J_z = 0$) produces a J/ψ having $\lambda = -1/3$ ($\lambda = +1$), with even an inversion of sign with respect to the direct J/ψ case [124, 125].

The above considerations are independent of the hadronization model. Therefore, in the low-$p_{\rm T}$, $2 \to 1$ dominance limit no substantial differences are expected between the NRQCD and CEM predictions of the $x_{\rm F}$ distributions and polarisations of the *individual* $q\bar{q}$ and gg terms. However, the two approaches differ at least formally in the hadronization factors. These weigh the relevant sub-processes, thereby possibly

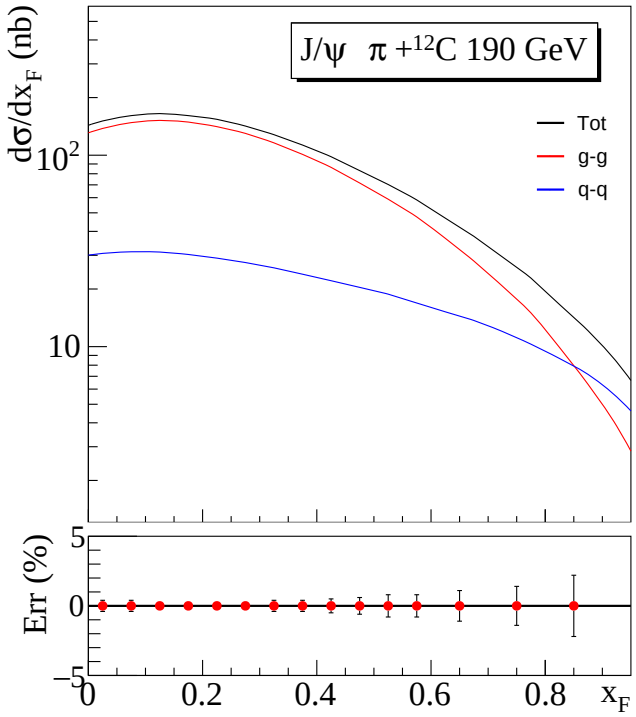

Figure 26: Top panel: Pion-induced J/ψ cross section prediction for a ^{12}C target computed with the ICEM model of Ref. [123] (black line). The red and blue lines show the $q\bar{q}$ and gg contributions, respectively. Bottom panel: estimated relative uncertainties in the proposed experiment.

determining in the two cases different mixtures of the $q\bar{q}$ and gg contributions and therefore different observed x_F distributions and polarisations.

A comparison of the different models to the measured x_F distribution (in different p_T regions) and polarization (as a function of x_F) will represent a thorough test of the theory of quarkonium production in the low-p_T domain. This addresses, on the one hand, the factorization ansatz and, on the other hand, the two hadronization models with their (possibly different) predictions for the $q\bar{q}$ and gg contributions to the J/ψ yield. This goal can be achieved with a high-statistics measurement, sensitive to the shape differences between the $q\bar{q}$ and gg x_F-differential cross sections and to the differences between the corresponding decay angular distributions.

Predictions of NRQCD [126, 127] and the most recent CEM [123] models for the low-p_T domain exist at LO in the k_T-factorization approach, including effects of gluon radiations and intrinsic transverse momenta. Figure 26 displays the x_F dependence of the charmonium production cross section as calculated using the improved CEM (ICEM) model of Ref. [123]. The calculation was performed at $\sqrt{s}$ = 18 GeV, using the CT10 global fit [128] for the nucleon and the GRS99 global fit [82] for the pion. The cross section is dominated by the gg component, except for $x_F > 0.8$ where the $q\bar{q}$ term becomes larger. The remaining qg contribution, also included in the calculation, is a small correction. The calculation also includes a k_T- factorization allowing for a p_T-dependence of the results. The ICEM-model scale factor was fixed to 2.04‰. The authors also quote the uncertainties due to the variation of the charm quark mass between 1.2 and 1.5 GeV. The mass uncertainty essentially shifts the prediction up or down, but can be absorbed in the overall scale factor.

The bottom panel of Fig. 26 shows the statistical precision of the proposed charmonium measurement,

assuming 1×10^6 reconstructed J/ψ mesons obtained using a positive pion beam. The error bars of the data points represent the statistical uncertainties only. The main sources of systematic uncertainties, *e.g.* luminosity, only contribute to the overall normalisation of the data. The shape of the x_F distribution should therefore be determined with minimized systematic uncertainties that could result from possible non uniformity of the detector or trigger efficiencies. Additional systematic uncertainties may result from the identification of the incident particles, as for the positive hadron beam pions are not the main component. However, purity and efficiency for this identification should not affect the final state of the reaction.

3.4.2 J/ψ measurements as constraints on the PDFs of the pion

After validation of the hadronization model within the limits of the precision allowed by the current knowledge of the PDFs, the measurement itself can be used as a new constraint on the relative contributions of the $q\bar{q}$ and gg PDF components and, using the polarisation as constraint, even on their kinematic shapes. In the energy domain of the proposed AMBER experiment and for sufficiently high x_F values, the $q\bar{q}$ component has a magnitude comparable or larger to that of the gg component. More precisely, the relative amount of both components is given by the overall amplitude and shape of the corresponding quark and gluon densities in the Bjorken x region between 0.05 and 0.95 for the pion and between 0.05 and 0.4 for the nucleon. Since the nucleon PDFs are well known, the data may be used to infer the gluon distribution in the pion, obviously within the uncertainties of the hadronization model.

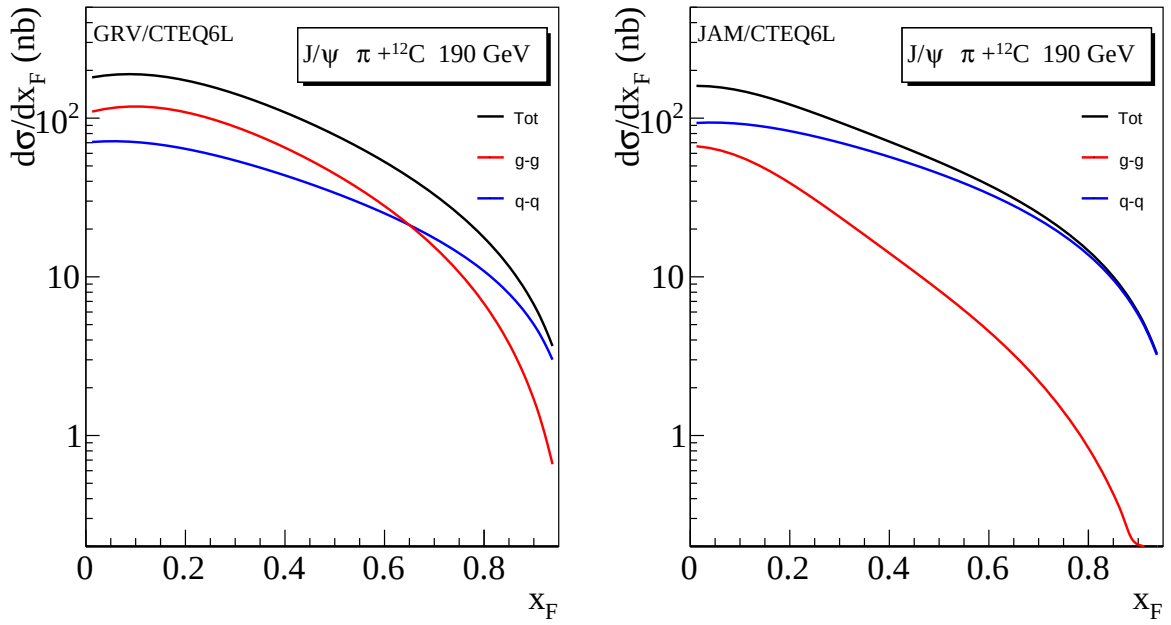

Figure 27: Pion-induced J/ψ production cross sections computed with the ordinary CEM at LO using the CTEQ6L nucleon PDFs and the GRV-NLO fit for the pion PDFs (left panel) or the JAM18 pion PDFs (right panel).

Figure 27 shows the standard CEM predictions for pion-induced J/ψ production on a ^{12}C target using for the pion PDFs either the GRV [81] (left panel) or the JAM [61] (right panel) global fits. The very recent JAM global fit includes leading neutron data (LN) from HERA, in addition to the available pion-induced Drell-Yan data. Since the LN data are taken at lower x values, they provide additional experimental constraints for the gluon and sea densities. In both calculations, nucleon PDFs from the CTEQ6L parameterisation are used. In the calculation with the GRV PDFs the $q\bar{q}$ term becomes dominant only beyond $x_F = 0.65$, whereas in the calculation with the JAM PDFs, it dominates for all positive x_F values. This striking difference is a direct consequence of the different gluon and valence quark densities in

the two parameterisations. The difference between the two global fits can be quantified by quoting the corresponding first moments. At a scale of $Q^2 = 5\,(\mathrm{GeV}/c)^2$, the gluons contribute for 0.50 and 0.35 ± 0.02 in the total momentum fraction for the GRV and JAM PDFs, respectively. The corresponding values for the valence quarks are 0.38 for GRV and 0.48 ± 0.01 for JAM.

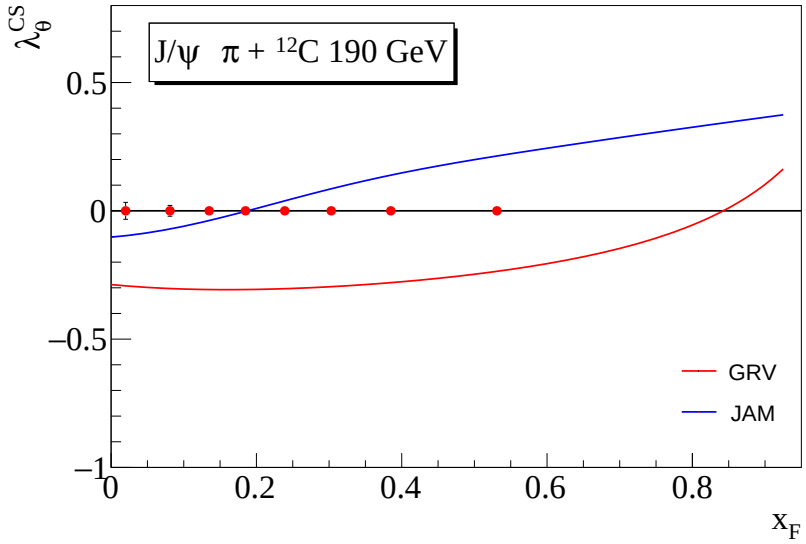

Figure 28: Pion-induced J/ψ polarisation as a function of x_F. The polarisation was computed assuming the ICEM average polarisation values of 0.4 for the $q\bar{q}$ and -0.6 for the gg contributions (Cheung and Vogt, priv. comm.). The pion PDFs are those of the GRV (red curve) and JAM (blue curve) parameterisations. The data points indicate the statistical accuracy achievable with the experimental assumptions described in the text.

The ICEM model also provides predictions for the average J/ψ polarisation: in the Collins-Soper frame the polarisation are $\lambda \simeq +0.4$ and -0.6 for the $q\bar{q}$ and gg components, respectively. These predictions include the contributions of feed-down from χ_{c1} and χ_{c2}. Interestingly, the model dependence of such predictions is minimal. As mentioned in Sec. 3.4.1, they simply follow, as a matter of fact, from angular momentum conservation and the spin/coupling properties of the colliding partons. For example, $q\bar{q}$ production (with no associated recoil) produces a polarised state with $J_z = \pm 1$ angular momentum projection, because of helicity conservation in the coupling of light- quarks to gluons. This corresponds to $\lambda = +1$ for directly produced J/ψ and $\lambda = -1/3$ for J/ψ coming from either χ_{c1} or χ_{c2} decays [124]. The quoted $\lambda \simeq +0.4$ combines these numbers using a χ_c feed-down fraction of around 35%.

The large polarisation difference between the $q\bar{q}$ and gg components, $\Delta\lambda \simeq 1$, can be used as an additional constraint to determine their individual contributions and, therefore, to test J/ψ hadronisation models. The strong dependence of λ on the x_F-dependent relative contribution of the $q\bar{q}$ and gg components is illustrated in Fig. 28. The prediction using either GRV or JAM pion PDFs differ by as much as 0.4; this difference is to be compared with expected statistical uncertainties of about 0.02-0.03. The systematic uncertainties on the polarisation measurement are more difficult to quantify. Preliminary analysis of the data presently available shows that they are limited to 0.05 or less.

3.5 Proposed charmonia measurements

Charmonium data will be collected simultaneously with the Drell-Yan data, using the same setup and the same trigger system. Most of the time data will be taken using a positive hadron beam, as the fraction of pions in the positive beam is only 24% . A similar amount of Drell-Yan data will be collected with a negative hadron beam, in which the pions contribute for nearly 97%.

3.5.1 J/ψ measurements [v2(++)]

For an incident beam momentum of 190 GeV/c on a ^{12}C target, and considering the dimuon mass range $3.0 < M_{\mu\mu}\ /(\mathrm{GeV}/c^2) < 3.3$ GeV/c^2, about 1.2×10^6 J/ψ events are expected for the positive pion fraction of the beam and about 1.8×10^6 J/ψ events for the negative pion fraction of the beam (assuming a positive/negative pion beam sharing as quoted in Sec. 3.2.2). The counting rates are based on the assumption that for an isoscalar target and assuming charge symmetry, the positive and negative pion-induced J/ψ-production cross sections are equal. For the two 6 cm long tungsten targets, the corresponding number of events is 5×10^5 and 7×10^5 for the positive and negative pion beam, respectively.

At this incident momentum, the positive hadron beam reaching EHN2 contains 74.6% of protons, three times the pion fraction. Since the proton-induced integrated cross section is about half of the pion-induced one [76] and accounting for the larger proton beam attenuation, the number of the corresponding J/ψ events should reach 1.5×10^6 for the ^{12}C targets and about 0.7×10^6 for the W targets. Analysed in parallel with the pion data, the large statistics of identified protons will allow for complementary studies of the charmonium production mechanism. In addition, serving as a reference, the well-known proton PDFs should provide further confidence in assessing the model dependence in the extraction of the pion parton densities.

The number of charmonium events given above assume experimental acceptance and efficiency corrections similar or identical to the ones that apply to the Drell-Yan data sets, as described in Sec. 3.2.2. Table 8 summarises the expected statistics and compares them with the largest fixed-target data sets available. We also note that some of the collaborations didn't publish their cross sections (e.g. NA3), didn't provide x_F and p_T dependent distributions (e.g. NA50,NA51), or only studied A-dependent ratios (e.g. E866). These observations provide further impetus for extensive studies on all charmonium observables with three different beam particles and two targets, all within the same experiment.

3.5.2 $\psi(2S)$ measurements

Access to the $\psi(2S)$ state strongly relies on the mass resolution. The proposed set of vertex detectors will allow for tracking in the vicinity of the targets and therefore provide a clear separation from the J/ψ peak. Although the magnitude of the $\psi(2S)$ is an order of magnitude smaller than that of the J/ψ, a high statistical precision can potentially be reached in the cross section as a function of x_F and in the polarisation determination. Such measurements would represent a crucial advance with respect to the present dimuon physics program of COMPASS. On one hand, $\psi(2S)$ data represent a more straightforward test of production models, since the comparison does not involve a disentangling of the unmeasured χ_{c1} and χ_{c2} feed-down contributions with their unknown long-distance factors, necessary in the J/ψ case. Moreover, the relation between the yields of quarkonium states of different masses provides interesting model-independent indications on the hadronisation mechanisms and on the validity of the factorisation hypothesis, based simply on dimensional scaling [135]. In particular, relative $\psi(2S)/J/\psi$ production measurements directly constrain the ratio of the $\psi(2S)$ and J/ψ long-distance factors, for which NRQCD and the improved CEM give (at least conceptually) very different predictions, which are based on velocity scaling and on the distance in mass from the di-meson threshold, respectively.

The $\psi(2S)$ polarisation is also a stronger discriminant of the $q\bar{q}$ and gg yields with respect to the J/ψ case, since without any feed-down smearing the two corresponding anisotropies are expected to approach the maximum opposite values of $\lambda = +1$ and -1, respectively. An estimate of the achievable statistical accuracy on the polarisation value is obtained by scaling the J/ψ uncertainties in Fig. 28 by a factor of about seven, corresponding to the lower number of $\psi(2S)$ events. However, depending on the actual mass resolution, the final systematic uncertainty may increase, as the tail of the J/ψ peak will have to be subtracted. Still, the expected statistics would be the largest ever measured.

Furthermore, measurements of $\psi(2S)$ and J/ψ with different targets open a window of opportunity on

Table 8: Statistics collected by earlier pion and proton-induced experiments (top rows), compared with the achievable statistics of the proposed experiment (bottom rows), in 213 days (π^+ and p beam) + 67 days (π^- beam). Only experiments that report number of events larger than 10^5 are quoted, except if they are part of the same publication. The number of events collected by COMPASS in 2015 and 2018 is an estimation based on the ongoing data analysis.

Experiment	Target type	Beam energy (GeV)	Beam type	J/ψ events
NA3 [76]	Pt	150	π^-	601000
		280	π^-	511000
		200	π^+	131000
			π^-	105000
E789 [129, 130]	Cu	800	p	200000
	Au			110000
	Be			45000
E866 [131]	Be	800	p	3000000
	Fe			
	Cu			
NA50 [132]	Be	450	p	124700
	Al			100700
	Cu			130600
	Ag			132100
	W			78100
NA51 [133]	p	450	p	301000
	d			312000
HERA-B [134]	C	920	p	152000
COMPASS 2015	110 cm NH_3	190	π^-	1000000
COMPASS 2018				1500000
This exp	75 cm C	190	π^+	1200000
			π^-	1800000
			p	1500000
	12 cm W	190	π^+	500000
			π^-	700000
			p	700000

the study of the *final-state* effects in the nuclear modification of quarkonium production. Such effects are of crucial interest as they are directly related to the mechanisms of bound-state formation. However, other quantitatively more important effects as PDF modifications and quark-energy loss dominate the individual J/ψ nuclear modification. In the ψ(2S)-to-J/ψ yield ratio initial-state effects cancel, and it becomes possible to observe how the formation of the two different bound states is affected by the presence of the nuclear matter.

3.6 Systematic uncertainties affecting Drell-Yan and Charmonia measurements [v2(+)]

As with any absolute cross-section measurement, control over the systematic uncertainties is of crucial importance. One of the main difficulties frequently mentioned in global fit analyses addressing the pion structure is the lack of information given by earlier pion-induced Drell-Yan experiments on the systematic uncertainties that affect their results. Although a full account of all components of the experimental

systematics is not possible at this stage of the project, several contributions are certainly present in the proposed measurement:

- assumption on the beam momentum,
- CEDAR particle identification,
- Drell-Yan induced by secondarily produced hadrons,
- trigger efficiency,
- smearing and acceptance effects,
- model related uncertainties,
- nuclear effects.

Given the common aspects between the Drell-Yan measurements from the COMPASS experiment and the ones proposed here, some of these factors are already studied and reliable numbers can be used. This is the case for the assumption on the beam momentum, which has a negligible effect. As in the COMPASS case, no beam momentum station is foreseen for the AMBER Drell-Yan measurements. A hadron beam momentum of 190 GeV/c is assumed in the event reconstruction according to the value resulting from the adopted beam optics in the M2 beam line. This average value was confirmed from a dedicated COMPASS data-taking period using the Beam Momentum Station (BMS) to measure the momentum of a lower-than-nominal intensity negative hadron beam. A 2% beam momentum spread was obtained. This spread does not affect the cross-section results.

One aspect of the proposed Drell-Yan measurement is the beam particle identification using two CEDAR detectors installed upstream of EHN2. The high intensity as well as the beam divergence limit the particle identification efficiency and purity. A careful tuning of the beam optics, alignment of the CEDARs and an adequate read-out system maximise the performance of the detector, see Sec. 5.2.3 for instrumentation details. The most difficult task is the proper discrimination between pions and kaons. However, given the fact that the kaon component in the beam represents less than 6% of the pion intensity for both positive and negative beams, the kaon contamination is highly suppressed and contributes only marginally to the systematic uncertainties. The most dangerous component is the contribution from the proton beam, which is three times more intense than the positive pion beam, as shown in Fig. 21. However, the discrimination between these two components is easier than in the pion-kaon case, as the Cherenkov rings of pions and protons are separated by about 0.9 mm allowing for an opening of the diaphragm that maximises the efficiency of the detector without compromising the purity.

Drell-Yan events induced by secondarily produced hadrons in the carbon and especially in the tungsten target are one of the sources of systematic uncertainty. This contamination in carbon is estimated in the order of 5%, and results in events with distorted kinematics (since the nominal beam intensity is assumed at reconstruction level), in particular at large x_F, and to an over-estimation of the cross section. In order to minimise this effect, short target cells are proposed. The quantification of the impact of this effect to the proposed measurements will be the subject of dedicated Monte-Carlo studies.

The determination of the flux will be based on reconstructed beam tracks from the same scintillating fibre detectors of fast response and fine pitch as used for physics analysis of Drell-Yan events, but from random trigger events. Most systematic effects (detector and reconstruction efficiencies) cancel out in the ratio with physics events, keeping the systematic uncertainties on the cross-section measurement from the luminosity normalisation within a few percent. A dimuon trigger based on hodoscopes, in a scheme very similar to the one used in the COMPASS Drell-Yan measurement, is foreseen for AMBER. But as explained in Sec. 5.4.3, the adoption of a new DAQ scheme with several trigger levels (from trigger-less

data acquisition "level-0" trigger to dimuon vertex reconstruction on-the-fly "level-2" trigger) eliminates the limitations of the DAQ lifetime and long dead-times derived from the inclusion of veto signals from the beam halo into the trigger logic. In addition to the increased efficiency of data collection, it removes the systematic uncertainties in the correction of the veto dead-time, which usually differs among trigger types. In order to control the proper operation of the trigger system and evaluate its efficiency, random samples of data will be collected at the different stages of the trigger decision. In addition, a permanent efficiency monitoring of the trigger read-out chain will be performed, by flashing light signals in front of the hodoscope slabs and by an additional dimuon calorimeter trigger covering the same acceptance of the hodoscopes system.

Model related uncertainties may affect the quantification of the background present in the Drell-Yan and J/ψ data. This issue is of particular importance in the proposed J/ψ analysis, where the assumptions on the production mechanisms present at generator level may lead to a systematic uncertainty affecting the acceptance corrections, the momentum fractions x_π, x_N and the Feynman-variable assignments for the analysed events. A quantitative assessment of the impact of model assumptions will be done from dedicated Monte-Carlo studies with a full simulation of the apparatus and its response.

Nuclear effects on carbon were measured on carbon from DIS interactions. The impact of carbon nuclear effects to the $\Sigma_{sea}/\Sigma_{val}$ measurement is estimated by propagating the uncertainties associated to nuclear PDFs (nCTEQ). A non-negligible systematic uncertainty is expected for $x_\pi > 0.2$, at the level of 4%.

Altogether, the systematic uncertainty of the proposed Drell-Yan measurement is expected to be much smaller than the estimated statistical uncertainty.

3.7 Setup and running plan [v2(+)]

CERN is presently the only place in the world where high-energy and high-intensity hadron beams of both charges are available. For the phase-1 programme, the hadron beam intensity at the M2 extraction line is limited by radio-protection (RP) regulations, since the corresponding experimental hall is located at the ground level. In order to meet the RP requirements, the shielding of the target region must be improved if higher beam intensities are extracted, which is in principle possible up to a factor of two. Investigations are underway to study such a possibility, but the estimates presented in Sec. 3.2.2 do not take into account yet higher beam intensities that may become possible by an improved shielding.

The present Compass apparatus is well suited for high-energy scattering experiments. With the existing two large forward spectrometers, the setup has a wide geometrical acceptance of about 40% for Drell-Yan dimuons produced by a 190 GeV incoming pion beam. This acceptance compares favourably to the acceptance of earlier Drell-Yan experiments, which was limited to about 10%. Therefore the setup proposed for the phase-1 programme follows the conceptual design of the Compass apparatus as it was used for the Drell-Yan measurements that were performed in 2015 and 2018.

The achievable Drell-Yan statistics reported in Table 7 is given for Drell-Yan pairs with invariant mass in the mass ranges $4.3 < M_{\mu\mu}\,/(\mathrm{GeV}/c^2) < 8.5$ and $4.0 < M_{\mu\mu}\,/(\mathrm{GeV}/c^2) < 8.5$. These high-mass regions avoid background from decays of the charmonia resonances as well as from D-meson semi-leptonic decays, and are practically free from combinatorial background originating from uncorrelated muons. The relatively large lower limit of the dimuon mass range (4.3 GeV/c^2 in the most conservative estimates) accounts for the poor resolution that is caused by multiple scattering of muons in the hadron absorber downstream of the target region. This limitation may largely be overcome if vertex detectors with good space and time resolution will be added to the setup. Using the additional information from such vertex detectors will allow us to reconstruct outgoing tracks with enough high accuracy to be sufficient for a more precise vertex reconstruction.

Monte-Carlo studies to define the number, the location and the specifications of such vertex detectors in this difficult region of high multiplicity and low redundancy are still ongoing. One of the studied scenarios

includes five detector stations. Each station measures four coordinates with a spatial resolution of 130 μm and a time resolution of 400 ps. Three stations are placed between the most downstream carbon target and the absorber to facilitate the bridging with the tracks reconstructed from the spectrometer, the other two are placed between the carbon targets. Note that upstream the three carbon targets, a thin tungsten target (2 cm thick) was included in the simulations in order to simultaneously investigate a possible optimisation of the targets configuration. Figure 29 illustrates the improvement in vertex reconstruction for this scenario. It can be clearly seen that by performing tracking upstream of the absorber the location of the vertex becomes better constrained (blue versus black curves), although there is room for even further improvement.

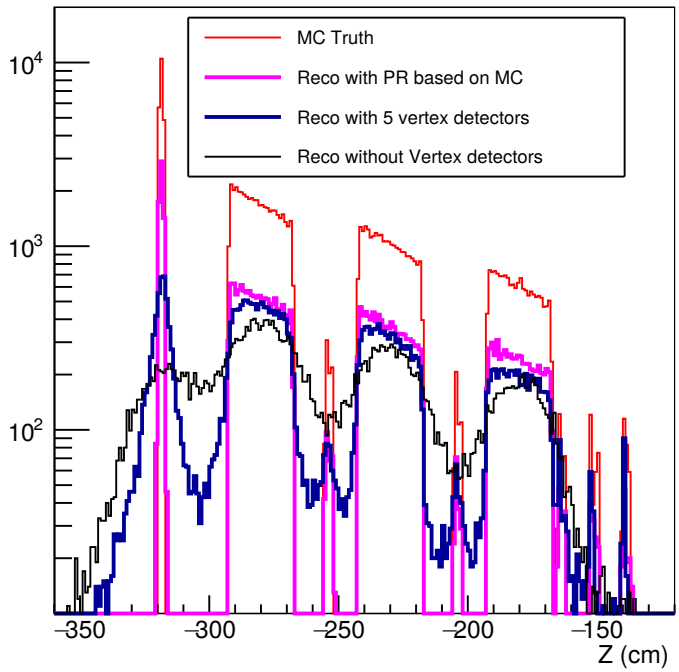

Figure 29: Vertex reconstruction of Monte-Carlo data with no vertex detectors upstream of the absorber (black line) and with five vertex detectors (blue line) are compared to the generated distribution in red and to the ideal reconstruction (tracking algorithm initialised on Monte-Carlo truth) in pink.

With the above described five new vertex detectors and the currently available reconstruction algorithm, a mass resolution of about 115 MeV can be achieved, as shown in Fig. 30. This is to be compared to the case of ideal reconstruction, *i.e.* making use of the generated true information, for which a mass resolution of 80 MeV is obtained as the experimentally attainable lower limit. We expect that further improvements in the reconstruction and optimisation of the setup may allow to eventually reach a mass resolution of 100 MeV.

Using additional vertex detectors as described above, the dimuon mass resolution improves by at least 60% as compared to that of the COMPASS Drell-Yan measurements, where an identical hadron absorber was used. Therefore, it becomes possible to enlarge the mass range for COMPASS++/AMBER Drell-Yan analyses towards lower values of the dimuon mass.

New analysis tools based on machine-learning techniques are expected to further extend the data analysis down to the region below 4.3 GeV. The setup configuration for the proposed measurements is presented in Fig. 31. It includes the envisaged vertex detectors, the specification of which is described in Sec. 5.4.

The proposed Drell-Yan physics programme relies on the development of new and improved instrumentation, including:

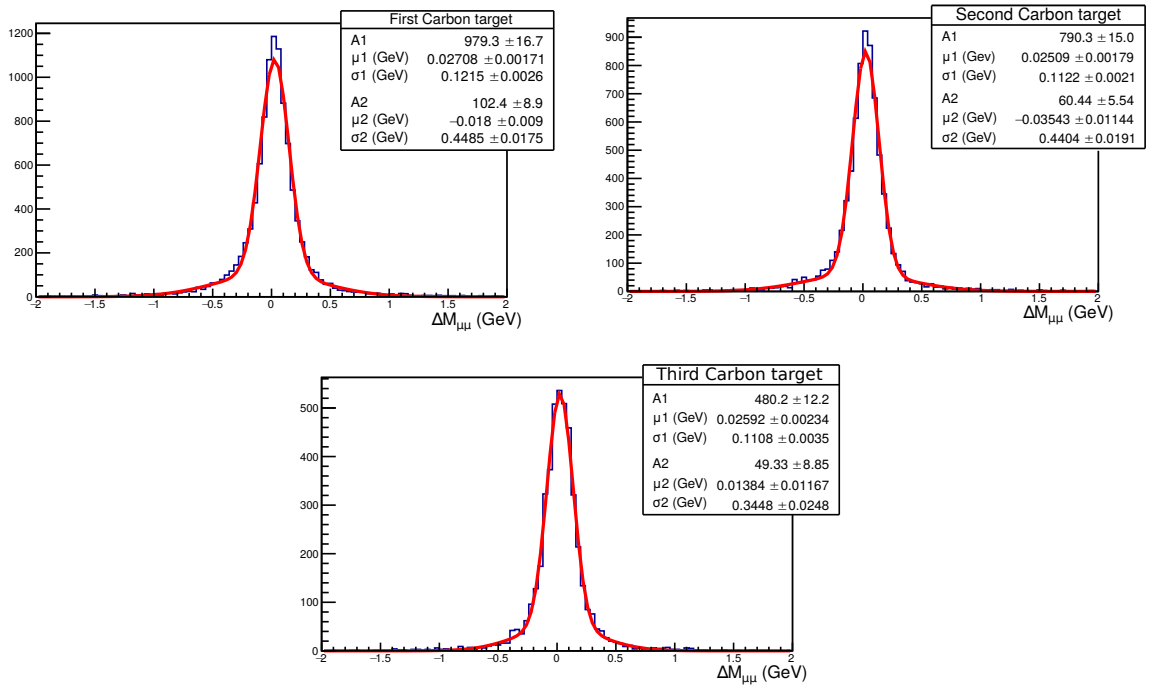

Figure 30: Dimuon mass resolution, for the upstream (top left), central (top right) and downstream Carbon target (bottom). The distributions are fitted by two Gaussians, with parameters given in the insert.

- two CEDAR detectors that are able to operate at high beam intensities and reach a beam-PID efficiency higher than 90% with high purity;
- beam trackers providing a precise beam reconstruction;
- a dedicated vertex-detection system for improved muon tracking in the target region, providing excellent vertex resolution;
- a high-efficiency dimuon trigger with target pointing capability;
- a DAQ system capable of processing very high-trigger-rate information

We propose to run for two equivalent years with both positive and negative hadron beams, with a time share between the two beam charges of 3:1, as explained previously. The target setup will include from upstream to downstream: (1) a segmented carbon target, (2) a segmented tungsten target and (3) the tungsten beam plug (not to be used as a target). The new vertex detectors will be placed downstream of each carbon target cell. The transverse dimension of these detectors must provide coverage for muon tracking at polar angles $\theta \lesssim 160$ mrad to match the acceptance of the spectrometer. The requirement of sufficient statistics to be taken with positive beam charge puts an additional constraint on the choice of the incident beam momentum. For a nominal momentum of 190 GeV/c, the fraction of the positive pions in the beam is 24%. This fraction could be further increased by installing a passive polyethylene absorber along the beam path. Due to different interaction lengths, protons in the beam are more absorbed than pions. With a 2 m long absorber, the NA3 experiment reached a π^+ fraction of 36% at 200 GeV/c. For an incident momentum of 190 GeV/c, this translates into a pion fraction of about 40%.

In all proposed measurements with negative hadron beams a good separation between pions and kaons is mandatory. For the positive hadron beam, the challenge is to identify the 24% pions against the most abundant protons. An excellent beam particle tagging system, with an efficiency at the level of 90% or higher, is hence crucial for the success of the program. The upgraded CEDARs that are used in the Compass experiment seem to fulfil these technical requirements.

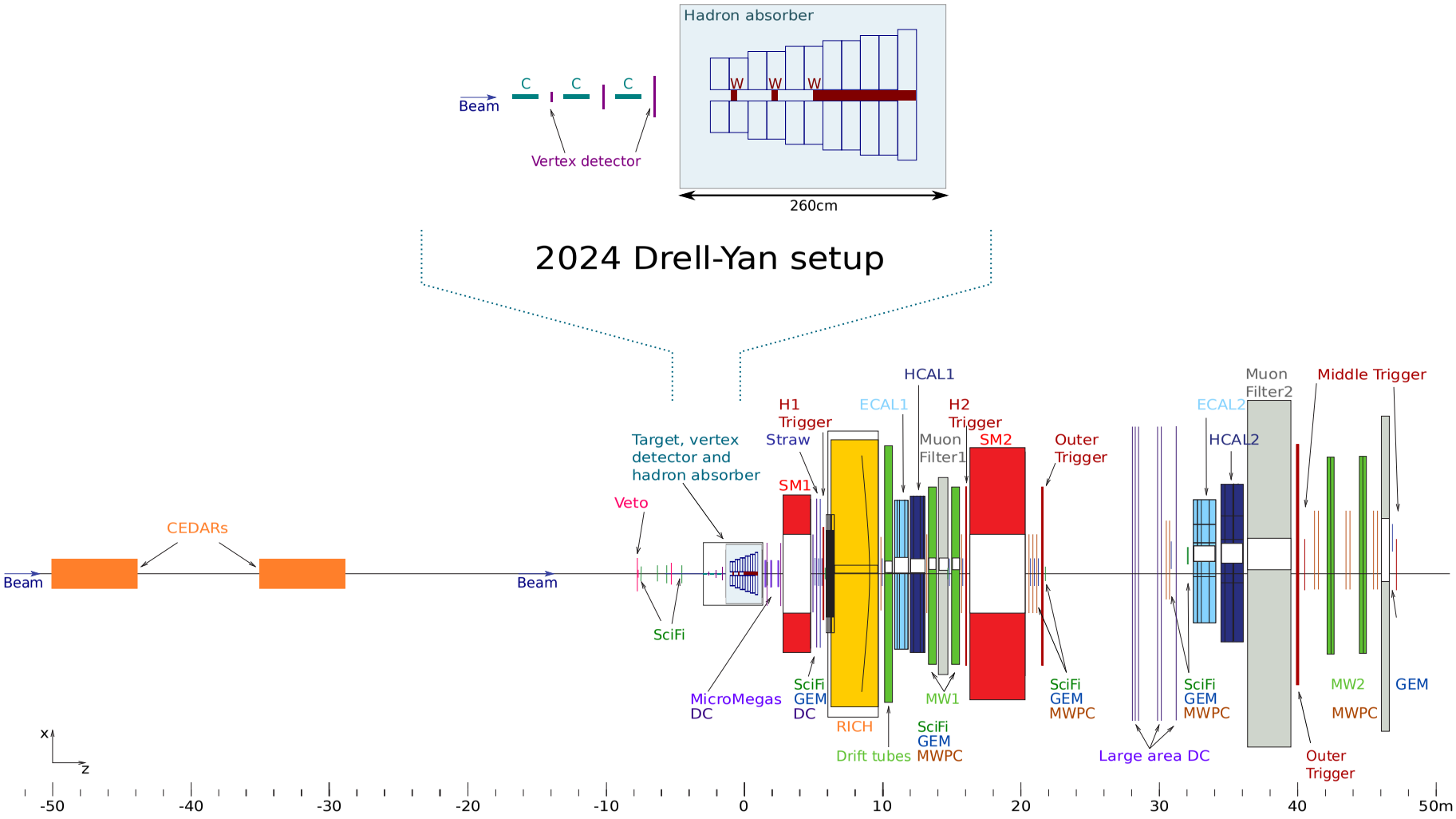

Figure 31: Experimental setup for the proposed Drell-Yan and charmonium measurements. Top: sketch of target system and hadron absorber. Bottom: Extended setup. The beam enters from the left.

In the described experimental conditions, the number of Drell-Yan events that could be collected in two "years", *i.e.* two times 140 effective physics data-taking days, would lead to a statistical accuracy better by an order of magnitude compared to that of NA3.

3.8 Competition and complementarity [v2(++)]

Studying the pion structure through pion-induced Drell-Yan and charmonium production processes, as described in this document, is presently without direct competition because high-energy pion beams are exclusively available at CERN. It is worth noting that the availability of pion-enriched beams of both charges is an additional advantage here. Although secondary meson beam lines are presently under construction at the J-PARC facility in Japan, the planned energies of up to 15 GeV remain too low for extensive studies of the pion structure.

The only alternative way to study meson structure is the Sullivan process, *i.e.* semi-inclusive Deep Inelastic Scattering (DIS) off the meson cloud that surrounds the target nucleon. Measuring the scattered lepton in coincidence with the recoiling nucleon (tagged DIS) opens access to the structure functions of the undetected meson in specific kinematic regions. This approach is inherently model-dependent as it relies on the validity of a model describing the meson cloud. The pion structure was studied through leading-neutron DIS [136] at HERA using electron-proton scattering, covering the Bjorken-x region below $x = 0.1$ where gluon and sea PDFs are dominant. The resulting structure function, which is directly related to the pion sea and gluon distributions, is subject to large model uncertainties that are mainly related to the normalisation of the pion flux.

The JLab TDIS experiment [72, 137] aims at studying the structure of pions and kaons. They plan to investigate the pion PDFs in the x region between 0.45 and 0.90, where valence quarks largely dominate, with an expected statistical accuracy comparable to that of existing DY data. Comparing the pion valence PDFs measured in alternative approaches by TDIS and Drell-Yan experiments may help to validate the model-dependent approach of the former. Although approved, the TDIS experiment is not yet (as of Sept. 2019) scheduled for data taking.

Access to the low-x domain, and therefore to sea and gluon PDFs, requires large centre-of-mass energies. Measurements of the Sullivan process at higher energies are envisaged at the proposed EIC facility to study the structure of pion and kaon using the tagged DIS technique. A White Paper summarising the possible meson structure experiments [138] was recently submitted for publication. Given the EIC decision making and construction schedules, it is unlikely that these experiments could be performed in the next decade.

Competition for the measurement of the flavour-dependent nuclear modifications, as proposed in this document, comes from JLab. The recently proposed EMC PVDIS experiment [139] plans to use parity-violating deep inelastic electron scattering in order to investigate the isovector-dependent EMC effects in a ^{48}Ca target. The experiment is not yet scheduled for data taking.

The charmonium production measurements proposed in this document follow many others that were performed in the past. In most of them, proton beams were used, but also pion-induced charmonium data are available. The measurements proposed here have several advantages. First, they will significantly increase the available statistics, thereby providing the richest sample of fixed-target charmonium production data available. Secondly, data for both positive-pion and proton beams will be collected simultaneously, which together with the negative-pion data will allow for extensive studies of formation mechanisms. Additionally, a large-statistics measurement of the ψ' will complement the experimental results.

4 Measurement of antiproton production cross sections for dark matter search

4.1 Physics case [v2(+)]

Multiple and concurring evidence indicates that the vast majority of the matter content of the universe is non baryonic and electrically neutral. This constituent of the universe is usually called dark matter (DM), for its lack of electromagnetic interactions.

The DM surrounds the galaxies and the large structures of the universe, and it is the major constituent of the gravitational fabric of the universe; the origin and nature of dark matter constitute the most intriguing puzzle that is completely unresolved. The most appealing hypothesis is that DM consists of weakly-interacting massive particles (WIMPs), which are presently supposed to be cold thermal relics of the Big Bang.

The indirect detection of DM is based on the search for the products of DM annihilation or decay. They should appear as distortions in the gamma-ray spectra or as anomalies in the rare components of cosmic rays (CRs). In particular cosmic-ray antimatter components, like antiprotons, antideuterons and positrons, promise to provide sensitivity to DM annihilation products on top of the standard astrophysical production

$$\chi + \chi \rightarrow q\bar{q}, W^-W^+, \ldots \rightarrow \bar{p}, \bar{d}, e^+, \gamma, \nu, \tag{26}$$

where χ is a generic symbol for a DM candidate particle.

The search for DM annihilation products motivated the development of new challenging experiments, either ground-based or in space, which produced spectacular results; among them the AMS-02 [140] experiment on the International Space Station.

When compared to the predictions of standard models for the production of cosmic positrons [141, 142], the observed excess cannot be uniquely interpreted as a signal of dark matter, since it could be due to the emission of positrons from galactic pulsars and/or from any nearby astrophysical sources of leptons [143–147]. The current observed isotropy (or anisotropy) of the cosmic positron flux can hence not be used to fully disentangle the competing scenarios [148]. The antiproton spectrum therefore remains a privileged channel for the indirect search for dark matter, and it is considered fundamental to evaluate the production and propagation uncertainties for antiprotons in the galaxy.

In the following, we briefly discuss how crucial the measurements of antiproton-production cross sections are for the indirect search of DM, in particular cross sections of antiprotons and antideuterons that can be produced by secondary beams at accelerators.

Antiproton production cross section The dominant part of the antiprotons in our galaxy originates from inelastic scattering of incoming cosmic rays off interstellar-medium (ISM) nuclei at rest and represents the background when searching for small contributions from exotic sources.

After the breakthrough from the satellite-borne PAMELA detector [149], the $\bar{p}$ flux and the $\bar{p}/p$ ratio have been measured with the unprecedented accuracy of a few percent by AMS-02 over an energy range from below 1 GeV up to a few hundreds of GeV. These measurements show that above about 60 GeV this ratio is quite flat.

The antiproton (secondary) component generated by cosmic rays is expected to decrease more rapidly than the primary proton spectrum, however the predictions are affected by several uncertainties. As shown in Fig. 32, one can identify two main sources of uncertainties which afflict the prediction of antiprotons for indirect dark matter search: the astrophysical uncertainty due to propagation in the galaxy and heliosphere [150–157], and the antiproton-production cross section [158–163]. The AMS-02 measurements will continue contributing to reduce the first one, constraining the propagation of CRs and refining the diffusion model of CRs in the galaxy and in the solar system. Recent realistic

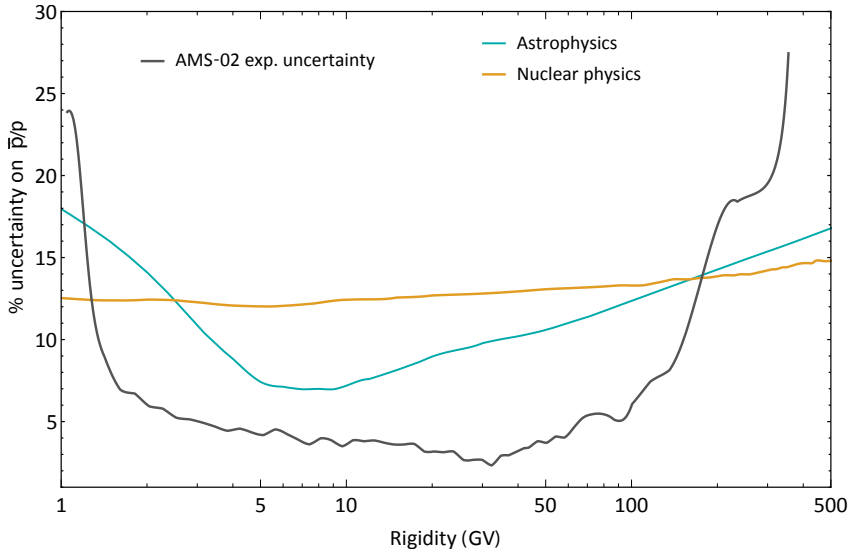

Figure 32: Relative uncertainty afflicting the prediction for the $\bar{p}$ / p ratio, shown in dependence on the rigidity p/Ze (expressed in GigaVolt): in light blue the up-to-date astrophysical uncertainty derived from [150–152] (based on AMS-02 data analysis), in dark yellow the mean of the nuclear physics uncertainties estimated in [159, 162]. In black for comparison the AMS-02 measurement uncertainties as reported in [140].

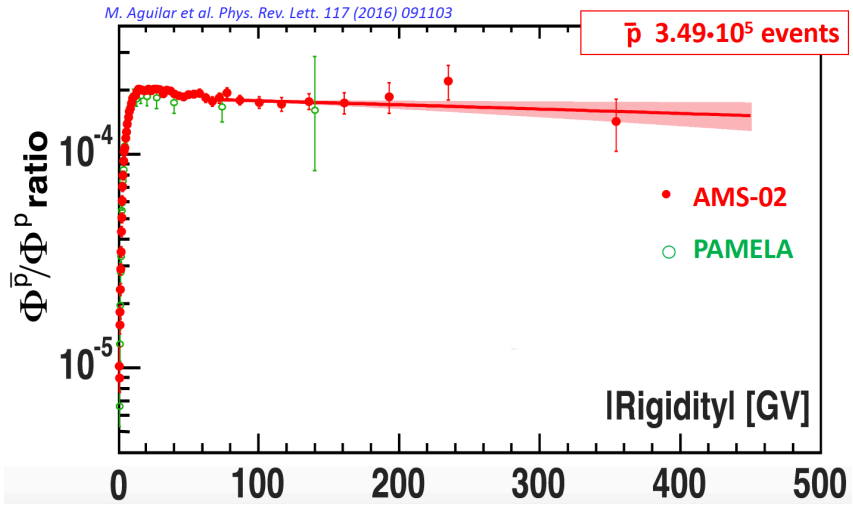

Figure 33: AMS-02 measurements of the $\bar{p}$/p ratio in cosmic rays as a function of rigidity, as reported in [140]

approaches [150, 157], guided by AMS-02 and Voyager-1 interstellar space data [164], have shown great improvements in modelling CRs. As of now, experimental uncertainties are smaller than the theoretical ones, and there is an obvious need of a more precise theory for cosmic rays and spallation in the ISM.

In order to be able to profit from the AMS-02 high-precision data, a similar accuracy has to be achieved in the computation of the $\bar{p}$ source term for all the production channels. Figure 32 reports the extrapolated AMS-02 relative uncertainty on the $\bar{p}/p$ ratio.

As shown in figure 33, AMS-02 $\bar{p}/p$ ratio data above 60 GV of rigidity show a substantial independence from the rigidity itself. Fitting these data with a straight line results in a slope compatible with zero, as discussed in [140]. When considering this linear model, the overall uncertainty on the measured $\bar{p}/p$

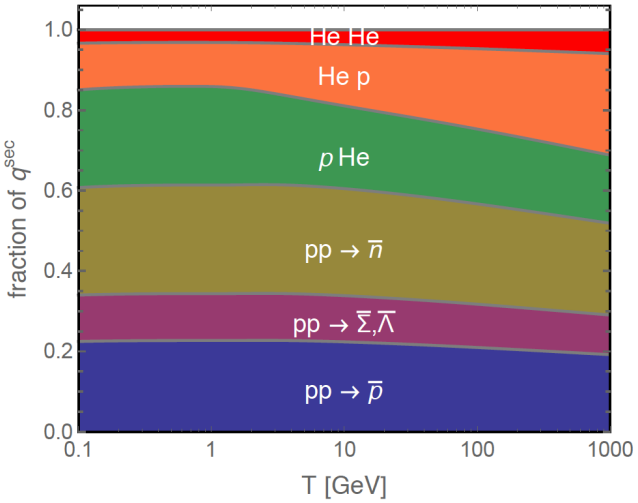

Figure 34: Fractional contribution to $\bar{p}$ production from different interactions on the Inter-Stellar Medium as a function of the kinetic energy of the produced $\bar{p}$.

ratio above 60 GV is of about 5%.

In order to obtain a significant sensitivity to DM signals, it is then very important to keep a small uncertainty on the prediction of cosmic anti-proton produced in the collision with the Inter Stellar Medium over the whole energy range covered by AMS-02.

Nuclei heavier than proton and helium give a small contribution to the secondary production of cosmic rays, either as projectiles or targets, and thus they play only a marginal role in the production of secondary antiprotons [162]. The dominant reactions are those involving protons and Helium ($p+p, p+{}^4He, {}^4He+p, {}^4He+{}^4He$). As shown in figure 34, the interactions involving ^{4}He as target or projectile represent about 40% of the $\bar{p}$ production over the whole energy spectrum. Accurate measurements of the $\bar{p}$ production cross section in $p+p$ collisions and $p+{}^4He$ collisions are thus of fundamental importance in a wide energy range from 10 GeV to a few TeV in order to reduce the uncertainty on the secondary $\bar{p}$ production cross section and eventually clarify if there is an evidence of exotic components coming from DM annihilation or decay in the AMS-02 data.

The contribution of anti-neutrons and anti-hyperons decaying to antiprotons has also to be taken into account, however the total $\bar{p}$ production cross section can be obtained accurately by re-scaling the prompt production, *i.e.*:

$$\sigma_{tot} = \sigma_{prompt}(2 + \Delta_{IS} + 2\Delta_{\Lambda}),$$

where Δ_{IS} is the enhancement factor of antineutron-over-antiproton production due to isospin effects, and Δ_{Λ} is the hyperon factor, which assumes that antiproton and antineutron production from hyperons are equally abundant. The combined uncertainty arising from antineutron and hyperon-induced production was evaluated to not exceed 5% and to be energy dependent [165].

The AMS-02 measurement of the $\bar{p}/p$ ratio (not shown) points towards two promising momentum ranges for DM discovery: $10-20$ GeV/c and $200-300$ GeV/c. The first energy window has been recently studied [166–170], indicating the possible existence of WIMP candidates in the mass range $50-90$ GeV/c^2. The discrepancy observed in the high energy window could originate from the annihilation products of a heavy, TeV-scale WIMP candidate, as suggested by combining positron and antiproton production measurements [171].

While on $p+p$ collisions a few experimental data sets are available [172–174], the very first data set

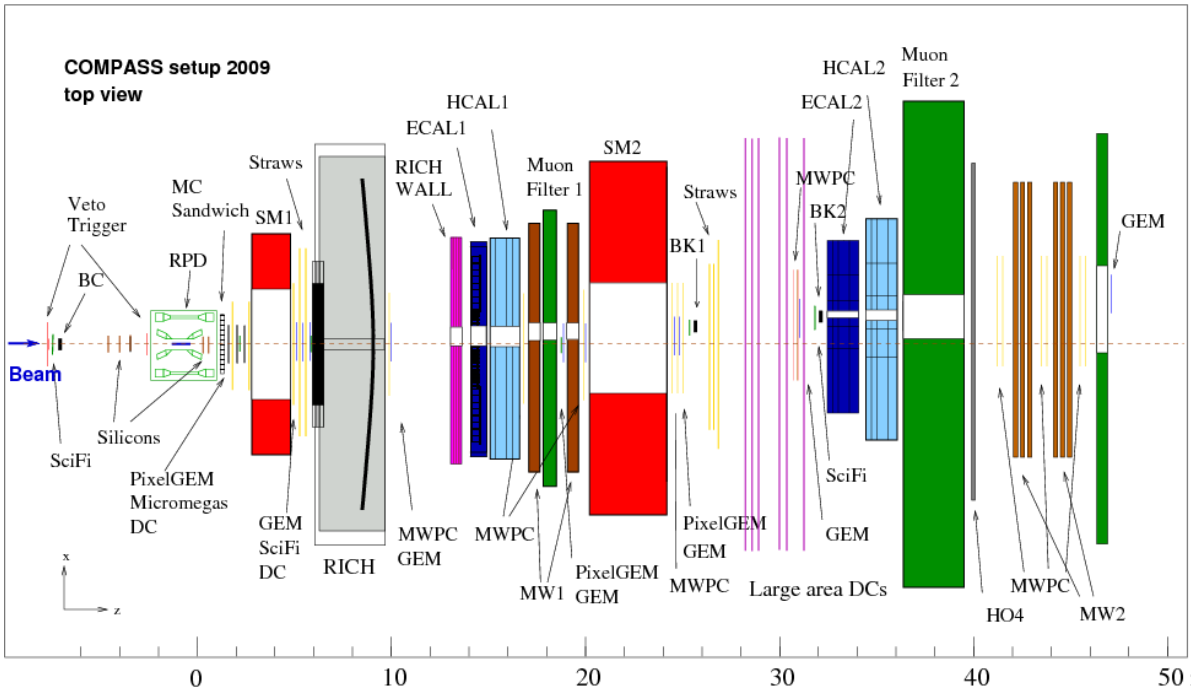

Figure 35: Top view of the 2009 Compass spectrometer setup for data taking with hadron beams.

on $p + {}^4He$ collisions was collected at the end of 2015 by the LHCb experiment using 4 TeV and 7 TeV protons and a ${}^4He$ target [175].

The collection of new data using a proton beam with energies ranging between 50 and 280 GeV in conjunction with a ${}^4He$ (or H) target would allow to extensively characterise the $\bar{p}$ production spectrum. This is a key point to derive and/or constrain $\bar{p}$ production models, which in turn may lead to a further decrease in the overall uncertainty on the $\bar{p}$ production cross section.

As will be shown below, the proposed Compass++/Amber experiment at the M2 beam line of the CERN SPS would be able to collect quickly large statistics on $p + p$ and $p + {}^4He$ collisions, from which precise data are expected to emerge that will contribute to significant advances in the search for dark matter.

4.2 Experimental Layout

The spectrometer layout will be based on the Compass set-up used in 2009 with the proton beam and the 40 cm long liquid hydrogen target. The 2009 spectrometer is shown in Fig. 35 and a detailed discussion of most of the components can be found in [176].

Beam line A secondary positive hadron beam is delivered by the CERN SPS M2 beam line during a time period of 9.6 s once every 30-48 s, using a 400 GeV/c proton beam impinging on a 500 mm thick primary Beryllium production target (T6). The typical particle composition of the hadron component of the positive beam is given in Table 9.

For beam particle identification, two CEDAR detectors are installed 30 m before the target region. They were designed to provide fast beam particle identification at high rates for pion/kaon separation up to 300 GeV/c and proton identification down to 60 GeV/c.

As the ratio of pressure over temperature, p/T, is proportional to(n-1), where n is the refractive index, the working point of the CEDAR detectors is determined by performing pressure scans. Pressure scan results with CEDAR1 for a positive hadron beam with at least 4, 6 or 8 PMTs in coincidence is shown in Fig. 36: from the measured rates and the known beam composition, a particle identification efficiency of

Table 9: Particle content, in percent, of the beam leaving the 500 mm thick primary Beryllium production target [177].

Beam Mom [GeV/c]	π^+	K^+	p
60	64.6 ± 0.8	9.7 ± 0.2	23.4 ± 0.6
120	42.8 ± 0.5	7.2 ± 0.08	49.0 ± 0.7
200	17.5 ± 0.5	3.44 ± 0.10	79.0 ± 0.9
300	2.01 ± 0.04	0.641 ± 0.012	97.3 ± 0.5

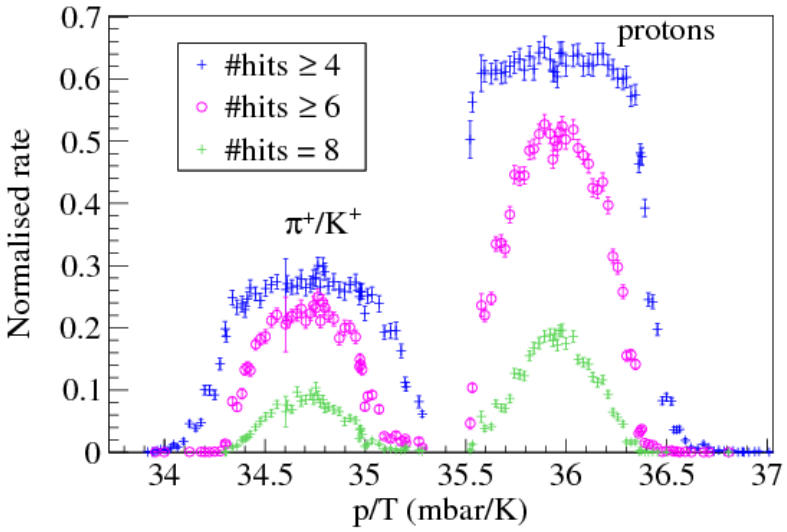

Figure 36: Pressure scan with CEDAR1 for a positive hadron beam with at least 4, 6 or 8 PMTs in coincidence, obtained at COMPASS in 2009 for a 190 GeV/c proton beam with a nominal intensity of 5 $\cdot 10^6$ p/s.

almost 90% for protons is estimated using a multiplicity of less than 4, with a high purity larger than 95%, for the chosen working point of the CEDAR in COMPASS 2009 data taking, with a 190 GeV/c secondary proton beam of nominal intensity of 5 $\cdot 10^6$ p/s.

For the proposed program the required secondary beam intensity will be a factor ten lower, about 5$\cdot 10^5$ p/s, and both CEDARs will be set to identify protons.

The two CEDARs have been object of an upgrade in 2018, including the improvement of the photomultipliers and of the read-out to withstand high-rate environments, the upgrade of the thermal system to control the stability, and the introduction of a PMT gain monitoring. See Sec. 5.2.3 for more detail.

Target The proposed physics program requires taking data with both a liquid hydrogen (LH_2) and a liquid helium (LHe) target. A description of the two target systems can be found in Sec. 5.5.

Trigger $^{\nu 2(+)}$ The beam intensity delivered to the M2 beam line will be adjusted to provide about 5 $\cdot 10^5$ p/s at the target. The rather low beam intensity will allow to run the DAQ in a completely not-triggered mode and save all data to disk for further offline analysis (See Sec. 5.2.4). The trigger decision will be made offline, based on a minimum-bias trigger, which includes:

- beam trigger + hodoscope veto, which ensures that the particle reaches the experiment within the geometrical target acceptance;
- sandwich veto, which excludes events with signals outside the target acceptance;

– beam killer, which is located 32 m behind the target, to remove non-interacting beam particles.

Simulations of the beam interactions with the target show that the "beam killer" request removes the non-interacting and the $p - e$ scattering events, leaving instead most of the quasi-elastic events. The amount of the latter is easily (and accurately) estimated using the Recoil Proton Detector (RPD) system, composed of 2 layers of scintillators surrounding the target as discussed in [176].

4.3 Measurement principle

The production cross section for antiprotons produced in $p + p$ and $p + {}^4$He collisions is known only with uncertainties of the order of 20% to 30%, depending on their energy. As this cross section cannot simply be constrained by a measurement of the other products of these interactions, a direct measurement is required.

We plan to measure this cross section as a double-differential one in the momentum and forward angle of the $\bar{p}$. Using the Compass magnetic spectrometer we can track the charged particles produced in the interactions of the primary beam with the LH_2 or LHe targets, measure their momentum from the curvature in the magnetic field and their velocity using the RICH detector [178]. The combined measurement of momentum and velocity will allow for particle identification and in particular for anti-proton selection.

The particle identification is reduced to the separation between $\pi^{\pm}$, $K^{\pm}$ and $p/\bar{p}$, since we require the track to originate from the primary vertex, and the RICH detector is placed about 6 m downstream the target. Electrons are otherwise identified by their showering behavior, and muons are recognised by their penetration capability that allow them to reach the end of the spectrometer.

The number of anti-proton events at a given (p, θ), where p is the momentum and θ the forward angle, over the number of collected events corrected for the DAQ efficiency and acceptance, is proportional to the wanted differential cross section, with the proportionality constant being the total $p - p$ cross section σ_{pp}:

$$\frac{d\sigma_{\bar{p}}}{dp\, d\theta}(p, \theta) = \sigma_{pp} \frac{N_{\bar{p}}(p, \theta)}{N_{tot}} \frac{1}{\Delta p \Delta \theta}. \tag{27}$$

A similar relation holds for $p - He$ interactions.

The acceptance in forward angle ranges from a minimum of about 7.3 mrad, defined by the transverse distance between the RICH radiator and the beam pipe, and a maximum of 180 mrad, defined by the target and the spectrometer maximum acceptance. This corresponds to the pseudorapidity η lying in the range [2.4,5.6].

We simulated $p + p$ and $p + {}^4He$ interactions to characterize the features of these events in term of multiplicity, energy and angular distributions of the produced particles, in particular the antiprotons, and we studied the performance of the Compass spectrometer to detect such events.

We present here the simulation results with two beam/target configurations:

1. 190 GeV/c protons on liquid H_2;
2. 190 GeV/c protons on liquid ${}^4He$.

At 190 GeV/c beam momentum, events with an antiproton represent about 7% of the total number of events, as summarized in Table 10. We are interested to understand the characteristics of these events in terms of the number of charged tracks, their forward angle, the number of produced antiprotons and their momentum distribution.

Table 10: Simulation results: the average charged-track multiplicity, the fraction of the antiproton events and the average momentum of the antiprotons are shown.

	$p+p$	$p+{}^4He$
Beam Mom	190 GeV/c	190 GeV/c
Mult ($Z \neq 0$)	9.9	11.07
$\bar{p}$ event fraction	7.1%	7.7%
$\langle p \rangle$ of $\bar{p}$ (GeV/c)	15.3	14.5

Below we present some results for $p + p$ interactions at 190 GeV/c. The average occurrence of particles, the distribution of the final-state multiplicity and the energy spectrum of the produced antiprotons are shown in Figs. 37, 38 and 39, respectively.

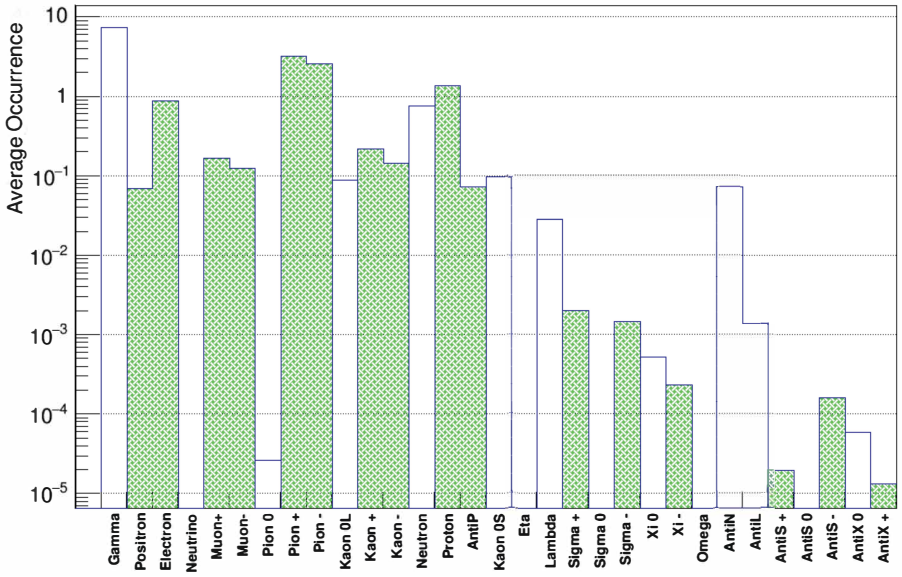

Figure 37: Particle type abundance in $p + p$ interactions at 190 GeV/c.

4.4 Kinematic domain and spectrometer performance

We studied the performance of a COMPASS-like spectrometer in terms of the

- ability to reconstruct the tracks within its geometric acceptance;
- resolution of the momentum measurement for a single track;
- vertex reconstruction and position resolution;
- particle identification (RICH).

The geometry of the COMPASS liquid hydrogen target allows for accepting particles with a polar angle smaller than 180 mrad (or about 10 deg or pseudo-rapidity $\eta > 2.4$), see Fig. 40.

Figure 42 shows the π^- track-reconstruction efficiency as a function of momentum and pseudo-rapidity. For momenta above 1 GeV/c and pseudo-rapidity above 2.4, the tracking efficiency is larger than 90% and mildly dependent on magnitude and direction of the momentum.

Similar efficiencies were observed for π^+, p and $\overline{p}$; Fig. 41 shows the momentum dependence of the tracking efficiency for these particles. The observed similarity between the π^+ and π^- efficiencies suggests

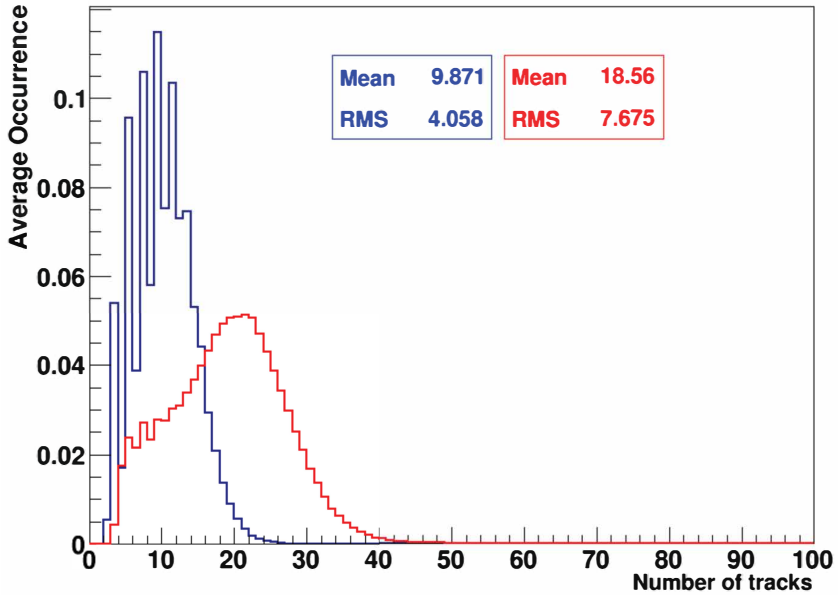

Figure 38: Track multiplicity in $p + p$ interactions at 190 GeV/c: in blue the charged tracks, in red all tracks.

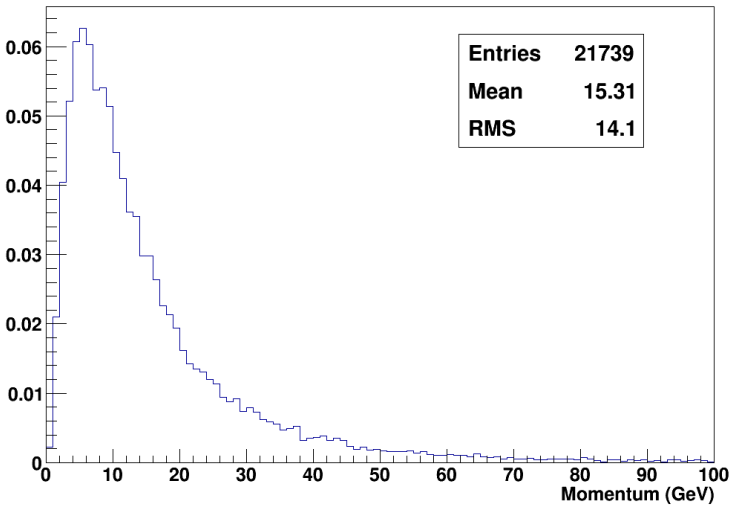

Figure 39: Momentum spectrum of $\overline{p}$ produced in $p + p$ interactions at 190 GeV/c

that the spectrometer behaves similarly for positive and negative tracks, hence it is safe to assume that p and $\overline{p}$ reconstruction efficiencies are the same.

The resolution in magnitude and direction of the momentum is also very good. The large-angle spectrometer yields $\sigma_p/p \approx 1\%$ for tracks with momentum smaller than 18 GeV/c, while the small angle spectrometer yields $\sigma_p/p \approx 0.3\%$. The angular resolution has a typical value of 0.8%, while staying always better than 3% in the pseudo-rapidity range $2.4 < \eta < 8$. Track association to vertices is very efficient. Within the spectrometer acceptance ($\eta > 2.4$, $p > 1$ GeV/c), the ratio of the reconstructed track multiplicity to the MC multiplicity at the primary vertex is 0.98 ± 0.05. The residual of the vertex

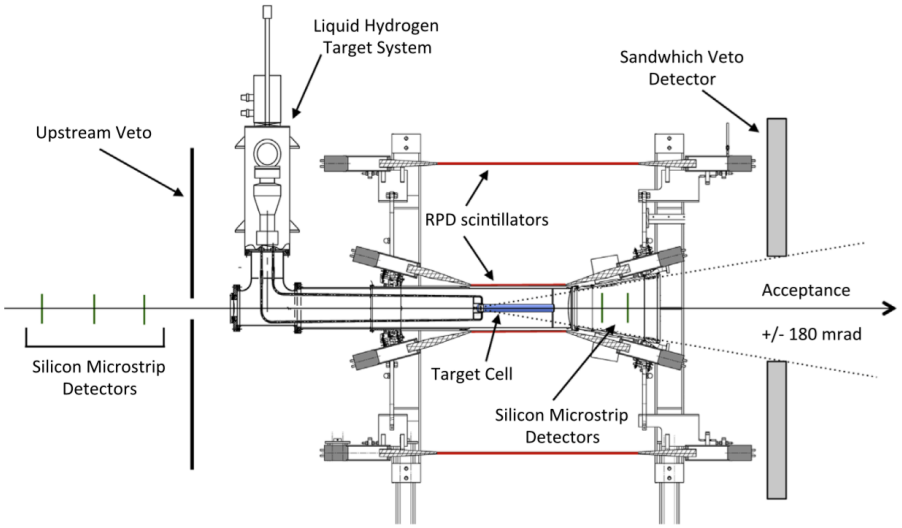

Figure 40: Longitudinal section of the COMPASS liquid H_2 target.

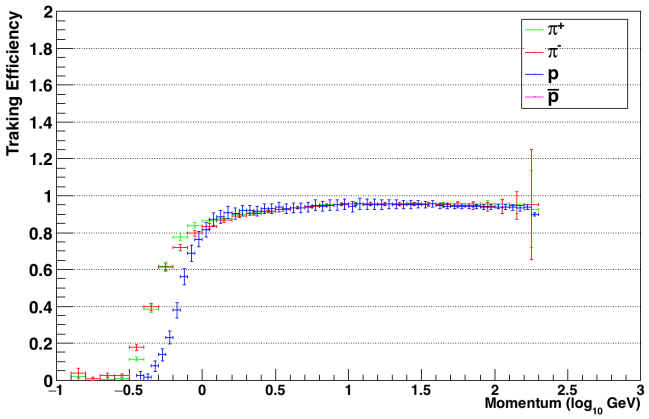

Figure 41: Tracking efficiency as a function of the particle momentum, for π^+ (green), π^- (red), p (blue).

position in the z direction has a width of about 0.7 mm.

Altogether, a COMPASS-like spectrometer performs very well in reconstructing the event topology as well as the sign and the momentum of the tracks. The tracking efficiency is close to unity for momenta above about 1 GeV/c, see Fig. 41. Very similar features and performance have been observed for the simulated $p - He$ interactions, results of these simulation have then been omitted.

4.5 Particle identification

Signals from the Ring-Imaging Cherenkov (RICH) detector allow us to measure the speed of a particle crossing this detector. An estimation of the particle mass is then obtained from the velocity and the rigidity measurement, thereby providing the means for particle identification. Considering a RICH position about 6 m downstream of the target, we expect to observe the following particles: $e^{\pm}$, $\mu^{\pm}$, $\pi^{\pm}$, $K^{\pm}$, p and $\overline{p}$ [2]. Muons are identified by their penetration capability and can be neglected for the moment.

[2]Also a few hyperon tracks could trigger the RICH but their expected abundance is negligible.

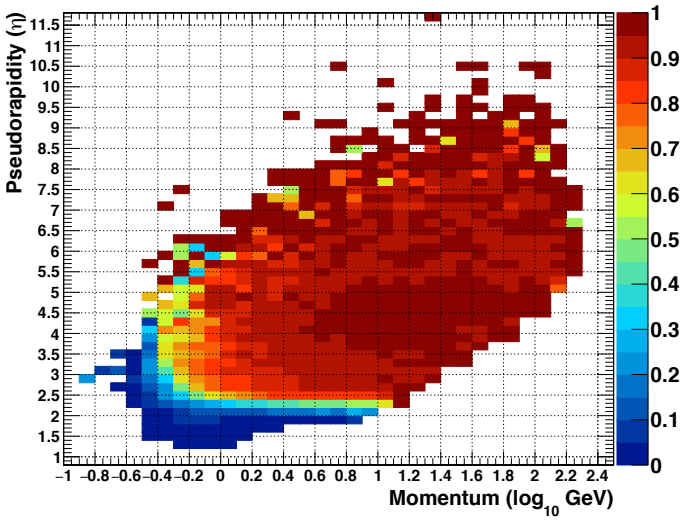

Figure 42: Double differential (η,$log_{10}(p)$) reconstruction efficiency for negative pions produced in 190 GeV/c $p+p$ interactions.

The RICH radiator is a volume of C_4F_{10} gas with refraction index n $\sim$ 1.0014; this corresponds to a threshold in velocity of $\beta = 0.9986$. The corresponding momentum threshold depends on the particle mass: $p_{min} = 2.6$ GeV/c for pions, $p_{min} = 9.3$ GeV/c for kaons, $p_{min} = 17.7$ GeV/c for protons. The RICH velocity measurement is efficient for tracks hitting a minimum distance of 4.5 cm from the beam line, this sets the upper limit in pseudorapidity to $\eta \approx 5.6$.

The RICH performance was studied using the data collected by the COMPASS collaboration in 2009 with a 190 GeV/c proton beam impinging on a LH_2 target. In these events we selected the secondary vertexes with only one positive and one negative outgoing tracks. Introducing the additional requests (1) no incoming charged track in the vertex, (2) total momentum pointing to the primary vertex, and (3) a minimal distance with respect the latter, we selected a clean sample of neutral particles decay.

Given the applied selection, we expect these vertices to originate from $\Lambda_0 -> p+\pi^-$, $\bar{\Lambda}_0 -> \bar{p}+\pi^+$ and $K^0 -> \pi^+ + \pi^-$ and $\bar{K}^0 -> \pi^+ + \pi^-$ decays. This is confirmed by the Armenteros plot shown in Fig. 43 and also by Fig. 44, which shows the invariant mass in the $\pi\pi$ hypothesis vs the one in the $p\pi$ hypothesis. With appropriate selections in the plane of the two invariant masses, it is possible to select pure samples of Λ_0 and K^0 vertices, and as a consequence pure samples of $p^\pm$ and $\pi^\pm$ over a wide momentum spectrum.

These pure samples allowed to study the RICH response and to characterise its behavior in term of efficiency and particle identification capabilities. The first notable result comparing the 4 particle samples is that the COMPASS RICH response is the same versus $p/m = \beta\gamma$. This in fact expected but the availability of pure samples allows to verify it and to produce a RICH response probability density function that can be used for particle identification. Figure 45 shows an example of such probability density function.

Considering the overall RICH performance as observed in the 2009 data, we are able to select two momentum ranges where an efficient identification of $\bar{p}$ is possible. The edges of these two contiguous ranges are the RICH K threshold ($\sim$ 10 GeV), the RICH p threshold ($\sim$ 18 GeV) and the limit where the proton velocity is compatible with 1, given the RICH β resolution ($\sim$ 45 GeV). In the first momentum range, [10,18] GeV, we use the so-called veto mode: pions and kaons are expected to produce a signal in the RICH, while protons are not. In the second momentum range, [18,45] GeV, a direct identification of $\bar{p}$ is performed instead.

The universal RICH response presented in Fig. 45 allows us to estimate the full particle identification

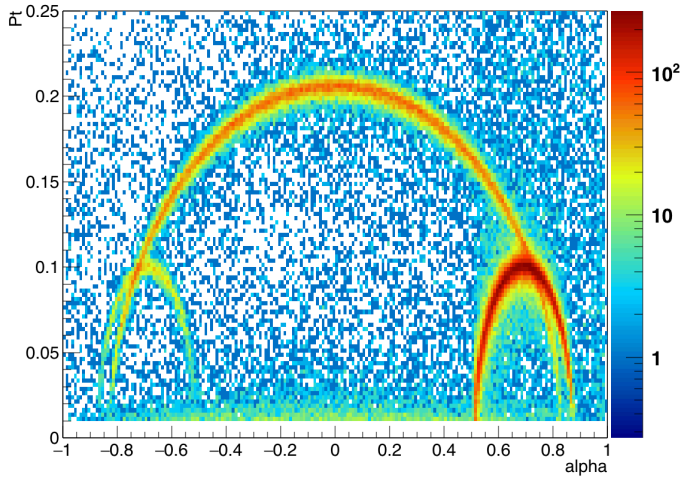

Figure 43: Armenteros plot for the selected neutral secondary vertices. It is possible to spot the main arch corresponding to K^0 and $\bar{K}^0$ decays and the smaller left and right arches corresponding to $\bar{\Lambda}_0$ and Λ_0 decays, respectively.

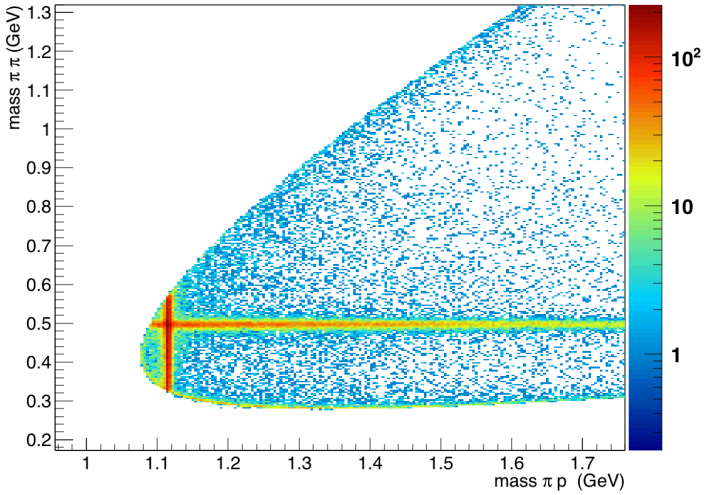

Figure 44: Invariant mass in the $\pi\pi$ hypothesis vs the $p\pi$ hypothesis. The vertical and horizontal bands correspond to Λ_0 and K^0 decays respectively.

probability matrix:

$$P_{\alpha,\beta} = Prob\,(\alpha \rightarrow \beta) \qquad \alpha, \beta = \pi, K, p$$

Combining this information with the expected particle multiplicity per event, as extracted from Monte Carlo data, it is possible to estimate the efficiency and the purity of a selection for p and $\bar{p}$.

Figure 46 compares the expected $\bar{p}$ spectrum for 190 GeV p primaries on LH_2 with the discussed ranges.

The very good separation of the proton signal from that of π and K allows for an unambiguous identification of protons, and hence antiprotons in the momentum range 18 to 45 GeV/c.

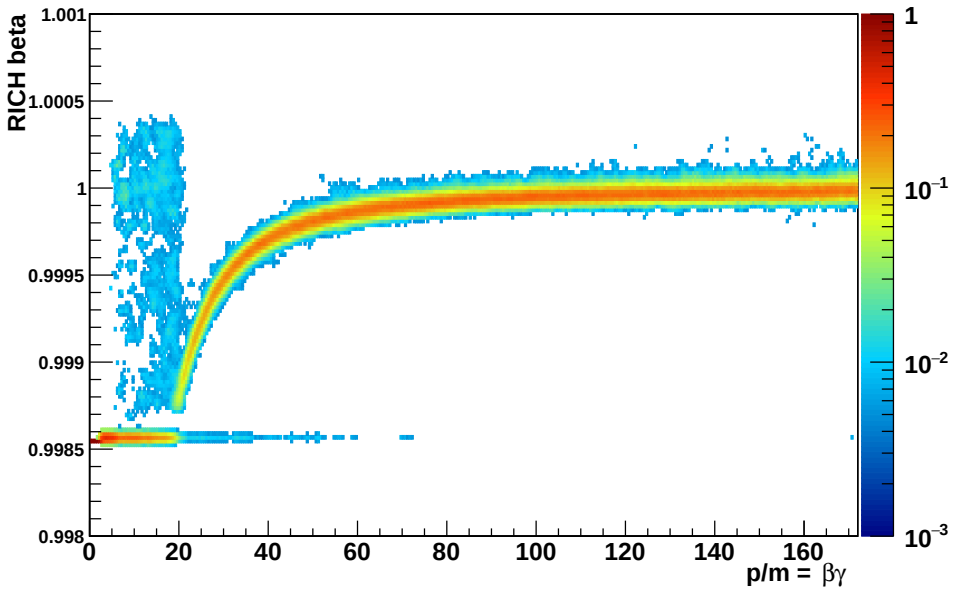

Figure 45: Each column in this scatter plot represents the p.d.f for the RICH-measured beta, for the corresponding particle with $\beta\gamma = p/m$.

Table 11: Efficiency and purity of the samples of p and $\bar{p}$ obtained with a realistic particle identification algorithm.

Range (GeV)	p Eff	p Pur.	$\bar{p}$ Eff	$\bar{p}$ Pur
[10,18]	75%	95%	75%	95%
[18,35]	95%	95%	95%	90%
[35,45]	90%	90%	90%	60%

4.6 Event rate, projected statistical precision and systematic uncertainties

As previously stated, we want to measure the antiproton production cross section double differential in angle and momentum for the $p + p$ and $p + {}^4He$ process. In each event, the antiproton track is identified and counted as a function of momentum and forward angle (or pseudo-rapidity).

Events will be counted separately for momenta in the range 18-45 GeV /c, where we can use the RICH to identify the antiprotons by their mass, and in the range 10-18 GeV /c, where we use the absence of the RICH signal, *i.e.* the veto mode, to identify the particle as not π or not K. In both cases, the counting must be corrected for several effects, including the reconstruction efficiency and the overall RICH efficiency. These efficiencies can be estimated with the MC simulation and also directly from the 2009 data.

The antiproton cross section is obtained as ratio of the (corrected) number of events with an antiproton to the total number of interactions, where the latter is taken from the number of triggers including corrections for several effects.

We present here an estimation of the expected $\overline{p}$ rate at COMPASS++/AMBER, for a proton beam of 190 GeV/c impinging on a LH_2 target. In this estimation, a total LH_2 target length of 40 cm is considered together with a proton beam intensity of $I_{beam} = 5 \times 10^5 s^{-1}$.

The resulting expected instantaneous luminosity is given by:

$$\mathcal{L} = \rho_{LH_2} \times \frac{N_A}{A_{eff}} \times L_{eff} \times I_{beam} = A \times I_{beam}, \tag{28}$$

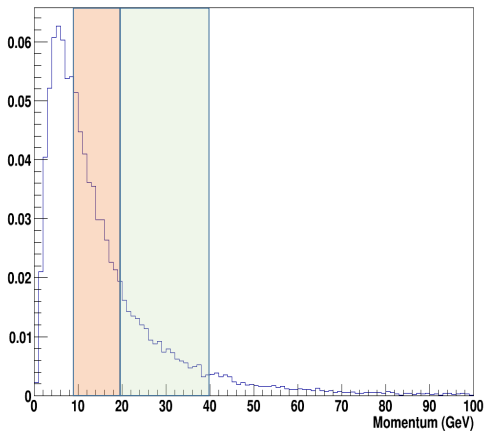

Figure 46: Expected $\bar{p}$ momentum spectrum for 190 GeV p primaries on LH_2. The two shaded areas represent the ranges where the $\bar{p}$ identification with RICH is effective. In the orange one $\bar{p}$ are identified in veto mode, in the green one the $\bar{p}$ identification is direct.

where $\rho_{LH_2} = 0.0708$ g/cm^3, N_A is the Avogadro Number, L_{eff} the effective target length and A_{eff} the effective mass number of LH_2 or LHe. Considering the LH_2 target we obtain $A = 1.78 \times 10^{24}$cm^{-2}, and an expected luminosity of $\mathcal{L} = 8.9 \times 10^{29}$cm^{-2}s^{-1} for the LH_2; considering instead the L^{4}He target we get $A = 0.79 \times 10^{24}$cm^{-2} and $\mathcal{L} = 3.9 \times 10^{29}$cm^{-2}s^{-1}

Considering a $p+p$ inelastic cross section of 30 mbarn, equivalent to $\sigma = 30 \times 10^{27}$cm^{-2}, a $\overline{p}$ multiplicity of 0.07, and a 75% proton fraction in the positive hadron beam, the $\overline{p}$ event rate per day is calculated according to the expression:

$$\mathcal{R} = \mathcal{L} \times \sigma \times 0.75 \times 0.07 \times n_{spill} \times d_{spill} \times Av_{SPS} \times Av_{spec} \times E_{tot}, \tag{29}$$

where $d_{spill} = 4.8$ s is the duration of the SPS spill, and $n_{spill} = 4320$ is the maximum number of spills per day assuming the typical SPS supercycle of 40 s. The accelerator and the spectrometer availabilities are $Av_{SPS} \approx 0.85$ and $Av_{spec} \approx 0.85$ respectively, where the latter estimate includes the trigger dead time, the run start-stop procedure and the DAQ availability.
The estimated overall detection efficiency E_{tot} is about 51%, given by:

$$E_{tot} = E_{trig} \times E_{CEDAR} \times E_{rec} \times E_{RICH} \tag{30}$$

where $E_{trig} \approx 0.90$ is the trigger efficiency, $E_{CEDAR} \approx 0.86$ is the CEDAR efficiency times purity, $E_{rec} \approx 0.95$ is the reconstruction efficiency, E_{RICH} is the antiproton identification efficiency times purity with the RICH, which varies from about 0.5 up to > 0.90. Assuming an overall $E_{RICH} \approx 0.70$, this leads to an estimated event rate per day $\mathcal{R} = 9 \times 10^6$ ev/ day. Considering that the antiproton identification momentum threshold is 10 GeV/c the expected event rate per day useful for the analysis drops to about 4×10^6 ev/ day.

Considering a measurement of the double-differential cross section with 10 bins in momentum and pseudorapidity each, a statistical uncertainty of $\approx 0.5\%$ per data point will be reached in 1 day of beam time.

We plan to take data with proton momenta of 50, 100, 150, 200 and 280 GeV/c, with both the LH_2 and the L^{4}He target. The change-over from one target system to the other will take approximately 10 days, including the commissioning of the spectrometer with the new target.

The statistical error is only a small contribution to the total error. Several corrections to the event and trigger counts are needed to obtain an accurate measurement. Each of these corrections contributes to the systematic uncertainty. Given the common aspects of the spectrometer layout foreseen for the measurement proposed here and of the COMPASS set-up used in 2009, some of these factors have already been studied. Here we give an estimation of the contributions from the most relevant ones.

The trigger count rate (N_{tot} in Eq. 27) must be corrected for particle identification efficiency and purity in selecting protons with CEDAR in the secondary beam, and trigger efficiency.
The antiproton event count needs to be corrected for the tracking reconstruction efficiency and the antiproton particle identification efficiency, which possibly depend on momentum and pseudo-rapidity.

As shown in Fig. 36 a very clean separation of protons from pions/kaons is achievable with CEDAR detectors; thus a larger diaphragm opening of 1.2 mm compensates any acceptance effect by beam divergence, as already proved in 2009 COMPASS data taking.
Moreover the new thermal stabilisation system, allowing for temperature stabilisation down to 0.1K over the whole vessel 5.2.3, reduces the systematic uncertainty in the p/T values in pressure scans, contributing to further reduce the systematic uncertainty on the purity in the proton identification. The dependence of the PID efficiency on the selected likelihood cut has also been studied and found to be very small for proton identification. The overall systematic uncertainty on CEDAR efficiency and purity is expected to be < 1%.

This experiment will be operated with a minimum-bias trigger system which is well under control, given the fact that it was successfully operated in the 2009 COMPASS hadron run with a factor ten higher beam intensity [176]. In addition, as explained in Sec. 5.2.4, the adoption of a new DAQ scheme with trigger-less data acquisition, in addition to increase the data collection efficiency, will remove the systematic uncertainties in the correction of the veto dead-time. Nevertheless dedicated data can be collected during the test measurement foreseen at the end of 2022, to control the proper operation of the triggering system and to evaluate the overall efficiency.

An evaluation of the performances of the tracking reconstruction efficiency as a function of the particle momentum using a simulation of the COMPASS setup is described in [176] and in Sec. 4.4. The systematic effects will be estimated from further Monte-Carlo studies; they are expected to be small.

The efficiency and purity of PID based on RICH likelihood ratio cuts must be quantified in order to measure the influence of the cuts on the event selection. Thus rather clean sources of protons, kaons and pions are preferred to study those cuts. As already shown in sec.4.5, easy and clean access to antiprotons and pions is given by analysis of so called V0s decays. The determination of the efficiency and purity of the RICH PID and of their dependence on the selected likelihood cuts has been already done for the COMPASS 2006 muon beam data and successively adapted to the 2009 hadron data for pion and kaon PID. The method will be retuned for proton PID on the 2009 hadron data.

Altogether, a total systematic uncertainty not exceeding 5% is expected.

4.7 Competitiveness and complementarity $^{v2(+++)}$

As already introduced in Sec. 4.1, the exceptional experimental accuracy of the order of a few % achieved by AMS-02 on the cosmic-ray $\bar{p}$ flux and the $\bar{p}$/p flux ratio poses the challenge of achieving a similar precision in phenomenological models that describe the CR $\bar{p}$ flux as produced by the interaction of the CR primary components with the ISM. Currently the large uncertainty on the antiproton production cross section is one of the main sources of models uncertainty. In order to cover all of the AMS-02 $\bar{p}$ energy range, precise $p + p \rightarrow \bar{p} + X$ and $p + {}^4He \rightarrow \bar{p} + X$ cross-section data are needed with a

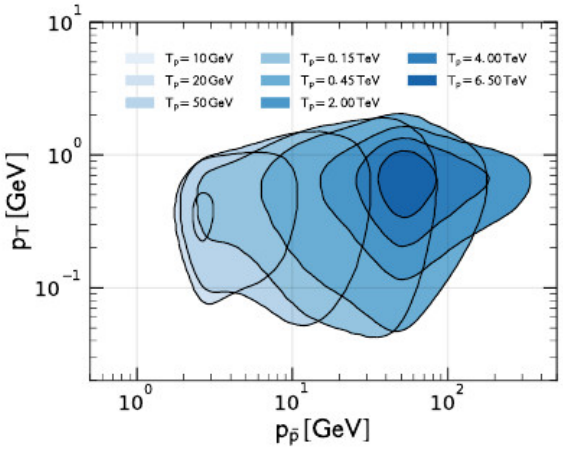

Figure 47: Parameter space for the $p + {}^4He$ channel corresponding to an exemplary fixed-target experiment. The different shaded areas correspond to different proton beam energies: a 3 % accuracy is required on the cross-section determination inside the blue shaded region, and a 30 % accuracy outside the contours [179].

proton-beam kinetic energy T_p ranging from 10 GeV to 6 TeV and a pseudorapidity η ranging from 2 to almost 8. Figure 47 shows the parameter space that has to be covered as a function of momentum $p_{\bar{p}}$ and transverse momentum p_T of the $\bar{p}$ at different kinetic energy T_p of the proton (the shaded areas), for the case of the $p + {}^4He \rightarrow \bar{p} + X$ cross section. In this figure, a 3 % accuracy is required on the cross-section determination inside the blue-shaded region, and a 30 % accuracy outside the contours, in order to guarantee the AMS-02 precision level on the $\bar{p}$ source term [179].

The data available on $p + p \rightarrow \bar{p} + X$ consist of early measurements [180–184] and the more recent measurements from the BRAHMS [185], NA49 [173] and NA61 [174] collaborations.

The only data available on $p + {}^4He \rightarrow \bar{p} + X$ are those collected in May 2016 by LHCb operating in fixed-target mode with the SMOG device [175] at 6.5 TeV ($\sqrt{S_{NN}} = 110$ GeV, pseudo-rapidity range $2 < \eta < 5$ and detected antiproton momentum range $12 < T_{\bar{p}} < 110$ GeV/c). The constraints on cosmic anti-proton production from the afore mentioned measurements are discussed in [186].

With the proposed fixed-target experiment at the CERN SPS M2 beam line one could perform measurements of antiproton production cross sections in $p - p$ and $p - He$ collisions at different momenta of the proton beam, from a few tens of GeV/c up to about 250 GeV/c, and for pseudo-rapidities $\eta > 2.4$. We performed an estimation of the possible impact of the proposed measurements in covering the interesting region for dark matter sensitivity with cosmic anti-protons; the method used in this calculation follows the one used in [186]. Figure 48 shows the impact of the proposed $p + p$ measurements on constraining the production of cosmic anti-protons versus their kinetic energy. Each curve represents the fraction of anti-proton production as constrained by our cross-section measurements over the full proposed range of beam momenta (dashed line, 50-250 GeV) or two sub-intervals of the same region. The thick black line represent the same quantity as covered by the NA61 measurements [174].

The proposed $p + p$ measurements have a large overlap with the already available ones, allowing for a direct comparison of the results and for a study of possible systematic effects. Furthermore, if we assume that the Lorentz invariant cross section does not depend on $\sqrt{s}$ between 10 GeV and 50 GeV [165], a more extensive comparison can be performed with all existing data.

Figure 49 shows the constrained anti-proton fraction for the case of $p - He$ and $He - p$, both constrained by the proposed $p - He$ measurements when applying conventional kinematics. It is evident that in this case the results of our measurement are essential to directly pin down the production of anti-protons

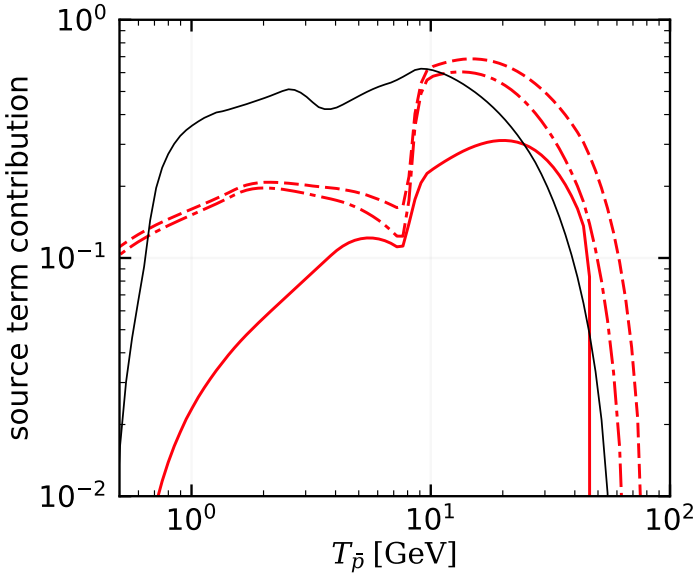

Figure 48: Source-term contribution of the COMPASS++/AMBER experiment to the total source term in the $p-p$ channel, shown in three different energy ranges: i) 100 GeV to 190 GeV (solid red line), ii) 50 GeV to 190 GeV (dashed-dotted red line), and iii) 50 GeV to 250 GeV (dashed red line). For comparison also shown is the contribution of the NA61 experiment (thin black line) [174].

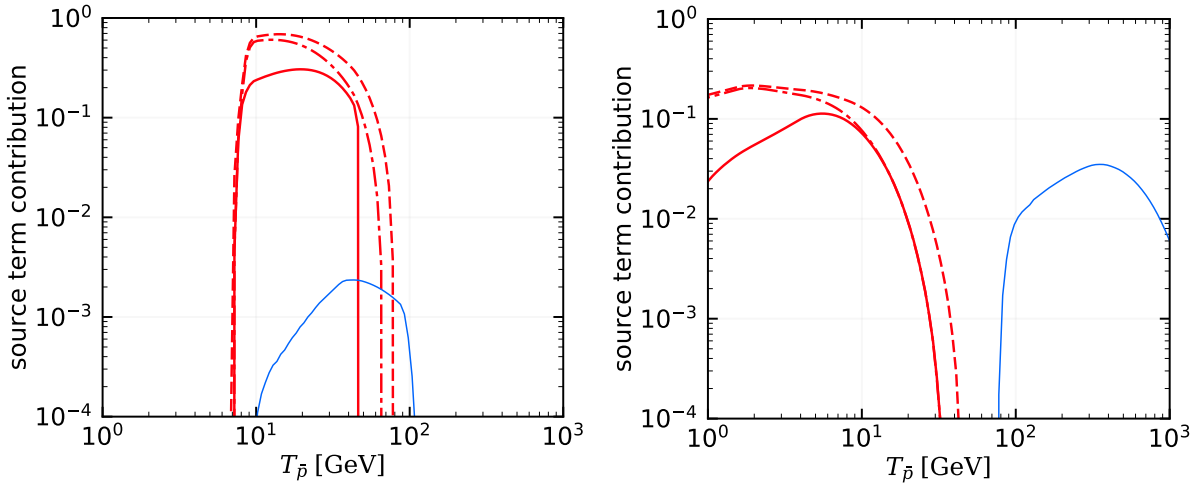

Figure 49: Source-term contribution of the COMPASS++/AMBER experiment to the total source term shown in three different energy ranges: i) 100 GeV to 190 GeV (solid red line), ii) 50 GeV to 190 GeV (dashed-dotted red line), and iii) 50 GeV to 250 GeV (dashed red line). Left: $p-He$ channel. Right: $He-p$ channel. For comparison we show also the contribution of the LHCb measurement (thin blue line) [175].

in a relevant kinetic energy region. Combined with the LHCb measurements at very high energy, the new data would yield the necessary kinematic coverage. This would contribute to a significant reduction of the uncertainty on the expected amount of secondary anti-protons produced by spallation of primary cosmic rays on the interstellar medium, which is currently one of the most limiting factors when using the AMS-02 data on the $\bar{p}$ flux and the $\bar{p}/p$ flux ratio as input for the indirect Dark Matter search.

Altogether, the proposed measurements will improve significantly the knowledge on the anti-proton production cross section from $p-p$ and $p-He$ interactions, thereby boosting the sensitivity to Dark Matter signals in the charged cosmic rays.

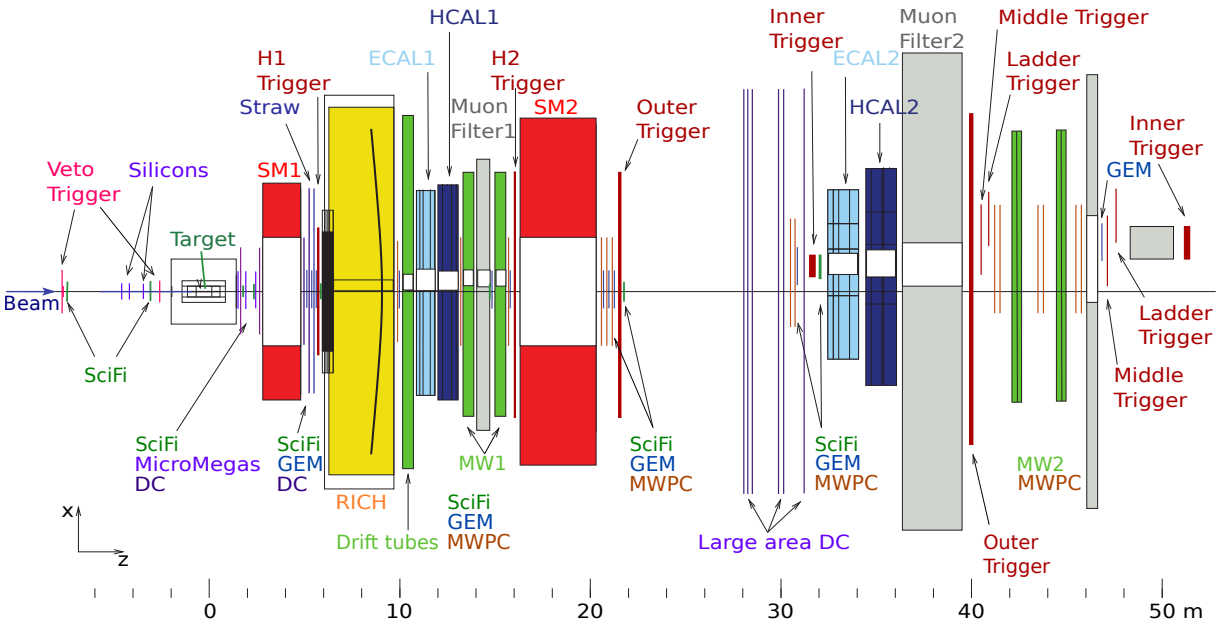

Figure 50: Top view of the 2021 COMPASS spectrometer setup.

5 Instrumentation

5.1 Overview

The physics programmes presented in this proposal are all based on the concept of using the present COMPASS setup [42, 187]. The setup for the approved COMPASS 2021 run is shown in Fig. 50: two large-gap dipole magnets with tracking stations before and after them, combined with calorimeters and particle identification detectors. In addition, the CEDARs located at the beam line are required in all hadron programmes for beam-particle identification.

The foreseen upgrades of this setup, from which all physics programmes will profit, are listed in Sec. 5.2. Specific programmes also require additional dedicated equipment, as will be explained below:

- Muon-proton elastic scattering: DAQ/Trigger, a high-pressure active TPC target (similar to A2 at MAMI) or hydrogen tube surrounded by SciFis; SciFi trigger system on scattered muon; silicon trackers to veto on straight tracks (kink trigger) (see Sec. 5.3).
- Drell Yan: high-purity and high-efficiency dimuon trigger; dedicated precise luminosity measurement; dedicated vertex-detection system; beam trackers; C/W target (Sec. 5.4).
- Anti-proton cross section measurement: a liquid helium target (see Sec. 5.5). In addition, a new, high-aperture RICH-0 would be desirable in order to identify hadrons at lower momenta (Sec. 5.6).

The specific parameters and hardware upgrades for each programme are summarized in Table 12.

5.2 General upgrades

The experimental backbone of the "New QCD facility at the M2 beam line of the CERN SPS" in the EHN2 experimental hall will include the following general upgrades of the existing spectrometer:

- New large-size PixelGEMs as replacement and spares for existing large-area GEMs (Sec. 5.2.1).
- New large-area micro-pattern gaseous detectors (MPGD) based on Micromegas technology to replace existing MWPCs (Sec. 5.2.2).

Table 12: Requirements for phase-I measurements at the M2 beam line beyond 2021.

Programme	Physics Goals	Beam Energy [GeV]	Beam Intensity [s^{-1}]	Trigger Rate [kHz]	Beam Type	Target	Hardware additions
muon-proton elastic scattering	Precision proton-radius measurement	100	$4 \cdot 10^6$	100	$\mu^{\pm}$	high-pressure H2	active TPC, SciFi trigger, silicon tracking
Drell-Yan	Pion PDFs	190	$7 \cdot 10^7$	50	$\pi^{\pm}$	C/W	target modification
Input for Dark Matter Search	$\overline{p}$ production cross section	20-280	$5 \cdot 10^5$	25	p	LH2, LHe	liquid helium target, RICH?

– High-rate-capable CEDARs (Sec. 5.2.3) for all hadron-beam programmes to identify the desired beam particle.

– New front-end electronics (FEE) and trigger logics that are compatible with triggerless read-out, which include an FPGA-based TDC with time resolution down to 100 ps and a digital trigger that is capable of rates up to 100-200 kHz (Sec. 5.2.4).

5.2.1 Large-area PixelGEM detectors

New large-area PixelGEM detectors will be designed and build by 2021 as replacement and spares for the existing large-area GEMs [188] in the COMPASS setup. Each detector will have 4,096 channels. The peripheral area will be covered by strips read out from both sides. The central region will be exposed to the full beam and will thus consist of hexagonal pixels of 1.5 mm outer radius with individual amplitude read-out. The active area of each detector will be between 30.7$times$30.7 cm^2 and up to 40×40 cm^2, about a factor of 10 larger than the existing COMPASS PixelGEM detectors [189]. The new large-area PixelGEMs will be equipped with new front-end electronics allowing for higher rates and self-triggering. One candidate chip fulfilling these requirements is the VMM [190, 191]. We are currently investigating the performance of a GEM detector equipped with the VMM chip in terms of signal-to-noise ratio and resolution.

5.2.2 Large-area multi-pattern gaseous detectors (MPGD)

New large area Micro Pattern Gaseous Detectors (MPGDs) will be designed and developed to replace the existing ageing MWPC tracking stations in the COMPASS setup. The new detectors will be based on Micromegas technology. Each station will have an active area of about 1.5 m^2, with two or three coordinate planes and about 2 mm pitch. The new detectors will be equipped with new front-end electronics. The total number of channels will be about 28,000.

A resistive Micromegas version of the detector is currently under investigation for the future application in COMPASS++/AMBER. The use of double resistive layers coupled to a floating mesh configuration looks promising from the production and performance point of view. A few small-sized prototypes with an active area of 10×10 cm^2 have been produced and are being tested (Fig. 51).

The main goal is to define an optimal design for a cost-effective replacement of the present MWPC chambers, taking also into account the compatibility with the future DAQ requirements.
For the read-out of the new detectors, front-end electronics based on the TIGER ASIC (Turin Integrated Gem Electronics for Read-out [192]) are under evaluation. This front-end chip can be used in trigger-less mode and provides both time and charge measurements.

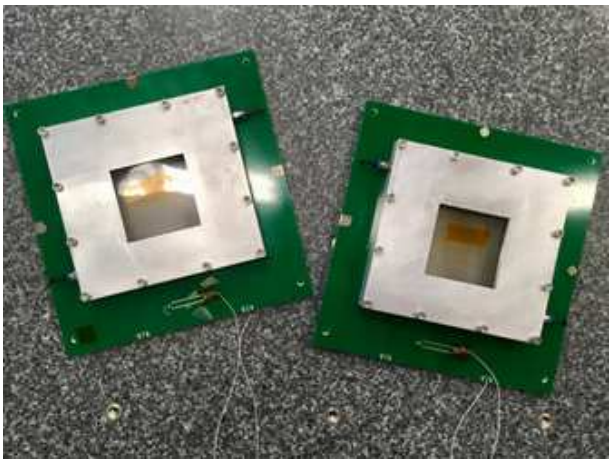

Figure 51: Two small-sized (10×10 cm^2 active area) Micromegas prototypes.

It is planned to build a medium-sized prototype (60×60 cm^2 active area) to be tested during the 2021 COMPASS data taking.

5.2.3 CEDARs at high rates

The purpose of the CEDAR detectors is the identification of the beam particle type on an event-by-event basis. Presently, two 6 m-long CEDAR stations are located in the M2 beam line, 30 m upstream of the COMPASS target. They are filled with helium gas at a pressure of approximately 10.5 bar. The emerging Cherenkov photons are focused by a mirror and then detected by eight PMTs arranged in a ring around the beam axis. The pion, kaon or proton ring is selected by tuning the diaphragm opening and the gas pressure.
In preparation for the 2018 COMPASS run with pion beam, the existing CEDARs were upgraded in winter 2017/2018 for a better rate capability and improved thermal stability. The project was carried out in collaboration between CERN and COMPASS members. In the course of this upgrade almost all major subsystems (except for the gas system) were replaced or significantly altered.

The ring size of the light resulting from passage of a charged particle strongly depends on the gas density. It is therefore important to make sure that a constant pressure-to-temperature ratio is maintained throughout the detector. To achieve this, a new thermal stabilisation system was designed and installed by CERN. It consists of a closed-loop air circulation system with a heat exchanger and a high-accuracy cooler. The system allows for temperature stabilisation down to 0.1 K over the whole vessel. This system was tested during 2018 run and was proven to work according to the design specification. A conceptual sketch of the upgraded thermal system is shown in Fig. 52.

Working with high intensity hadron beams puts a strong pressure on a read-out system – in 2018 the pion beam intensity was about $8 \cdot 10^7$/s. Withstanding this level of rates required significant modifications to the whole read-out chain. New multi-channel PMTs were used (Hamamatsu R11265U-203-M4 with anode pulse widths of 2-3 ns and ultra-bialkali photocathodes). Thus the incident light can be distributed among the four channels of the single PMT, reducing the overall per-channel rate (though one should note that single event usually gives hits in more than one channel). The PMTs were positioned outside the focal point of the light exiting the detector, so that efficiency loss due to dead area between the neighbouring channels could be minimised. To further improve rate tolerance, the PMTs are supplied via an active voltage divider, which ensures a low-impedance driver path for each of the dynodes. This mitigates gain fluctuations that could be caused by high average anode currents, while still allowing low power operation. In fact, the idle power consumption of the dividers was low enough that the dividers could be placed inside the thermal housing without special radiators and without deteriorating the temperature uniformity. No problems were observed related to radiation effects on the dividers – all of the installed

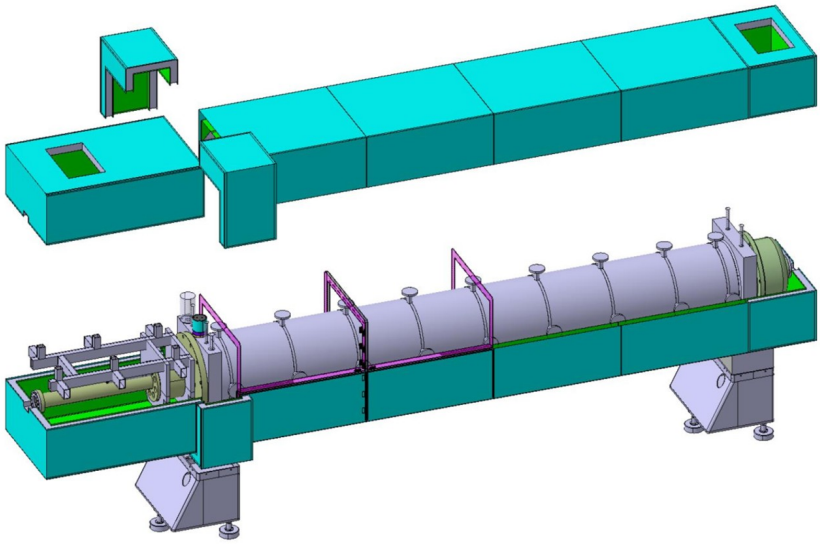

Figure 52: CEDAR 2018 upgrade of the thermal stabilisation system: new housing with improved insulation and connection to a high-accuracy closed-loop air circulation system.

bases worked flawlessly during the whole 2018 run.

Signals from the PMTs are amplified by preamplifiers installed on the PMT bases and are then fed into twisted pair cables. They are received by new discriminator cards, which were confirmed to work with rates exceeding 40 MHz per channel. Digital LVDS signals from the discriminators are fed into iFTDC cards for time stamping and amplitude measurement. The whole acquisition system consists of eight discriminator cards (each serving two PMTs), six iFTDCs and a data concentrator. Four iFTDCs are used for pulse timing and two for measuring amplitudes of low-pass filtered signals via the time-over-threshold technique. Slow control is implemented using the MODBUS protocol, with a communication link over a serial line connection (RS485). The new setup also introduced an optical system that allows monitoring of the PMT gain. It provides light pulses from a single source to all PMTs using passive light splitters. The goal is to have a long-term monitoring of gain stability and PMT health.

The modified CEDARs were commissioned and used during the 2018 COMPASS run. It was confirmed that they can operate at per-channel rates of approx. 20M hits/s. It is therefore expected that they can successfully operate at the desired beam intensities of the proposed future measurement programmes. The experience gained during the run also resulted in some future upgrade propositions:

- Careful beam line tuning is required to maintain a parallel beam at the CEDAR location, as beam divergence significantly degrades performance. This is especially true if one intends to use the CEDARs as part of the trigger system.
- It would be beneficial to install a tracking system for the CEDARs to correct the beam-track trajectories. One option could be the XBPF upgrade, a new SciFi-based instrumentation developed at the CERN North Area to measure beam profiles and momenta [193].
- Beam halo and the amount of showers generated upstream of the CEDARs should be limited. Their presence was observed during 2018 run as a high geometry-related inequality of the measured rates. It was further confirmed by observing large-amplitude signals (several photoelectrons) in a blinded PMT that were in coincidence with other PMTs in the detector.
- The signal-to-noise ratio of the signals arriving at the discriminators should be improved. This will require several upgrades – first, a revised design of the discriminator cards with improved shielding

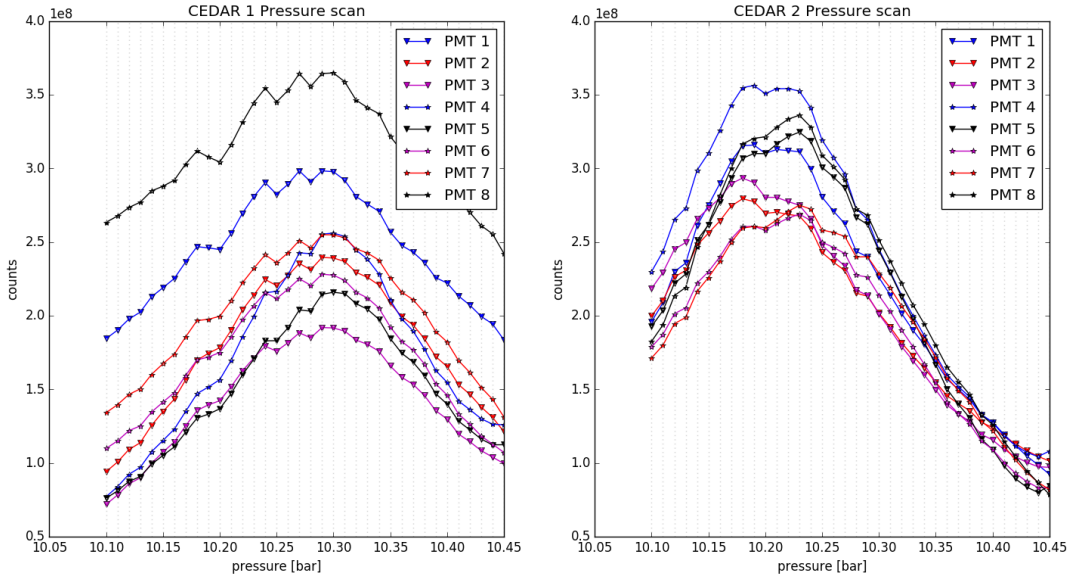

Figure 53: Example results of CEDAR alignment procedure, with detector axis parallel to the beam axis.

is needed. Second, one should consider removing the preamplifiers for the base and only using symmetrizing transformers with unequal impedance ratio. Third, the twisted pair cables need to be replaced with low-loss ones.

– Read-out electronics should be moved out of the beam line tunnel, to mitigate lock-ups related to radiation.

– The gain monitoring system requires slight modification – currently the fibre termination inside the base causes too high variation in the amount of light exiting the fibre.

Finally, during the commissioning phase it was decided to adopt a new alignment method to position CEDARs parallel to the beam axis. It is based on alignment of pressure-scan peaks for individual PMTs (Fig. 53). Contrary to the procedure used in the past, this method allows an alignment without the need for dedicated beam settings (*i.e.* it is no longer necessary to have a scrubbed low-intensity beam). Furthermore, it is not sensitive to the quality of efficiency equalisation of the PMTs.

5.2.4 The future continuous read-out iFDAQ framework

The rapid development of technology is starting to enable a transition from the classical trigger based data acquisition to a scheme, in which detector subsystems deliver continuous time-stamped data streams for real-time processing in later stages of the DAQ (e.g. High Level Triggering / Feature extraction) and dead time free storage of the whole data stream. The development of the Compass DAQ in the past led to a new design, where most of the traditional computers were substituted with FPGA. This new iFDAQ [194] was introduced for the Compass run in 2014 and successive further development has led to a very stable and modular DAQ system, which was successfully used in the last years of the Compass II data taking. For the design of the new data acquisition system it is proposed to adopt a rather far-looking approach to allow the use in a wide range of physics cases and needs in the Compass++/AMBER framework. The logical step is to go to a continuous data acquisition with a digital trigger system, which is tightly integrated in the iFDAQ framework. (Fig. 54).
For this approach all detectors have to be equipped with front-end electronics, which is able to digitize the analogue signals of the detectors dead-time free in real time and stream their data continuously to the DAQ. After the front-ends, the data is split into two data streams. Each detector sends a data-stream to the

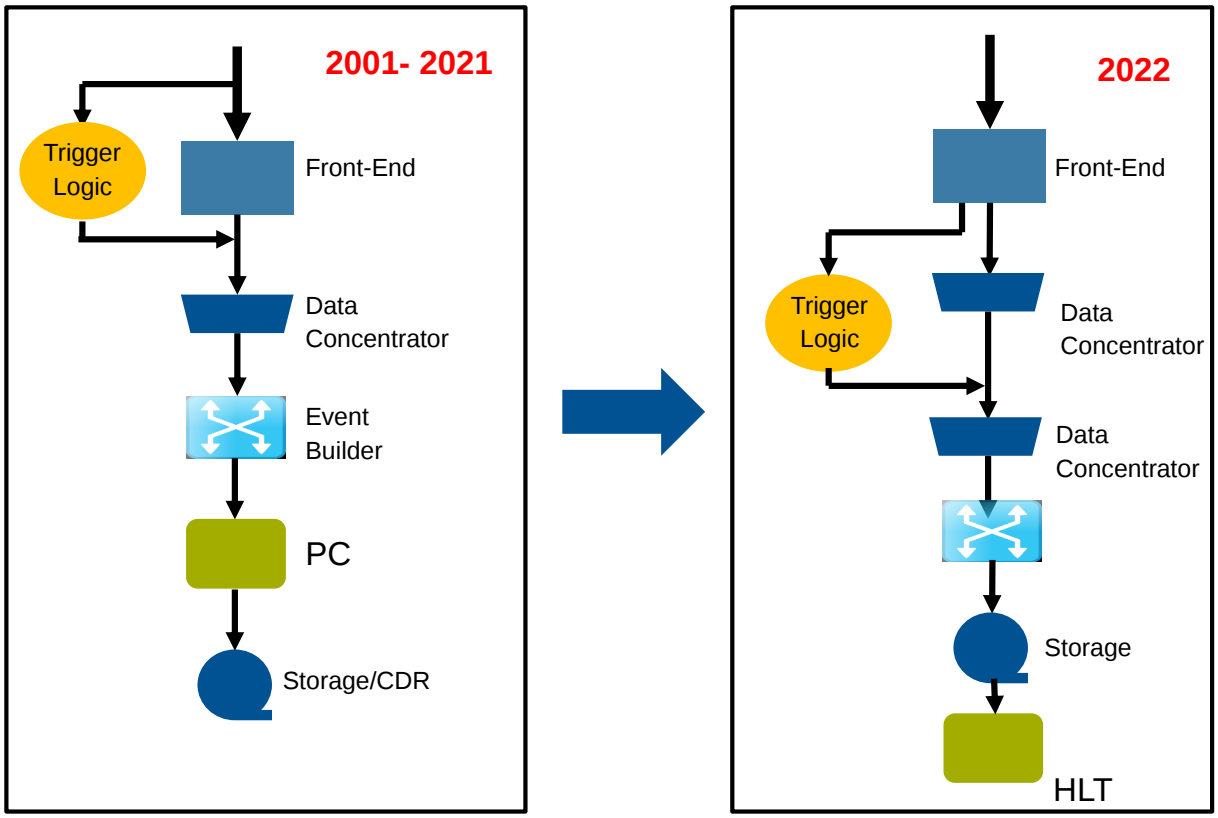

Figure 54: Evolution of iFDAQ

DAQ, where it is buffered until the trigger decision is made. Detectors, which participate in the trigger decision, have a second data stream that is sent to the trigger logic and is used to make the selection of data that is later stored to disk. The scheme of the different DAQ components and their interconnection is shown in Fig. 55.

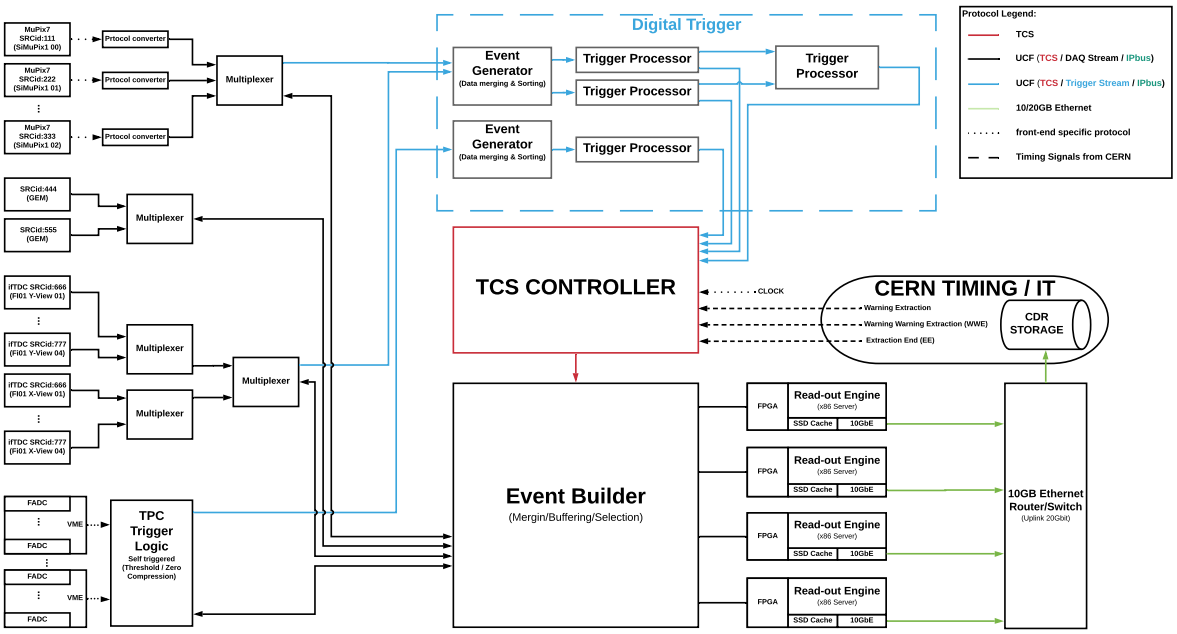

Figure 55: Logical scheme of the different components of the future DAQ system

5.2.4.1 DAQ Principle of Operation The new DAQ can run in two different operation modes. One is a completely not-triggered data taking, where we can save everything to disk for further offline analysis. The other one is a digital (multi-level) trigger mode, where the information of the detector systems is send to the trigger-processors to perform the trigger decision on multiple levels with a different granularity of information. The data of all detectors is buffered in between to enable a trigger latency in the order of tens of seconds. For both modes all detectors must be equipped with continuous read-out enabled front-end electronics. All front-ends are synchronized via a global clock of 40 MHz distributed via the TCS network. In addition, the TCS system distributes information about the begin of a time-slice, which is in the order of 128 μs. This begin of time-slice information is a kind of synchronized artificial global trigger for all front-ends. The time-slices are further divided into sub-time-slices, so called images with a minimal image length of currently 128 ns. The length of an image, which is equivalent to the traditional

Figure 56: Overview for the time-slicing

read-out-gate, can have a different size for each detector sub-system according to their time-resolution and hit rate (Fig. 56). This image length must be an integer multiple of the minimal image length. Thus data from different detectors can be combined to an event before they are saved to disk. At the beginning of each new time-slice the front-end boards send two data words as header with the number of images in the time-slice, the global number of the time-slice and the global time of the beginning of the time-slice. Except of the number of images in the time-slice this information is common for all front-ends. At the beginning of a new image the front-end electronics sends an image data header word, which contains the start of the image in units of 25 ns of the global clock, followed by all data words with hit-information for the corresponding detector sorted in time. At the end of a time-slice a trailer data word is sent, which contains the check-sum of the data sent during that time-slice as well as error flags to indicate errors during processing at the stage of the front-ends. These data-streams of individual front-end boards of one detector system are then further concentrated in a multiplexer. The purpose of the multiplexer is to combine data from different front-ends of one sub-detector to one data-stream on the level of the images (Fig. 57). The hit information of different front-ends is grouped and time-wise sorted under one image-header and a begin of group / end of group header/trailer pair is added. This additional information is used to group data from one detector/view for further processing and to indicate the path of the data through the DAQ system for debugging purpose. In addition the multiplexer are used to split the data-stream if the detector is used for trigger decision. In both cases one data-stream is going to an event-builder, which collects the data from different detectors, merges them to an event and buffers the data until they can be written to disk or the trigger decision is made. The event building is either done at the scale of the time-slices for the not-triggered data-taking mode or on the level of two consecutive images around the image, in which the trigger occurred for data reduction in the multi-level trigger mode. For storage the data of the event builder is then sent to the read-out-engines, which store the data locally on disk before they can be transferred to the central storage pool.

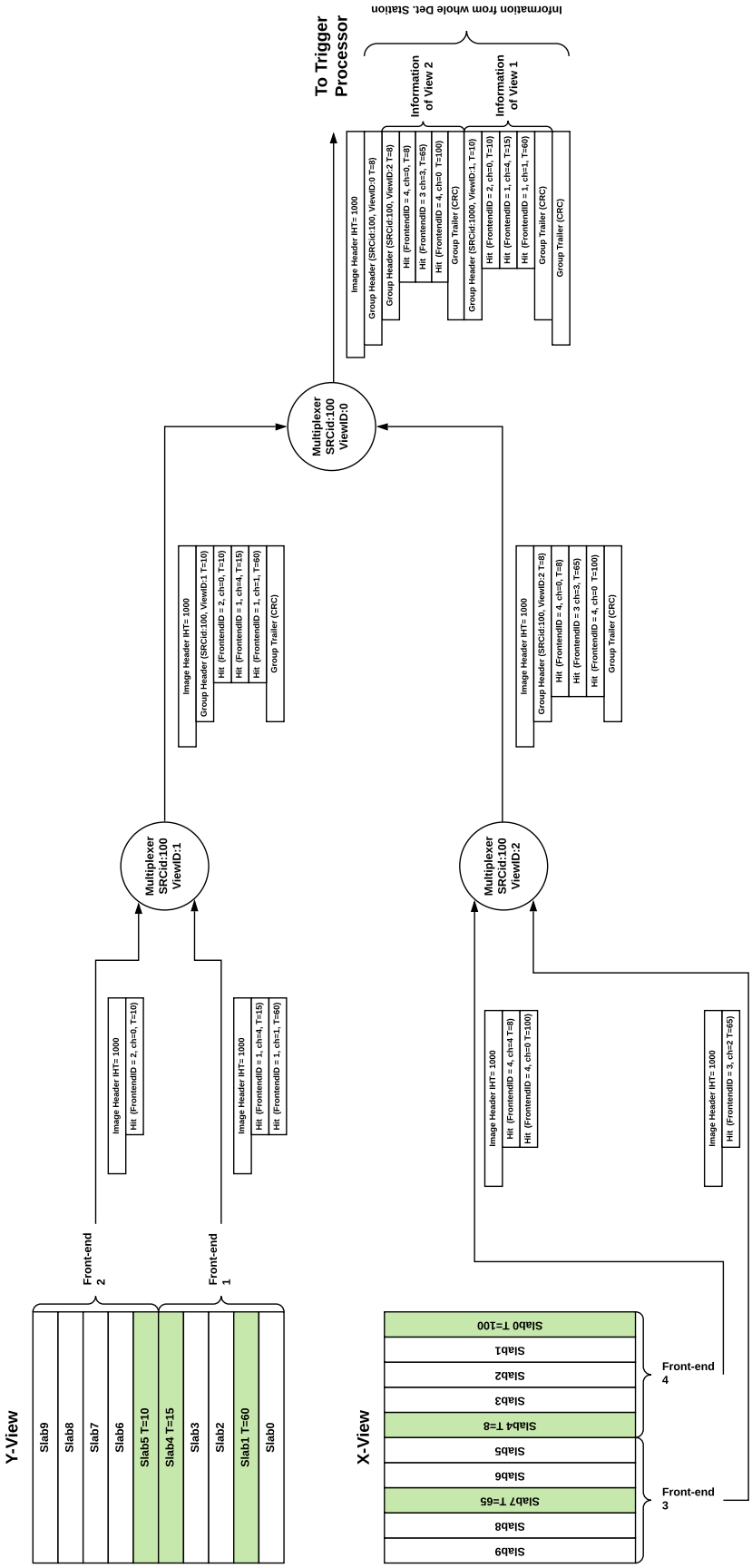

Figure 57: Data-flow through the DAQ of hit information of one Image. Front-ends sent only hit information with image header. These front-end data streams are concentrated in the multiplexer and a group header/trailer pair is added to indicated the origin of the hits before the combined data stream is further sent to the Trigger Processor.

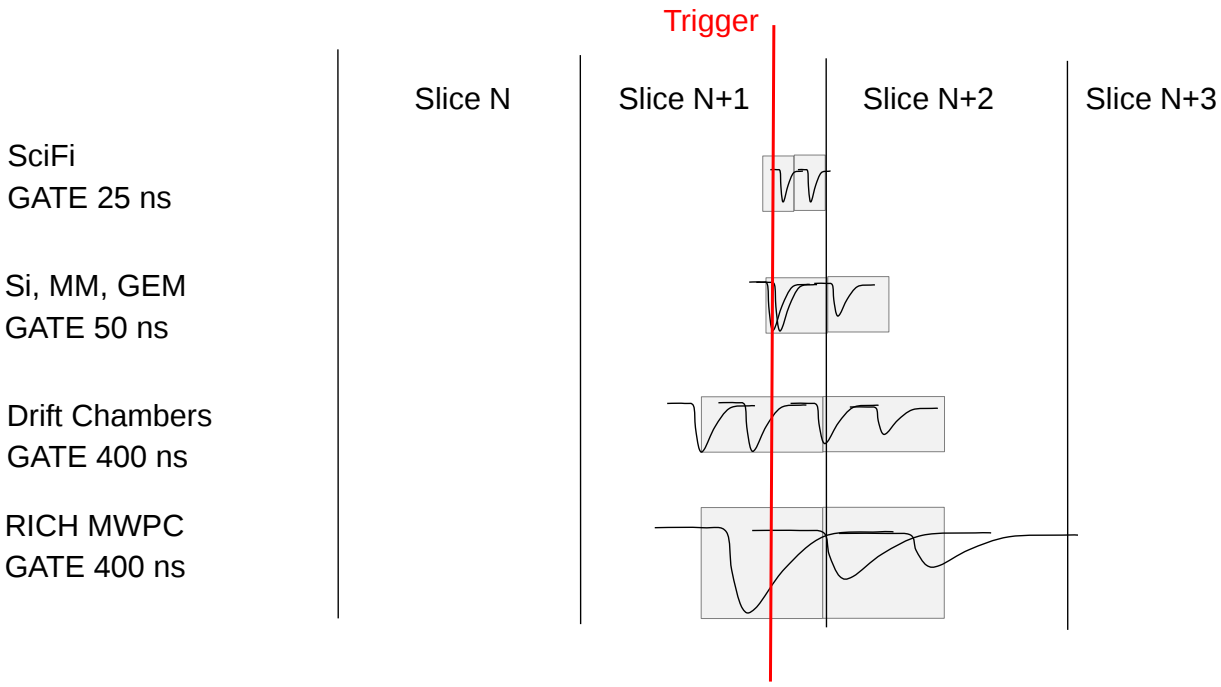

Figure 58: Selection of data which is stored to disk after a trigger is issued.

5.2.4.2 Digital Trigger System The digital trigger system consists out of two stages. One is the event generator, which receives the continuous data streams from the detectors that participate in the trigger decision, and builds events of interest (EOI) according to time correlation of the hits. This data stream is then sent to the trigger processor in a common data format, which is compatible to the general DAQ protocol. The trigger processor can be either a single stage or a multi-stage approach, where every trigger processor adds the results to the data stream for the next stage. This approach, in addition to the DAQ-compatible data format, enables us to analyse and debug the output of each stage by plugging in a read-out engine on the output of that stage.
The different trigger processors are programmable FPGA units, which can be used to select interesting data with different kinds of algorithms. This results in a flexible system that can be adapted to the different physics requirements of measurements. After a trigger decision is made, the information on the image, in which it happened, is transferred to the TCS controller. It distributes this information to the data concentrator modules to select the data from the buffers, which is then send to the event builder where the assembled events are distributed between the read-out engines and stored to disk. To minimize the amount of data only two consecutive images of each detector are saved to disk (Fig. 58). The structure of the trigger-logic as well as the large trigger latency in the order of tens of seconds make it possible to investigate also the use of CPU/GPU solutions for high-level trigger stages and online reconstruction.

5.2.4.3 Developments of DAQ Hardware components:

iFTDC The iFTDC is a Xilinx Artix7 FPGA board with 64 LVDS inputs/outputs and 4 high speed serial links with a maximum rate of 3.5 Gb/s. There are five different TDC firmware versions with different number of channels and resolution. The firmware features are summarized in Table 13.

The firmware version with 0.8 ns bin size was successfully tested with different detector systems (CEDARs, MWPCs, PRM Trigger) during 2018 COMPASS run. A special high rate capable firmware version was developed for CEDAR detectors (see Sec. 5.2.3), which is able to digitize more than 10 MHz hit per channel. This firmware works in triggered mode only.

Table 13: Parameters for the different firmware configurations for the iFTDC.

Inputs	Bin width	Double hit resolution	DNL	TDC channels	Comment
64	0.8 ns	8 ns	10%	64	
64	0.4 ns	4 ns	20%	64	40 MHz maximum hit rate
64	0.4 ns	4 ns	20%	64	Trigger-less version
32	0.2 ns	4 ns	30%	32	
64	0.2 ns	4 ns	30%	32	64ch mean-timer input

MSADC The MSADC system [195] is used for read out of the ECAL0 and ECAL2 calorimeters. It consists of 4 thousand channels of 12-bit ADCs digitizing analogue signal at 80 MSPS. Although the system performance fulfils detector requirements it requires an upgrade for integration in the new DAQ scheme. We plan to modify the firmware in such a way that it processes detector information in a continuous mode. The firmware will include few digital filters for suppression of noise and improvement of S/N ratio. We expect that the firmware will be able to detect signals and perform feature extraction by measuring signal amplitude and time for signals that exceed by factor 4 the noise level. In order to increase data rate capability and provide enough FPGA resources for signal processing, the MSADC's FPGA will be backed up by ARTIX-7 FPGA. The ARTIX card will provide an external interface for synchronization, data transmission, and control of the module.

iFDAQ DHMx FPGA card The iFDAQ DHMx card is a Virtex6 FPGA card with 16+2 6 Gb/s high speed serial links via SFP ports. This kind of card was intensively used in the current design of the iFDAQ as Multiplexer/Switch/Event-Builder and will be used as Multiplexer in the future.

Cross-point Switch The cross-point switch is used to interconnect the different components of the iFDAQ in a highly configurable way. The cross-point switch is a matrix of 144x144 serial links with bandwidths of up to 6.5 Gbps. The switch houses a Vitesse VSC3144 non-blocking crosspoint switch chip. The chip is capable to connect any input with any output. The switch is protocol independent and has no restriction on the phase, frequency or signal pattern of transmitted data. The crosspoint switch is configured by a Xilinx Artix7 FPGA mounted on the same card. The FPGA has 4 high-speed serial interfaces for control and monitoring. The crosspoint switch was successfully deployed during the 2018 DY-Compass run. A successor version of this device with a bandwidth of 12.5 Gbps/port is planned.

iFDAQ XCKU Card The iFDAQ XCKU card is a development, for which currently a first prototype production and evaluation is ongoing. It is a FPGA board equipped with a XILINX UltraScale XCKU095 FPGA, 16 GB of DDR4 memory with a maximum throughput of 5 GB/s (possible upgrade to faster GDDR6 memory with »10GB/s throughput) and 64 optical links using Samtec FireFly transceivers with a bandwidth of up to 16 Gbps per link. This card is an universal FPGA board which will be used in the framework of the iFDAQ as Mulitplexer/Event-Builder and Trigger-Processor. To reduce the costs we introduced a new mechanical form factor for enclosure and a carrier board. The carrier board can host two iFDAQ XCKU cards in a 2U 19" enclosure and provides power, cooling and a small XILINX Artix7 FPGA for system management.

Read-Out Engines/Spill-buffer The read-out engines are common X86 servers equipped with commercially available XILINX Kintex Ultrascale PCIe cards to receive the data from the DAQ via optical links. The first performance tests demonstrate that it will be feasible to achieve 500 MB/s which is mostly limited by a disk I/O. The server verifies consistency of the data, provides diagnostics in case of errors and writes the data to local disk storage. The storage is a temporal location for the data to decouple the data taking from the Central Data Recording facilities. For a moment it is not envisaged to filter out data, therefore the full amount of data will be copied to the CDR. For a safe operation two days of storage are

required. This corresponds to ≈100 TB of disk space in each server. Although the total data rate scales with number of servers, the maximum sustained rate will be limited by the bandwidth of the optical link between the DAQ room and the CDR. We plan to increase the link bandwidth from 1 GB/s to 2 GB/s. Due to the duty cycle of the SPS, which is more than a factor of three larger than the spill length, the maximum allowed on-spill data rate can be three times higher, thus reach 6 GB/s.

5.3 Instrumentation for Proton Radius Measurement

The minimum setup of detectors for the Proton Radius Measurement and their general parameters are shown in Table 14. Additional detectors like pixel GEMs might possibly be included into the setup to increase the resolution of the spectrometer for the second data taking period.

Table 14: The first column shows the naming convention for the respective stations. The second column gives the active area per detector, while the third column specifies the coordinates measured by the detector. Column 4 and 5 gives the numbers of pixel/stripes. The columns of spacial and time resolution as well as noise represent typical values at standard COMPASS muon beam conditions. These numbers correspond to an average over all detectors of this kind in the experiment, and hence may include contributions from pile-up, magnetic fringe fields, or reconstruction inefficiencies. [42]

Station	Active Area /cm	Planes per det.	#Pixel per det.	#Stripes	Resolution	σ_t	Usage
BM01	6-12 x 9-23	Y		64	1.3-2.5 mm	0.3 ns	Beam Momentum Station
BM02	6-12 x 9-23	Y		64	1.3-2.5 mm	0.3 ns	Beam Momentum Station
BM03	6-12 x 9-23	Y		64	1.3-2.5 mm	0.3 ns	Beam Momentum Station
BM04	6-12 x 9-23	Y		64	1.3-2.5 mm	0.3 ns	Beam Momentum Station
BM05	12 x 16	Y		128	0.7 mm	0.5 ns	Beam Momentum Station
BM06	12 x 16	Y		128	0.4 mm	0.5 ns	Beam Momentum Station
PRMSi01	6 x 7.4	P1, P2	2.5M		23μm	≤20 ns	Tracking
PRMSi02	6 x 7.4	P1, P2	2.5M		23μm	≤20 ns	Tracking
PRMSi03	6 x 7.4	P1, P2	2.5M		23μm	≤20 ns	Tracking
PRMSi04	6 x 7.4	P1, P2	2.5M		23μm	≤20 ns	Tracking
PRMSciFi01	5 x 5	X1, X2, Y1, Y2		1000	100μm	<0.6 ns	Timing/Kink-Trigger/Lumi
PRMSciFi02	5 x 5	X1, X2, Y1, Y2		1000	100μm	<0.6 ns	Timing/Kink-Trigger/Lumi
PRMSciFi03	5 x 5	X1, X2, Y1, Y2		1000	100μm	<0.6 ns	Timing/Kink-Trigger
TPC	R=60	R1, R2, R3, R4	$128_{(pads)}$		0.4 cm	64 μs	Recoil Proton
SciFi01	3.9 x 3.9	X, Y		192	130μm	0.4 ns	BeamMonitoring/Lumi
SciFi05	8.4 x 8.4	X, Y		320	170μm	0.4 ns	Tracking SAS
SciFi55	6.8 x 12.3	U, V		192		0.4 ns	Tracking SAS
SciFi06	10.0 x 10.0	X, Y, U		462	210μm	0.4 ns	Tracking SAS
SciFi07	10.0 x 10.0	X, Y		286	210μm	0.4 ns	Tracking SAS
SciFi08	12.3 x 12.3	X, Y		352	210μm	0.4 ns	Tracking SAS
HI5	35.3 x 51	X		64	0.6cm	0.4,ns	μ-Identification
ECAL	10x10(cells)	1	100		cell size	≈ 1 ns	Photon detection
Total:			9830628	5380			

5.3.1 *The active-target Time Projection Chamber* v2(+)

Several versions of hydrogen TPCs have been developed at PNPI for various applications [196–198], including the experiments WA9 and NA8 at CERN for studies of small-angle πp and pp scattering at high energies. At present, a new high-pressure hydrogen TPC is under construction at PNPI for the above-mentioned recoil proton experiment at Mainz, which aims at a high-precision measurement of the proton charge radius in ep scattering [199]. The design of the new TPC for the programme proposed in this document follows closely the one of the Mainz experiment. This similarity will provide a virtually identical calibration of recoil energy with respect to Q^2 in both experiments. The main difference is the larger length of the active target region: while the Mainz version has one 400 mm drift cell, the new TPC proposed here will have four 400 mm drift cells.

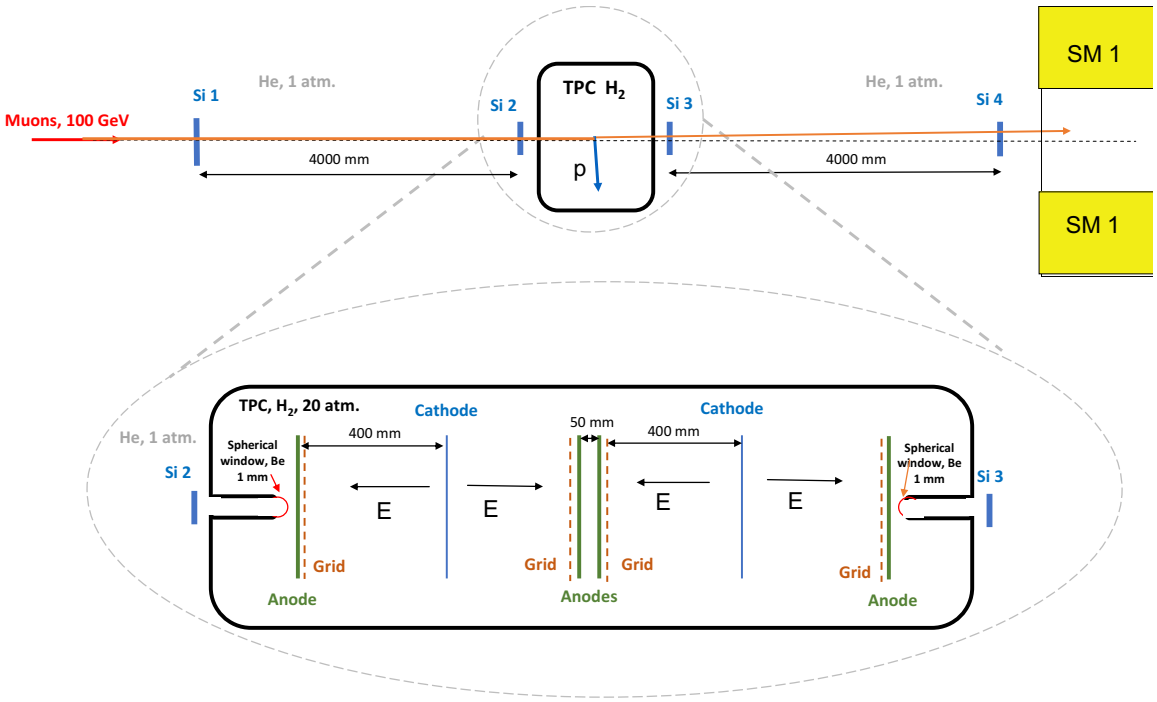

Figure 59: Schematic layout of the planned TPC with four drift cells. The TPC operates in ionisation chamber mode. The cathode grid space determines 400 mm drift zones.

A schematic view of the TPC is presented in Fig. 59. The main operating parameters of the TPC are given in Table 15. The TPC is operated in ionisation-chamber mode, *i.e.* no gas amplification. The cathode–grid distance of 400 mm determines the drift zone. The "active target" region is selected within the drift zone, in order to exclude wall effects. With the TPC, the recoil proton energy T_R, the recoil proton angle θ_R and the z-coordinate of the interaction point along the beam direction are measured.

Table 15: TPC operational parameters

cathode–grid distance (drift zone)	400.0 mm
grid–anode distance	10.0 mm
grid wire diameter	0.1 mm
grid wire spacing	1.0 mm
grid transparency	1.8%
anode outer diameter	600 mm
hydrogen pressure	20 bar and 4 bar
electric field in drift space E/P	0.116 kV/(cm bar)
electric field in grid–anode zone E/P	0.340 kV/(cm bar)
electron drift velocity in the drift zone	0.41 cm/μs
electron drift velocity in the grid–anode space	0.70 cm/μs

The TPC will be operated at two gas pressures, 20 bar and 4 bar, with respective maximal energy of protons stopped in the TPC sensitive volume of 10 MeV and 4 MeV. For protons with higher energies, both the energy deposited in the sensitive volume of the TPC is measured (e.g. about 5 MeV for a 20 MeV proton in 20 bar H_2) as well as the angle. In CH_4 gas at 20 bar, protons are stopped up to 22 MeV energy,

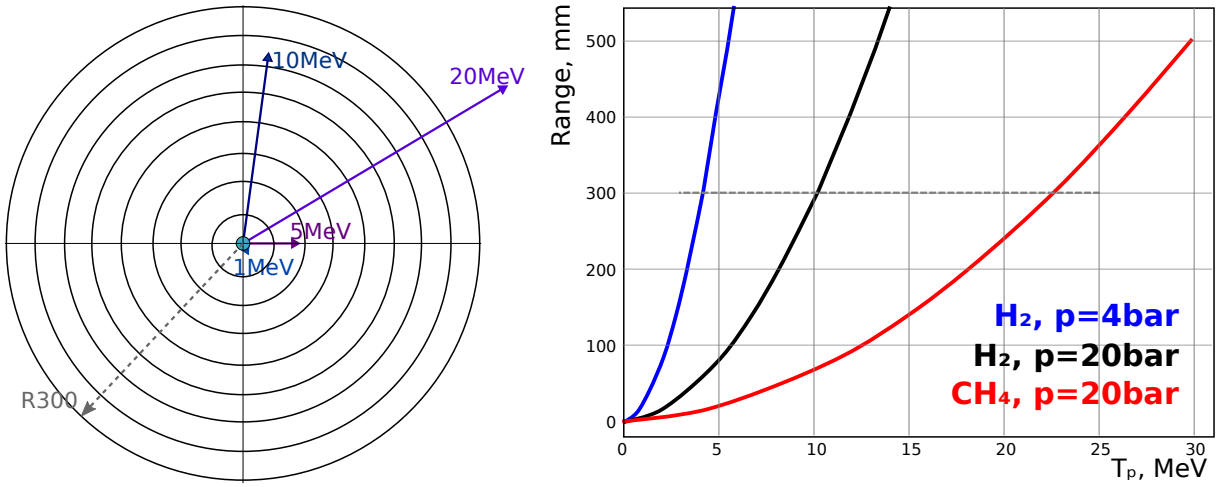

Figure 60: Left panel: TPC anode structure, consisting of a 10 mm diameter circle surrounded by 8 rings. Right panel: proton range vs. energy for H_2 gas at 4 bar and 20 bar and for CH_4 at 20 bar.

see Fig. 60.

In order to guarantee a H_2 purity to a level of $\leq$ 1 ppm, a permanently operating gas circulation and purification system is foreseen. The electric field in the drift zone and the pressure will be kept within 0.01% absolute precision. At the same time, the TPC temperature will be stabilised and measured with 0.015% absolute precision. Under these conditions, the proton density in the active target is known with 0.025% precision.

The electron drift velocity in the TPC will be determined with about 0.01% precision at the Mainz experiment, operating with identical condition in terms of electric field, pressure and temperature. Alternatively, it can be measured in the muon beam at EHN2 with a similar method as in the Mainz experiment. The target length will be measured with 0.02% systematic uncertainty, which allows to determine the number of protons in the effective target length with 0.045% absolute precision.

Resolution in the recoil proton energy E_R:

The anode read-out channels will be equipped with low-noise preamplifiers with noise at the level of 20 keV (sigma), giving the lower limit for the recoil proton energy resolution. Depending on the range of the proton, its energy is obtained by summing up the energies deposited in the respective anode rings. The noise adds up as well. Accordingly, the recoil proton energy varies from 20 to 60 keV, depending on the number of anode rings in which energy is deposited. In addition, noise produced by the beam needs to be taken into account. This reaches values of about 80 keV for 20 bar, as depicted in Fig. 61. Assuming a circular beam profile constraint to a diameter of 10 mm, only the signal of the innermost ring would be affected by this noise. For the muon beam in the M2 beam line, this noise will also be relevant for the outer rings, albeit on a lower level expected to be about 35 keV per ring at 2 MHz beam intensity.

Resolution in the vertex position Z_R:

The resolution of determining the recoil signal is expected to be 40 ns (sigma), assuming an outer time reference that is much more precise than this resolution. This corresponds to 160 μm resolution in the reconstruction of the vertex position along the beam, Z_R. The uncertainty introduced by fluctuations in the diffusion of the electrons has been studied in [200, 201] and amounts to about 380 μm (sigma) for the maximal drift length of 400 mm, which is still more precise than the expected resolution for the vertex from the muon scattering kinematics and thus can be neglected.

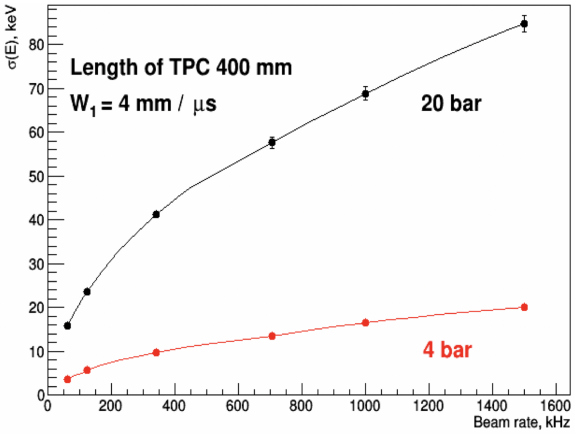

tb]

Figure 61: Noise due to ionisation by the beam muons as obtained from Monte Carlo simulations for different beam intensities.

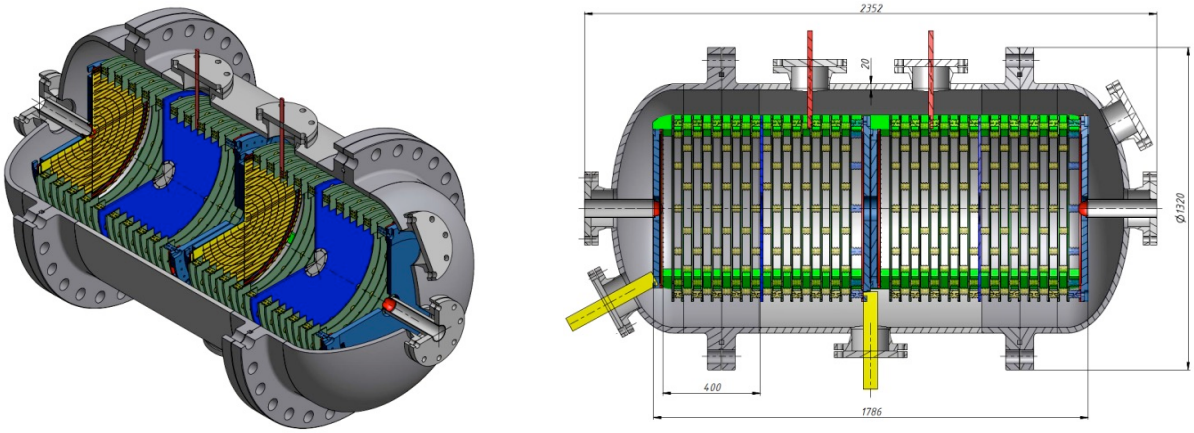

Figure 62: Engineering design for the four-cell hydrogen TPC.

Resolution of the recoil scattering angle:

The angle θ_R of the recoiling proton with respect to the direction perpendicular to the beam is approximately given by $\sin(\theta_R) = \sqrt{T_R/2M}$ and varies from 17 to 107 mrad in the Q^2 range from 0.001 to 0.04 GeV$^2/c^2$. This angle can be determined from the difference in the arrival times of the signals on the anode pads crossed by the proton. This is possible for sufficiently long tracks detected by at least two anode pads, so for $T_R > 4.5$ MeV at 20 bar and for $T_R > 2$ MeV at 4 bar pressure. The precision of this determination ranges from 10 mrad (sigma) for short tracks to 2 mrad (sigma) for long tracks. Coulomb scattering of the proton adds about 10 mrad (sigma) to this, such that the recoil angular resolution ranges from 11 to 15 mrad for proton ranges of 300 and 70 mm, respectively.

The engineering design of the four-cell hydrogen TPC is shown in Fig. 62.

5.3.2 TPC Read-out and Slow Control

The TPC detector is supposed to be read out using Flash Analogue Digital Converters (FADCs) and digital pulse shape analysis (PSA). It allows flexible trigger concepts, high rate capability and pile-up handling and, in addition, reduction the amount of cables and electronic elements such as splitters, delays and discriminators. Signal processing and noise suppression can be performed using energy and FFT filters. The read-out electronics of the TPC will consist of a front-end part (charge-sensitive preamplifiers and shaping amplifiers), the FADCs and a trigger/processing part. The charge-sensitive preamplifiers and shaping amplifiers can be similar to those designed at the Petersburg Nuclear Physics Institute (PNPI)

and used during test experiment at COMPASS in 2018. The input stage of each preamplifier is based on a N-channel JFET transistor, an amplification stage is made using a low-noise operational amplifiers. The gain of the amplifiers is adjustable to suit the signals, so a large dynamic range (≈100) can be covered. The energy resolution of the amplification part reaches 15 keV (at a realistic input capacity of 20 pF). FADCs are VME digitizers, model SIS3316 from Struck Innovative Systeme GmbH. Most important parameters are:

1. 250 MSPS per channel (simultaneous sampling),
2. 14-bit resolution,
3. 64 MSamples memory/channel,
4. Offset DACs,
5. Internal/External clock,
6. Multi event mode,
7. Double memory banks allowing for dead-time free operation,
8. Readout in parallel to acquisition,
9. Internal trigger generation,
10. SFP cage (Gigabit Ethernet or Multi-Gigabit optical link connection).

All modules can run synchronously using an internal or external clock. Using oversampling, several consecutive data points can be averaged reducing the noise influence. Each FADC is equipped with a FPGA able to generate individual triggers using Moving Average Window (MAW) and Constant Fraction Discriminator (CFD) algorithms. The FPGA firmware can perform full signal processing that reduces the data size drastically; raw data can be saved in parallel. A common OR signal of individual triggers of each FADC will be connected to the logic VME module with FPGA. This module can process triggers coming from other subsystems (Start detector, Tracking System, SciFi detector) and generate a trigger decision for the whole TPC system. During test experiment in 2018, a capability of independent trigger generation has been demonstrated. RIO4 VME processor, a TRIDI1 trigger module, are additional modules proposed for the TPC DAQ system. A time-stamp based event synchronisation with other subsystems of the experiment using a White Rabbit protocol or simplified version (used during test experiment in 2018) is foreseen. The TPC detector, in comparison to other systems (tracking system, SciFi) is slower because of its nature. Physical event can happen almost immediately after the muon passes through the detector or after a maximum time defined by the drift time of electrons. To enable the TPC detector to trigger independently and not to block the other systems, the data from the various sub detectors will not be assembled to multi-detector physics events before storage or processed in a real time using dedicated processor farm.

In addition to the main read-out solution described above, an alternative solution with a better spatial resolution is investigated to equip the central part of the read-out planes, close to the beam. This solution would employ an anode plane which would collect the primary ionisation electrons on a large number of small pads on the central area, with a typical pitch of 5 mm. The purpose of this high spatial resolution measurement would be to determine with a good precision at the millimetre level the lateral position of the vertex as well as the distance travelled by the recoil protons. The measurement of this distance would bring an independent access to the proton momentum compared to the measurement of the number of primary electrons deposited by the proton, thus improving the determination of its momentum, in particular at low Q^2.

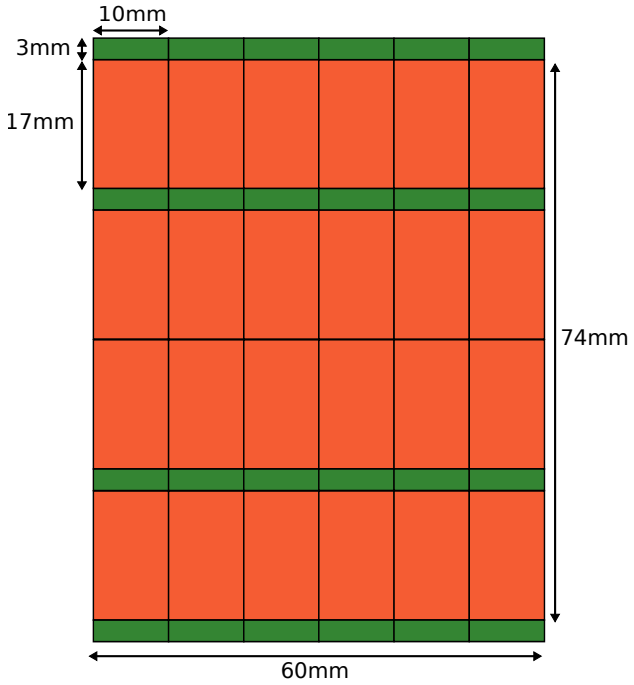

Figure 63: Layout of one MuPix8 station: The active pixel area of each sensor is shown in orange and the digital section in green. 24 individual sensors are arranged in a matrix of 6×4 sensors in order to cover an area of $60 \times 74\text{mm}^2$. To avoid dead areas due to the digital section of the chip, a second plane, shifted by 3 mm in vertical direction, can be added.

The large concentration of read-out pads would be read by IDeF-X ASICs, which are very low-noise front-end chips developed for solid detector read-out [202] and adapted for primary electron read-out in liquid Xenon [203]. The bare chips would be mounted and bonded on the backside of the read-out plane, and would preamplify signals from 32 pads per chip before to transmit them through flat cables to a shaping and digitizing electronics. This electronics would be built upon VMM [204] or SAMPA [205] chips which have triggerless capabilities and thus would be compatible with the triggerless data acquisition system described in the Sec. 5.2.4. The size of the IDeF-X LXE chip is very limited, 6.4x2.8 mm^2 with a thickness around 1 mm, the impact on the scattered particle will be limited, with an average radiation length at the level of 0.02% X_0.

Research and development is presently worked on at CEA Saclay IRFU to validate such a very low-noise read-out electronics based on the IDeF-X LXE chip. Electronics noise at the level of 100 electrons per channel are aimed, by combining the IDeF-X chips with small low capacitance pads and high-voltage focusing strips on the read-out plane. Noise level and detection performance of this read-out scheme will be evaluated before to study the application to the TPC read-out.

The ionisation chamber needs a constant monitoring of operation parameters. An EPICS-based slow control program for reading out the temperature, pressure, current and setting and reading of HV will be used. This program is running on a dedicated computer allowing controlling all parameters with 0.01% precision required for the experiment. The use of EPICS provides also a possibility of monitoring the parameters via the campus network and sending alarms in critical cases. There is an established way to have the EPICS slow control data correlated to the physical events (data recorded by the DAQ). It will provide a possibility to correct data measured by the TPC due to the change, for example, of gas pressure or temperature.

5.3.3 *Pixelized Silicon Tracking Stations*

In order to provide a good resolution in terms of scattering angle and vertex position, silicon-pixel tracking stations will be used. We will use the MuPix10 chip, which is being developed by the Karlsruhe Institute of Technology group for the Mu3e experiment. Future versions of the chip are being evaluated, but the final design is not yet fully decided. Here we will describe the setup in terms of the already available MuPix8 sensor [206]. In general, the MuPix sensors are monolithic silicon-pixel detectors [207] with a pixel size of $80 \times 81\ \mu m^2$. The detector has integrated front-end electronics, which allow to digitise the signals directly on the sensor and send out the received hits via a high-speed serial link operated at 1.6 Gbit/s.

The MuPix8 detector is arranged in a matrix of 128×200 pixel covering an active area of $1 \times 1.7\ cm^2$. The digital part of the sensor is placed below the matrix in vertical direction and has a width of approximately 3 mm. In order to cover a larger active area, several sensors have to be stacked, see Fig. 63. This may be done by gluing the sensors in one layer. Since the digital part of the sensor causes two dead areas of $60 \times 3 mm^2$, a second plane has to be added with a shift in vertical direction to compensating for this dead area. An additional shift in both coordinates can compensate for inefficiencies at the joint. One silicon station will consist of 4 detector planes with 24 individual sensors, resulting in a total of 2.5×10^6 pixels.

A test beam campaign [208] has proven the excellent performance of MuPix8 sensors. 99% efficiency with an equivalent threshold level of 600 electrons and corresponding noise count rate of 1 Hz/pixel were achieved. The time resolution was measured to be less than 20 ns. The minimal spatial resolution of the sensor was 23 µm. This can be improved by using amplitude information and charge sharing between individual pixels. In addition, the use of four detector planes per station will further improve the spatial resolution.

Currently, a prototype system from the KIT group is used for first tests, to evaluate the handling of the system and to measure first characteristics using a ^{55}Fe source. In parallel the system is used for the development of the firmware, which will be compatible with the DAQ discussed in Sec. 5.2.4. The read-out is foreseen to utilise an ARTIX-7 FPGA, which will be connected via its high-speed links to the detector and further processes the data. The control of the pixel detector will be done via the Ethernet-based IPBus interface [209].

Four stations of these detectors will have in total 10 Million pixels. The data rate of the detector can be estimated from noise rate, beam rate and averaged cluster size. For a beam of $2 \cdot 10^6$/s about 200 MB/s are expected. The data rate and number of serial links suggests to read one plane of the detector by four ARTIX-7 FPGA cards similar to those, which are used for iFTDC. Four stations will be read out by 64 FPGA cards. The control of the pixel detector will be done via Ethernet based IPBUS interface.

5.3.4 *SciFi Tracker Stations*

It is planned to build three SciFi Tracker Stations to gather trigger, luminosity and timing information. Each detector consists of four layers of scintillating-plastic fibres with a 200-μm square cross section (Kuraray SCSF-78[3]). Two layers are oriented in x-direction and two in y-direction. In both orientations the layers are shifted by 100 μm relative to each other to increase the detection efficiency. The relative shift also increases the tracking resolution (pixel size) from $200 \times 200\ \mu m^2$ to $100 \times 100\ \mu m^2$ in the best case. Each layer consists of 250 fibres, resulting in an overlap region of $5 \times 5\ cm^2$ that can be used for tracking (compared to an active area of $6 \times 7.4\ cm^2$ for the silicon trackers) and in a total of 1000 fibers per detector. If required, the tracking area of the last detector can be easily enlarged by scaling up the layer sizes, to increase the range of Q^2-values that the trigger is sensitive to.

[3] https://www.kuraray.com/products/psf

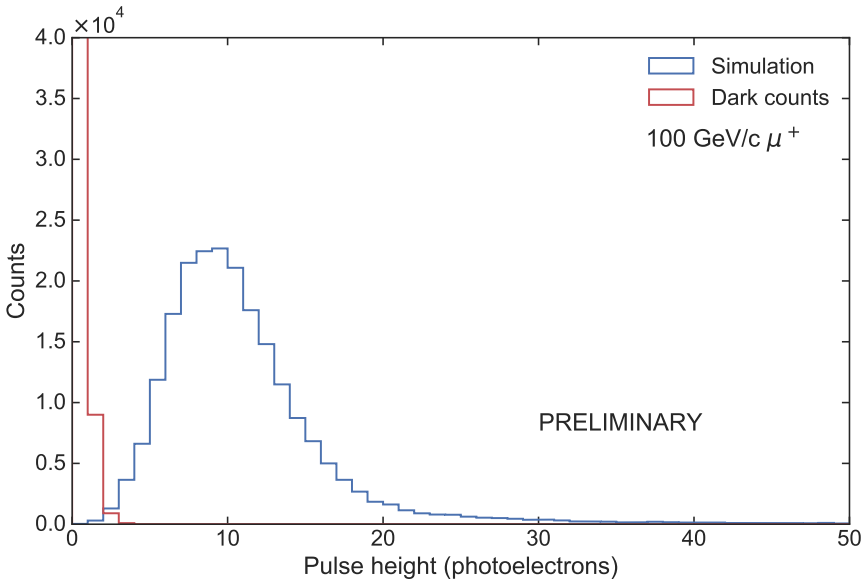

Figure 64: Simulated pulse-height spectrum (blue) for 100-GeV/c muons in a 200-μm scintillating-plastic fiber, generated with a simulation framework tuned to reproduce experimental data. Also shown is the dark-count spectrum of a KETEK PM1125-WB SiPM at room temperature (red).

Each scintillating fibre is coupled to individual silicon photomultipliers (SiPMs) on both ends, giving a total of 2000 channels per detector. The SiPM signals are read out by NINO ASICs, ultra-fast amplifier-discriminators that were originally developed for the ALICE time-of-flight detector [210], and digitized by FPGA-based time-to-digital converters (iFTDC, see Sec. 5.2.4.3 for details).

The design of the new SciFi detectors builds on experience we obtained from developing several other scintillator detectors. For most of them we used the same type of scintillating-plastic fibres that we plan to use for the new detectors, but with a 2-mm square cross section. We also used the same type of SiPM on multiple occasions, mostly with an active area of $3 \times 3\,\mathrm{mm}^2$. We performed several measurements with a 450-MeV/c pion beam at the πM1 beam line at Paul Scherrer Institute to characterise the materials and components of the detectors. We use this extensive data set to calibrate our GEANT4-based simulation framework.

A challenge in using 200-μm fibres is the low light output of such thin scintillators. Here light yield of 8000 photons per MeV deposited energy is assumed for all calculations and simulations. Using data from measurements with low-energy protons that are stopped in a detector made from SCSF-78 fibres, we calculated that about 200 photons reach a SiPM at the end of 2-mm fibre with a length of about 10 cm. This corresponds to an energy deposition of 0.4 MeV for a minimum-ionising particle. The simulation framework was tuned to reproduce this measurement and to calculate the expected light output for 200-μm fibres. For the proposed detectors, minimum-ionising particles generate about 350 photons in a single fibre, of which 20 to 30 reach a SiPM at either end of a straight fibre. Taking into account the photodetection efficiency of the SiPM, this translates into 12 photoelectrons on average (with a most probable value of 10 photoelectrons) for 100-GeV/c muons. Some of the fibres in the proposed detectors will have to be curved; for these, we expect an average of 6 photoelectrons.

To suppress the intrinsic thermally induced noise of the SiPMs (*dark counts*; in the order of 100 kHz at room temperature for the KETEK PM1125-WB[4], which would be a suitable candidate for this experiment). The two read-out channels of each fibre must cross the discriminator threshold in coincidence in order

[4]https://www.ketek.net/sipm/sipm-products/wb-series/

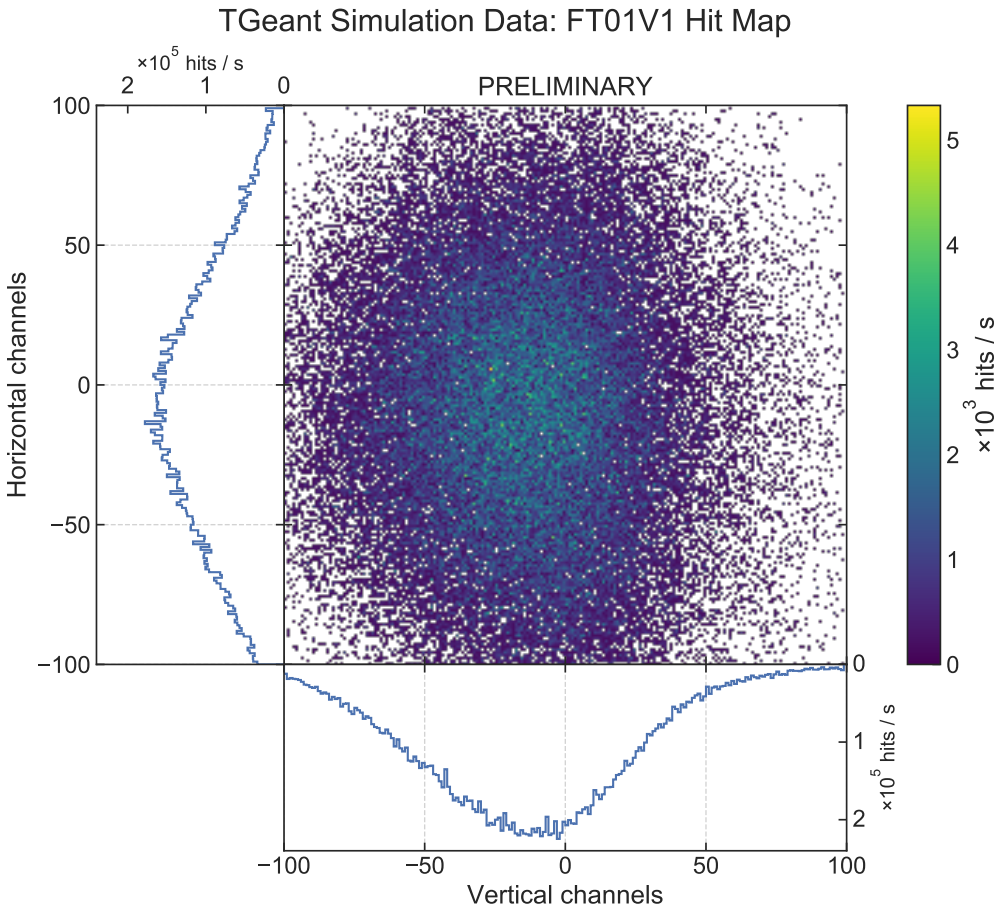

Figure 65: Hit map of one SciFi tracking layer (one vertical layer, one horizontal layer) with a pixel size of $200 \times 200\,\mu\text{m}^2$, simulated with TGeant. Each detector consists of two tracking layers shifted by $100\,\mu$m in each direction relative to each other.

to register as a hit. For this configuration, a discriminator threshold corresponding to 1.5 photoelectrons yields a calculated reduction of the noise rate to about 10 to 100 Hz per fibre. The noise rate could be reduced even further by cooling the detectors: operating them at 0° C or -40° C would lower the rate to 20 kHz or 1 kHz, respectively. The design of a cooling system capable of achieving such temperatures would be straightforward.

Figure 65 shows a hit map of one tracking layer, consisting of one vertical and one horizontal layer with a resulting pixel size of $200 \times 200\,\mu\text{m}^2$. Each SciFi detector consists of two such tracking layers, shifted by $100\,\mu$m in each direction relative to each other (see above). This map was generated from data generated with a TGeant simulation of the relevant sections of the Compass spectrometer with beam parameters appropriate for the proton-radius measurement.

5.3.5 Beam Momentum Station

The six stations of the Beam Momentum System have a total number of 512 channels. The system is used since many years in the Compass experiment and shows a stable behaviour. Therefore we plan to keep the current front-end electronics in form of discriminators and only exchange the current F1-TDC read-out by the new iFTDC development with the firmware for 32 channels and a bin width of 0.2 ns to make the detector system compatible with the continuous DAQ. A total number of 16 iFTDC cards is needed.

5.3.6 *COMPASS SciFis*

The 6 stations of the SciFi detectors have in total 1804 channels. The discriminators are the same as used in the BMS and have a good performance. Therefore we plan to only exchange the currently used F1-TDC by the new ones to make them ready for the streaming read-out. The time resolution of these detectors will make the use of the 32 ch 200 ps/bin iFTDC firmware necessary. To cover the 1800 channels 60 iFTDC cards are necessary.

5.3.7 *Hodoscope*

The 64 channels of the Inner5 hodoscope, which is used for muon identification behind an iron absorber at the end of the setup, are equipped with a single read-out photo-multiplier per channel. The analogue signals are discriminated by a NINO front-end [210] and digitized by two iFTDC in 200 ps/bin mode with 32 channels each.

5.3.8 *DAQ/Trigger for Proton Radius Measurement*

The measurement of the proton radius will be split into two data taking periods. The first one will use a beam intensity of $2 \cdot 10^6$/s. In the second period we aim to increase the beam intensity according to the experience with the first data taking period to a maximum of $2 \cdot 10^7$/s. The rather low beam intensity of the first data taking period enables us to run the DAQ in the completely not-triggered mode and save all data to disk for further offline analysis. This will allow us to debug and validate the new approach of the continuous iFDAQ and the new trigger system without losing any physics data. For the higher beam intensity of the second data taking period, a fully working trigger system is mandatory to reduce the amount of recorded data to a level, which can be stored and analysed with a reasonable offline computation power.

In order to estimate the data rate we take into account the number of stations and planes, the noise figure as well as the cluster size per detector, the protocol overhead, the sample size per hit and we assume that all detectors are hit by the full beam flux. The parameters for the different detector subsystems are shown in Table 16. The time-slice length is 128 μs and each hit-data-word has 4 bytes. Figure 66 shows

Table 16: Parameters as input for the bandwidth calculations for each detector subsystem. (*) Main noise contribution already included as MIPS beam particle signals ($2 \cdot 10^6$).

Det. subsystem	# of Stations	Total # of Views	Image length	Cluster Size	Noise	# DWords per hit
TPC	1	4	64 μs	2	(*)	26
PRMFIBER	3	12	128 ns	2	100 Hz/ch	1
Silicons	4	16	128 ns	1.2	$\leq$1 Hz/ch	1
FIBER	6	13	128 ns	2.8	60 Hz/ch	1
BMS	6	6	128 ns	2	60 Hz/ch	1
Hodoscopes	1	1	128 ns	2	120 Hz/ch	1
ECAL	1	1	256 ns	12	100 Hz/ch	17

the data rate per detector subsystem as function of the beam intensity per second for the range of beam intensities that will be used for this measurement. For the lower beam intensity we expect a data rate of 14.4 GB/spill (4.8 s), which is a very conservative estimate. The distribution for the different detector sub-systems is shown in Fig. 68.

To estimate the necessary storage we assume approximately 500k spills in 200 days of data-taking, as was delivered in 2018. This results in an average number of about 2500 spills per day. This number is used to extrapolate to the total size of collected data for the Proton Radius Measurement as a function of beam days as shown in Fig. 67. For the whole year, including the commissioning time and assuming 100% efficiency of the experiment, we end up with 7.1 PB of data as an upper limit (Fig. 67 blue curve).

This is about four times the data as were collected in previous COMPASS runs (e.g. 2018) and only requires a factor of four more computation power for storage and offline analysis, which is feasible. To

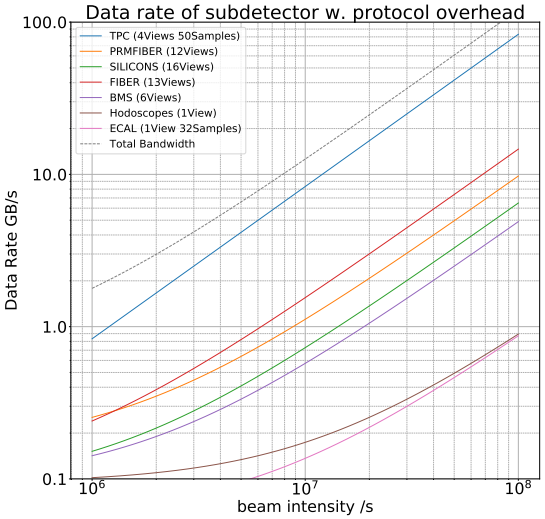

Figure 66: Prediction of bandwidth requirements per detector sub system (conservative cluster size)

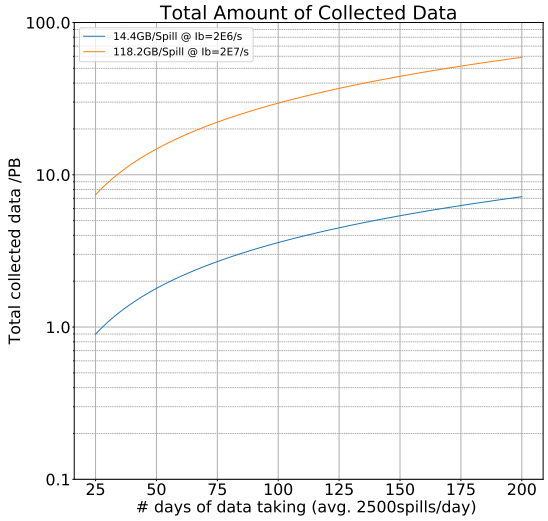

Figure 67: Expected storage needs for an average spill delivery of 2500 spills/day for different beam intensities

estimate the necessary bandwidth between the experiment location and the central storage as well as the amount of local storage needed to store at least the data of one day locally, we will assume a maximum of 4000 spills/day. This is the highest number of spills delivered at one day during the 2018 COMPASS data taking under the best super cycle conditions. The maximum amount of data per day is about 58 TB. This data will be stored locally on disk on the read-out engines and will be then transferred to the central storage. Each read-out engine is equipped with a local storage of 120 TB, thus enabling us to run for at least 2 days even in the case of issues with the connection or service of the central storage. To transfer this amount of data to the central storage an up-link capacity of about 6 Gbit/s(sustained) is needed.

For the case of a beam intensity of $2 \cdot 10^7$/s a total on-spill data rate of 118.2 GB/spill is obtained, which sums up to about 60 PB for the whole year. This shows that for the second period of data taking we have to reduce the amount of data, which we want to store to disk by a factor of 5 to 10. This can be done with a digital trigger system, which uses the information on the incoming and scattered muon in order to select elastic events. This so called kink-trigger system is described in Sec. 5.3.9.

5.3.9 PRM elastic-muon trigger system

To deal with the high beam rate, a trigger system is needed to select events with Q^2-values in the region of interest (see Sec. 2.5 for a discussion of the region of interest and Sec. 2.7 for a discussion of the uncertainties introduced by multiple scattering). It consists of the three SciFi tracking detectors (see Sec. 5.3.4), two placed upstream of the TPC and one downstream. We use the hit information of the two upstream detectors to calculate the track parameter of the incident muon in real time. The hit information of the third detector is then used to decide whether a muon was scattered in the TPC gas (or some other material) or not and can be used as a trigger.

As presented in the general description of the new DAQ framework (see Sec. 5.2.4.1), the data streams of these detectors are duplicated at the level of the multiplexer and sent to the digital trigger system for real-time analysis. The event generator searches for coincidence of hits in time and builds events of interest (EOI). These EOI are sent to the first trigger processor unit, which does clustering and space-point extraction. From this information, the track parameters of the incoming and outgoing tracks are

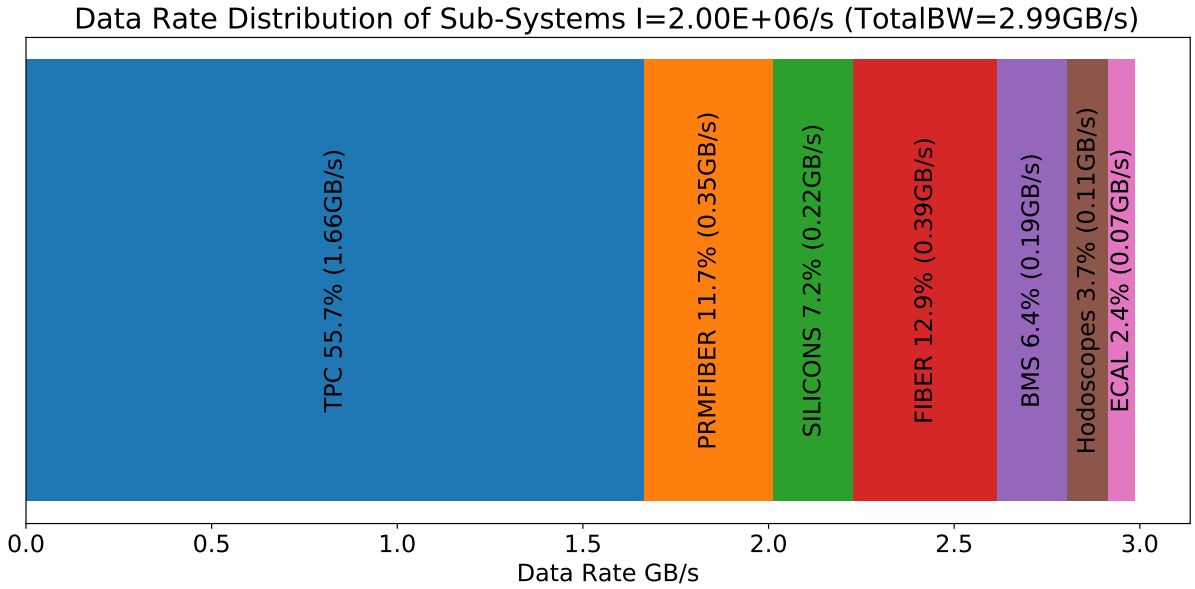

Figure 68: Distribution of data rate for different detector systems for an beam intensity of 2E6.

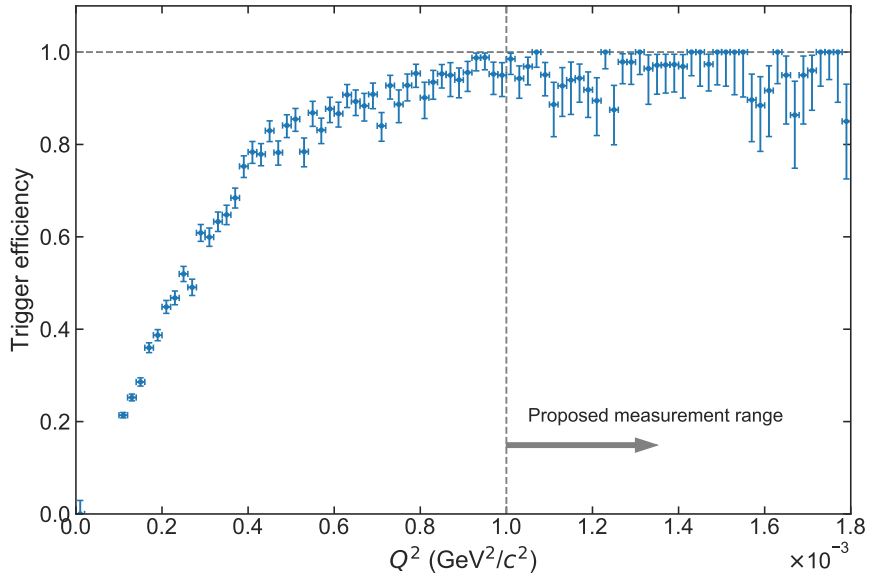

Figure 69: Predicted efficiency of the elastic-muon trigger for the proton radius measurement, which is about 97 % for the proposed measurement range ($0.001 < Q^2/(\mathrm{GeV}^2/c^2) < 0.04$). The increased uncertainties at larger Q^2-values are due to the limited size of the data set at the moment used for this graph.

determined. Several algorithms are under investigation to determine the scattering angle and therefore the Q^2-value of the event to do the trigger decision.

Figure 69 shows the Q^2-dependent trigger efficiency for an exemplary algorithm: Using the hit information of the two upstream SciFi detectors, the hit point of a muon in the downstream detector is predicted. The minimal distance (in the detector plane) between this predicted point and the true hit point is a measure of the scattering angle (and thus of the Q^2-value) and can be used to select events in the region of interest. For the measurement range we propose ($Q^2 > 1 \cdot 10^{-3}\,\mathrm{GeV}^2/\mathrm{c}^2$), simulation data shows that a trigger efficiency of about 97% with a background rejection of better than 96.5% can be achieved.

5.4 Instrumentation for Drell-Yan

5.4.1 Radiation environment [v2(new)]

The EHN2 hall being a surface experimental area, a study of the radiation dose inside and in the vicinity of the building must be performed to design an appropriate shielding of the target region to:

- Satisfy the limits for radio-protections
- Evaluate the radiation hardness required for the detectors
- Optimise the beam intensity

As it was done in previous Drell-Yan experiments, a hadron absorber will be installed downstream of the target to reduce the high secondary particle flux produced by the interaction of the pion beam in the target and absorb the non-interacting beam. The absorber considered in the current setup is identical to that used by COMPASS [211]. It maximises the number of interaction lengths crossed by the produced hadrons, while minimising the number of radiation lengths to keep the energy loss and the multiple scattering of the Drell-Yan muons as small as possible. In order to keep the environmental radiation dose within safe limits, the absorber is surrounded with a concrete shielding of 2 m thickness. The dominant contribution to the dose recorded in the EHN2 building and its vicinity during the COMPASS Drell-Yan Runs was coming from neutrons emitted upstream of the absorber and towards the sky [212, 213]. In order to address this issue, the target area will be embedded in a concrete bunker 2 m thick on the sides, 1.6 m thick on the top and on the bottom, and 3 m long. FLUKA simulations [214, 215] [216] were performed with this configuration, to assess the radiation environment inside and outside the experimental hall, as illustrated in Fig. 70. For safety purposes, we assume here a more favourable SPS super cycle of 4,000 spills/day and an intensity larger by 10% than the one considered in the evaluation of the projections presented in Sec. 3. In any case, the equivalent dose is found to be below the radiation protection limits inside the building, as well as outside. The equivalent dose at the ceiling of the building can be further decreased by reducing the opening of the bunker to the size of the beam spot. Outside of the building, the equivalent dose is also found well below the limits for radio-protection in a non-designated area of 2.5 μSv/hour, or equivalently 1 mSv/year.

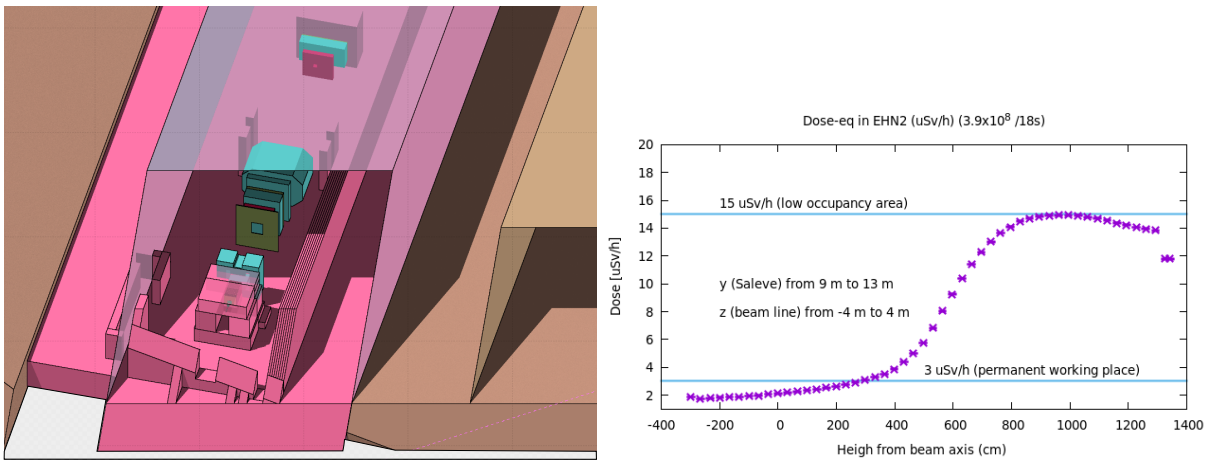

Figure 70: Left: Solid view of the concrete shielding around the target. Right: Equivalent dose as a function of height, behind the protection wall and at the location of the target. The building is classified as a low-occupancy supervised area, which imposes a limit for radio-protection of 15 μSv/h.

Vertex detectors will be located inside the bunker between the target and the absorber. It corresponds to the hottest point in terms of radiation. In order to identify the appropriate technology and ensure the life

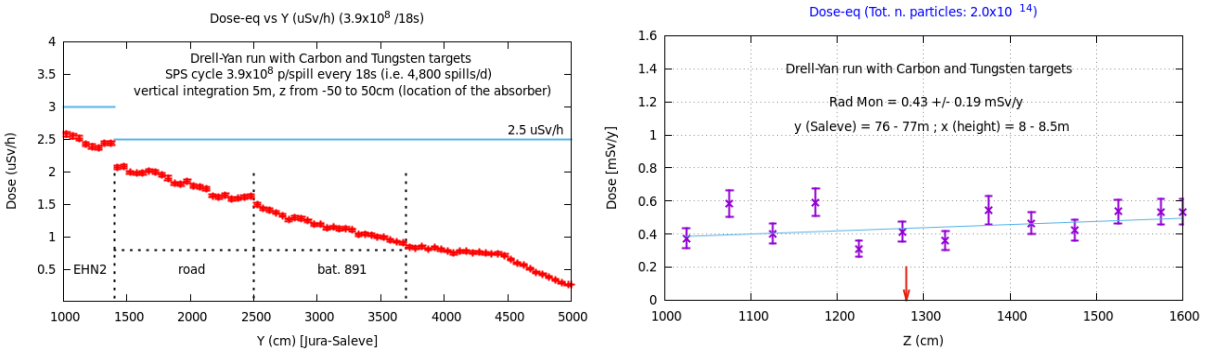

Figure 71: Left: Equivalent dose as a function of the distance to the experimental hall. Right: Equivalent dose at the fence of CERN.

expectancy of the detector over the data-taking campaign, the radiation level was evaluated with FLUKA simulations. The distribution of the 1 MeV neutron-equivalent fluence is shown in Fig. 72.

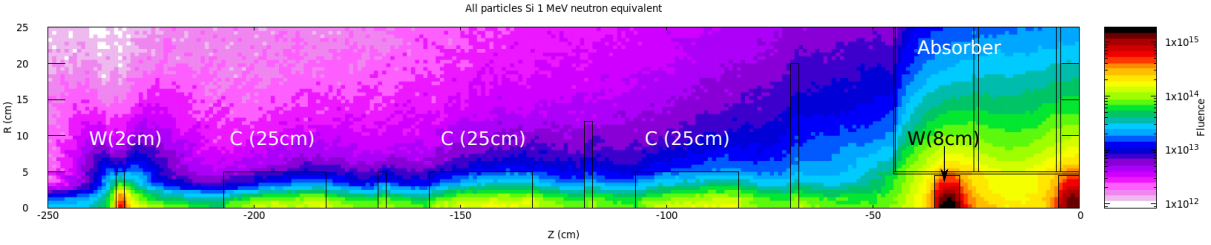

Figure 72: 1 MeV neutron-equivalent fluence (1 MeV $n_{eq}\,cm^{-2}$) in the target location for an integrated beam intensity of 40×10^{13} particles. Z is along the beam axis and R corresponds to the radius around the beam-axis. The three considered locations for the vertex detectors are at Z equals -170, -120 and -70 cm.

The projections along the beam axis and along the radius around the beam axis are shown in Fig. 73. The 1 MeV neutron-equivalent fluence for 40×10^{13} beam particles (*i.e.* two years of Drell-Yan data taking) is at the level of 10^{13}cm^{-2} and decreases rapidly with the distance to the beam axis. Despite the hostile environment, the dose is not incompatible with Silicon technology [217, 218].

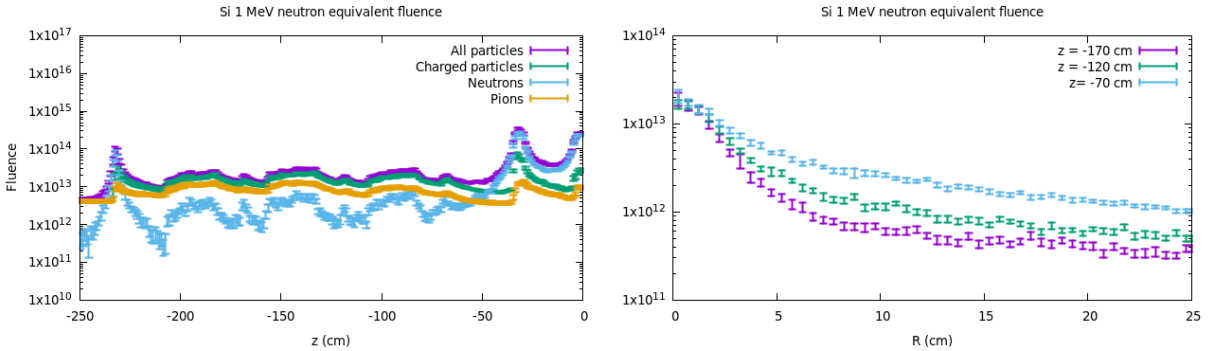

Figure 73: 1 MeV neutron-equivalent fluence (1 MeV $n_{eq}\,cm^{-2}$) along the beam axis (R=0) and separated by particle species on the left, and as a function of the radius to the beam axis at three different Z locations for all particles on the right.

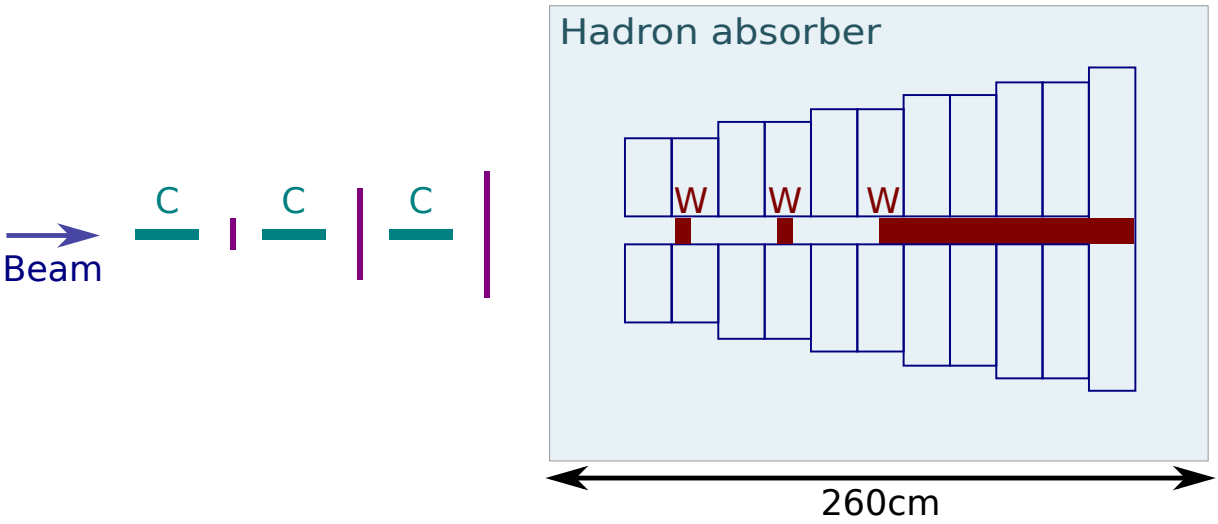

Figure 74: Conceptual representation of the Drell-Yan target system, showing the three 25 cm carbon sections interspersed with tracking detector planes, followed by the two 6 cm tungsten targets and the tungsten plug inside the hadron absorber.

5.4.2 Target and tracking [v2(+)]

For the new experiment, a segmented target consisting of carbon – as a light isoscalar material advantageous for the measurement of pion sea-valence separation – and tungsten – for the nuclear-dependence studies – is proposed. One of the studied configurations for the target region consists of three carbon sections, each 25 cm long ($0.48\lambda_\pi$) followed downstream by two sections on tungsten, each 6 cm long ($0.53\lambda_\pi$). Although estimates and simulation results included in this proposal correspond to that configuration, other possibilities are being studied, like the possibility of having a very thin (2 cm) tungsten section at the most upstream position. The overall target length is restricted on both the upstream and downstream ends. As the target length extends further upstream, the acceptance for Drell-Yan event decreases, becoming kinematically more restrictive. On the downstream side, it must remain in front of absorber and first magnet.

Because multiple scattering and energy loss of the muons in both target material and the absorber material further downstream of the target degrade the kinematic resolution, active tracking planes will be placed between the target and the hadron absorber. A schematic view of this target is shown in Fig. 74. Three to five stations of four projective planes each are being considered, with increasing transverse dimension from 10×10 to 40×40 cm^2. This scheme would allow the reconstruction of tracklets with minimal multiple scattering distortion. Preliminary tests have shown good bridging efficiency of these with the spectrometer tracks.

Additionally, small beam counter detectors in between the target sections are also being studied, as an option that would allow a precise control over the beam flux crossing and the constrained vertex search along the beam line.

As noted earlier in Sec. 3, the improved mass resolution from the target tracking planes reduces the charmonia resonance tails, that extend less into the Drell-Yan signal region. This improvement has important impact in the achievable statistics (see Table 7.)

There are several technologies that the COMPASS++/AMBER collaboration is exploring for use as the target-region tracking planes. Leading technologies for these trackers include scintillating fibres, Micromegas, and pixel sensors based on, for example, the ALPIDE chip [217]. The key criteria being used to evaluate these technologies include the ability to handle high rates, overall robustness (in particular radiation hardness), resolution, and cost. The specific values that each of these criteria need to meet is still being

studied by the collaboration, so that no definitive choice of technology can be made at this time. Rate estimates will be based on existing COMPASS data and Monte Carlo with the new AMBER configuration. For an order of magnitude estimate, consider the Micromegas detectors used in COMPASS in 2008-2009 [187]. At that time, for the strips near the central dead spot (beam axis) a rate of 100 kHz was measured on a 0.36 mm wide strip for a 5.5 % nuclear interaction length (λ) target running with 1/16 of the proposed AMBER beam intensity of O(50-100) MHz/mm/λ. Note that this estimate is for a *strip* and not a pixel detector, but it is clear that any strip-based detector near the beam region must be extremely narrow.

5.4.3 Trigger and DAQ for Drell-Yan

For the Drell-Yan measurement identification of the outgoing dimuon pair is necessary to select events of interest. The COMPASS muon hodoscope trigger system will be partly reused for this purpose. It consists out of several subsystems for different kinematic ranges. Each trigger subsystem is made out of two or more plastic scintillator hodoscopes with horizontal slabs. The use of horizontal slabs allows for target pointing in the non-bending (vertical) plane. Each slab has a double sided read-out by photomultipliers. To perform muon selection one of the hodoscope, of each sub system, is placed after an absorber. A coincident hit in time in both detectors signals a muon track. It is planned to reuse the Middle, Outer and LAS trigger hodoscopes (see Fig. 31).
From the experience of past Drell-Yan runs at COMPASS the main objective for the trigger and DAQ for future DY data taking is to reduce the Veto and DAQ dead time and to improve the efficiency of the LAS H1 trigger hodoscope. The implementation of the new Drell-Yan dimuon trigger will be done in the framework of the new continuous iFDAQ (see Sec. 5.2.4).

Digital dimuon Trigger

In order to take full advantage of the high-rate-capable streaming approach, all detectors, which participate in the measurement, must be equipped with continuous read-out enabled front-ends to eliminate DAQ dead time. The number of detector planes, as well as the beam intensity, result in huge data rate for a DY experiment, which make it difficult to achieve a full trigger-less approach where everything is directly written to disk with no data reduction at all. The limiting factors are the bandwidth of the uplink to the central storage system, the needed storage capacity and the computation power needed to process the data offline to get physics results. Therefore the function of the analogue trigger logic, as it was used in previous DY measurements, has to be implemented into the new digital trigger processors architecture.
In order to accomplish this, a multi-stage trigger architecture is foreseen (see Fig. 75). All data streams of the detectors, which participate in the trigger decision, are duplicated on the level of the multiplexer and sent to the trigger processor. The first stage (L0) of the trigger processor performs the T0 correction of the hit time, sorts the incoming data from different front-ends in time and forms the events of interest by grouping coincident-in-time hits. These events of interest are then sent to the second trigger processor stage (L1). This stage uses the geometrical information of the trigger elements to perform target pointing of the selected tracks. It requires that the tracks originate in the target region by checking the combination of hits in the hodoscopes of a trigger subsystem. The muon candidate tracklets are then sent to the third stage (L2) with a rate in the order of 650 kHz, in which the track multiplicity of the single events is calculated. If a track multiplicity greater than two in the LAS subsystem or a track multiplicity greater than one for at least two subsystems is found, a signal is sent via TCS to the data concentrators to select the images in the buffer, which belong to the trigger and save them to disk. The output rate of this stage is expected to be in the order of 100 kHz. The selected data is saved to disk for physics analysis. Possible further high level trigger stages, which could utilise information from more (tracking) detectors, could be daisy chained to purify the selected sample further for physics analysis by tagging the images with additional trigger information. The COMPASS dimuon triggers included an anticoincidence signal from the veto hodoscopes system at the output of the target pointing matrices, in order to suppress the beam halo. Test measurements during the 2018 Drell-Yan data taking showed that the dimuon trigger system

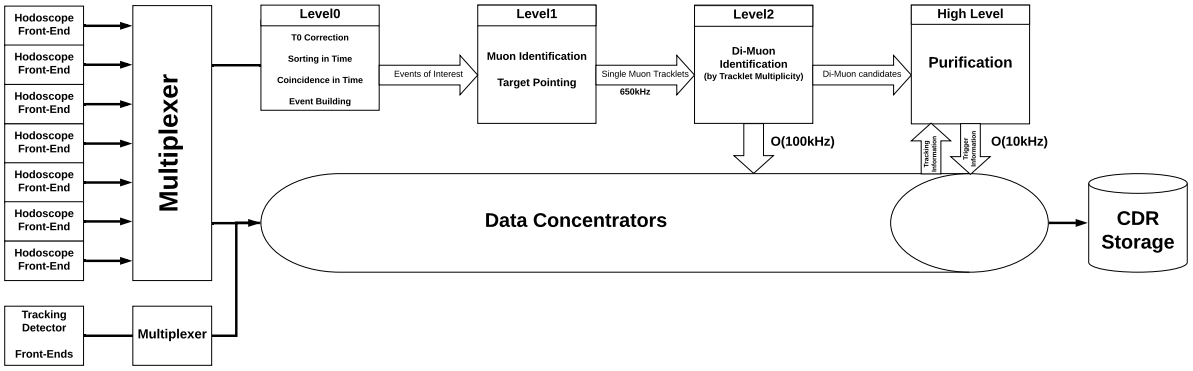

Figure 75: Scheme of the multi-level trigger for Drell-yan

is able to suppress the halo component of the beam by a factor of 3 to 7 with respect to the single muon triggers without using any veto information leading to a typical trigger rate of 100 kHz (see Table 17) for all dimuon triggers. The design of the new DAQ architecture is able to process this data rate.

Table 17: Measurements of physics trigger rates for different veto conditions, from 2018 Drell-Yan run at nominal beam intensity.

Trigger	w. Veto /kHz	w/o. Veto /kHz
LAS	98.3	333.4
OT	35.5	250.2
MT	38.1	29.2
LASLAS	22.9	52.0
OLAS	1.5	33.3
MLAS	0.7	10.4
Sum of di-μ Trigger	25.1	95.7

A new H1 Hodoscope

To improve the efficiency and stability of future Drell-Yan data taking it is planned to rebuild the H1 trigger hodoscope. The current design was optimised for a material budget as small as possible, since the hodoscope had to be placed in the acceptance of the RICH detector. It turned out that the current design was not rigid enough over the years, resulting in inefficiencies. Since low material budget is not required for a Drell-Yan measurement the H1 hodoscope will be rebuilt with acrylic light guides in the central part instead of air light guides. In addition, thicker scintillator material (2 cm instead of 0.8 cm) will be used. These changes will improve the photon collection efficiency especially in the central part of the detector.

5.5 The target system for antiproton cross-section measurements

The proposed physics program foresees to collect data using a proton beam with energies ranging between 50 and 280 GeV/c on both a liquid hydrogen (LH_2) as well as a liquid helium (L^4He) target.
The LH_2 target used in the Compass 2009 run ([176]) is still available and can be re-used after some standard maintenance. In this apparatus the liquid hydrogen is enclosed within a Mylar cylinder of 125 μm thickness, with a length of 40 cm along the beam axis and a diameter of 3.5 cm. The entire 2009 LH_2 target system is shown in Fig. 76. A cryostat tube, made from aluminium, surrounds the target cell, with an overall diameter of 185 mm and it is terminated towards the spectrometer with a 250 μm thin Mylar window. Its diameter was chosen sufficiently large that the forward-going particles which can be detected by the spectrometer will avoid the aluminium cryostat and pass through the window.

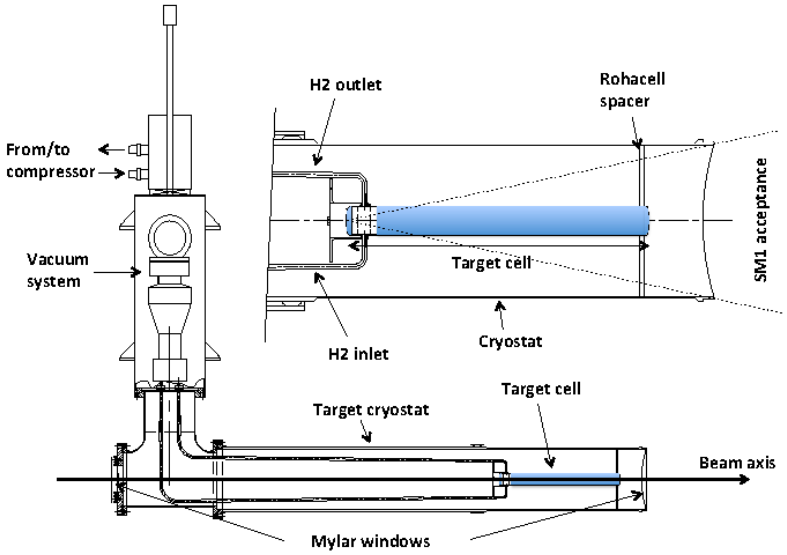

Figure 76: Side view of the liquid hydrogen target system. A closer view of the cylindrical Mylar cell and hydrogen piping is shown in the inset.

The new L^4He target will be realised starting from an existing apparatus used for the COMPASS deuteron polarised target. In particular the dilution refrigerator is well suited also for this L^4He target. The new L^4He target cell will be 40 *cm* long and 3.5 *cm* in diameter. It will be newly constructed, using 2 *mm* thick glass fibre. The surrounding vacuum chamber, 45 *cm* long with 8 *cm* diameter, will be constructed from 1 *mm* thick carbon fibre. The temperature of the liquid helium during the operation is expected to be 1 *K*, *i.e.* filled with helium of a density of $0.145\,g/cm^3$. The change-over between the target systems is expected to take one week, including warm-up and cool-down times.

5.6 Hadron PID perspectives: RICH

The RICH-1 Cherenkov-imaging detector [178, 219–221] is the backbone for hadron PID in the COMPASS 2 setup. It has a large acceptance, *i.e.* ±200 mrad in the vertical plane and ±250 mrad in the horizontal plane. It uses C_4F_{10} as heavy and low-chromaticity radiator gas, where image focusing is provided by a wall of spherical UV mirrors. Presently, the photon detection system is formed by MAPMTS coupled to individual fused silica-lens telescopes in the central region, covering 25% of the instrumented surface, where the rate is higher, and gaseous detectors in the peripheral region. Two types of gaseous detectors are in use, both equipped with CsI photo-converters: MWPC detectors and novel ones, which are based on a hybrid MPGD architecture with two THick GEM (THGEM) layers that are followed by a Micromegas multiplication stage. The first THGEM also acts as photo-converter substrate. The RICH-1 detector provides hadron PID in the range from 3 to 60 GeV/c, where 3 GeV/c is the effective threshold for pion identification, and pions can be separated from kaons at 90% confidence level at 60 GeV/c [178].

As described in Sec. 4.5, it is desirable to complement the existing RICH-1 by new Cherenkov counters that extend the momentum range for the positive identification of hadrons: For low momenta (RICH-0), a DIRC counter enriched with a focusing system [222] with horizontal radiator bars arranged in a planar configuration can be used in order to separate hadrons in the range 0.2 GeV/c up to 5-6 GeV/c. Fused silica bars are the default choice, while the use of Plexiglas bars [223] is an alternative option to be analysed. The default read-out sensors are MAPMTs, while other fast, pixelized photon detectors as MCP-PMTs can be considered. A relevant feature is the reduced physical length of such a detector that may require no more than a 20 cm space-slot along the beam line.

5.7 Equipment and responsibilities

As described above, the proposed measurements will make use of the existing COMPASS spectrometer, with a number of new additions, upgrades and modifications. In cases of existing equipment, the responsibility for maintenance and operation will in general stay with the same group as in the COMPASS experiment, extended by the entire COMPASS++/AMBER collaboration. A tentative list of responsibilities for the different subsystems can be found in Table 18. This list is still in an early stage. The individual assignments are preliminary, *i.e.* subject to change, depending on the outcome of the discussions with funding agencies.

Apart from the contributions by the institutes listed in Table 18, the new experiment would require from CERN as host laboratory the continuation of the services granted for the present COMPASS experiment, in particular in cryogenics and central data recording.

Table 18: Tentative responsibilities for detector construction/upgrades, operation and maintenance. The assignments are still preliminary and subject to change according to funding. The new components concern predominantly the phase-1 presented in this document, several developments, such as the new DAQ, are however in view of the complete future running plan. Several major detector developments that are presently envisaged for measurements beyond phase-1 are omitted here. This table will be updated along with forthcoming proposals for further measurements at the COMPASS++/AMBER facility.

Equipment	Responsible (tentative)	Status
Beam	CERN	new/existing
BMS	Bonn	existing
CEDAR	CERN, Warsaw	existing/upgrad
Luminosity measurement	Freiburg, Mainz	upgrade
C/W target	Lisbon	new
LH_2,LHe_2 target	CERN, Czech G., Virginia, Yamagata	existing/new
DY vertex detector		new
Silicon detectors	Munich, Torino	new/existing
TPC and pressure tank	Gatchina, GSI	new
TPC gas system	Gatchina	new
TPC RO	Bonn, Freiburg, Gatchina, GSI	new
SciFi target	Munich	new
SciFi tracker	Bonn	existing
GEM	Bonn	refurbish
Micromegas		existing
Straws	Illinois	existing
MWPC	JINR, Torino	upgrade
DC	Illinois	existing
RICH	Atlanta, Calcutta, Czech G., Trieste	existing/upgrade/new
RICHWALL	JINR, Torino	existing
HCAL1	JINR	existing
HCAL2	IHEP Protvino	existing
ECAL1	IHEP Protvino	existing
ECAL2	IHEP Protvino	existing
MW1	JINR	existing
MW2	IHEP Protvino	existing
W45	CERN	existing
DAQ/Computing	Czech Group, Munich, Tomsk, Warsaw	upgrade
Trigger	Bonn, Mainz	upgrade
PRM Trigger	Mainz, Munich	new
Front-end		upgrade
Slow control	Lisbon	existing
Infrastructure	CERN	existing

6 Outlook: The ”New QCD facility at the M2 beam line" beyond LS3

6.1 RF-separated hadron beams in the M2 beam line

In view of several proposals to perform new experiments with high-energy hadron beams at CERN, a study of a possible enrichment of desired particle species in the M2 beam has been launched by EN-EA in the context of the Physics Beyond Colliders Initiative (PBC). Contrary to the case of lower energies, at higher energies an enrichment of antiprotons is not naturally given by decays of other particles over the length of a beam line, which is due to higher lifetimes of particles in the laboratory frame. In addition, several proposals prefer a higher content of kaons and positive pions in the beam.
Starting from studying limitations in terms of production of particles, there are several possibilities to enrich the content of a wanted particle species in the beam, usually by suppression of unwanted particles. Due to the $1/p^3$ dependence of electro-static separators, it is not reasonable to use such a method at beam energies higher than a few GeV. While in principle an enrichment by differential absorption would be feasible, the very low efficiency, high losses, and small suppression factors for unwanted particles leave only the possibility of radio-frequency (RF) separated beams.
The method of RF-separation was first employed at CERN in the 1960s based on ideas of Panofsky and Schnell as for instance described in Ref. [224]. The main idea is based on the different velocities of particle species in a beam with defined momentum.

As displayed in Fig. 77, two dipole RF cavities (RF1 + RF2) with frequency f are implemented at a given distance L. The transverse kick of RF1 is either amplified or compensated by RF2 depending on the phase difference between both. This phase difference is given by the difference of velocities of the various particle species. For two species i ($i = 1, 2$) with masses m_i and velocities β_i, the phase difference reads $\Delta\Phi = 2\pi(Lf/c)(\beta_1^{-1} - \beta_2^{-1})$. In the limit of large momenta, the phase difference can be expressed as a mass difference between the two species at the beam momentum p:

$$\Delta\Phi = 2\pi(Lf/c)\frac{m_1^2 - m_2^2}{2p^2}$$

For kaons as wanted particles, the phase difference could be chosen at $\Delta\Phi_{\pi p} = 2\pi$, which results in $\Delta\Phi_{\pi K} = 94^\circ$. This means that the kick for both protons and pions would be compensated by RF2 and they would be absorbed in the beam stopper. The kaons would receive a close-to-maximum transverse kick and mostly go around the stopper. For antiproton beams, the phase difference could be chosen at $\Delta\Phi_{\pi\bar{p}} = \pi$, which results in $\Delta\Phi_{\bar{p}K} = 133^\circ$ and $\Delta\Phi_{\bar{p}e} = 184^\circ$. In this case, the antiprotons would receive an acceptable deflection while electrons and pions are dumped effectively. Recently, a first version of beam line optics has been prepared, which includes a new section for momentum selection that was placed after the high-acceptance front-end consisting of six strong-gradient quadrupole magnets (Fig. 78). The new section comprises an additional vertical achromat in contrast to the old horizontal momentum selection. With four additional dipole magnets, displaced collimators and optimised field

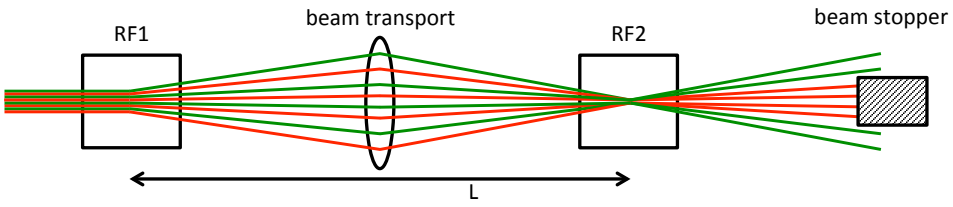

Figure 77: Panofsky-Schnell method for RF-separated beams. The unwanted particles (red) are stopped by a beam stopper while the wanted particles (green) receive a net deflection by the combination of the RF1 and RF2 dipole RF cavities out of the central axis, which is sufficient to go around the stopper.

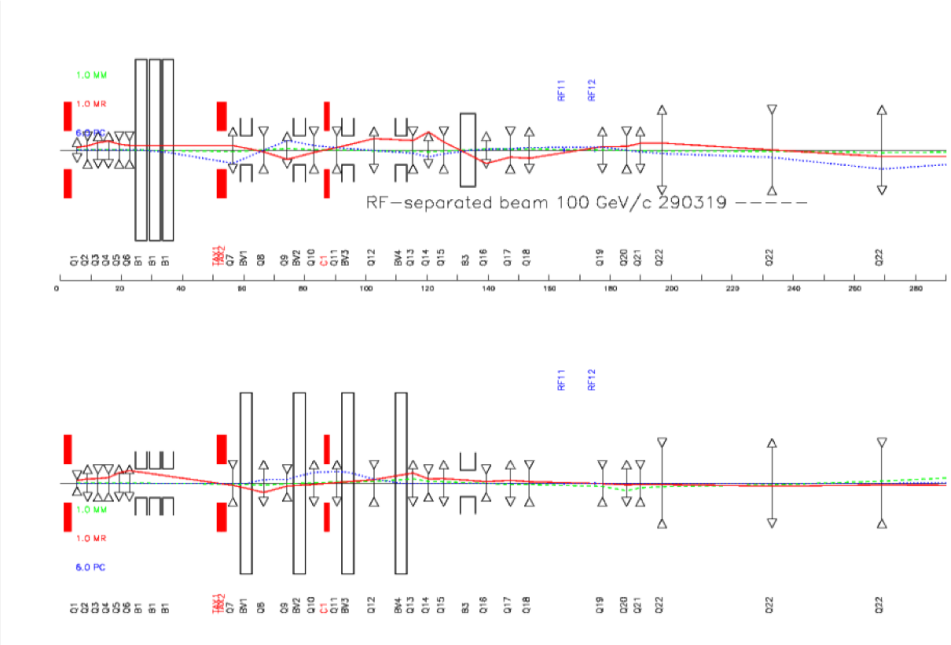

Figure 78: First outcome of optics studies for an RF-separated beam in the M2 beam line. The beam momentum selection will be achieved by including a vertical achromat comprising four strong dipole magnets (BV1-BV4).

lens quadrupoles, the momentum selection has been improved from initially dp/p = 10% to only 0.8%, which is an important requirement as will become clear below.

In the current optics, the two FODO sections of the M2 beam have been kept unchanged, which has the benefit of keeping the possibility to change back to the muon beam configuration at a rather moderate cost and within a shorter time compared to a complete change of all M2 beam line elements. Depending on evolving requirements and further optimisation, the option to go back to muon beams could be checked in more detail. The current placement of the two cavities RF1 and RF2 would allow a separation length L of about 829 m.

Based on a study by J.Doornbos at TRIUMF for CKM, we assume a similar input for frequency (f = 4.2 GHz instead of 3.9 GHz at CKM) and kick strength of the RF cavities (dp_T = 15 MeV/c). In such a study case, the upper momentum limitation for RF-separated kaon beams would be about 75 GeV/c and about 108 GeV/c for RF-separated antiproton beams, see Fig. 79. As the phase difference depends quadratically on the chosen momentum, such beams would deliver acceptable separation only in a small momentum band. In addition, the dispersion of the beam $\Delta p/p$ needs to be limited to about 1 % in order to prevent a phase shift of $\Delta\Phi_f = \Delta\Phi_i(1 - 2\Delta p/p)$ and thus a lower separation efficiency.

With the given acceptance values and target efficiency an exemplary calculation was performed for the case of a 100 GeV/c antiproton beam. Assuming that 80 % of the antiprotons would pass the beam stopper and an optimisation of the solid angle to 10 π µsterad, one would expect about $8 \cdot 10^7$ antiprotons in the experimental hall EHN2 for 10^{13} incident protons at the T6 target. Due to the current radiation protection restrictions for EHN2 of 10^8 particles per 4.8 s spill, the limit would be given only by the to-be-achieved purity of the beam. Assuming 50 % purity, this would be about $5 \cdot 10^7$ antiprotons per spill.

Further steps will include an optimisation of the optics, including a realistic beam dump and a section for beam particle identification with e.g. CEDARs or threshold Cherenkov detectors. In addition, studies for the required dipole RF cavities, necessary infrastructure and costing will be launched. Further optimisation of the existing shielding with respect to the ambient radiation might also turn out useful to

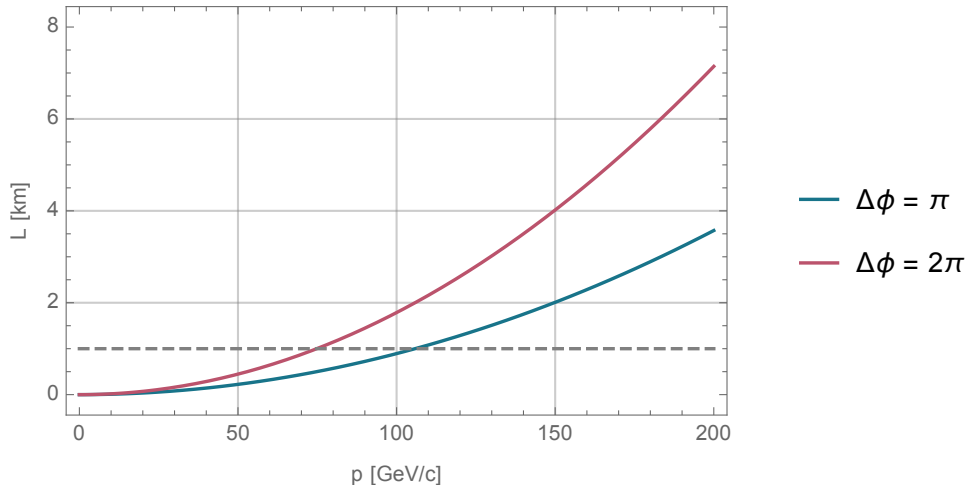

Figure 79: Dependence of the final beam momentum p as a function of length L between the RF cavities for two different phase differences. The case of $\Delta\Phi = 2\pi$ (red) corresponds to kaons as wanted particles while $\Delta\Phi = \pi$ (blue) would be the choice for antiprotons. The dashed horizontal line indicates the maximum momentum possible for the given particle type at the M2 beam line.

increase the current limit of particles per spill in EHN2 moderately.

More details can be found in the PBC Conventional Beams Working Group report [43].

6.2 Experiments planned beyond phase-1

Drell-Yan physics and hadron spectroscopy with high-intensity kaon and antiproton beams The availability of a kaon beam such as the one envisaged by radio-frequency separation of charged hadrons at the SPS M2 beam line, would provide a unique opportunity for performing extensive studies of the parton structure of the kaon. A high-intensity kaon beam would allow for Drell-Yan measurements with unprecedented statistical precision. A detailed comparison between the quark structure of the two lightest hadrons becomes possible. The Drell-Yan kaon data should be complemented with J/ψ production and prompt-photon measurements, thereby also paving the way for a determination of the gluon structure of the kaon.
The availability of an RF-separated antiproton beam would make measurements of nucleon single-spin asymmetries with reduced systematic uncertainties possible and the u-quark Boer-Mulders distribution of the nucleon can be accessed.

– **Valence quark distributions in the kaon** (see LoI sect. 4.3.2)
The presence of the valence strange-quark significantly alters the properties of the kaon in comparison to those of the pion. Being much heavier than the light quarks, it carries a larger fraction of the kaon momentum. Accordingly, the valence content of the kaon is expected to be significantly different from that of the pion. Of special interest is the comparison to theoretical calculations in the framework of Dyson-Schwinger equations. The kaon valence distribution $u_K(x)$ can be determined with much improved accuracy in a dedicated Drell-Yan measurement. Using a 100 GeV RF-separated hadron beam with an intensity of 7×10^7 per second, a kaon purity of about 30% and assuming 2×140 days of data taking, about 65.000 kaon-induced Drell-Yan events should be collected in total. It is foreseen to use a 100 cm long carbon target (4×25 cm) in conjunction with a new large-acceptance active absorber downstream of it.

– **Separation of valence and sea distributions in the kaon** (see LoI sect. 4.3.3)
The kaon sea distribution and its composition are presently unknown. They can be determined through a comparison between K^+ and K^--induced Drell-Yan measurements using an RF-separated hadron beam with a momentum of about 100 GeV/c and a light isoscalar target. In such measurements, the K^+ cross section is sensitive to valence-sea and sea-sea terms only, so that the difference between K^- and K^+ beams is sensitive to $\bar{u}^{K^-} u^N$ valence-valence terms only.

– **The J/ψ production mechanism and the gluon distribution in the kaon** (see LoI sect. 4.3.4)
It is expected that the heavier quark in the kaon radiates less gluons than the lighter quarks in the pion. A natural consequence of this expectation is that the gluons in the kaon carry less momentum than the gluons in the pion. Using the Dyson-Schwinger-Equation approach, it was found that at the hadronic scale the gluons contribute to only 5% of the total momentum in the kaon, as compared to about one third in the pion. A stringent check of this prediction requires the measurement of the presently unknown gluon distribution in the kaon, which can in principle be inferred through a measurement of kaon-induced J/ψ production. A comparison between kaon-induced J/ψ cross sections measured with the two beam-charge signs can be used to both improve our understanding of the J/ψ production mechanism and infer the gluon distribution in the kaon.

– **Electric polarisability of the kaon measured via the Primakoff reaction** (see LoI sect. 4.5.1)
A measurement of the so-called Primakoff reaction $K^- Z \to K^- \gamma Z$ using an RF-separated hadron beam, in which kaons are enriched, provides a unique opportunity to perform the first measurement of the kaon polarisability α_K. For the measurement with a 100 GeV/c RF-separated kaon beam ($5 \times 10^6 s^{-1}$) the same spectrometer configuration as in the analogous Compass measurements of the pion polarisability in 2009 and 2012, *i.e.* the CEDAR detector in the beam line, a 0.3 X_0 thick nickel target with silicon-based telescopes upstream and downstream of the target, but the new DAQ system with the capability to accept trigger rates up to 100 kHz will be used. The expected statistical accuracy of the α_K extraction under the assumption $\alpha_K + \beta_K = 0$ is 0.03×10^{-4} fm^3.

– **High-precision strange-meson spectroscopy** (see LoI sect. 4.2.1)
The Particle Data Group lists 25 strange mesons that have been measured in the mass range from 0.5 to 3.1 GeV/c^2. Only 13 of them are included in the summary tables, the remaining 12 states still need further confirmation. For two of them, even their spin-parity quantum numbers are still unknown. While for some well-known kaon states the quark-model prediction agrees well with the experimental observations, many predicted states have not yet been observed and some of the observed states do not fit into the quark-model picture.
In analogy to the 2008 and 2009 Compass measurements of non-strange mesons in the $\pi^-\pi^-\pi^+$ final state, the flagship final state for strange-meson spectroscopy will be $K^-\pi^-\pi^+$. In order to apply novel analysis techniques developed for the analysis of the $\pi^-\pi^-\pi^+$ final state, a total dataset of at least 10×10^6 events is acquired. This is about a factor of 10 more than the present world data and hence requires the RF-separated M2 hadron beam with a high intensity. In order to be dominated by diffractive production, a minimum beam momentum of 50 GeV/c is necessary.

– **Study of the gluon distribution in the kaon via prompt-photon production** (see LoI sect. 4.4)
Recent progress in theoretical calculations makes the gluon distributions in pion and kaon especially important. Gluons not only significantly contribute to the internal structure of mesons, they also play a major role in the generation of their mass. However, in contrast to the rather well mapped gluon distribution in the nucleon, the gluon content of mesons is essentially unknown. Compared to other approaches, measuring prompt-photon production in gluon Compton scattering has the advantage of manageable systematics. Albeit the cross section of this process is low, it is known at least up to NLO. In order to determine the gluon structure of charged kaons, we propose to measure the differential cross section of prompt-photon production using a positive RF-separated kaon beam of 100 GeV/c momentum with an intensity of 5×10^6 kaons per second. A two-meter

long liquid hydrogen target (0.2 X_0) should be used, which is transparent for any produced photon. Also a solid target of low-Z material could be considered.

– **Direct measurement of the lifetime of the neutral pion** (see LoI sect. 4.5.2)
The lifetime of the neutral pion is a quantity that is relevant in low-energy QCD, as it is related to the chiral-anomaly hypothesis. To date a 1% accuracy has been reached in the theoretical lifetime prediction, while the experimental value $(8.52 \pm 0.18) \times 10^{-17}$ s has an uncertainty of 2.1%.
The exclusive reaction $\pi^- Ni \rightarrow \pi^- Ni\,\pi^0$ will be studied. The idea of the direct measurement is based on the estimation of the length of the decay path of the produced neutral pion. This length is a few 100 micrometers for pions produced in the forward direction for energies above 10 GeV. The measurement proposed here makes use of the full spectrometer in order to reconstruct π^0 decays, both the main decay into two photons and the decay into $e^+e^-\gamma$, which has to be taken into account when interpreting the fraction with converted photons. For a one-year parasitic running along with the kaon Primakoff run, the statistical precision of the π^0 lifetime is expected to be better than 1%.

– **Vector-meson production off nuclei by pion and kaon beams** (see LoI sect. 4.6)
The production of unstable particles off different nuclei provides the possibility to determine the total cross section for the interaction of vector mesons with nucleons. The investigation of vector-meson production in the charge-exchange exclusive reactions $\pi^- A \rightarrow V(\rho, \omega, \phi)\, A'$ and $K^- A \rightarrow K^*(892)\, A'$ provides the opportunity to obtain the not-yet-measured total cross section for longitudinally polarised vector mesons interacting with nucleons. The knowledge of this cross section is important to describe the color-screening effect in vector-meson leptoproduction.
A hadron beam with a momentum of about 100 GeV/c will be used in conjunction with a set of nuclear targets having different atomic numbers ranging from hydrogen to lead. The expected cross sections are sufficiently large to collect reasonable statistics within a short time or to take data in parallel to other physics programmes.

– **Heavy-quark meson spectroscopy with low-energy antiprotons** (see LoI sect. 3.2.1)
The main objective of this experiment is a significant improvement in the understanding of the nature of the so-called X, Y, Z states, which remains so far unclear in spite of worldwide efforts in the last 15 years. The discovery of narrow resonance-like signals at e^+e^--colliders, which have masses above the open-charm threshold and decay to charmonium, had triggered a wealth of theoretical interpretations ranging from conventional excited charmonium to multi-quark states and hybrid mesons. Of particular interest is the production of states in association with a recoil particle, which opens the possibility of observing states with spin-exotic quantum numbers such as hybrids or glueballs. The annihilation of low-energy antiprotons with momenta below 20 GeV provides a unique tool to study these states.
An early experiment at the M2 beamline of the SPS using low-energy antiprotons and a liquid hydrogen target can reach luminosities of the order of $10^{30}\ cm^{-2}s^{-1}$. It is expected to make important contributions to the production and spectroscopy of these long sought-after states even before the start of PANDA at FAIR, where such a measurement is in the planning state. Owing to the low beam momentum, the experiment requires a dedicated target spectrometer including charged-particle tracking and electromagnetic calorimetry, in addition to the forward spectrometer in EHN2.

– **Studies of the nucleon spin structure with antiproton beam and transversely polarised target** (see LoI sect. 4.3.1.)
Studying the Drell-Yan process with an antiproton beam and a transversely polarised proton target shall provide an ideal opportunity to study the transverse-momentum-dependent (TMD) PDFs of the nucleon. Compared to the pion-induced Drell-Yan studies presently being performed at Compass the uncertainties related to the limited knowledge of the pion structure shall be eliminated. Studying this process using a transversely polarised proton target is the most promising way to access the

Boer-Mulders function of the nucleon. Because of charge symmetry, the antiproton-induced Drell-Yan process is only sensitive to convolutions of valence-quark TMD PDFs of the nucleon. Two transverse spin-dependent modulations can be measured, which result from convolutions of the $\bar{u}$-valence Boer-Mulders function in the antiproton with the u-valence transversity function in the proton or with the u-valence pretzelosity function in the proton. Given the present knowledge of the u-transversity distribution in the nucleon, the u-Boer-Mulders distribution of the nucleon can be accessed.

Hard exclusive reactions using a muon beam and a transversely polarised target

– **Measurement of the GPD E in Deeply Virtual Compton Scattering** (see LoI sects. 2.2.1-2.2.2)
The main goal of this experiment is to extend our fundamental knowledge on the angular-momentum structure of the nucleon, which can be accomplished by measurements of Generalized Parton Distributions (GPDs). These functions describe the correlations between longitudinal momentum fractions and transverse spatial positions of partons in the nucleon, commonly known as "3-dimensional" picture of the nucleon. Experimental data on these GPDs are required over the largest possible domain of the Bjorken-x variable, as the evaluation of the total angular momentum J_f carried by quarks of flavour f through the Ji sum rule requires an integration over the sum of the GPDs H^f and E^f . While some experimental knowledge on the GPDs H^f exists already for u and d quarks, only scarce experimental data exists on the "elusive" GPDs E^f. Access to the GPDs E^f is possible by measuring certain cross section asymmetries in Deeply Virtual Compton Scattering, using a polarised charged-lepton beam and a transversely polarised target. A measurement in the so-far uncharted Bjorken-x domain between 0.005 and 0.05, where phenomenological models predict a large sensitivity to E^f, can only be performed using the high-energy self-polarised muon beam of the CERN SPS M2 beam line. A new 3-layer Silicon detector has to be constructed and installed inside of the existing polarised target, in order to accomplish identification of the target recoil proton by the dE/dx method and to measure its momentum and trajectory.

– **Measurements of Deeply Virtual Meson Production** (see LoI sect. 2.2.3)
In deeply virtual exclusive vector meson production (DVMP) on a transversely polarised target there exists sensitivity to various types of GPDs and different quark flavours, depending on the quark content and the quantum numbers of the produced meson. Because of this property DVMP can be regarded as a quark flavour filter, which motivates to study a wide spectrum of mesons. Compared to the present Compass experiment, the future polarised solid-state target combined with the detection of recoil particles will allow for the selection of exclusive events without SIDIS background. The resulting precise angular distributions of vector meson decays will allow us to separate their longitudinal and transverse contributions. Using the assumption of s-channel helicity conservation, which was found experimentally to be valid at the 10% level, will provide a separation of transverse and longitudinal virtual-photon contributions, the latter giving access to the GPDs E^f at leading twist.

Acknowledgements

We are grateful to Craig Roberts for his kind support in shaping the physics case, in particular for making the fundamental aspect of the emergence of hadronic mass a major motivation for the Drell-Yan measurements. Many thanks to Vincent Cheung and Ramona Vogt for providing us with their theoretical ICEM predictions for the charmonium measurements.

References

[1] Adams, B. and others, Letter of Intent: A New QCD facility at the M2 beam line of the CERN SPS (COMPASS++/AMBER), arXiv:1808.00848, Tech. rep., CERN-SPSC-2019-003 (SPSC-I-250). (Cited in Secs. Preamble, Executive Summary and 1.)

[2] B. Adams, et al., COMPASS++/AMBER: Proposal for Measurements at the M2 beam line of the CERN SPS Phase-1: 2022-2024, Tech. Rep. CERN-SPSC-2019-022. SPSC-P-360, CERN, Geneva (May 2019).
URL http://cds.cern.ch/record/2676885 (Cited in Sec. Preamble.)

[3] L. Chang, I. C. Cloet, J. J. Cobos-Martinez, C. D. Roberts, S. M. Schmidt, P. C. Tandy, Imaging dynamical chiral symmetry breaking: pion wave function on the light front, Phys. Rev. Lett. 110 (13) (2013) 132001. (Cited in Secs. Executive Summary and 3.1.)

[4] C. D. Roberts, Perspective on the origin of hadron masses, Few Body Syst. 58 (1) (2017) 5. (Cited in Secs. Executive Summary and 3.1.)

[5] LHC long-term schedule.
URL https://lhc-commissioning.web.cern.ch/lhc-commissioning/schedule/LHC-long-term.htm (Cited in Sec. Executive Summary.)

[6] R. E. Taylor, Deep inelastic scattering: The Early years, Rev. Mod. Phys. 63 (1991) 573–595. (Cited in Sec. 1.)

[7] H. W. Kendall, Deep inelastic scattering: Experiments on the proton and the observation, Rev. Mod. Phys. 63 (1991) 597–614. (Cited in Sec. 1.)

[8] J. I. Friedman, Deep inelastic scattering: Comparisons with the quark model, Rev. Mod. Phys. 63 (1991) 615–629. (Cited in Sec. 1.)

[9] Y. Nambu, Quasiparticles and Gauge Invariance in the Theory of Superconductivity, Phys. Rev. 117 (1960) 648–663, [,132(1960)]. (Cited in Secs. 1 and 3.1.)

[10] J. Goldstone, Field Theories with Superconductor Solutions, Nuovo Cim. 19 (1961) 154–164. (Cited in Secs. 1 and 3.1.)

[11] H. Yukawa, On the Interaction of Elementary Particles I, Proc. Phys. Math. Soc. Jap. 17 (1935) 48–57, [Prog. Theor. Phys. Suppl.1,1(1935)]. (Cited in Sec. 1.)

[12] G. Arcadi, M. Dutra, P. Ghosh, M. Lindner, Y. Mambrini, M. Pierre, S. Profumo, F. S. Queiroz, The waning of the WIMP? A review of models, searches, and constraints, Eur. Phys. J. C78 (3) (2018) 203. (Cited in Sec. 1.)

[13] R. Hofstadter, R. W. McAllister, Electron Scattering From the Proton, Phys. Rev. 98 (1955) 217–218. (Cited in Sec. 2.1.)

[14] J. C. Bernauer, P. Achenbach, C. Ayerbe Gayoso, R. Böhm, D. Bosnar, L. Debenjak, M. O. Distler, L. Doria, A. Esser, H. Fonvieille, J. M. Friedrich, J. Friedrich, M. Gómez Rodríguez de la Paz, M. Makek, H. Merkel, D. G. Middleton, U. Müller, L. Nungesser, J. Pochodzalla, M. Potokar, S. Sánchez Majos, B. S. Schlimme, S. Širca, T. Walcher, M. Weinriefer, High-precision determination of the electric and magnetic form factor s of the proton, Phys. Rev. Lett. 105 (2010) 242001.
URL https://link.aps.org/doi/10.1103/PhysRevLett.105.242001 (Cited in Sec. 2.1.)

[15] J. C. Bernauer, Precise form factors from elastic electron scattering, J. Phys. Conf. Ser. 381 (2012) 012006. (Cited in Sec. 2.1.)

[16] R. Pohl, et al., The size of the proton, Nature 466 (2010) 213–216. (Cited in Secs. 2.1 and 2.2.)

[17] R. Pohl, The Lamb shift in muonic hydrogen and the proton radius puzzle, Hyperfine Interact. 227 (1-3) (2014) 23–28. (Cited in Secs. 2.1 and 2.2.)

[18] A. Dainese, et al., Physics Beyond Colliders: QCD Working Group Report (2019).
URL https://arxiv.org/abs/1901.04482 (Cited in Secs. 2 and 2.2.)

[19] J. C. Bernauer, M. O. Distler, Avoiding common pitfalls and misconceptions in extractions of the proton radius, in: ECT* Workshop on The Proton Radius Puzzle Trento, Italy, June 20-24, 2016, 2016, pp. 1–12.
URL http://inspirehep.net/record/1468073/files/arXiv:1606.02159.pdf (Cited in Sec. 2.)

[20] R. Pohl, et al., Deuteron charge radius and Rydberg constant from spectroscopy data in atomic deuterium, Metrologia 54 (2017) L1. (Cited in Sec. 2.2.)

[21] F. Biraben, et al., Proposal for an experiment at PSI: Lamb shift in muonic helium (2017).
URL https://www.ethz.ch/content/dam/ethz/special-interest/phys/particle-physics/precisionphysicsatlowenergy-dam/Research/Proposal_muHe_pdf.pdf (Cited in Sec. 2.2.)

[22] A. Beyer, L. Maisenbacher, A. Matveev, R. Pohl, K. Khabarova, A. Grinin, T. Lamour, D. C. Yost, T. W. Hänsch, N. Kolachevsky, T. Udem, The rydberg constant and proton size from atomic hydrogen, Science 358 (6359) (2017) 79–85.
URL https://science.sciencemag.org/content/358/6359/79 (Cited in Sec. 2.2.)

[23] H. Fleurbaey, S. Galtier, S. Thomas, M. Bonnaud, L. Julien, F. Biraben, F. Nez, M. Abgrall, J. Guéna, New Measurement of the $1S - 3S$ Transition Frequency of Hydrogen: Contribution to the Proton Charge Radius Puzzle, Phys. Rev. Lett. 120 (18) (2018) 183001. (Cited in Sec. 2.2.)

[24] N. Bezginov, T. Valdez, M. Horbatsch, A. Marsman, A. C. Vutha, E. A. Hessels, A measurement of the atomic hydrogen lamb shift and the proton charge radius, Science 365 (6457) (2019) 1007–1012.
URL https://science.sciencemag.org/content/365/6457/1007 (Cited in Sec. 2.2.)

[25] P. Mergell, U. G. Meissner, D. Drechsel, Dispersion theoretical analysis of the nucleon electromagnetic form-factors, Nucl. Phys. A596 (1996) 367–396. (Cited in Sec. 2.2.)

[26] A. H. Gasparian, The New Proton Radius Experiment at Jefferson Lab, JPS Conf. Proc. 13 (2017) 020052. (Cited in Sec. 2.3.)

[27] A. Gasparian, Preliminary Results from the JLab PRad Experiment, Workshop ECT Trento . (Cited in Sec. 2.3.)

[28] F. Borkowski, P. Peuser, G. G. Simon, V. H. Walther, R. D. Wendling, Electromagnetic Form-Factors of the Proton at Low Four-Momentum Transfer, Nucl. Phys. B93 (1975) 461–478. (Cited in Sec. 2.3.)

[29] G. G. Simon, C. Schmitt, F. Borkowski, V. H. Walther, Absolute electron Proton Cross-Sections at Low Momentum Transfer Measured with a High Pressure Gas Target System, Nucl. Phys. A333 (1980) 381–391. (Cited in Sec. 2.3.)

[30] J. C. Bernauer, et al., High-precision determination of the electric and magnetic form factors of the proton, Phys. Rev. Lett. 105 (2010) 242001. (Cited in Sec. 2.3.)

[31] J. C. Bernauer, et al., Electric and magnetic form factors of the proton, Phys. Rev. C90 (1) (2014) 015206. (Cited in Sec. 2.3.)

[32] priv. comm. J.C. Bernauer. (Cited in Sec. 2.3.)

[33] J. M. Alarcon, D. W. Higinbotham, C. Weiss, Z. Ye, Proton charge radius extraction from electron scattering data using dispersively improved chiral effective field theory, Phys. Rev. C99 (4) (2019) 044303. (Cited in Sec. 2.3.)

[34] T. Suda, Electron scattering experiment off proton at ultra-low q^2 (2016).
URL http://www2.yukawa.kyoto-u.ac.jp/~min2016/slides/Suda_MIN2016.pdf
(Cited in Sec. 2.3.)

[35] M. Mihovilovic, et al., The proton charge radius extracted from the Initial State Radiation experiment at MAMI, arXiv . (Cited in Sec. 2.3.)

[36] A. Vorobyov, Proton radius status and perspective, incl.: Proposal for high precision measuremens of the *ep* differential cross sections at small t values with the recoiled proton detector (2016).
URL https://indico.cern.ch/event/544849/contributions/2213665/attachments/1301151/1942517/Vorobyev_ep_report_27_june_2016.pdf (Cited in Sec. 2.3.)

[37] R. Gilman, et al., Studying the Proton "Radius" Puzzle with μp Elastic Scattering (2013).
URL https://arxiv.org/pdf/1303.2160.pdf (Cited in Sec. 2.3.)

[38] S. Belostotski, N. Sagidova, A. Vorobyev, Proton radius reconstruction from simulated electron-proton elastic scattering cross sections at low transfer momenta, arXiv . (Cited in Sec. 2.5.)

[39] A. A. Vorobyov, G. A. Korolev, V. A. Schegelsky, G. Ye. Solyakin, G. L. Sokolov, Yu. K. Zalite, A method for studies of small-angle hadron-proton elastic scattering in the coulomb interference region, Nucl. Instrum. Meth. 119 (1974) 509–519. (Cited in Sec. 2.5.)

[40] S. Ilieva, et al., Nuclear-matter density distribution in the neutron-rich nuclei 12,14 Be from proton elastic scattering in inverse kinematics, Nucl. Phys. A875 (2012) 8–28. (Cited in Sec. 2.5.)

[41] A. Afanasev, P. G. Blunden, D. Hasell, B. A. Raue, Two-photon exchange in elastic electron-proton scattering, Prog. Part. Nucl. Phys. 95 (2017) 245–278. (Cited in Sec. 2.6.)

[42] P. Abbon, et al., The COMPASS experiment at CERN, Nuclear Instruments and Methods in Physics Research Section A: Accelerators, Spectrometers, Detectors and Associated Equipment 577 (3) (2007) 455 – 518. (Cited in Secs. 2.7, 5.1 and 14.)

[43] L. Gatignon, J. Bernhard, D. Banerjee, M. Brugger, N. Charitonidis, G. L. D'Alessandro, N. Doble, M. Van Dijk, A. Gerbershagen, E. Montbarbon, M. Rosenthal, Report from the Conventional Beams Working Group to the Physics beyond Colliider Study and to the European Strategy for Particle Physics, Tech. Rep. CERN-PBC-REPORT-2018-002, CERN, Geneva (Dec 2018).
URL https://cds.cern.ch/record/2650989 (Cited in Secs. 7, 2.8, 8 and 6.1.)

[44] M. Tanabashi, et al., Review of particle physics, Phys. Rev. D 98 (2018) 030001.
URL https://link.aps.org/doi/10.1103/PhysRevD.98.030001 (Cited in Sec. 3.)

[45] A. Caldwell, D. Kollàr, K. Kröninger, Bat — the bayesian analysis toolkit, Computer Physics Communications 180 (11) (2009) 2197 – 2209.

URL http://www.sciencedirect.com/science/article/pii/S0010465509002045 (Cited in Sec. 2.9.3.)

[46] X. Yan, D. W. Higinbotham, D. Dutta, H. Gao, A. Gasparian, M. A. Khandaker, N. Liyanage, E. Pasyuk, C. Peng, W. Xiong, Robust extraction of the proton charge radius from electron-proton scattering data, Phys. Rev. C 98 (2018) 025204.
URL https://link.aps.org/doi/10.1103/PhysRevC.98.025204 (Cited in Sec. 2.9.3.)

[47] M. Hoffmann, A feasibility test for measuring the proton charge radius in high-energy muon-proton elastic scattering, Master's thesis, Helmholtz-Institut für Strahlen- und Kernphysik, Universität Bonn (May 2019). (Cited in Sec. 2.10.)

[48] Z. F. Ezawa, Wide-Angle Scattering in Softened Field Theory, Nuovo Cim. A23 (1974) 271–290. (Cited in Sec. 3.1.)

[49] G. R. Farrar, D. R. Jackson, Pion and Nucleon Structure Functions Near x=1, Phys. Rev. Lett. 35 (1975) 1416. (Cited in Sec. 3.1.)

[50] E. L. Berger, S. J. Brodsky, Quark Structure Functions of Mesons and the Drell-Yan Process, Phys. Rev. Lett. 42 (1979) 940–944. (Cited in Sec. 3.1.)

[51] J. Badier, et al., Measurement of the K^-/π^- Structure Function Ratio Using the Drell-Yan Process, Phys. Lett. B93 (1980) 354–356. (Cited in Sec. 3.1.)

[52] J. Badier, et al., Experimental Determination of the pi Meson Structure Functions by the Drell-Yan Mechanism, Z. Phys. C18 (1983) 281. (Cited in Secs. 3.1, 20, 3.2 and 22.)

[53] B. Betev, et al., Observation of Anomalous Scaling Violation in Muon Pair Production by 194-GeV/$c\pi^-$ Tungsten Interactions, Z. Phys. C28 (1985) 15. (Cited in Secs. 3.1 and 3.2.)

[54] S. Falciano, et al., Angular distributions of muon pairs produced by 194-gev/c negative pions, Z. Phys. C31 (1986) 513. (Cited in Sec. 3.1.)

[55] M. Guanziroli, et al., Angular Distributions of Muon Pairs Produced by Negative Pions on Deuterium and Tungsten, Z. Phys. C37 (1988) 545. (Cited in Sec. 3.1.)

[56] J. S. Conway, et al., Experimental Study of Muon Pairs Produced by 252-GeV Pions on Tungsten, Phys. Rev. D39 (1989) 92–122. (Cited in Secs. 3.1 and 3.2.)

[57] R. J. Holt, C. D. Roberts, Distribution Functions of the Nucleon and Pion in the Valence Region, Rev. Mod. Phys. 82 (2010) 2991–3044. (Cited in Sec. 3.1.)

[58] M. B. Hecht, C. D. Roberts, S. M. Schmidt, Valence quark distributions in the pion, Phys. Rev. C63 (2001) 025213. (Cited in Sec. 3.1.)

[59] K. Wijesooriya, P. E. Reimer, R. J. Holt, The pion parton distribution function in the valence region, Phys. Rev. C72 (2005) 065203. (Cited in Sec. 3.1.)

[60] M. Aicher, A. Schafer, W. Vogelsang, Soft-gluon resummation and the valence parton distribution function of the pion, Phys. Rev. Lett. 105 (2010) 252003. (Cited in Sec. 3.1.)

[61] P. C. Barry, N. Sato, W. Melnitchouk, C.-R. Ji, First Monte Carlo Global QCD Analysis of Pion Parton Distributions, Phys. Rev. Lett. 121 (15) (2018) 152001. (Cited in Secs. 3.1 and 3.4.2.)

[62] K.-F. Liu, S.-J. Dong, Origin of difference between anti-d and anti-u partons in the nucleon, Phys. Rev. Lett. 72 (1994) 1790–1793. (Cited in Sec. 3.1.)

[63] X. Ji, Parton Physics on a Euclidean Lattice, Phys. Rev. Lett. 110 (2013) 262002. (Cited in Sec. 3.1.)

[64] A. Radyushkin, Nonperturbative Evolution of Parton Quasi-Distributions, Phys. Lett. B767 (2017) 314–320. (Cited in Sec. 3.1.)

[65] A. V. Radyushkin, Quasi-parton distribution functions, momentum distributions, and pseudo-parton distribution functions, Phys. Rev. D96 (3) (2017) 034025. (Cited in Sec. 3.1.)

[66] A. J. Chambers, R. Horsley, Y. Nakamura, H. Perlt, P. E. L. Rakow, G. Schierholz, A. Schiller, K. Somfleth, R. D. Young, J. M. Zanotti, Nucleon Structure Functions from Operator Product Expansion on the Lattice, Phys. Rev. Lett. 118 (24) (2017) 242001. (Cited in Sec. 3.1.)

[67] J.-H. Zhang, J.-W. Chen, L. Jin, H.-W. Lin, A. SchÃ¤fer, Y. Zhao, First direct lattice-QCD calculation of the x-dependence of the pion parton distribution function, Phys. Rev. D100 (3) (2019) 034505. (Cited in Sec. 3.1.)

[68] N. Karthik, T. Izubichi, L. Jin, C. Kallidonis, S. Mukherjee, P. Petreczky, C. Shugert, S. Syritsyn, Renormalized quasi parton distribution function of pion, PoS LATTICE2018 (2019) 109. (Cited in Sec. 3.1.)

[69] J. Karpie, K. Orginos, A. Rothkopf, S. Zafeiropoulos, Reconstructing parton distribution functions from Ioffe time data: from Bayesian methods to Neural Networks, JHEP 04 (2019) 057. (Cited in Sec. 3.1.)

[70] R. S. Sufian, J. Karpie, C. Egerer, K. Orginos, J.-W. Qiu, D. G. Richards, Pion Valence Quark Distribution from Matrix Element Calculated in Lattice QCD, Phys. Rev. D99 (7) (2019) 074507. (Cited in Sec. 3.1.)

[71] M. Ding, K. Raya, D. Binosi, L. Chang, C. D. Roberts, S. M. Schmidt, Symmetry, symmetry breaking, and pion parton distributions, arXiv:1905.05208 . (Cited in Secs. 3.1, 20 and 3.2.)

[72] A. Camsonne, et al., Measurement of Tagged Deep Inelastic Scattering (TDIS), JLAB proposal C12-14-010 . (Cited in Secs. 3.1 and 3.8.)

[73] A. Accardi, et al., Electron Ion Collider: The Next QCD Frontier, Eur. Phys. J. A52 (9) (2016) 268. (Cited in Sec. 3.1.)

[74] C. Chen, L. Chang, C. D. Roberts, S. Wan, H.-S. Zong, Valence-quark distribution functions in the kaon and pion, Phys. Rev. D93 (7) (2016) 074021. (Cited in Sec. 3.1.)

[75] J. J. Aubert, et al., The ratio of the nucleon structure functions $F2_n$ for iron and deuterium, Phys. Lett. 123B (1983) 275–278. (Cited in Secs. 3.1 and 3.3.)

[76] J. Badier, et al., Experimental J/ψ Hadronic Production from 150-GeV/c to 280-GeV/c, Z. Phys. C20 (1983) 101. (Cited in Secs. 3.1, 3.2.2, 3.5.1 and 8.)

[77] M. Corden, et al., Production of muon pairs in the continuum region by 39.5 GeV/c $\pi^{\pm}$, $K^{\pm}$, p and $\bar{p}$ beams incident on a tungsten target, Phys. Lett. 96B (1980) 417–421. (Cited in Sec. 3.2.)

[78] M. Bonesini, et al., High Transverse Momentum Prompt Photon Production by π^- and π^+ on Protons at 280-GeV/c, Z. Phys. C37 (1988) 535. (Cited in Sec. 3.2.)

[79] C. De Marzo, et al., Measurement of direct photon production at large transverse momentum in π^-p, π^+p, and pp collisions at 300 GeV/c, Phys. Rev. D 36 (1987) 8–15. (Cited in Sec. 3.2.)

[80] P. J. Sutton, A. D. Martin, R. G. Roberts, W. J. Stirling, Parton distributions for the pion extracted from Drell-Yan and prompt photon experiments, Phys. Rev. D45 (1992) 2349–2359. (Cited in Secs. 20, 3.2, 3.2.2 and 22.)

[81] M. Gluck, E. Reya, A. Vogt, Pionic parton distributions, Z. Phys. C53 (1992) 651–656. (Cited in Secs. 20, 3.2 and 3.4.2.)

[82] M. Gluck, E. Reya, I. Schienbein, Pionic parton distributions revisited, Eur. Phys. J. C10 (1999) 313–317. (Cited in Secs. 20, 3.2 and 3.4.1.)

[83] S. Chekanov, et al., Leading neutron production in e+ p collisions at HERA, Nucl. Phys. B637 (2002) 3–56. (Cited in Secs. 3.2 and 22.)

[84] F. D. Aaron, et al., Measurement of leading neutron production inÂ deep-inelasticÂ scattering at hera, The European Physical Journal C 68 (3) (2010) 381–399.
URL https://doi.org/10.1140/epjc/s10052-010-1369-4 (Cited in Secs. 3.2 and 22.)

[85] P. C. Barry, N. Sato, W. Melnitchouk, C.-R. Ji, First Monte Carlo Global QCD Analysis of Pion Parton Distributions, Phys. Rev. Lett. 121 (2018) 152001.
URL https://link.aps.org/doi/10.1103/PhysRevLett.121.152001 (Cited in Secs. 20, 3.2, 3.2.1 and 22.)

[86] G. F. de Téramond, T. Liu, R. S. Sufian, H. G. Dosch, S. J. Brodsky, A. Deur, Universality of generalized parton distributions in light-front holographic qcd, Phys. Rev. Lett. 120 (2018) 182001.
URL https://link.aps.org/doi/10.1103/PhysRevLett.120.182001 (Cited in Sec. 3.2.)

[87] J. Lan, C. Mondal, S. Jia, X. Zhao, J. P. Vary, Parton distribution functions from a light front hamiltonian and qcd evolution for light mesons, Phys. Rev. Lett. 122 (2019) 172001.
URL https://link.aps.org/doi/10.1103/PhysRevLett.122.172001 (Cited in Sec. 3.2.)

[88] R. S. Sufian, J. Karpie, C. Egerer, K. Orginos, J.-W. Qiu, D. G. Richards, Pion valence quark distribution from matrix element calculated in lattice qcd, Phys. Rev. D 99 (2019) 074507.
URL https://link.aps.org/doi/10.1103/PhysRevD.99.074507 (Cited in Sec. 3.2.)

[89] J. T. Londergan, G. Q. Liu, E. N. Rodionov, A. W. Thomas, Probing the pion sea with pi D Drell-Yan processes, Phys. Lett. B361 (1995) 110–114. (Cited in Sec. 3.2.1.)

[90] M. Glück, E. Reya, A. Vogt, Dynamical parton distributions revisited, Eur. Phys. J. C5 (1998) 461–470. (Cited in Sec. 3.2.2.)

[91] P. R. Norton, The EMC effect, Rept. Prog. Phys. 66 (2003) 1253–1297. (Cited in Sec. 3.3.)

[92] K. Rith, Present Status of the EMC effect, Subnucl. Ser. 51 (2015) 431–449. (Cited in Sec. 3.3.)

[93] O. Hen, G. A. Miller, E. Piasetzky, L. B. Weinstein, Nucleon-Nucleon Correlations, Short-lived Excitations, and the Quarks Within, Rev. Mod. Phys. 89 (2017) 045002. (Cited in Sec. 3.3.)

[94] J. Seely, et al., New measurements of the EMC effect in very light nuclei, Phys. Rev. Lett. 103 (2009) 202301. (Cited in Sec. 3.3.)

[95] P. Paakkinen, K. J. Eskola, H. Paukkunen, Applicability of pion-nucleus drell-yan data in global analysis of nuclear parton distribution functions, Physics Letters B 768 (2017) 7 – 11.
URL http://www.sciencedirect.com/science/article/pii/S0370269317300990
(Cited in Secs. 23, 3.3 and 25.)

[96] K. Kovarik, et al., nCTEQ15 - Global analysis of nuclear parton distributions with uncertainties in the CTEQ framework, Phys. Rev. D93 (8) (2016) 085037. (Cited in Sec. 3.3.)

[97] K. Eskola, H. Paukkunen, C. Salgado, Eps09 - a new generation of nlo and lo nuclear parton distribution functions, Journal of High Energy Physics 2009 (04) (2009) 065.
URL http://stacks.iop.org/1126-6708/2009/i=04/a=065 (Cited in Sec. 3.3.)

[98] K. J. Eskola, P. Paakkinen, H. Paukkunen, C. A. Salgado, EPPS16: Nuclear parton distributions with LHC data, Eur. Phys. J. C77 (3) (2017) 163. (Cited in Sec. 3.3.)

[99] J. G. Heinrich, et al., Measurement of the Ratio of Sea to Valence Quarks in the Nucleon, Phys. Rev. Lett. 63 (1989) 356–359. (Cited in Sec. 3.3.)

[100] P. Paakkinen, K. J. Eskola, H. Paukkunen, Pion-nucleus drell-yan data as a novel constraint for nuclear pdfs, Proceedings of Science, DIS2017 (2017) 205 – 2010.
URL https://pos.sissa.it/297/205/pdf (Cited in Sec. 3.3.)

[101] I. C. Cloet, W. Bentz, A. W. Thomas, EMC and polarized EMC effects in nuclei, Phys. Lett. B642 (2006) 210–217. (Cited in Sec. 3.3.)

[102] I. Cloet, W. Bentz, A. Thomas, Isovector EMC effect explains the NuTeV anomaly, Phys.Rev.Lett. 102 (2009) 252301. (Cited in Sec. 3.3.)

[103] A. Majumder, M. Van Leeuwen, The Theory and Phenomenology of Perturbative QCD Based Jet Quenching, Prog. Part. Nucl. Phys. 66 (2011) 41. (Cited in Sec. 3.3.)

[104] Y. Mehtar-Tani, J. G. Milhano, K. Tywoniuk, Jet physics in heavy-ion collisions, Int. J. Mod. Phys. A28 (2013) 1340013. (Cited in Sec. 3.3.)

[105] N. Armesto, E. Scomparin, Heavy-ion collisions at the Large Hadron Collider: a review of the results from Run 1, Eur. Phys. J. Plus 131 (2016) 52. (Cited in Sec. 3.3.)

[106] F. Arleo, C.-J. Naïm, S. Platchkov, Initial-state energy loss in cold QCD matter and the Drell-Yan process, JHEP 01 (2019) 129. (Cited in Secs. 3.3 and 25.)

[107] M. A. Vasiliev, et al., Parton energy loss limits and shadowing in drell-yan dimuon production, Phys. Rev. Lett. 83 (1999) 2304–2307.
URL https://link.aps.org/doi/10.1103/PhysRevLett.83.2304 (Cited in Sec. 3.3.)

[108] P. Bordalo, et al., Observation of a Nuclear Dependence of the Transverse Momentum Distribution of Massive Muon Pairs Produced in Hadronic Collisions, Phys. Lett. B193 (1987) 373. (Cited in Sec. 3.3.)

[109] P.-J. Lin, Measurement of quark energy loss in cold nuclear matter at fermilabe906/seaquest, phD thesis defended on 2017 (2017).
URL http://lss.fnal.gov/archive/thesis/2000/fermilab-thesis-2017-18.pdf (Cited in Sec. 3.3.)

[110] F. Arleo, R. Kolevatov, S. PeignÃ©, M. Rustamova, Centrality and pT dependence of J/psi suppression in proton-nucleus collisions from parton energy loss, JHEP 05 (2013) 155. (Cited in Sec. 3.3.)

[111] G. T. Bodwin, E. Braaten, G. P. Lepage, Rigorous QCD analysis of inclusive annihilation and production of heavy quarkonium, Phys. Rev. D51 (1995) 1125–1171, [Erratum: Phys. Rev.D55,5853(1997)]. (Cited in Sec. 3.4.1.)

[112] F. Maltoni, et al., Analysis of charmonium production at fixed-target experiments in the NRQCD approach, Phys. Lett. B638 (2006) 202–208. (Cited in Sec. 3.4.1.)

[113] N. Brambilla, S. Eidelman, B. Heltsley, R. Vogt, G. Bodwin, et al., Heavy quarkonium: progress, puzzles, and opportunities, Eur. Phys. J. C 71 (2011) 1534. (Cited in Sec. 3.4.1.)

[114] V. D. Barger, W.-Y. Keung, R. J. N. Phillips, On psi and Upsilon Production via Gluons, Phys. Lett. 91B (1980) 253–258. (Cited in Sec. 3.4.1.)

[115] V. D. Barger, W.-Y. Keung, R. J. N. Phillips, Hadroproduction of ψ and Υ, Z. Phys. C6 (1980) 169. (Cited in Sec. 3.4.1.)

[116] G. T. Bodwin, E. Braaten, J. Lee, Comparison of the color-evaporation model and the NRQCD factorization approach in charmonium production, Phys. Rev. D72 (2005) 014004. (Cited in Sec. 3.4.1.)

[117] N. Brambilla, S. Eidelman, P. Foka, S. Gardner, A. Kronfeld, et al., QCD and Strongly Coupled Gauge Theories: Challenges and Perspectives, Eur. Phys. J. C 74 (10) (2014) 2981. (Cited in Sec. 3.4.1.)

[118] P. Faccioli, The return of quarkonia, CernCourrier . (Cited in Sec. 3.4.1.)

[119] K.-T. Chao, Y.-Q. Ma, H.-S. Shao, K. Wang, Y.-J. Zhang, J/ψ Polarization at Hadron Colliders in Nonrelativistic QCD, Phys. Rev. Lett. 108 (2012) 242004. (Cited in Sec. 3.4.1.)

[120] P. Faccioli, C. Lourenço, M. Araújo, J. a. Seixas, I. Krätschmer, V. Knünz, From identical S- and P-wave p_{T} spectra to maximally distinct polarizations: probing NRQCD with χ states, Eur. Phys. J. C78 (3) (2018) 268. (Cited in Sec. 3.4.1.)

[121] P. Faccioli, C. Lourenco, NRQCD colour-octet expansion vs LHC quarkonium production: signs of a hierarchy puzzle?, to appear in Eur. Phys. J. . (Cited in Sec. 3.4.1.)

[122] Y.-Q. Ma, R. Vogt, Quarkonium Production in an Improved Color Evaporation Model, Phys. Rev. D94 (11) (2016) 114029. (Cited in Sec. 3.4.1.)

[123] V. Cheung, R. Vogt, Production and polarization of prompt J/ψ in the improved color evaporation model using the k_T-factorization approach, Phys. Rev. D98 (11) (2018) 114029 and private communication. (Cited in Secs. 3.4.1, 26 and 3.4.1.)

[124] P. Faccioli, C. Lourenco, J. Seixas, H. K. Wohri, Determination of χ_c and χ_b polarizations from dilepton angular distributions in radiative decays, Phys. Rev. D83 (2011) 096001. (Cited in Secs. 3.4.1 and 3.4.2.)

[125] P. Faccioli, C. Lourenço, M. Araújo, V. Knünz, I. Krätschmer, J. a. Seixas, Quarkonium production at the LHC: A data-driven analysis of remarkably simple experimental patterns, Phys. Lett. B773 (2017) 476–486. (Cited in Sec. 3.4.1.)

[126] S. P. Baranov, A. V. Lipatov, N. P. Zotov, Prompt charmonia production and polarization at LHC in the NRQCD with k_T -factorization. Part I: $\psi(2S)$ meson, Eur. Phys. J. C75 (9) (2015) 455. (Cited in Sec. 3.4.1.)

[127] S. P. Baranov, A. V. Lipatov, N. P. Zotov, Prompt charmonia production and polarization at LHC in the NRQCD with kt-factorization. Part II: χ_c mesons, Phys. Rev. D93 (9) (2016) 094012. (Cited in Sec. 3.4.1.)

[128] H.-L. Lai, M. Guzzi, J. Huston, Z. Li, P. M. Nadolsky, et al., New parton distributions for collider physics, Phys.Rev. D82 (2010) 074024. (Cited in Sec. 3.4.1.)

[129] M. S. Kowitt, et al., Production of J / psi at large x(F) in 800-GeV/c p copper and p beryllium collisions, Phys. Rev. Lett. 72 (1994) 1318–1321. (Cited in Sec. 8.)

[130] M. H. Schub, et al., Measurement of J/ψ and ψ' production in 800-GeV/c proton - gold collisions, Phys. Rev. D52 (1995) 1307, [Erratum: Phys. Rev.D53,570(1996)]. (Cited in Sec. 8.)

[131] M. J. Leitch, et al., Measurement of J / psi and psi-prime suppression in p-A collisions at 800-GeV/c, Phys. Rev. Lett. 84 (2000) 3256–3260. (Cited in Sec. 8.)

[132] B. Alessandro, et al., Charmonia and Drell-Yan production in proton-nucleus collisions at the CERN SPS, Phys. Lett. B553 (2003) 167–178. (Cited in Sec. 8.)

[133] M. C. Abreu, et al., Charmonia production in 450-GeV/c proton induced reactions, Phys. Lett. B444 (1998) 516–522. (Cited in Sec. 8.)

[134] I. Abt, et al., Measurement of the J/ψ production cross section in 920-GeV/c fixed-target proton-nucleus interactions, Phys. Lett. B638 (2006) 407–414. (Cited in Sec. 8.)

[135] P. Faccioli, C. Lourenço, M. Araújo, J. Seixas, Universal kinematic scaling as a probe of factorized long-distance effects in high-energy quarkonium production, Eur. Phys. J. C78 (2) (2018) 118. (Cited in Sec. 3.5.2.)

[136] F. D. Aaron, et al., Measurement of Leading Neutron Production in Deep-Inelastic Scattering at HERA, Eur. Phys. J. C68 (2010) 381–399. (Cited in Sec. 3.8.)

[137] K. Park, Measurement of Kaon Structure Function through Tagged Deep Inelastic Scattering (TDIS), JLAB proposal C12-15-006A . (Cited in Sec. 3.8.)

[138] A. C. Aguilar, et al., Pion and Kaon Structure at the Electron-Ion Collider, arXiv:1907.08218 . (Cited in Sec. 3.8.)

[139] S. Riordan, et al., The EMC PVDIS Experiment: A Constraint on Isovector Dependent Nuclear Modification Effects Using Parity-Violating Deep Inelastic Scattering, JLAB proposal C12-14-007 . (Cited in Sec. 3.8.)

[140] M. Aguilar, et al., Antiproton Flux, Antiproton-to-Proton Flux Ratio, and Properties of Elementary Particle Fluxes in Primary Cosmic Rays Measured with the Alpha Magnetic Spectrometer on the International Space Station, Phys. Rev. Lett. 117 (9) (2016) 091103. (Cited in Secs. 4.1, 32, 33 and 4.1.)

[141] L. Accardo, et al., High Statistics Measurement of the Positron Fraction in Primary Cosmic Rays of 0.5 - 500 GeV with the Alpha Magnetic Spectrometer on the International Space Station, Phys. Rev. Lett. 113 (2014) 121101. (Cited in Sec. 4.1.)

[142] M. e. l. Aguilar, Towards Understanding the Origin of Cosmic-Ray Positrons, Phys. Rev. Lett. 122 (4) (2019) 041102. (Cited in Sec. 4.1.)

[143] S. D. Torre, M. Gervasi, P. Rancoita, D. Rozza, A. Treves, Pulsar wind nebulae as a source of the observed electron and positron excess at high energy: The case of vela-x, Journal of High Energy Astrophysics 8 (2015) 27 – 34.
URL http://www.sciencedirect.com/science/article/pii/S2214404815000427
(Cited in Sec. 4.1.)

[144] T. Linden, S. Profumo, Probing the Pulsar Origin of the Anomalous Positron Fraction with AMS-02 and Atmospheric Cherenkov Telescopes, Astrophys. J. 772 (2013) 18. (Cited in Sec. 4.1.)

[145] M. D. Mauro, F. Donato, N. Fornengo, A. Vittino, Dark matter vs. astrophysics in the interpretation of ams-02 electron and positron data, Journal of Cosmology and Astroparticle Physics 2016 (05) (2016) 031–031, exported from https://app.dimensions.ai on 2019/05/21.

URL https://app.dimensions.ai/details/publication/pub.1059143087 (Cited in Sec. 4.1.)

[146] B. Wang, X. Bi, S. Lin, P. Yin, Explanations of the DAMPE high energy electron/positron spectrum in the dark matter annihilation and pulsar scenarios, Sci. China Phys. Mech. Astron. 61 (10) (2018) 101004. (Cited in Sec. 4.1.)

[147] S. Manconi, M. D. Mauro, F. Donato, Multi-messenger constraints to the local emission of cosmic-ray electrons, Journal of Cosmology and Astroparticle Physics 2019 (04) (2019) 024–024.
URL https://arxiv.org/abs/1803.01009 (Cited in Sec. 4.1.)

[148] S. Manconi, M. D. Mauro, F. Donato, Dipole anisotropy in cosmic electrons and positrons: inspection on local sources, Journal of Cosmology and Astroparticle Physics 2017 (01) (2017) 006–006.
URL https://app.dimensions.ai/details/publication/pub.1059143509andhttp://arxiv.org/pdf/1611.06237 (Cited in Sec. 4.1.)

[149] O. Adriani, G. A. Bazilevskaya, G. C. Barbarino, Measurement of the flux of primary cosmic ray antiprotons with energies of 60 mev to 350 gev in the pamela experiment, JETP Letters 96 (10) (2013) 621–627.
URL https://doi.org/10.1134/S002136401222002X (Cited in Sec. 4.1.)

[150] M. J. Boschini, S. D. Torre, M. Gervasi, D. Grandi, G. Johannesson, M. Kachelriess, G. L. Vacca, N. Masi, I. V. Moskalenko, E. Orlando, S. S. Ostapchenko, S. Pensotti, T. A. Porter, L. Quadrani, P. G. Rancoita, D. Rozza, M. Tacconi, Solution of heliospheric propagation: Unveiling the local interstellar spectra of cosmic-ray species, The Astrophysical Journal 840 (2) (2017) 115, exported from https://app.dimensions.ai on 2019/05/20.
URL https://app.dimensions.ai/details/publication/pub.1085528582andhttp://iopscience.iop.org/article/10.3847/1538-4357/aa6e4f/pdf (Cited in Secs. 4.1 and 32.)

[151] M. J. Boschini, S. D. Torre, M. Gervasi, D. Grandi, G. Johannesson, G. La Vacca, N. Masi, I. V. Moskalenko, S. Pensotti, T. A. Porter, L. Quadrani, P. G. Rancoita, D. Rozza, M. Tacconi, Helmod in the works: From direct observations to the local interstellar spectrum of cosmic-ray electrons, The Astrophysical Journal 854 (2) (2018) 94, exported from https://app.dimensions.ai on 2019/05/20.
URL https://app.dimensions.ai/details/publication/pub.1101074143andhttps://boa.unimib.it/bitstream/10281/185721/1/2018_ApJ_GALPROP_electrons.pdf (Cited in Secs. 4.1 and 32.)

[152] M. J. Boschini, S. D. Torre, M. Gervasi, D. Grandi, G. Johannesson, G. L. Vacca, N. Masi, I. V. Moskalenko, S. Pensotti, T. A. Porter, L. Quadrani, P. G. Rancoita, D. Rozza, M. Tacconi, Deciphering the local interstellar spectra of primary cosmic-ray species with helmod, The Astrophysical Journal 858 (1) (2018) 61, exported from https://app.dimensions.ai on 2019/05/20.
URL https://app.dimensions.ai/details/publication/pub.1103825751andhttps://boa.unimib.it/bitstream/10281/196816/1/2018_ApJ_GALPROP_ions.pdf (Cited in Secs. 4.1 and 32.)

[153] C. Evoli, P. Blasi, G. Morlino, R. Aloisio, Origin of the cosmic ray galactic halo driven by advected turbulence and self-generated waves, Phys. Rev. Lett. 121 (2018) 021102.
URL https://link.aps.org/doi/10.1103/PhysRevLett.121.021102 (Cited in Sec. 4.1.)

[154] V. Bresci, E. Amato, P. Blasi, G. Morlino, Effects of reacceleration and source grammage on secondary cosmic rays spectra, arXiv . (Cited in Sec. 4.1.)

[155] C. Evoli, R. Aloisio, P. Blasi, Galactic Cosmic Rays after AMS-02, arXiv . (Cited in Sec. 4.1.)

[156] Y. Génolini, et al., Cosmic-ray transport from AMS-02 B/C data: benchmark models and interpretation, arXiv . (Cited in Sec. 4.1.)

[157] M. Boschini, S. D. Torre, M. Gervasi, G. L. Vacca, P. Rancoita, The helmod model in the works for inner and outer heliosphere: From ams to voyager probes observations, Advances in Space Research .
URL http://www.sciencedirect.com/science/article/pii/S0273117719302509
(Cited in Sec. 4.1.)

[158] M. di Mauro, F. Donato, A. Goudelis, P. D. Serpico, New evaluation of the antiproton production cross section for cosmic ray studies, Phys. Rev. D 90 (2014) 085017.
URL https://link.aps.org/doi/10.1103/PhysRevD.90.085017 (Cited in Sec. 4.1.)

[159] J. Feng, N. Tomassetti, A. Oliva, Bayesian analysis of spatial-dependent cosmic-ray propagation: Astrophysical background of antiprotons and positrons, Phys. Rev. D 94 (2016) 123007.
URL https://link.aps.org/doi/10.1103/PhysRevD.94.123007 (Cited in Secs. 4.1 and 32.)

[160] M. W. Winkler, Cosmic Ray Antiprotons at High Energies, JCAP 1702 (02) (2017) 048. (Cited in Sec. 4.1.)

[161] F. Donato, M. Korsmeier, M. Di Mauro, Prescriptions on antiproton cross section data for precise theoretical antiproton flux predictions, Phys. Rev. D 96 (2017) 043007.
URL https://link.aps.org/doi/10.1103/PhysRevD.96.043007 (Cited in Sec. 4.1.)

[162] M. Korsmeier, F. Donato, M. Di Mauro, Production cross sections of cosmic antiprotons in the light of new data from the na61 and lhcb experiments, Phys. Rev. D 97 (2018) 103019.
URL https://link.aps.org/doi/10.1103/PhysRevD.97.103019 (Cited in Secs. 4.1, 32 and 4.1.)

[163] A. Reinert, M. W. Winkler, A Precision Search for WIMPs with Charged Cosmic Rays, JCAP 1801 (01) (2018) 055. (Cited in Sec. 4.1.)

[164] A. C. Cummings, E. C. Stone, B. C. Heikkila, N. Lal, W. R. Webber, G. Johannesson, I. V. Moskalenko, E. Orlando, T. A. Porter, Galactic cosmic rays in the local interstellar medium: Voyager 1 observations and model results, The Astrophysical Journal 831 (1) (2016) 18, exported from https://app.dimensions.ai on 2019/05/21.
URL https://app.dimensions.ai/details/publication/pub.1071473884andhttp://iopscience.iop.org/article/10.3847/0004-637X/831/1/18/pdf (Cited in Sec. 4.1.)

[165] M. W. Winkler, Cosmic Ray Antiprotons at High Energies, JCAP 1702 (02) (2017) 048. (Cited in Secs. 4.1 and 4.7.)

[166] A. Cuoco, M. Krämer, M. Korsmeier, Novel dark matter constraints from antiprotons in light of ams-02, Phys. Rev. Lett. 118 (2017) 191102.
URL https://link.aps.org/doi/10.1103/PhysRevLett.118.191102 (Cited in Sec. 4.1.)

[167] A. Cuoco, J. Heisig, M. Korsmeier, M. Kramer, Constraining heavy dark matter with cosmic-ray antiprotons, JCAP 1804 (04) (2018) 004. (Cited in Sec. 4.1.)

[168] A. Cuoco, J. Heisig, L. Klamt, M. Korsmeier, M. Kramer, Scrutinizing the evidence for dark matter in cosmic-ray antiprotons, Phys. Rev. D99 (10) (2019) 103014. (Cited in Sec. 4.1.)

[169] M.-Y. Cui, X. Pan, Q. Yuan, Y.-Z. Fan, H.-S. Zong, Revisit of cosmic ray antiprotons from dark matter annihilation with updated constraints on the background model from AMS-02 and collider data, JCAP 1806 (06) (2018) 024. (Cited in Sec. 4.1.)

[170] I. Cholis, T. Linden, D. Hooper, A Robust Excess in the Cosmic-Ray Antiproton Spectrum: Implications for Annihilating Dark Matter, FERMILAB-PUB . (Cited in Sec. 4.1.)

[171] N. Masi, M. Ballardini, A conservative assessment of the current constraints on dark matter annihilation from cosmic rays and cmb observations, International Journal of Modern Physics D 26 (06) (2017) 1750041.
URL https://doi.org/10.1142/S0218271817500419 (Cited in Sec. 4.1.)

[172] C. Alt, et al., Inclusive production of charged pions in p+p collisions at 158-GeV/c beam momentum, Eur. Phys. J. C45 (2006) 343–381. (Cited in Sec. 4.1.)

[173] T. Anticic, et al., Inclusive production of protons, anti-protons and neutrons in p+p collisions at 158-GeV/c beam momentum, Eur. Phys. J. C65 (2010) 9–63. (Cited in Secs. 4.1 and 4.7.)

[174] A. Aduszkiewicz, et al., Measurements of $\pi^{\pm}$, $K^{\pm}$, p and $\bar{p}$ spectra in proton-proton interactions at 20, 31, 40, 80 and 158 GeV/c with the NA61/SHINE spectrometer at the CERN SPS, Eur. Phys. J. C77 (10) (2017) 671. (Cited in Secs. 4.1, 4.7 and 48.)

[175] R. Aaij, et al., Measurement of Antiproton Production in pHe Collisions at $\sqrt{s_{NN}}$ = 110 GeV, Phys. Rev. Lett. 121 (22) (2018) 222001. (Cited in Secs. 4.1, 4.7 and 49.)

[176] P. Abbon, et al., The COMPASS Setup for Physics with Hadron Beams, Nucl. Instr. Meth. A 779 (2015) 69–115. (Cited in Secs. 4.2, 4.2, 4.6 and 5.5.)

[177] H. W. Atherton, C. Bovet, N. Doble, G. von Holtey, L. Piemontese, A. Placci, M. Placidi, D. E. Plane, M. Reinharz, E. Rossa, Precise Measurements of Particle Production by 400-GeV/c Protons on Beryllium Targets, CERN . (Cited in Sec. 9.)

[178] P. Abbon, M. Alexeev, H. Angerer, G. Baum, R. Birsa, et al., Particle identification with COMPASS RICH-1, Nucl. Instr. Meth. A 631 (2011) 26–39. (Cited in Secs. 4.3 and 5.6.)

[179] F. Donato, M. Korsmeier, M. Di Mauro, Prescriptions on antiproton cross section data for precise theoretical antiproton flux predictions, Phys. Rev. D96 (4) (2017) 043007. (Cited in Secs. 47 and 4.7.)

[180] H. W. Atherton, et al., DIRECT MEASUREMENT OF THE LIFETIME OF THE NEUTRAL PION, Phys. Lett. 158B (1985) 81–84. (Cited in Sec. 4.7.)

[181] H. Atherton, L. Celnikier, B. French, J. Kinson, K. Myklebost, et al., Two-body hyperon production by 5.7 GeV/c antiprotons on protons, Phys. Lett. B 30 (1969) 494–497. (Cited in Sec. 4.7.)

[182] D. Dekkers, J. A. Geibel, R. Mermod, G. Weber, T. R. Willitts, K. Winter, B. Jordan, M. Vivargent, N. M. King, E. J. N. Wilson, Experimental study of particle production at small angles in nucleon-nucleon collisions at 19 and 23 gev/c, Phys. Rev. 137 (1965) B962–B978.
URL https://link.aps.org/doi/10.1103/PhysRev.137.B962 (Cited in Sec. 4.7.)

[183] P. Capiluppi, G. Giacomelli, A. Rossi, G. Vannini, A. Bertin, et al., Charged particle production in proton-proton inclusive reactions at very high energies, Nucl.Phys. B79 (189). (Cited in Sec. 4.7.)

[184] T. O. D. R. R. S. e. a. J. Johnson, R. Kammerud, Inclusive production of $\pi^{\pm}$, $k^{\pm}$, p, $\bar{p}$ in high-energy p-p collisions, Phys.Rev.Lett. 39 (1173). (Cited in Sec. 4.7.)

[185] I. Arsene, et al., Single Transverse Spin Asymmetries of Identified Charged Hadrons in Polarized p+p Collisions at $\sqrt{s}$ = 62.4 GeV, Phys. Rev. Lett. 101 (2008) 042001. (Cited in Sec. 4.7.)

[186] M. Korsmeier, F. Donato, M. Di Mauro, Production cross sections of cosmic antiprotons in the light of new data from the NA61 and LHCb experiments, Phys. Rev. D97 (10) (2018) 103019. (Cited in Sec. 4.7.)

[187] P. Abbon, et al., The COMPASS setup for physics with hadron beams, Nuclear Instruments and Methods in Physics Research Section A: Accelerators, Spectrometers, Detectors and Associated Equipment 779 (2015) 69 – 115.
URL http://www.sciencedirect.com/science/article/pii/S0168900215000662
(Cited in Secs. 5.1 and 5.4.2.)

[188] B. Ketzer, Q. Weitzel, S. Paul, F. Sauli, L. Ropelewski, Performance of triple gem tracking detectors in the compass experiment, Nuclear Instruments and Methods in Physics Research Section A: Accelerators, Spectrometers, Detectors and Associated Equipment 535 (1) (2004) 314 – 318, proceedings of the 10th International Vienna Conference on Instrumentation.
URL http://www.sciencedirect.com/science/article/pii/S0168900204016687
(Cited in Sec. 5.2.1.)

[189] B. Ketzer, et al., A triple gem detector with pixel readout for high-rate beam tracking in compass, Nuclear Science Symposium Conference Record, 2007. NSS '07. IEEE, Vol. 1, IEEE, Piscataway, NJ 1 (2007) 242–244. (Cited in Sec. 5.2.1.)

[190] J. Metcalfe, G. De Geronimo, J. Fried, S. Li, N. Nambiar, V. Polychronakos, E. Vernon, Design and characterization of the VMM1 ASIC for micropattern gas detectors, Nucl. Instrum. Meth. A732 (2013) 526–529. (Cited in Sec. 5.2.1.)

[191] G. Iakovidis, VMM - An ASIC for micropattern detectors, EPJ Web Conf. 174 (2018) 07001. (Cited in Sec. 5.2.1.)

[192] M. D. R. Rolo, et al., A custom readout electronics for the BESIII CGEM detector, Journal of Instrumentation 12 (07) (2017) C07017–C07017.
URL https://doi.org/10.1088 (Cited in Sec. 5.2.2.)

[193] I. Ortega, Accurate profile measurement of the low intensity secondary beams in the cern experimental areas, phD defense February 23, 2018 (2018).
URL https://indico.cern.ch/event/678621/attachments/1610907/2557875/phd_public_defence_Inaki_Ortega.pdf (Cited in Sec. 5.2.3.)

[194] Y. Bai, M. Bodlak, V. Frolov, V. Jary, S. Huber, I. Konorov, D. Levit, J. Novy, D. Steffen, M. Virius, Overview and future developments of the fpga-based daq of compass, Journal of Instrumentation 11 (02) (2016) C02025.
URL http://stacks.iop.org/1748-0221/11/i=02/a=C02025 (Cited in Sec. 5.2.4.)

[195] A. Mann, I. Konorov, H. Angerer, M. Kramer, S. Huber, B. Grube, J. Friedrich, B. Ketzer, S. Uhl, F. Haas, A.-M. Dinkelbach, S. Grabmuller, S. Paul, The universal sampling adc readout system of the compass experiment, in: IEEE Nuclear Science Symposium Conference Record, 2009, pp. 2225 – 2228. (Cited in Sec. 5.2.4.3.)

[196] J. P. Burq, et al., Soft $\pi^- p$ and pp Elastic Scattering in the Energy Range 30-GeV to 345-GeV, Nucl. Phys. B217 (1983) 285–335. (Cited in Sec. 5.3.1.)

[197] A. V. Dobrovolsky, et al., Study of the nuclear matter distribution in neutron-rich Li isotopes, Nucl. Phys. A766 (2006) 1–24. (Cited in Sec. 5.3.1.)

[198] V. A. Andreev, et al., Measurement of Muon Capture on the Proton to 1% Precision and Determination of the Pseudoscalar Coupling g_P, Phys. Rev. Lett. 110 (1) (2013) 012504. (Cited in Sec. 5.3.1.)

[199] A. Vorobyev, Precision measurement of the proton charge radius in electron proton scattering, in: 8th Workshop on Hadron Structure and QCD: From Low to High Energies (HSQCD 2018) Gatchina, Russia, August 6-10, 2018, 2019, pp. 1–10. (Cited in Sec. 5.3.1.)

[200] J. J. Lowke, J. H. Parker, Theory of Electron Diffusion Parallel to Electric Fields. 2. Application to Real Gases, Phys. Rev. 181 (1969) 302–311. (Cited in Sec. 5.3.1.)

[201] L. W. Cochran, D. W. Forester, Diffusion of slow electrons in gases, Phys. Rev. 126 (1962) 1785–1788.
URL https://link.aps.org/doi/10.1103/PhysRev.126.1785 (Cited in Sec. 5.3.1.)

[202] A. Michalowska, O. Gevin, O. Lemaire, F. Lugiez, P. Baron, H. Grabas, F. Pinsard, O. Limousin, E. Delagnes, Idef-x hd: A low power multi-gain cmos asic for the readout of cd(zn)te detectors, in: IEEE Nuclear Science Symposuim Medical Imaging Conference, 2010, pp. 1556–1559. (Cited in Sec. 5.3.2.)

[203] L. Gallego Manzano, et al., XEMIS: A liquid xenon detector for medical imaging, Nucl. Instrum. Meth. A787 (2015) 89–93. (Cited in Sec. 5.3.2.)

[204] Iakovidis, George, Vmm - an asic for micropattern detectors, EPJ Web Conf. 174 (2018) 07001.
URL https://doi.org/10.1051/epjconf/201817407001 (Cited in Sec. 5.3.2.)

[205] J. Adolfsson, et al., SAMPA Chip: the New 32 Channels ASIC for the ALICE TPC and MCH Upgrades, JINST 12 (04) (2017) C04008. (Cited in Sec. 5.3.2.)

[206] H. Augustin, N. Berger, S. Dittmeier, F. Ehrler, C. Grzesik, J. Hammerich, A. Herkert, L. Huth, J. Kröger, F. Meier Aeschbacher, I. Perić, M. Prathapan, R. Schimassek, A. Schöning, I. Sorokin, A. Weber, D. Wiedner, H. Zhang, M. Zimmermann, Mupix8 large area monolithic hvcmos pixel detector for the mu3e experiment, Nuclear Instruments and Methods in Physics Research Section A: Accelerators, Spectrometers, Detectors and Associated Equipment . (Cited in Sec. 5.3.3.)

[207] I. Peric, A novel monolithic pixelated particle detector implemented in high-voltage CMOS technology, Nucl. Instrum. Meth. A582 (2007) 876–885. (Cited in Sec. 5.3.3.)

[208] L. Huth, The mupix8 telescope (2019).
URL https://indico.cern.ch/event/731649/contributions/3263101/attachments/1779545/2894482/bttb7_huth_final.pdf (Cited in Sec. 5.3.3.)

[209] C. Ghabrous Larrea, K. Harder, D. Newbold, D. Sankey, A. Rose, A. Thea, T. Williams, IPbus: a flexible Ethernet-based control system for xTCA hardware, JINST 10 (02) (2015) C02019. (Cited in Sec. 5.3.3.)

[210] F. Anghinolfi, P. Jarron, F. Krummenacher, E. Usenko, M. Williams, NINO: An Ultrafast Low-Power Front-End Amplifier Discriminator for the Time-of-Flight Detector in the ALICE Experiment, IEEE Transactions of Nuclear Science 51 (5) (2004) 1974–1978. (Cited in Secs. 5.3.4 and 5.3.7.)

[211] The COMPASS Collaboration, COMPASS-II Proposal, CERN-SPSC-2010-014, SPSC-P-340 .
URL https://cds.cern.ch/record/1265628 (Cited in Sec. 5.4.1.)

[212] H. Vincke, Shielding optimization for 2018 drell-yan run, Tech. rep., CERN, Geneva (Nov. 2017).
URL https://indico.cern.ch/event/678411/contributions/2779552/attachments/

1552346/2439351/Shielding_optimization.pdf (Cited in Sec. 5.4.1.)

[213] H. M. C. Ahdida, M. Casolino, Compass - 2018 radiation protection survey, Tech. Rep. 2006094, CERN, Geneva (Jan. 2019).
URL https://edms.cern.ch/ui/file/2006094/1/Compass-RP-Survey_2.pdf (Cited in Sec. 5.4.1.)

[214] T. Böhlen, F. Cerutti, M. Chin, A. Fassò, A. Ferrari, P. Ortega, A. Mairani, P. Sala, G. Smirnov, V. Vlachoudis, The fluka code: Developments and challenges for high energy and medical applications, Nuclear Data Sheets 120 (2014) 211 – 214.
URL http://www.sciencedirect.com/science/article/pii/S0090375214005018 (Cited in Sec. 5.4.1.)

[215] A. Ferrari, P. R. Sala, A. Fasso, J. Ranft, FLUKA: A multi-particle transport code (Program version 2005), CERN-2005-010, SLAC-R-773, INFN-TC-05-11 . (Cited in Sec. 5.4.1.)

[216] V. Vlachoudis, Flair: A powerful but user friendly graphical interface for fluka, in: Proceedings of the International Conference on Mathematics, Computational Methods and Reactor Physics, 2009, pp. 1–11. (Cited in Sec. 5.4.1.)

[217] G. A. Rinella, The alpide pixel sensor chip for the upgrade of the alice inner tracking system, Nuclear Instruments and Methods in Physics Research Section A: Accelerators, Spectrometers, Detectors and Associated Equipment 845 (2017) 583 – 587, proceedings of the Vienna Conference on Instrumentation 2016.
URL http://www.sciencedirect.com/science/article/pii/S0168900216303825 (Cited in Secs. 5.4.1 and 5.4.2.)

[218] I. Mandić, Silicon sensors for hl-lhc tracking detectors, Nuclear Instruments and Methods in Physics Research Section A: Accelerators, Spectrometers, Detectors and Associated Equipment 732 (2013) 126 – 129, vienna Conference on Instrumentation 2013.
URL http://www.sciencedirect.com/science/article/pii/S0168900213008504 (Cited in Sec. 5.4.1.)

[219] E. Albrecht, et al., Status and characterisation of compass rich-1, Nuclear Instruments and Methods in Physics Research Section A: Accelerators, Spectrometers, Detectors and Associated Equipment 553 (1) (2005) 215 – 219, proceedings of the fifth International Workshop on Ring Imaging Detectors.
URL http://www.sciencedirect.com/science/article/pii/S0168900205016001 (Cited in Sec. 5.6.)

[220] P. Abbon, et al., Read-out electronics for fast photon detection with compass rich-1, Nuclear Instruments and Methods in Physics Research Section A: Accelerators, Spectrometers, Detectors and Associated Equipment 587 (2) (2008) 371 – 387.
URL http://www.sciencedirect.com/science/article/pii/S0168900207024576 (Cited in Sec. 5.6.)

[221] P. Abbon, M. Alexeev, H. Angerer, R. Birsa, P. Bordalo, et al., Design and construction of the fast photon detection system for COMPASS RICH-1, Nucl. Instr. Meth. A 616 (2010) 21–37. (Cited in Sec. 5.6.)

[222] B. Dey, M. Borsato, N. Arnaud, D. W. G. S. Leith, K. Nishimura, D. A. Roberts, B. N. Ratcliff, G. Varner, J. Va'vra, Design and performance of the Focusing DIRC detector, Nucl. Instrum. Meth. A775 (2015) 112–131. (Cited in Sec. 5.6.)

[223] C. Adolph, W. Eyrich, J. Jaus, J. Heimlich, A. Schmidt, A. Teufel, K. Ulbrich, C. Vogel, Prototype tests for a dirc detector for the wasa-at-cosy experiment, Nuclear Instruments and Methods in Physics Research Section A: Accelerators, Spectrometers, Detectors and Associated Equipment 639 (1) (2011) 185 – 189, proceedings of the Seventh International Workshop on Ring Imaging Cherenkov Detectors.
URL http://www.sciencedirect.com/science/article/pii/S0168900210023260
(Cited in Sec. 5.6.)

[224] P. Bernard, P. Lazeyras, H. Lengeler, V. Vaghin, Particle separation with two-and three-cavity RF separators at CERN, CERN Yellow Reports: Monographs, CERN, Geneva, 1968.
URL http://cds.cern.ch/record/275757 (Cited in Sec. 6.1.)